Study on the Unsteady Pressure Characteristics of Bluff Bodies focusing on Flutter Stabilization of Long-Span Bridges

Cristiano Augusto Trein

2009

Abstract

With the increase of the spans in the last decades, new concepts of projects and perceptions about bridges around the world have imposed the need of the development of new design techniques. Aerodynamic instabilities, which were not being of concern not long time ago, started to demand special care during all phases of the projects. Among them, *coupled-flutter* instability has gained remarkable importance, due to its catastrophic consequences and impacts on the safety of the structure.

Concerning *coupled-flutter*, *aerodynamic derivatives* have been regarded as fundamental components for the assessment of the stability of long-span bridges, resulting in that the focus during the proposition of the bridge deck geometry has been put essentially on the control of those empirical indices. The relationships between bridge deck geometric characteristics and the values assumed by those indices are recognized to be non-linear and straightforward approaches for their prompt evaluation are still not available. Because of that, trial and error experimental techniques based on wind tunnel tests have been regarded as main tools in the search of geometric configurations of bridge decks that satisfy the flutter stability requirements from the aerodynamic derivatives point of view.

Since aerodynamic derivatives are resultant from the unsteady pressure characteristics developed along the bridge deck, it must be more rational to search for relationships between deck geometry and flutter stabilization from the unsteady pressure characteristics point of view. However, the complex geometric characteristics associated to modern long-span bridges may impose difficulties on the pressure measurements in wind tunnel tests, becoming counter-productive. So, the direct evaluation of the aerodynamic derivatives through alternative methods has been preferred in wind tunnel tests.

In this research, the impacts of the deck geometric characteristics on the aerodynamic

derivatives and, consequently, on flutter stabilization are assessed from the unsteady pressure characteristics point of view. Rectangular cross-sections arranged in single box and two-box configurations are used as base geometries and the influences of different *geometric singularities* (geometric modifications as leading edges, vertical plates and slots) on the unsteady pressure characteristics of those cylinders are systematized through the proposition of semi-empirical formulations. The knowledge generated herein may serve as a base for the development of a design framework based on the direct *manipulation* of the unsteady pressure characteristics of the deck through the use of *geometric singularities*, aiming the flutter stabilization by controlling indirectly the aerodynamic derivatives. Such a framework is to be used in substitution of some stages of wind tunnel test campaigns, and its feasibility is evaluated along the study.

It was concluded that the relationships of *geometric singularities* with the unsteady pressure characteristics are much more linear and predictable than their relationships with the *aerodynamic derivatives*, opening a new methodology for the proposition of geometric improvements. Data regarding the geometries studied herein are also provided along the study, as reference for future development.

Contents

List of Figures

List of Tables

List of Symbols

ROMAN SYMBOLS

A_i^* - aerodynamic derivatives for pitching moment

A_ψ - *amplitude* of the phase difference distribution approximated by a sinusoidal equation

a - distance from the rotational center to the midchord, normalized by b

a_H - coefficient of Bessel function

B - width of the deck [m]

B^* - width of the individual box in a two-box cross-section [m]

BD_{eq} - equivalent side ratio

B_{2box} - total width of the two-box cross-section, defined by B_{2box}= 2.B^*+ gap length

B/D - side ratio of the deck

$(B/D)_{ap}$ - apparent side ratio

b - half-width of the deck; b=$B/2$ [m]

b_{eq} - equivalent half-width b [m]

b_H - coefficient of Bessel function

C_L - aerodynamic lift coefficient

C_M - aerodynamic moment coefficient

CD - acronym for *corner down*, referring to leading edge with a triangular fairing with its corner aligned with the lower surface of the body

CEVA - acronym for Complex Eigenvalue Analysis

CU - acronym for *corner up*, referring to leading edge with a triangular fairing with its corner aligned with the upper surface of the body

$C_p(x^*,\ t)$ - total pressure coefficient at location x^* in time t; $C_p(x^*, t) = \overline{C}_p(x^*) + \tilde{C}_p(x^*, t)$

$\tilde{C}_p(x^*)$ - amplitude of the unsteady pressures

$\tilde{C}_p(x^*,\ t)$ - unsteady pressure coefficient for time t at x^*

$\tilde{C}_{pmax}$ - maximum amplitude of unsteady pressures

$\tilde{C}_p N(x^*)$ - unsteady pressure amplitude distribution normalized by its peak value

$\tilde{C}_{p0}$ - bias value of the normalized unsteady pressure amplitude distribution approximated by an *Weibull distribution*

$\overline{C}_p(x^*)$ - mean pressure coefficient

$C(k)$ - Theodorsen function

c_H - coefficient of Bessel function

D - thickness of the deck [m]

DOF - Degree Of Freedom

D_{eq} - equivalent thickness [m]

d_H - coefficient of Bessel function

F_b - time-varying buffeting lift force per unit span [N/m]

F_{se} - time-varying self-excited lift force per unit span [N/m]

$F(k)$ - real part of the Theodorsen function

f - oscillation frequency [Hz]

f_φ - torsional frequency [Hz]

f_η - heaving frequency [Hz]

$G(k)$ - imaginary part of the Theodorsen function

H_i^* - aerodynamic derivatives for lift force

I - mass moment of inertia per unit span of a bridge deck $[t.m^2.s^2/m/m]$

k - reduced frequency; $k = 2.\pi.f/U$

$L(t)$ - time-varying lift force per unit span of bridge deck [N/m]

$L_{\varphi 0}$ - amplitude of the lift force in forced torsional motion [N]

$L_{\eta 0}$ - amplitude of the lift force in forced heaving motion [N]

M_b - time-varying buffeting moment per unit span [N.m/m]

M_{se} - time-varying self-excited moment per unit span [N.m/m]

$M(t)$ - time-varying moment per unit span of bridge deck [N.m/m]

$M_{\varphi 0}$ - amplitude of the moment in forced torsional motion [N.m]

$M_{\eta 0}$ - amplitude of the moment in forced heaving motion [N.m]

m - mass per unit span of a bridge deck [kg/m]

m_{chen} - mass coefficient used in Chen‘s formulation

NF - acronym for *no fairing*, referring to leading edge with no fairing

P_i^* - aerodynamic derivatives for drag force

$\overline{p}_{max}$ - average of the maxima in the pressure signal

$\overline{p}_{min}$ - average of the minima in the pressure signal

$P_{se}(t)$ - time-varying self-excited drag force per unit span [N/m]

$P(t)$ - time-varying drag force per unit span [N/m]

p - along-wind displacement [m]

RMS - root mean square

r - radius of gyration [m]

r_m - mass radius of gyration

SC - acronym for *semi-circular*, referring to leading edge with semi-circular fairing

T - period of oscillation [s]

t - time [s]

U - mean wind velocity [m/s]

U_{cr} - flutter onset velocity [m/s]

U_r - reduced wind velocity; U_r=U/f.B or U_r=U/f.b

$U_{r_{2box}}$ - reduced wind velocity for two-box cross-sections, considering the total width B_{2box}

w - weight of the bridge [N]

x - x coordinate

x^* - location coordinate at the body surface, normalized by the half-width b and zero valued at the midchord point

x_R - reattachment length from the leading edge (distance from the leading edge on the body's surface where the flow reattachment occurs)

x_{cp} - x coordinate defined by $x_{cp}= x^*+ 1$

x_d^* - location at the downstream half of the body surface, normalized by the half-width b and zero at midchord point ($x_d^* \geq 0$)

x_u^* - location at the upstream half of the body surface, normalized by the half-width b and zero at midchord point ($x_u^* \leq 0$)

x_0^* - location of the peak of the normalized amplitude distribution $\tilde{C}_p N(x^*)$

x_1^* - crossing point in the x axis for the phase difference distribution

x_2^* - crossing point in the x axis for the phase difference distribution

GREEK SYMBOLS

α_{cp} - scale parameter of the *Weibull distribution*

$\Delta\tilde{C}_p$ - difference between 2 values of unsteady pressure amplitude $\tilde{C}_p(x^*)$ of two different locations on the body surface

Δx^* - distance between 2 points in the x axis

Δt - time interval [s]

Δx_{cp}^* - normalized width of peak of amplitude distribution

Δx_{ψ}^* - normalized distance between crossing points in the x axis of the phase difference distribution, equivalent to the wave half-length $\lambda/2$ normalized by b

ϕ_{ψ} - *pseudo phase difference* of the phase difference distribution approximated by a sinusoidal equation [°]

φ - torsional displacement, positive nose-up [°]

$\varphi(t)$ - torsional displacement at a given time t, positive nose-up [°]

φ_0 - amplitude of $\varphi(t)$[°]

γ_{cp} - shape parameter of the *Weibull distribution*

γ_{chen} - aerodynamic index used in Chen‘s formulation

η - heaving displacement, positive downward [m]

$\eta(t)$ - heaving displacement at a given time t [m]

η_0 - amplitude of $\eta(t)$

λ - wave length of the flow; $\lambda = U/f$ [m]

λ_b - wave length normalized by half-width b

λ_{beq} - wave length normalized by equivalent half-width b_{eq}

ρ - air density $[kg/m^3]$

ω_p - circular frequency $2.\pi.f_p$ of the along-wind oscillation of the bridge deck

ω_φ - circular frequency $2.\pi.f_\varphi$ of the torsional oscillation of the bridge deck

ω_η - circular frequency $2.\pi.f_\eta$ of the heaving oscillation of the bridge deck

ω_ψ - *pseudo circular wave number* of the phase difference distribution approximated by a sinusoidal equation

$\psi_{L\varphi}$ - phase lag from the maximum angle of attack to the lift forces in forced torsional motion [°]

$\psi_{L\eta}$ - phase lag from the maximum angle of attack to the maximum lift force in forced heaving motion [°]

$\psi_{M\varphi}$ - phase lag from the maximum angle of attack to the maximum pitching moment in forced torsional motion [°]

$\psi_{M\eta}$ - phase lag from the maximum angle of attack to the maximum pitching moment in forced heaving motion [°]

ψ_0^* - position of the inflection point in the positive zone of the phase difference distribution

$\psi(x^*)$ - phase lag from the maximum relative angle of attack of the whole body to the maximum negative pressure at x^* [°]

$\psi(x_d^*)$ - values of phase difference presented in the downstream side of the deck, in relation to the midchord point [°]

$\psi(x_u^*)$ - values of phase difference presented in the upstream side of the deck, in relation to the midchord point [°]

ζ_p - structural damping ratio to critical for along-wind motion.

ζ_φ - structural damping ratio to critical for torsional motion

ζ_η - structural damping ratio to critical for heaving motion

Acknowledgements

Moving to a foreign country with the purpose of taking a Ph.D. course at a worldwide recognized university is not an easy task. Without help, I would not have achieved this objective, and I am sincerely thankful for all support I had from a number of people that is difficult to fit in a so limited space.

Even before leaving my country (Brazil), the Consulate General of Japan in Manaus provided me with all the assistance and information I needed regarding the scholarship offered by the Ministry of Education, Culture, Sports, Science and Technology of Japan – Monbukagakusho –, which made possible this big step in my life.

At that point, I received the letters of recommendation from Prof. Acir Mércio Loredo-Souza – advisor Professor of my Master course in Brazil –, Prof. Ruy Carlos Ramos de Menezes (both from the Federal University of Rio Grande do Sul – UFRGS) and from Eng. Paulo Roberto Marcondes de Carvalho, director of Stabile Engineering.

During all my stay in Japan, Kyoto University, through the *Foreign Students Division* and the *Graduate School of Engineering*, was always there to help me in solving issues that occasionally appeared. Also, both Japanese and foreign friends took important part in my everyday life, sharing moments and providing me with the energy necessary to face the challenges inherent to the research activities. The entire Japanese society also knew how to receive me as a foreigner, and that was a key point for the balance in my private life in Japan.

The students of the *Kyoto University Bridge and Wind Engineering Laboratory* were essential components for the development of my research. In this sense, a special thanks to

Dr. Ginan Kim, Dr. Jaehyung Lee and Dr. Le Thai Hoa, also Ph.D. foreign students at the time I arrived in Japan, who welcome me into the laboratory and gave me important advices concerning my research. The senior members of the *flutter team* – Mr. Yasuaki Ito, Mr. Hisato Matsumiya and, especially in my last year, Mr. Shinya Fujiwara – contributed enormously to my investigations, transferring knowledge regarding experimental techniques. Also, Mr. Do Bao Van was of great help in the pressure measurement experiments. Still regarding the experiments, I should mention Mr. Yasuhiro Miyasaka, who contributed with his experience and know-how in the preparation of the models. To all students of the laboratory my thankful feelings are also extended.

All of that would not have happened without the acceptance of Prof. Masaru Matsumoto, as my Advisor Professor and tutor in Japan. Prof. Matsumoto started my research and gave me the directions I should follow. Even after his retirement, he was always there, with constant inducements and available for any consultation.

After Prof. Matsumoto‘s retirement, the continuation of the my research was conducted by Prof. Hiromichi Shirato, to whom I am deeply thankful. Always available, with an incredible willing to help, through counseling both in my private life and research activities. The long conversations and discussions we had about the themes involved in my research were fundamental for the results I achieved, and from them a learned a lot. Thank you very much.

Also, Prof. Hiromasa Kawai from the Division of Atmospheric and Hydrospheric Disasters of the Disaster Prevention Research Institute and Prof. Kunitomo Sugiura from the Laboratory of Structural Mechanics of the Department of Civil and Earth Resources Engineering of the Graduate School of Engineering, both from Kyoto University, are thankfully acknowledged for the valuable questions and comments to the draft of this thesis.

The list of *sensei*s is completed with Prof. Tomomi Yagi, who took care of me as a student of the laboratory, assuring the maintenance of all bureaucratic procedures.

Finally, I would like to thank my family in Brazil; dad, mom, sisters, wife and son. The support I always received from them during all the time, despite the difficulties, were determinant in my accomplishments in Japan. Especially my son, Pedro, who was born in Brazil while I was in Japan, to whom I dedicate this thesis. Amo vocês!

To all people and entities cited above, including those who were not mentioned but

that also took part in this journey, I address my sincere "thank you". You were part of my life for three years and a half, and will be with me forever.

Part I

Introductory Chapters

Chapter 1

Introduction

Bridges have been used by humankind since before the 2^{nd} century AD, when the Alconétar Bridge, probably the oldest surviving stone segmental arch bridge in the world nowadays, was built. Since then, the technology regarding materials and structural engineering as well as the usage bridges have been meant to - pedestrian, carriages, cars, trucks, trains - evolved. Associated to the greed for even longer and wider structures, these factors pushed the dimensions of bridges to limits never imagined by Apollodorus of Damascus - the architect who designed Alconétar Bridge.

This evolution had a setback in November 7^{th}, 1940, with the tragic and famous episode of the old Tacoma Narrows Bridge failure (Fig.1.1). The third longest suspension bridge in the world at that time got its $853m$ long main span destroyed only four months after its completion, due to a divergent torsional flutter instability [9] caused by winds of about $19m/s$. By that time, only techniques based on the deflection theory were being used [10] and, as a consequence, the dynamic effects of the wind were not being properly considered in structures design. That fact started a new era for the *Wind Engineering* in the construction industry, becoming the most remarkable example of this kind of divergent instability.

Since then, much more attention has been paid to avoid the occurrence of aerodynamic instabilities in bridges, and the fundaments set by researchers as Theodorsen, Kàrmàn and Sears in 1930s and 1940s in the aeronautic field, motivated by the increase of the speed of the aircrafts, have been important components for the knowledge attained in the *Bridge*

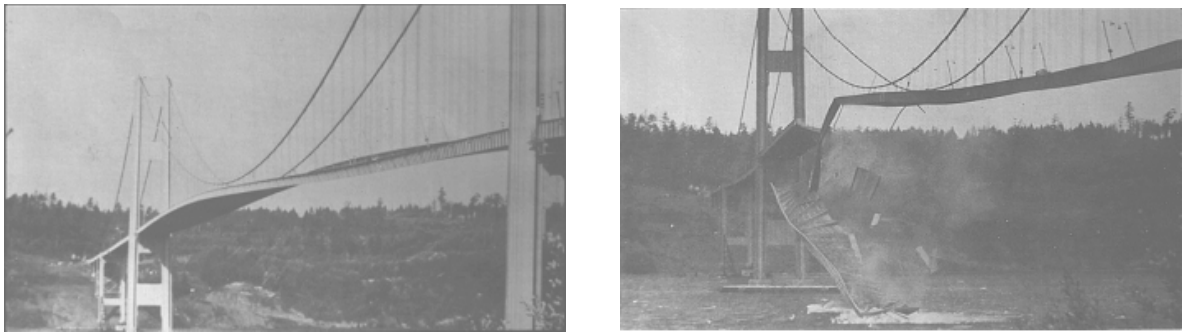

(a) Torsional oscillation (b) Failure

Figure 1.1: Old Tacoma Narrows Bridge failure, November 1940

Engineering nowadays.

With the increase of the spans along the last century, torsional and heaving natural frequencies of bridges have decreased [11, 12] and gotten closer and closer [12, 13], making room for the arising of 2-DOF (*degree of freedom*) coupled flutter instability, instead of the more common 1-DOF torsional flutter [14]. Configurations of bridge decks that used to be suitable for a certain range of spans started to present instability for longer spans. This led to the necessity of new cross-sections, more stable against aerodynamic instabilities, bringing new challenges for designers and researchers. Also, the need for more aesthetical and comfortable solutions, with reduced environmental impacts, has become an important issue.

In this scenario, two-box girders have fulfilled the stability requirements for modern long span bridges in the world. The characteristics of the gap between girders (grating, length, appendages) are recognized to play a major role in the definition of the aerodynamic derivatives of the whole deck, being an important factor for the aerodynamic stability of such a kind of structure [15, 16, 17, 18]. However, future development demands even more stable cross-sections, which led to the introduction of solutions like hybrid types (cable-stayed suspension bridges), multi-box girders (Messina Straits Bridge) and even concepts such as *Equivalent Aerodynamic Derivatives* [19], with the combination of different cross-sections along the span [18].

In this context, this study attempts to bring contributions for the expansion of the knowledge frontiers regarding the design of long-span bridges considering the influences of

the wind. The focus is put on the relationships between geometry of the bridge decks and their unsteady pressure characteristics, tracing the consequent relations of that with the stabilization of **flutter instability**.

1.1 Motivation

The design of modern bridges has evolved greatly during the latter decades, and constrictions that did not exist not long time ago have become important components for the decision making process in all stages of the projects nowadays. The focus of the first phases of the bridge design has been changed gradually from structural and economical to conceptual issues, as aesthetics and environmental impacts. Consequently, after the first propositions of geometry, not always based on structural and stability requirements, improvements should still be done in order to make the structure stable, safe and technically feasible.

These improvements have been decided through both wind tunnel experiments and *Computational Fluid Dynamics* (CFD) simulations, in a trial and error iterative basis, in which geometric modifications are proposed and the resulting stability level of the structure is evaluated. Of course, this trial and error system is based on accumulated experiences that guide the proposition of the geometric modifications; however, it is still a trial and error approach that sounds dissonant with the technology status attained nowadays, incurring in costs for the projects and stretching the time needed for the final results.

Concerning flutter stability assessment, wind tunnel tests campaigns are basically divided into two test stages: one with sectional models and other with full bridge aeroelastic models. During the first stage, the aerodynamic empirical coefficients used in the evaluation of the flutter stability, i.e. aerodynamic derivatives, are extracted through some system identification method. So the flutter onset velocity of the proposed cross-section is evaluated and through the implementation of geometric improvements the process is repeated until the safety requirements are satisfied. In a second moment, after a stable cross-section is obtained, the overall behavior of the bridge is fine tuned through tests with full bridge aeroelastic models.

The final cost of the project is directly related to these investigations, which depend highly on the ability of the designers in the proposition of better candidate geometries.

Abbreviations in this phase are of great value, bringing contributions to the agility of the process and to cost reduction, resulting directly in the improvement of the overall quality of the final project.

Because of technical difficulties and limitations of cost and time, generally the wind tunnel investigations do not include pressure distribution measurements. Usually, the focus has been put directly on the effects of the deck geometry on the values of the aerodynamic derivatives, and finally on their relationships with the flutter stability. It is well known, however, that these relationships present a non-linear behavior that can not be easily systematized in a closed set of equations, resulting in that some strategies and geometric combinations that bring benefits for one kind of basic cross-section, in terms of aerodynamic derivatives, may not work fine for other geometries. So the pros and cons of the geometric improvements have been related to each specific cross-section. As a consequence of that, a complete generalization has not been possible even nowadays and a high degree of complexity and uncertainty is still present in the cross-section optimization phase of the projects.

Since the relationships between aerodynamic derivatives and flutter stability itself have been extensively discussed in the technical literature and values of aerodynamic derivatives that lead to flutter proof cross-sections can be delineated, the author felt motivated to work on a step before, i.e. on the understanding of how geometric configurations of cross-sections are related to the flutter stability, through their influences on the unsteady pressure characteristics along the bridge deck.

With a better understanding of these relationships, a more agile evaluation of the impacts of a given geometric improvement on the unsteady pressure characteristics during the optimization stage of a bridge deck design can be obtained. So the bridge deck designers can be provided with a more rational way for estimating the aerodynamic derivatives of some proposed geometry, reducing *a priori* the number of cases to be investigated through wind tunnel tests. Thus, it would be possible to judiciously decide about the geometry during the fine tuning of the cross-section, by considering directly the impacts of the geometric modifications on the unsteady pressures distribution of the deck.

Based on that, the author proposes a fine tuning process based on the direct manipulation of the unsteady pressure characteristics along the bridge deck through the use of *geometric singularities* (geometric discontinuities as separation points, gaps and gratings) instead of focusing directly on the aerodynamic derivatives, as it is commonly done. In order to accomplish that, a systematization of equations to be used in the estimation of

the unsteady pressure distributions along bridge decks and investigations on the impacts of individual *geometric singularities* on these equations should be conducted.

With such a framework, designers would be able to, in a deterministic fashion, propose modifications in the deck geometry towards the composition of appropriate unsteady pressure characteristics, convenient for flutter stabilization, without the necessity of doing that directly in wind tunnel experiments. By doing so, wind tunnel tests can be reserved to more advanced stages of the design process and the trial and error process can be abbreviated so that the optimization stage can be shortened.

1.2 Objectives

This research is inserted in a context in which the feasibility of a bridge deck design framework based on the *manipulation* of the unsteady pressure characteristics along the bridge deck, through the use of *geometric singularities* and from a flutter stabilization point of view, is assessed.

The complete development of such a framework in a generic format is a very complex task, which demands a huge effort. So the main contribution of the present thesis will be restricted to the deepening of the understanding of the relationships between geometry and unsteady pressure characteristics along the bride deck, as part of the proof of concept of the whole proposition.

Through a case study-like approach using rectangular cylinders as base geometries, formulations that describe the interactions and the impacts of the geometry of the deck on its inherent unsteady pressure characteristics will be investigated through wind tunnel experiments. Initially, equations based on empirical coefficients will be proposed. However, considerations about the aerodynamic fundaments behind the proposed equations and empirical coefficients should be discussed from the fluid mechanics point of view, providing hints for the development of analytical solutions, so that they can be extended to cover generic cross-sections, as bridge decks, in future works.

The main results will include the evaluation of the unsteady pressure characteristics appropriate for flutter stabilization, proposition of methods to be used in the estimation of

the unsteady pressure characteristics of generic cross-sections and identification of strategies to judiciously impose modifications on them.

The use of *geometric singularities* will be introduced as a resource to be used in the manipulation of the unsteady pressure characteristics along the deck, with the objective of leading them to assume configurations decided in advance. The singularities planned to be investigated include vertical plates and slots, in a manner that the effects of blockages, flow separation points and also the aerodynamic interferences caused by the gaps on the unsteady pressure characteristics can be addressed, focusing on how to use them in advantage for flutter stabilization. The effects of slotting (gaps and gratings) will be included due to the increasing demand for two-box girders in modern bridges.

The choice for rectangular cross-sections was made to take advantage of the infinitude of data available in the literature regarding this geometry. The conclusions of this work should be understood as a base to be extended towards a generalization to include any geometry of cross-section, in the definition of a rational framework to be used by bridge decks designers in the fine tuning of the geometry of the deck during the geometric conception phase, aiming the stabilization against flutter. This research is not intended to be a conclusive work about the theme, but a proposition of strategies which should be kept under investigation so that the precise control of aerodynamic instabilities in bridge decks through the manipulation of their geometric characteristics can be obtained.

1.3 Organization

In the present chapter the scope of this thesis is introduced. The background information about the subjects addressed herein will be provided in the next chapter, and these two chapters compound the introductory part of the thesis.

In Chapter 3 the flutter stabilization is studied from an unsteady pressure characteristics point of view, so that conditions for its maintenance are provided, through the proposition of optimal configurations of unsteady pressure characteristics, namely *optimal unsteady pressure characteristics*. Chapter 4 provides considerations about unsteady pressure characteristics of rectangular cross-sections, with the proposition of mathematical relationships between geometry and these characteristics. So the use of *geometric singularities* with the

objective of attaining a fine tuning of the unsteady pressure characteristics in bridge decks is introduced in Chapter 5, with the use of vertical plates, and in Chapter 6, by addressing the case of two-box cross-sections and the effects of the gap on their unsteady pressure characteristics.

Finally, the last chapter provides a summary of the results with the conclusions of the study.

Chapter 2

General Background

Along the last two centuries, longer spans had been an exclusivity of suspension bridges, which dominated the scenario of long span bridges in the world. Since Brooklyn Bridge, completed in 1883 in New York with a main span of $486m$ and considered a starting point for the modern suspension bridges construction industry, the limits have been stretched resulting in that the current longest span surpass over 4 times that first mark. Akashi Kaikyo Bridge in Japan was completed in 1998 and exhibits a main span of $1991m$, the longest in the world. However, it is already planned to be beaten with the projects of Messina Straits Bridge in Italy (with a main span of $3300m$) and Gibraltar Straits Bridge, which will connect Morocco and Spain (with a main span of $5000m$).

Nevertheless, with the advances of the technology regarding materials, design and aerodynamics, cable-stayed bridges were also introduced to the world, with the completion of the Strömsund bridge in Sweden in 1955, with a main span of $183m$. This type of bridge has also evolved and after 1990 records have been successively broken. With Normandie Bridge in France, completed in 1994 ($856m$), and Tatara Bridge in Japan, in 1998 ($890m$), cable-stayed bridges have entered in the domain of long spans bridges [20]. These marks have been broken in 2008 with the completion of Sutong Bridge in China, whose main span is $1088m$, surpassing the Stonecutters Bridge in Hong Kong (under construction when this thesis was being written), which is planned to have a main span of $1018m$.

This development has been attained necessarily through the reduction of the weight of

the structures, associated to geometric and structural improvements. Also, an optimization of the use of the cables has been made necessary, since they are responsible for large part of the total weight and the aerodynamic loads of cable supported bridges.

For the deck, cable-stayed bridges have widely adopted box girders, while truss-girders have been used in suspension bridges [21]. However, the increase of spans has brought new geometric concepts, towards more streamlined shapes, enhancing the sensitivity of the aerodynamic loads to geometric variations, like traffic and geometric improvements.

Cables are supposed to have an intrinsic limit, related to their ability in supporting their own weight [21], and this has imposed the need of optimizations regarding the materials they have been made of. Also, with the increase of the lengths, cables have demanded innovative countermeasures for the mitigation of vortex and rain-wind induced vibrations [22] as well as other forms of instability, such as wake galloping and vibrations induced by other elements, like pylons and decks, that may become serious problems if not properly treated. In this sense, the roughness of the surface of the cables has been used as an important resource in the mitigation of aerodynamic instabilities, allied to aerodynamic devices and damping systems.

In terms of global behavior, it has been reported that the cable sag, which is directly associated to the cables length, may have an important effect on the overall stability of the bridge. With its increase, the torsional frequency may be also increased, impacting substantially on the flutter onset [23]. In addition, the height of the towers increases directly with the increase of the spans, becoming subjected to lateral motion and bringing additional complexities to the bridge system. Also, the proportion between side span and main span lengths is important parameter to be considered in the stabilization of long span bridges, since short side spans are beneficial for aerodynamic stability [23].

Concerning the deck, long-span cable supported bridges present a number of possibilities of aerodynamic phenomena, as consequence of the aerodynamic forces. These aerodynamic forces have been usually divided into static, self-excited and buffeting forces. The self-excited forces change the aerodynamic coupling of structural modes, impacting on the eigenmodes of the structure and providing additional aerodynamic damping and stiffness to the system [24], being directly related to the occurrence of flutter.

Also, phenomena such as Kàrmàn vortex induced vibrations, buffeting and galloping (not usual) may be originated by the forces mentioned above, and strategies to stabilize one

instability may incur sometimes in the destabilization of other. In addition, the interference between different aerodynamic phenomena, e.g. heaving vortex induced vibration and torsional flutter (in this case, dependent on the Scruton numbers of the oscillations), may be of concern [9]. Furthermore, earthquakes and traffic induced vibrations have been of major concern in the design of such a kind of structure; and the problems mentioned above are not restricted only to the completed structure, during the erection stages a sort of cautions should be taken as well.

Vortex induced vibrations are usually stronger in box girders, compared to truss girders [25], and even not being potentially destructive as flutter, compromises the structures by interfering with other aeroelastic effects and influencing on their fatigue lives [26]. A phenomenon associated to the turbulence of the flow, buffeting also may lead to structural fatigue, affecting at the same time the safety of the vehicles. With the increase of the spans the combination of buffeting and flutter responses has increased in importance [27], being considered the two main mechanisms nowadays [28].

Geometric improvements, as the use of fairings and the installation of appendages, allied to the use of passive and active controls, as TMD (*tuned mass dampers*), moving flaps [25] and other devices [29], have been used as important components in the aerodynamic stabilization of the deck. However, improvements are still necessary to face the new forms of aerodynamic phenomena, i.e. not occurring in shorter span bridges, associated to super long span bridges [26, 29].

All these conditions impose new challenges to engineers and researchers, and in this context health monitoring techniques have been of great value in the control and maintenance of modern bridges, providing a precise and *in real time* assessment of the general conditions of the whole structure. Every structure presents a typical behavior that can be regarded as a *vibrational signature* and any change in this characteristic during the lifetime of a bridge may provide information for the evaluation of its structural integrity. By using ambient vibration testing techniques, important feedback information through full-scale measurements have been acquired, which have been used in improvements of the design techniques and helped in the fine tuning of the understanding about the aerodynamic phenomena related to long span bridges.

In this chapter, a brief overview of the background necessary for the reading of this thesis is given, providing the conventions adopted for the development of the investigations.

2.1 Flutter Instability in Bridge Decks

Flutter is a flow-induced and self-excited divergent aerodynamic instability phenomenon, which arises from interactions between wind and a given elastic body, for which mass, stiffness, damping and geometrical shape of the body, as well as the characteristics of the flow, such as velocity and angle of attack, play fundamental roles. Basically, it is a composition of 2 simultaneous modes of vibration – heaving and torsional. In some kinds of bluff bodies this phenomenon can be also presented as a single torsional or heaving oscillation, as in the case of torsional flutter and galloping respectively, though.

Flow separation is not a requirement for the occurrence of flutter and structures liable to this instability are those in which substantial bending and torsional deflections can be established, like in suspension bridges [2]. In Fig.2.1, it is possible to see a sketch of a long structure experiencing flutter instability. In (a) the restoring moment that arises due to the aerodynamic forces tends to stabilize the torsion oscillation; in (b) the bending oscillation changes the relative direction of the wind throughout the cycle, generating aerodynamic forces that act in the opposite direction of the motion. The combination of both oscillations can be seen in (c), for a particular case with phase difference of 90° between torsional and heaving motions and aerodynamic center at the downstream half-chord.

The genesis of flutter can be explained in a simplistic way by the fact that when a body is immersed in a flow the aerodynamic loads may change the original form and position of such bodies, modifying in turn the patterns of the flow around them. Due to the shed vorticity, this adjustment in the patterns of flow does not happen instantaneously [1]. As a consequence of that, forces commonly called *aeroelastic* or *self-excited forces*, which are dependent on the history of these motions, arise.

These forces can act feeding energy to the oscillation, being understood as a negative damping that is imposed to the system *body-flow*, increasing the level of the vibrations until the limit in which the energy spent by the total damping of the structure, composed by both aerodynamic and structural damping, surpass the energy input, forcing the aerodynamic loads to decrease.

From that point on, the initial state of the body tends to be restored and the reestablishment of the original loads is attained, leading to a new cycle of oscillation. In some cases, during the reduction of the loads, the elasticity of the body makes it overpass its equilibrium

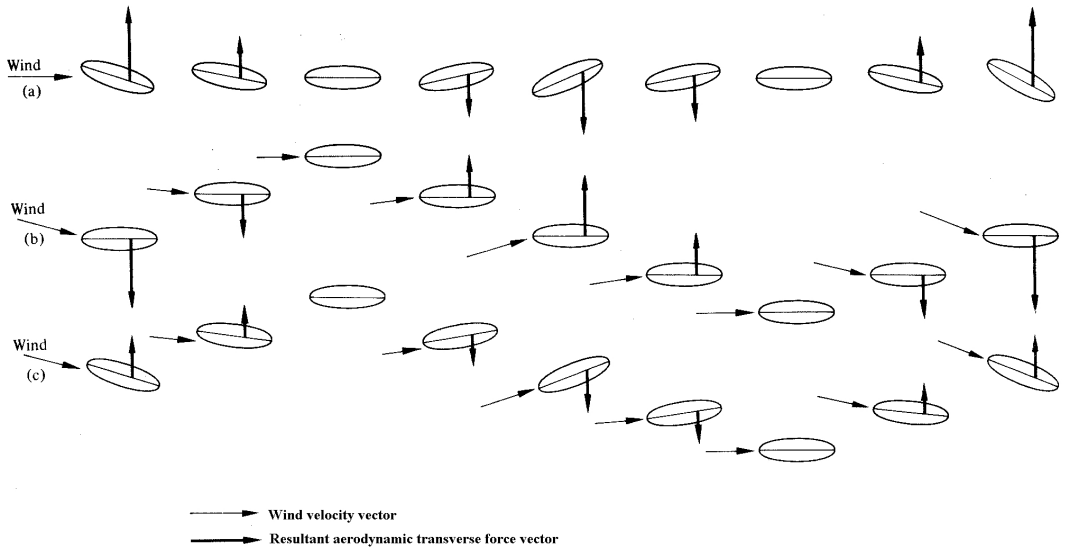

Figure 2.1: (a) Torsional oscillation; (b) Bending oscillation (angle of attack motion [1]); (c) Torsional and bending oscillation (angular velocity motion[1, 2])

position, causing a new aerodynamic load in the opposite direction of the previous one, so the oscillation cycle has its direction inverted. In case the aerodynamic interactions result in a continuous increasing of the initial loads, the body enters in a divergent oscillation, leading the structure to the failure.

Concerning bridge decks, the combination of the characteristics of the flow with the geometric characteristics of the bridge deck itself may induce different types of flutter instability, which present different frequency characteristics [3, 30] and motion patterns. Although nowadays it is recognized the existence of at least 2 majors classes – *Torsional Flutter* and *Coupled Flutter* –, some authors also include *Galloping* as a heaving oscillation type of flutter. The *Coupled Flutter*, a composition of both heaving and torsional oscillations phenomenon that is similar to the one observed in airplane wings, has been the most common type of flutter in long span bridges and its stabilization is key factor in the design of such a kind of structure.

Considering the dependence between the shape of the cross-section and the type of flutter, Matsumoto et al. [30] accounted for the existence of 5 types of flutter: *low-speed torsional flutter* - occurring in bluff sections, e.g. rectangular cylinders with side ratio B/D=5;

high-speed torsional flutter - for still bluff sections, but with a higher side ratio, e.g.: B/D=10 (the generation mechanism is different from the previous one [31]); *torsional branch coupled flutter* - for slender cross-sections, e.g.: rectangular cylinders with side ratio B/D=20 (it is the most common type of flutter, similar to one occurring in thin airfoils and flat plates); *heaving branch coupled flutter* - slender cross-sections with some modifications, e.g.: central barrier, occurs for $A_2^*<<0$; *hybrid branches coupled flutter* - complex slender cross-sections, e.g.: grating girders. So the study on flutter stabilization may be conducted by taking that classification into account.

In the coupled-flutter instability, the torsional system is recognized to be more easily excited than the heaving system [32]. Yang [33], studying a group of 13 different cross-sections, concluded that the more streamlined a cross-section is, the more the heaving participates for the flutter onset, rising the flutter speed. Based on that study, it was concluded by Ge & Xiang [34] that an optimum level of beneficial effects provided by the heaving motion in flutter stabilization is obtained with the use of a central barrier, beyond which flutter speed gradually goes down.

Flutter instability occurs when the total damping of the system, composed by structural and aerodynamic damping, turns negative. Its stabilization can be obtained through 2 different approaches [17, 29, 35], which should be integrated in order to maximize their advantages: *structural control* and *aerodynamic control*.

In the first approach, the designer operates on the stiffness and on the vibration modes of the bridge, improving its response characteristics towards the increase of the structural resistance. Since the effectiveness of the increasing of the torsional stiffness gets reduced with the increase of the span [36, 37], more complex structural approaches, aiming a better distribution of the aerodynamic energy, have to be considered for modern long span bridges. Such approaches may include strategies as changing the center of mass and modes of vibration of the structure [36].

In the second approach, the proposition of proper cross-sections based on aerodynamic considerations is performed, with the objective of reducing the loads on the bridge.

In spite of being effective in the improvement of the stability, the first option implies necessarily in the increasing of the weight of the structure, leading the torsional steel requirements to rise with the square of the span [38], which impacts directly on the final cost of the bridge. So the importance of aerodynamic improvements, introduced in the end of 1960‘s

[35], is enhanced. However, the stabilization problem should be treated as an interactive discipline, in which both aerodynamic and structural characteristics should be integrated towards an optimal configuration.

For values of frequency ratio f_φ/f_η greater than 1, the critical flutter onset velocity is generally proportional to (as a fraction of) the divergence velocity. Divergence occurs when the torsional stiffness is eliminated by the action of the wind and because of that it is highly dependent on the torsional natural frequency f_φ of the structure. Since the increase of the wind velocity barely impacts on the heaving natural frequency f_η, the frequency ratio of the structure can be regarded as a measure of its aerodynamic stability. For values of frequency ratio equal to the unity, critical flutter velocity tends to become very high; however, in that state the torsional motion is only weakly damped throughout the whole wind velocity range [38].

Values of frequency ratio that provide good stability conditions are usually greater than 2; nevertheless, depending on the general characteristics of the bridge, this "safety limit" may vary. In modern suspension bridges, the frequency ratio has been usually in the range of 1.4 to 2.0 [39]. For illustration purposes, Table 2.1 (adapted from [18, 34, 39]) presents the natural frequencies and frequency ratios of some suspension and cable-stayed bridges around the world.

In terms of structural system, it has been analytically accounted for the better aerodynamic stability presented by continuous decks, in comparison with discontinuous solutions [23]. Also, modern long-span bridges have generally adopted three-span arrangements, instead of the single-span system; the former leads to a lower vertical stiffness without presenting differences in terms of torsional stiffness from the latter, leading consequently to a higher frequency ratio [23]. More stable solutions have also been tried with the use of perforated decks [40], and subsequent theoretical studies on such a kind of bridge deck has lead to the development of the concept of two-box girders [38], which have shown very good stability characteristics against flutter.

2.1.1 Mathematical considerations

When a sudden change in the angle of attack occurs, the consequent increase of the circulation imposes an increase in the lift forces that should be counterbalanced by the shedding of

Table 2.1: Frequency ratios of some suspension and cable stayed bridges

	span (m)	f_η(Hz)	f_φ(Hz)	f_φ/f_η
Suspension bridges				
First Tacoma Narrows (USA)	854	0.130	0.200	1.5385
First Bosporus Strait (Turkey)	1074	0.162	0.371	2.2901
Akashi Kaikyo (Japan)	1991	0.0659	0.1592	2.4158
Messina Strait (Italy)	3300	0.0605	0.0796	1.3157
Yichang (China)	960	0.1050	0.3580	3.4095
Jiangyin (China)	1385	0.0890	0.2581	2.9000
Humen (China)	888	0.1117	0.3612	3.2337
Honguang (China)	380	0.1915	0.3591	1.8752
Kitan Strait (Japan)	2500	0.053	0.188	3.547
Cable-stayed bridges				
all'Indiano (Italy)	189	0.573	1.179	2.0576
Rio Guamá (Brazil)	320	0.331	0.649	1.9607
Tsurumi Fairway (Japan)	510	0.204	0.486	2.3824
Normandy (France)	856	0.220	0.500	2.2727
Yangpu (China)	602	0.2733	0.5093	1.8635
Qingzhou (China)	605	0.2075	0.5346	2.5764
2^{nd} Nanjing (China)	628	0.2426	0.7275	2.9988
Jingsha (China)	500	0.1987	0.3983	2.0045
Haikou (China)	340	0.2728	0.6248	2.2903
Nanpu (China)	423	0.3518	0.4498	1.2786

vortices from the trailing edge. When these vortices are far enough way in the wake of the deck, the unsteady forces are reduced to zero and the lift reaches its steady state. Because of that, the unsteady components of the circulatory forces, represented by the aerodynamic derivatives, have been extensively investigated and considered for the understanding of what happens aerodynamically for the occurrence of flutter.

In the evaluation of the flutter onset, the wind is usually considered perpendicular to the bridge axis in the horizontal plane. This situation has been regarded as the most

unfavorable condition, and for different incidence directions (skew winds) the "cosine rule" has been adopted through simple vector decomposition. However, studies based on wind tunnel tests have accounted for a inaccuracy of this decomposition approach for situations in which the angle of attack is not zero. Depending on the angle of attack and on the geometry of the deck, as the existence of transverse beams and other appendages, skew wind directions may lead to worse situations, resulting in that the use of the "cosine rule" may incur in an underestimation of the loads [41].

For the description of the motion of bridge decks immersed in the wind flow, it has been widely accepted the consideration of only the vertical η and the torsional φ oscillations, Fig.2.2. The system is modeled as a rigid body balanced mechanically around its mid-chord rotation axis, whose linearized equations for the forces are described by Eq.2.1 and Eq.2.2.

$$L(t) = m.\left(\ddot{\eta} + 2\zeta_\eta\omega_\eta\dot{\eta} + \omega_\eta^2\eta\right) \tag{2.1}$$

$$M(t) = I.\left(\ddot{\varphi} + 2\zeta_\varphi\omega_\varphi\dot{\varphi} + \omega_\varphi^2\varphi\right) \tag{2.2}$$

where: $L(t)$ and $M(t)$ are the time-varying lift force and moment per unit span; ω_η and ω_φ are the circular frequencies $2.\pi.f_\eta$ and $2.\pi.f_\varphi$ of the vertical and torsional oscillations; η is the heaving displacement (positive downward); φ the torsional displacement (positive nose-up); the dots $\dot{()}$ and $\ddot{()}$ represent the derivatives in relation to time t; m is the mass per unit span of the bridge deck; I is the mass moment of inertia per unit span of the bridge deck; ζ_η and ζ_φ are the structural damping ratios to critical in heaving and torsional motions.

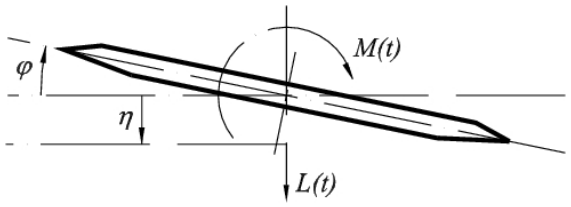

Figure 2.2: Section of a body immersed in a flow in 2-DOF motion

Eq.2.1 and Eq.2.2 are aerodynamically coupled without being mechanically coupled and the time-dependent lift $L(t)$ and moment $M(t)$ provided by them are the resultant of the loads due to the turbulence of the flow and to the self-excited forces, Eq.2.3 and Eq.2.4.

However, only the latter, which are represented by Eq.2.5 and Eq.2.6, assuming purely sinusoidal motion and linear behavior, should be considered for flutter stability analysis.

$$L(t) = L_{se}(t) + L_b(t) \tag{2.3}$$

$$M(t) = M_{se}(t) + M_b(t) \tag{2.4}$$

where: subindex *se* refers to *self excited*; subindex b refers to *buffeting*;

$$L_{se}(t) = \frac{1}{2}\rho(2.b)\,U^2 \left\{ k.H_1^* \frac{\dot{\eta}}{U} + k.H_2^*.b.\frac{\dot{\varphi}}{U} + k^2.H_3^*.\varphi + k^2.H_4^*\frac{\eta}{b} \right\} \tag{2.5}$$

$$M_{se}(t) = \frac{1}{2}\rho(2.b^2)\,U^2 \left\{ k.A_1^* \frac{\dot{\eta}}{U} + k.A_2^*.b.\frac{\dot{\varphi}}{U} + k^2.A_3^*.\varphi + k^2.A_4^*\frac{\eta}{b} \right\} \tag{2.6}$$

where: $L_{se}(t)$ and $M_{se}(t)$ are the time-varying self-excited lift force and moment per unit span; ρ is the air density; U is the mean wind velocity; b is half-width of the deck; k is reduced frequency, $k = b.\omega/U$; ω is the circular frequency $2.\pi.f$; H_i^* and A_i^* are the aerodynamic derivatives for lift and pitching moment respectively; η is the heaving displacement (positive downward); φ the torsional displacement (positive nose-up); the dot $\dot{()}$ represents the first derivative in relation to time t.

A simplified proposition for Eq.2.5 and Eq.2.6 can be obtained by using the aerodynamic coefficients C_L and C_M to represent the aerodynamic lift and moment coefficients, Eq.2.7 and Eq.2.8 [42].

$$L_{se}(t) = \frac{1}{2}\rho(2.b)\,U^2 \left\{ C_L\left[\frac{\eta}{b}\right] + C_L\left[\varphi\right] \right\} \tag{2.7}$$

$$M_{se}(t) = \frac{1}{2}\rho(2.b^2)\,U^2 \left\{ C_M\left[\frac{\eta}{b}\right] + C_M\left[\varphi\right] \right\} \tag{2.8}$$

With the increase of the span, the flexibility of the structure is also increased, resulting in a more prominent deformation under the static wind load. This deformation is not constant along the span and leads to non-linear wind-structure interactions that impact substantially on the vertical and on the torsional displacements, without deforming significantly the along-wind displacements linearity. So, non-linear wind-structure interactions have gained importance in the analysis of long-span bridges [43].

In addition, it has been observed that by neglecting the aeroelastic coupling between modes, an underestimation of the torsional responses may occur [27]. Based on that, improvements have been done in the analysis methods by considering non-linear effects of the deformed structures, influences of full-coupled aerodynamic derivatives and full-mode flutter analysis [44]. So the equations have included one more DOF in the horizontal direction, Eq.2.9, and the participation of several modes of vibration.

$$P(t) = m.\left(\ddot{p} + 2\zeta_p\omega_p\dot{p} + \omega_p^2.p\right) \tag{2.9}$$

where: $P(t)$ is the time-varying drag force per unit span; ω_p is the circular frequency $2.\pi.f_p$ of the along-wind oscillation; p is the along-wind displacement,ζ_p is the structural damping ratio to critical in along-wind motion.

Also additional aerodynamic derivatives should be included in the formulation, so that the self-excited forces and moment for the 3-DOF system can be expressed, Eq.2.10 to Eq.2.12.

$$L_{se}(t) = \frac{1}{2}\rho(2.b)\,U^2\left\{k.H_1^*\frac{\dot{\eta}}{U} + k.H_2^*.b.\frac{\dot{\varphi}}{U} + k^2.H_3^*.\varphi + k^2.H_4^*\frac{\eta}{b} + k.H_5^*\frac{\dot{p}}{U} + k^2.H_6^*.\frac{p}{b}\right\} \tag{2.10}$$

$$M_{se}(t) = \frac{1}{2}\rho(2.b^2)\,U^2\left\{k.A_1^*\frac{\dot{\eta}}{U} + k.A_2^*.b.\frac{\dot{\varphi}}{U} + k^2.A_3^*.\varphi + k^2.A_4^*\frac{\eta}{b} + k.A_5^*\frac{\dot{p}}{U} + k^2.A_6^*.\frac{p}{b}\right\} \tag{2.11}$$

$$P_{se}(t) = \frac{1}{2}\rho(2.b)\,U^2 \left\{ k.P_1^* \frac{\dot{\eta}}{U} + k.P_2^*.b.\frac{\dot{\varphi}}{U} + k^2.P_3^*.\varphi + k^2.P_4^*\frac{\eta}{b} + k.P_5^*\frac{\dot{p}}{U} + k^2.P_6^*.\frac{p}{b} \right\} \tag{2.12}$$

where: $P_{se}(t)$ is the time-varying self-excited drag force per unit span; P_i^* are aerodynamic derivatives for drag force.

For the calculation of the flutter onset, i.e. wind velocity for which flutter stability occurs, several methods have been used and proposed in the latter decades. In this study, despite the increasing of the importance of a three-dimensional evaluation of the stability problems, the analyses will be restricted to a two-dimensional approach, by using *Complex Eigenvalue Analysis* (CEVA) for flutter analysis purposes.

2.2 Unsteady Pressure Characteristics

The pressure distribution measured along the surface of a body immersed in the wind flow is important information for the study of the aerodynamic instabilities this body may be subjected to.

A common representation for these pressures at every location x^* in a harmonically oscillating body, Eq.2.13 for torsion and Eq.2.14 for heaving, at a given time t is a composition of a *mean* and a *fluctuating* components. These components are dependent on the wind velocity and in order to assume values comparable among different situations they are usually normalized by the dynamic pressure $1/2.\rho.U^2$, where ρ is the air density and U is the wind velocity, resulting in the *pressure coefficients* $\overline{C}_p(x^*)$ and $\tilde{C}_p(x^*,\ t)$ of Eq.2.15, respectively.

$$\varphi(t) = \varphi_0.cos(2.\pi.f_\varphi.t) \tag{2.13}$$

where: $\varphi(t)$ is the torsional displacement at a given time t; φ_0 is the amplitude of $\varphi(t)$; f_φ is the torsional vibration frequency.

$$\eta(t) = \eta_0 . cos(2.\pi.f_\eta.t) \tag{2.14}$$

where: $\eta(t)$ is the heaving displacement at a given time t; η_0 is the amplitude of $\eta(t)$; f_η is the heaving vibration frequency.

$$C_p(x^*, t) = \overline{C}_p(x^*) + \tilde{C}_p(x^*, t) \tag{2.15}$$

where: $C_p(x^*, t)$ is the total pressure coefficient at location x^* in time t; $\overline{C}_p(x^*)$ is the mean pressure coefficient; $\tilde{C}_p(x^*, t)$ is the unsteady pressure coefficient for time t at x^*.

The mean pressure coefficient is obtained by averaging the pressures along the time, and it assumes nearly similar values regardless the body is in motion or in stationary state. Since the main focus of this study will be put on the unsteady components of the total pressure, i.e. $\tilde{C}_p(x^*, t)$, the discussions about mean pressures will not be deepened.

The fluctuating component $\tilde{C}_p(x^*, t)$ shows a dependence on the amplitude of vibration and because of that it is sometimes normalized by it, which is not the case of the values reported throughout this study. For its definition, Eq.2.16, two parameters should be considered, the amplitude $\tilde{C}_p(x^*)$ and the phase difference $\psi(x^*)$ existent between the maximum relative angle of attack of the whole body and the maximum negative pressure at x^*. As a physical interpretation, positive values of $\psi(x^*)$ indicate a delay of the pressure fluctuation in relation to the motion of the body, Fig.2.3.

$$\tilde{C}_p(x^*, t) = -\tilde{C}_p(x^*) . cos(2.\pi.f.t - \psi(x^*)) \tag{2.16}$$

As already mentioned above, the amplitude $\tilde{C}_p(x^*)$ is normalized by the dynamic pressure $1/2.\rho.U^2$ and represents the half average fluctuation of the pressures along the sampling time, given by Eq.2.17.

$$\tilde{C}_p(x^*) = \frac{\overline{p}_{max} - \overline{p}_{min}}{2.\frac{1}{2}.\rho.U^2} \tag{2.17}$$

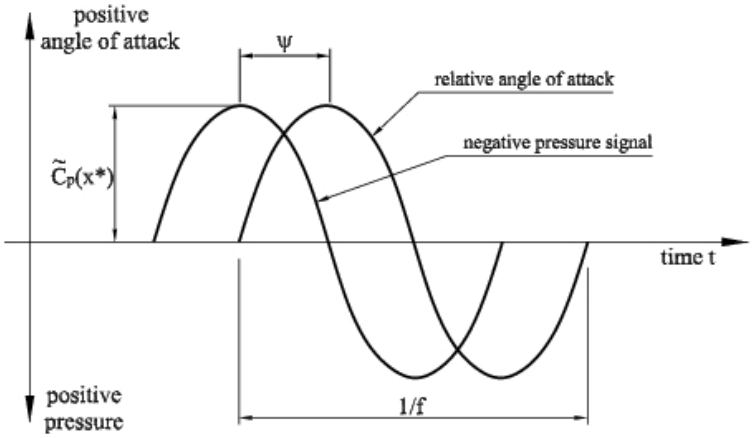

Figure 2.3: Unsteady pressure characteristics on the upper surface of the body

where: $\overline{p}_{max}$ is the average of the maxima in the pressure signal; $\overline{p}_{min}$ is the average of the minima in the pressure signal; ρ is the air density; U is the wind velocity.

Based on the definitions of this thesis, the imaginary part of $\tilde{C}_p(x^*, t)$, which is proportional to the velocity of the motion and defined by $\tilde{C}_p(x^*).\sin\psi(x^*)$, is related to the damping of the system. In heaving motion, positive values of $\tilde{C}_p(x^*).\sin\psi(x^*)$ in the upper surface act as exciting forces, inputing energy into the vibration, and negative values as damping forces. In torsional motion the same can be said in relation to leading and trailing edges [45], and the opposite for the inferior side surface.

In order to obtain the total lift forces due to the unsteady pressure, $L_{se}(t)$, Eq.2.16 should be integrated over the whole surface of body, leading to Eq.2.18. The same can be done for the moments, $M_{se}(t)$, leading to Eq.2.19.

$$L_{se}(t) = -\frac{1}{2}.\rho.U^2.b\int_{-1}^{1}\tilde{C}_p(x^*).cos(2.\pi.f.t-\psi(x^*))dx^* \tag{2.18}$$

$$M_{se}(t) = -\frac{1}{2}.\rho.U^2.b^2\int_{-1}^{1}\tilde{C}_p(x^*).x^*.cos(2.\pi.f.t-\psi(x^*))dx^* \tag{2.19}$$

These equations can be transformed in Eq.2.5 and Eq.2.6, respectively, which use the

aerodynamic derivatives to described each component of the unsteady forces. This subject will be addressed in more details in the following sections of this thesis.

2.3 Aerodynamic Derivatives

The concept of *aerodynamic derivatives* has been used for a long time, since the first theoretical expressions proposed by Birnbaum in 1924 [46]. Throughout the last century, many researchers addressed the idea, and the fundaments proposed by Theodorsen [47] in 1934 had a major influence on the studies of flutter instability in the aeronautical field.

Before 1940, the application of the theories regarding aerodynamic derivatives was mostly performed in studies on airfoil shapes. However, with the years, the resemblances between airfoils and bridge decks induced engineers to start gradually applying such concepts to civil engineering problems, and a number of authors dealt with the phenomena regarded to both shapes as similar.

Nowadays, the limitations of such a kind of similar approach are understood. Since the classic work published by Scalan & Tomko in 1971 [46] several specific investigations have been conducted on the aerodynamic behavior of bridges considering these aerodynamic derivatives as empirical coefficients. Since they are a representation of the aeroelastic forces in a frequency domain, they can be understood as frequency filters, mapping the state of the motion of the body into the self-excited forces [48], being of great value in the evaluation of the flutter properties in bridge decks.

Until the present, days it has not been possible to develop precise analytic expressions for the inference of the values of these derivatives for bluff bodies. Theories applicable to airfoil shapes, based on the potential flow, may serve as guidelines in the studies of bridge decks; however, they do not provide accurate results for cross-sections which do not present a very streamlined shape, due to the separated flow inherent to such a kind of cross-section. Because of that the only reliable way for obtaining them has still been by resorting to wind tunnel tests (see Section 2.3.1).

Alternative techniques, as *Computational Fluid Dynamics* (CFD) and even the usage of *Neural Networks* [49, 50], have been tried for the assessment of the aerodynamic derivatives of

bridge decks. However, due to the huge complexity of the aerodynamic interactions, powerful computational resources should be employed and additional research is still needed before CFD can be widely applied to practical situations. In spite of that, CFD has been used as a complement for wind tunnel tests and even as an alternative method in investigations of simpler structures, showing that with the advances of the computational resources the applicability of CFD will surely expand.

The choice for a CFD method should be made based not only on its accuracy, but also on its versatility, computational cost and ease of use [51]. An example of the application of CFD in investigations related to aerodynamic derivatives is the one conducted by Bruno & Fransos [52], in which a relevant dependence between aerodynamic derivatives and Reynold's number was identified for flat plates, especially for H_1^* and A_2^*. These influences showed a tendency to be suppressed with the increase of the Reynold's number, which is related to the thickness of the attached boundary layer and the definition of the conditions of separation of the shear layers [53]. For $Re > 10^5$ the aerodynamic derivatives showed an excellent agreement with the Theodorsen function, that does not consider the effects of Reynold's number.

However, considering that in wind tunnel tests the values of Reynold's number are smaller by a factor of 10^2 to 10^3 than the full scale values, this theme should deserve more attention. In this sense, experimental studies have also accounted for some dependence between Reynold's number and aerodynamic derivatives, which varies with the angle of attack [54, 55].

Despite that, the effects of Reynold's number on the aerodynamic derivatives have been generally ignored and in wind tunnel tests good approximations for the aerodynamic derivatives are expected by considering only reduced wind velocity, geometry of the cross-section and the relative angle of attack [56].

With the increase of the oscillation amplitudes, the mean reattachment point of the flow in a body in torsional motion is moved to downstream, and this brings important impacts on the values of A_2^* and H_2^* [57]. However, in spite of the dependence on the amplitude of oscillation [57, 58], aerodynamic derivatives obtained in wind tunnel tests are usually considered not affected by it, since the amplitude of oscillation assumed in the tests are generally of small magnitude.

Initially, Scanlan & Tomko [46], based on the concepts introduced by Theodorsen [47],

proposed only 6 aerodynamic derivatives - A_1^*, A_2^*, A_3^*, H_1^*, H_2^* and H_3^*. However, the need for a clearer understanding of the aerodynamic phenomena concerning the interactions fluid-structure has lead to the inclusion of additional coefficients.

Considering only a two-dimensional motion, two more aerodynamic derivatives, i.e. A_4^* and H_4^*, have been included, and when the investigations are conducted in a three-dimensional basis (3 DOF systems), the formulation is complemented by increasing the total number to 18 aerodynamic derivatives [59, 60]. These additional coefficients necessary for 3 DOF systems are associated to the along-wind motion, and their contributions to the multimodal response of bridges have not been totally clarified [59]. So the importance of considering them in the estimation of the flutter onset velocity will depend on the structural and aerodynamic characteristics of the bridge [61].

Although different representations for these index have already been proposed [62, 63, 64], as attempts to provide different points of view for the aeroelastic forces, the system proposed by Scanlan & Tomko [46], as the real and the imaginary parts of the transfer function between forces and displacements in a non-dimensionalized form, became a kind of common sense in the investigations on bridge decks, being widely used in the literature.

Even not being perfectly suitable, the aerodynamic derivatives corresponding to the classical theoretical case of a linearized thin airfoil (flat plate) submitted to a two-dimensional motion have been repeatedly used as benchmark for comparison purposes among bridge decks. These indices can be calculated by consulting the Appendix I of Theodorsen [47] and Scanlan & Tomko [46], which lead to the following equations for the eight aerodynamic derivatives:

$$k.H_1^* = -2.\pi.F(k) \tag{2.20}$$

$$k.H_2^* = -\pi.\left\{2.\left[\left(\frac{1}{2}-a\right).F(k)+\frac{G(k)}{k}\right]+1\right\} \tag{2.21}$$

$$k.H_3^* = -2.\pi.\left(\frac{F(k)}{k}-\left(\frac{1}{2}-a\right).G(k)\right) \tag{2.22}$$

$$k.H_4^* = 2.\pi.G(k) \tag{2.23}$$

$$k.A_1^* = 2.\pi.\left(a + \frac{1}{2}\right).F(k) \tag{2.24}$$

$$k.A_2^* = -\pi.\left\{-2.\left(a + \frac{1}{2}\right).\left[\left(\frac{1}{2} - a\right).F(k) + \frac{G(k)}{k}\right] + \frac{1}{2} - a\right\} \tag{2.25}$$

$$k.A_3^* = -2.\pi.\left(a + \frac{1}{2}\right).\left\{\left(\frac{1}{2} - a\right).G(k) - \frac{F(k)}{k}\right\} \tag{2.26}$$

$$k.A_4^* = -2.\pi.\left(a + \frac{1}{2}\right).G(k) \tag{2.27}$$

where: k is the reduced frequency $b.\omega/U$; b is the half width of the deck; ω is the circular frequency; U the wind velocity; *F(k)* and *G(k)* are the real and imaginary parts of the Theodorsen function *C(k) = F(k) + iG(k)*, which is defined by Hankel function (Eq. 2.28); a is distance from the rotational center to the midchord, normalized by b.

$$C(k) = \frac{H_1^{(2)}(k)}{H_1^{(2)}(k) + iH_0^{(2)}(k)} = F(k) + iG(k) \tag{2.28}$$

where: $H_v^{(2)}(k)$ is the Hankel function of second kind; *F(k)* and *G(k)* are defined as the Laplace transformation of R.T.Jones indicial function, according to Eq.2.29 and Eq.2.30.

$$F(k) = 1 - \frac{a_H.k^2}{b_H^2 + k^2} - \frac{c_H.k^2}{d_H^2 + k^2} \tag{2.29}$$

$$G(k) = \frac{k.a_H.b_H}{b_H^2 + k^2} + \frac{k.c_H.d_H}{d_H^2 + k^2} \tag{2.30}$$

where: a_H=0.165; b_H=0.0455; c_H=0.335; d_H=0.3

In the case of bridges decks, these equations can be simplified by considering $a=0$, which leads to:

$$k.H_1^* = -2.\pi.F(k) \tag{2.31}$$

$$k.H_2^* = -2.\pi.\left(\frac{F(k)}{2} + \frac{G(k)}{k} + \frac{1}{2}\right) \tag{2.32}$$

$$k.H_3^* = -2.\pi.\left(\frac{F(k)}{k} - \frac{G(k)}{2}\right) \tag{2.33}$$

$$k.H_4^* = 2.\pi.G(k) \tag{2.34}$$

$$k.A_1^* = \pi.F(k) \tag{2.35}$$

$$k.A_2^* = \pi.\left(\frac{F(k)}{2} + \frac{G(k)}{k} - \frac{1}{2}\right) \tag{2.36}$$

$$k.A_3^* = \pi.\left(\frac{F(k)}{k} - \frac{G(k)}{2}\right) \tag{2.37}$$

$$k.A_4^* = -\pi.G(k) \tag{2.38}$$

Each one of these coefficients can be associated to a physical description of the aerodynamics involved in the interactions fluid-body. In the case of A_i^* derivatives, A_1^* and A_2^* are related to the heaving and torsional aerodynamic damping respectively, A_3^* to the torsional aerodynamic stiffness and A_4^* to the heaving displacement. For the H_i^* derivatives the associations are similar: H_1^* and H_2^* are related to the heaving and torsional aerodynamic damping respectively, H_3^* to the torsional stiffness and H_4^* to the heaving displacement. Furthermore, in the quasi-steady state ($F(k)= 1$ and $G(k)= 0$), $k.H_1^*$ is the slope of the lift force curve; $k.A_1^*$, the slope of the pitching moment curve; $k.H_2^*$ is related to the force arising from the angular velocity of the body and $k.A_2^*$ to the moment arising from the angular velocity of the body.

There is a distinction between the so-called *non-coupled derivatives* - A_2^*, A_3^*, H_1^* and H_4^* - and the *coupled derivatives* - H_2^*, H_3^*, A_1^* and A_4^*: while the former affect the same degree of freedom that they are associated to, the latter affect the other degree of freedom.

The *coupled derivatives* related to the torsional motion excited in a frequency ω_φ induce a lift force in the heaving system. This torsional motion lags the induced lift force by a phase angle of $tan^{-1}(H_2^*/H_3^*)$ and presents an amplitude proportional to $\omega_\varphi^2.\sqrt{(H_2^*)^2 + (H_3^*)^2}$. On the other hand, the *coupled derivatives* obtained in the heaving motion with frequency ω_η excite the torsional system, which will present an amplitude proportional to $\omega_\eta^2.\sqrt{(A_1^*)^2 + (A_4^*)^2}$ and a phase angle of $tan^{-1}(A_1^*/A_4^*)$ [8].

Although the physical interpretation of such derivatives presents an equivalence between flat plate theory and bridge decks, the differences among the fluid structure around these bodies in motion do not allow a direct application of Eq.2.31 to Eq.2.38 in the calculation of the aerodynamic derivatives of bridge decks. So, as mentioned above, investigations based on wind tunnel tests are required in this sense, and Section 2.3.1 addresses this subject.

2.3.1 Obtaining Aerodynamic Derivatives

In order to obtain the flutter derivatives and to evaluate the effects of the wind on bluff bodies, experimental approaches through some *system identification method* either in the frequency or in the time domain should be employed [60]. A number of methods has already been tried and can be found in the literature [28, 39, 65, 66, 67, 68, 69, 70, 71], including forced and free vibration techniques. The latter are less expensive; however, in the high

velocity range the vertical motion of the model decays rapidly, reducing the length of time history that can be used in the analysis, introducing difficulties to the system identification [72].

As an assumption for the use of forced vibration techniques, it is considered that the bridge deck should present a harmonic motion during flutter instability [54]. In this section only two methods, based on this technique, will be delineated.

Firstly, the aerodynamic coefficients without the presence of wind are measured, so the same coefficients are obtained for different wind velocities in wind tunnel tests with the model subjected to forced vibration either in heaving or in torsional motion. Then the effects of the wind can be isolated by subtracting the former set of results from the latter, so that the aerodynamic derivatives can be calculated.

With the use of load cells, the lift forces and the moments associated to 1-DOF forced heaving motion can be evaluated by using Eq.2.39 to Eq.2.41.

$$L(t) = L_{\eta 0}.cos(\omega_\eta.t - \psi_{L\eta}) \tag{2.39}$$

$$M(t) = M_{\eta 0}.cos(\omega_\eta.t - \psi_{M\eta}) \tag{2.40}$$

$$\eta(t) = \eta_0.sin(\omega_\eta.t) \tag{2.41}$$

where: $L_{\eta 0}$ is the amplitude of the lift force in forced heaving motion (down is positive); $M_{\eta 0}$ is the amplitude of the moment in forced heaving motion (nose-up is positive); $\psi_{L\eta}$ is the phase lag from the maximum angle of attack to the maximum lift force (down is positive) in forced heaving motion; $\psi_{M\eta}$ is the phase lag from the maximum angle of attack to the maximum moment (nose-up is positive) in forced heaving motion; η_0 is the amplitude of the heaving motion; ω_η is the heaving circular frequency and t is time.

In the case of single DOF heaving motion, Eq.2.5 and Eq.2.6 can be re-written as follows:

$$L(t) = \frac{1}{2}\rho(2.b)\,U^2 \left\{ k.H_1^* \frac{\dot{\eta}}{U} + k^2.H_4^* \frac{\eta}{b} \right\} \tag{2.42}$$

$$M(t) = \frac{1}{2}\rho(2.b^2)\,U^2 \left\{ k.A_1^* \frac{\dot{\eta}}{U} + k^2.A_4^* \frac{\eta}{b} \right\} \tag{2.43}$$

So combining and rearranging Eq.2.39, Eq.2.40, Eq.2.42 and Eq.2.43, the values for the aerodynamic coefficients can be expressed, through the following equations:

$$H_1^* = \frac{L_{\eta 0}.cos(\psi_{L\eta})}{\rho.b^2.\omega_\eta^2.\eta_0} \tag{2.44}$$

$$H_4^* = \frac{L_{\eta 0}.sin(\psi_{L\eta})}{\rho.b^2.\omega_\eta^2.\eta_0} \tag{2.45}$$

$$A_1^* = \frac{M_{\eta 0}.cos(\psi_{M\eta})}{\rho.b^3.\omega_\eta^2.\eta_0} \tag{2.46}$$

$$A_4^* = \frac{M_{\eta 0}.sin(\psi_{M\eta})}{\rho.b^3.\omega_\eta^2.\eta_0} \tag{2.47}$$

Similarly, the aerodynamic derivatives for the single DOF torsional motion can be expressed by the following equations:

$$H_2^* = -\frac{L_{\varphi 0}.sin(\psi_{L\varphi})}{\rho.b^3.\omega_\varphi^2.\varphi_0} \tag{2.48}$$

$$H_3^* = \frac{L_{\varphi 0}.cos(\psi_{L\varphi})}{\rho.b^3.\omega_\varphi^2.\varphi_0} \tag{2.49}$$

$$A_2^* = -\frac{M_{\varphi 0}.sin(\psi_{M\varphi})}{\rho.b^4.\omega_\varphi^2.\varphi_0} \tag{2.50}$$

$$A_3^* = \frac{M_{\varphi 0}.cos(\psi_{M\varphi})}{\rho.b^4.\omega_\varphi^2.\varphi_0} \tag{2.51}$$

where: $L_{\varphi 0}$ is the amplitude of the lift force in forced torsional motion (down is positive); $M_{\varphi 0}$ is the amplitude of the moment in forced torsional motion (nose-up is positive); $\psi_{L\varphi}$ is the phase lag from the maximum angle of attack to the maximum lift forces (down is positive) in forced torsional motion; $\psi_{M\varphi}$is the phase lag from the maximum angle of attack (down is positive) to the maximum pitching moment (nose-up is positive) in forced torsional motion; φ_0 is the amplitude of the torsional motion; ω_t is the heaving circular frequency.

This technique has the advantage of being precise and easily applicable to any kind of geometry; however, it does not provide any information about the pressure distribution along the body. For that purpose, a technique based on the direct measurement of the local pressures along the model should be applied, followed by a mathematical treatment as explained in Section 2.2 and in the next lines.

The pressure signals are acquired by using pressure taps at suitable locations in a specific sampling ratio and converted into pressure coefficients $\tilde{C}_p(x^*)$ and phase difference $\psi(x^*)$, as described in Appendix C. So the aerodynamic derivatives are evaluated by using Eq.2.52 to Eq.2.59.

$$H_2^* = \frac{1}{k^2.\varphi_0}\int_{-1}^{1} \tilde{C}_p(x^*).sin\ \psi(x^*).dx^* \tag{2.52}$$

$$H_3^* = -\frac{1}{k^2.\varphi_0}\int_{-1}^{1} \tilde{C}_p(x^*).cos\ \psi(x^*).dx^* \tag{2.53}$$

$$A_2^* = \frac{1}{k^2.\varphi_0}\int_{-1}^{1} x^*.\tilde{C}_p(x^*).sin\ \psi(x^*).dx^* \tag{2.54}$$

$$A_3^* = -\frac{1}{k^2.\varphi_0}\int_{-1}^{1} x^*.\tilde{C_p}(x^*).cos\ \psi(x^*).dx^* \tag{2.55}$$

$$H_1^* = -\frac{U}{k.\omega_\eta.\eta_0}\int_{-1}^{1} \tilde{C_p}(x^*).cos\ \psi(x^*).dx^* \tag{2.56}$$

$$H_4^* = -\frac{U}{k.\omega_\eta.\eta_0}\int_{-1}^{1} \tilde{C_p}(x^*).sin\ \psi(x^*).dx^* \tag{2.57}$$

$$A_1^* = -\frac{U}{k.\omega_\eta.\eta_0}\int_{-1}^{1} x^*.\tilde{C_p}(x^*).cos\ \psi(x^*).dx^* \tag{2.58}$$

$$A_4^* = -\frac{U}{k.\omega_\eta.\eta_0}\int_{-1}^{1} x^*.\tilde{C_p}(x^*).sin\ \psi(x^*).dx^* \tag{2.59}$$

This technique is more susceptible to mistakes and misinterpretations during the extraction of the experimental data; however, provides insight on the characteristics of the flow around the body in motion and was chosen to be used in the development of the present research.

2.3.2 Aerodynamic Derivatives Interdependence

Even existing eight aerodynamic derivatives to be considered in a two-dimensional aerodynamic characterization of bridge decks, the existence of interdependence between them, which would lead to simplifications in this characterization, had already been pointed out in the technical literature early in 1978, by Nakamura [42]. This interdependence has been mentioned by other researchers in posterior publications [3, 4, 48, 73, 74].

Matsumoto and Matsumoto et al. [3, 74], by carrying out wind tunnel investigations on rectangular cylinders with side ratio B/D ranging from 5 to 20 submitted to forced tor-

sional and heaving sinusoidal motions, presented physical evidences of this interdependence, described by Eq.2.60 to Eq.2.63.

$$H_1^* = k.H_3^* \tag{2.60}$$

$$H_4^* = -k.H_2^* \tag{2.61}$$

$$A_1^* = k.A_3^* \tag{2.62}$$

$$A_4^* = -k.A_2^* \tag{2.63}$$

Furthermore, since the equivalent Wagner function, defined as the inverse Fourier transformation of the equivalent Theodorsen function, should be a real function, it is possible to relate A_2^* and A_3^* in the torsional motion and H_1^* and H_4^* in the heaving motion, according to [3]. Combining these assumptions with Eq.2.60 to Eq.2.63, it was concluded that there are only two independent aerodynamic derivatives, which can be characterized by the two parameters of the unsteady pressure characteristics: amplitude $\tilde{C}_p(x^*)$ and phase difference $\psi(x^*)$ [4].

Although these relationships hold for some streamlined bridge decks, they were found to fail or to present different patterns for other kinds of cross-sections [73]. Because of that, this interdependence, the way it is presented in Eq.2.60 to Eq.2.63, can not be extended to all geometries as a generalization.

The accuracy of these equivalence relationships is maximized in the quasi-steady limit, for a situation in which a strong similarity between the unsteady pressure characteristics of heaving and torsional oscillations under the same relative angle of attack is presented. So Eq.2.31 to Eq.2.38 can be evaluated by considering the reduced frequency k tending to zero. Consequently, *F(k)* and *G(k)* approach their asymptotic limit values, according to Eq.2.64 and 2.65, and mathematical manipulation considering the Theodorsen function can lead indeed to Eq.2.60, Eq.2.62 and Eq.2.63.

$$lim_{k\to 0}F(k) = 1 \tag{2.64}$$

$$lim_{k\to 0}G(k) = 0 \tag{2.65}$$

However, Eq.2.61 can not be approximated by the quasi-steady assumption, which actually leads to Eq.2.66.

$$H_4^* = -k.(H_2^* + 2.A_1^*) \tag{2.66}$$

Equivalence relationships can be also obtained by considering the equations of motion, forces and moments along the deck in the quasi-steady limit [48]. By this approach, although Eq.2.61 is also verified, Eq.2.60 presents a slight difference.

Because the equivalence relationships Eq.2.60 to Eq.2.63 are based on the assumption of the existence of a strong similarity between the unsteady pressure characteristics of torsional and heaving motions in a quasi-steady limit, their usage should be limited to well-streamlined cross-sections and be considered with some reserve for other shapes. In real bridge decks this similarity is deformed, and if an equivalent Theodorsen function can be established for generic bridge deck shapes the values of *F(k)* and *G(k)* will be different among motions.

2.4 Concluding Remarks

An overview of the aerodynamic problems related to long-span bridges was presented, with emphasis on the flutter instability. Also, considerations about the formulations used in the calculations developed in this study, especially for the aerodynamic derivatives, can be found in this chapter, which should be used as reference during the reading of the thesis.

Part II

Results

Chapter 3

Coupled Flutter Stabilization from the Unsteady Pressure Characteristics Point of View

3.1 Introduction

The formulation of the relationships between geometry, aerodynamic derivatives, structural properties, wind characteristics and flutter instability is a very complicated problem in modern bridges, whose frontiers have not been completely clarified until the present days. The search for a better understanding about the connections between all these factors has motivated investigations throughout the world, and the knowledge obtained from experiences with different kinds of bridges has provided general initial frameworks of concepts, to be used in the proposition of flutter resistant cross-sections during the design phase of a new project.

After the classic Scanlan & Tomko's paper [46], the studies on aerodynamic stabilization of bridges gained a new direction, and the usage of the so-called aerodynamic derivatives established a kind of common sense in the *Bridge Engineering*. By understanding the relationships between these aerodynamic derivatives and the aerodynamic instabilities themselves, comparisons between bridge decks have been possible.

Through such studies, it was found that depending on the cross-section the flutter instability may be increased or decreased by the addition of appendages and vertical plates along the bridge deck. In the case of central barrier, it was demonstrated by Nakamura [42] and Matsumoto [75] that the addition of such a device is sometimes effective in the augmentation of the aeroelastic stability of some kinds of cross-sections, contributing to an increasing of the critical flutter velocity. For bridges with two-edge girders, it was shown that the characteristics of the flutter instability are greatly influenced by the distance between girders and tends to be stabilized for smaller distances [76].

Also, flat diamond-shaped bodies were proved to have advantages in flutter stabilization [32]. They lead to a larger torsional rigidity and consequently higher torsional eigenfrequency, associated to an aerodynamic stabilization caused by the existence of two points of flow separation. This aerodynamic stabilization mechanism is also presented in elliptical cylinders, inverse triangle sections and rectangular cylinders with vertical plate at the mid-chord of the cross-section.

The spread of openings along the surface of bodies subjected to the wind flow has also a high influence on the flutter instability these bodies may experience; depending on the opening ratio as well as on their location, peculiar flutter phenomena may be observed [16], through a hybrid type of torsional branch and heaving branch in coupled flutter. Also the combination of 2 different kinds of cross-sections along the spans proved itself to be a good strategy for flutter stabilization, with cost benefits [18].

Although a large amount of studies has been focused on matching aerodynamic derivatives, cross-sections and instabilities, exact explanations based on the physical phenomena involved in the generation mechanism of the aerodynamic instabilities are still needed. Since aerodynamic derivatives are resultant of the unsteady pressure characteristics developed along the bridge deck, it must be more rational to search for relationships between deck geometry and flutter stabilization from the unsteady pressure characteristics point of view. This may finally lead to the ability of controlling the aerodynamic derivatives through a direct *manipulation* of these unsteady pressure characteristics, via the proposition of suitable geometric compositions.

Based on that, the proposition of this chapter is to assess the flutter stabilization problem from the unsteady pressures characteristics point of view, generating as an output configurations of unsteady pressure characteristics a bridge deck should present in order to prevent flutter, namely *optimal unsteady pressure characteristics*.

The results of the analyses conducted herein may serve as *target configurations* in the design framework proposed in the Chapter 1, in which the geometry of the bridge deck is proposed by consciously considering its influences on the inherent unsteady pressure characteristics of the deck, instead of focusing solely on the aerodynamic derivatives. By understanding the effects of the introduction of geometric modifications (*geometric singularities*) in the deck, it is expected to be attained the ability of driving the unsteady pressure characteristics to present configurations of aerodynamic derivatives proper for flutter stabilization. This subject will be addressed in the subsequent chapters of the thesis.

The influences of external factors, as the turbulence of the approaching flow, the surroundings and even the clearance under the girder [77], have been recognized to have an important impact on the unsteady pressure characteristics of the bridge. Because of that, they should also be taken into account in the design. However, in this study such aspects will not be approached.

Firstly, the flutter stability is discussed from an aerodynamic derivatives point of view, in Section 3.2. So, from the conclusions of this section, unsteady pressure characteristics which lead to flutter proof configurations of aerodynamic derivatives are presented, in Section 3.3, being fine tuned through flutter analysis. Finally, in Section 3.4, concluding considerations about this approach are presented.

3.2 Role of aerodynamic derivatives

Due to the low-level damping inherent to long span bridges, the decaying and growing of the motions has little influence on the self-excited forces these structures may experience, and because of that the aerodynamic derivatives can be understood to be not dependent on the structural damping [8].

However, some sources of potential nonlinearities can be related to the dependence the flutter onset velocity may have on the whole set of dynamic properties of the bridge; more precisely, on how the modal frequencies, damping ratios and intermodal coupling can be influenced by the self-excited forces and how these interactions consequently affect the flutter onset velocity itself, in a retro feeding process.

In this sense, multimode flutter analysis frameworks, which take in consideration the interactions between structural characteristics of multiple modes and aerodynamic properties of the bridge deck, have been used for advanced prediction of coupled flutter in bridges. By making use of them, it has already been shown that bridge flutter is usually controlled by the fundamental torsional and vertical modes, with only minor contributions from other modes [8, 13]. Also, it has been accepted as a reasonable approximation for wind tunnel tests that the dynamic properties of the model, when considered in terms of reduced frequency, do not affect critically the results of the investigations in terms of onset velocity. Based on that, results obtained from wind tunnel tests can be extended to any prototype that presents similarity of geometry, mass properties and dynamic characteristics [39].

On the other hand, the influences each aerodynamic derivative has on the flutter onset velocity are still not fully understood and many researchers have put efforts in finding out how to interpolate all the relevant factors in a common formulation. From such studies, it could already be verified that these influences may vary according to the different classes of flutter, which are dependent on the geometry of the cross-sections. For example, slender cross-sections usually present $H_1^*<0$ and $A_2^*<0$, which lead to a coupled flutter instability, enhancing the importance of both coupled (H_2^*, H_3^*, A_1^*, A_4^*) and uncoupled (H_1^*, H_4^*, A_2^*, A_3^*) aerodynamic derivatives [8]; single-vertical-mode flutter (galloping) or single-torsional-mode flutter (torsional flutter) can be developed only when $H_1^*>0$ and $A_2^*>0$, respectively [8].

In the case of coupled flutter, the complexity of the traditional methods of flutter analysis based on eigenvalue problems permits obtaining information about the flutter generation mechanism only through extensive parametric studies [4, 8]. That led to the need of searching different approaches, resulting in that a number of alternative formulations to assess the aerodynamic stability of bridges have already been proposed.

Considering a supposed independence between the influences of the aerodynamic characteristics and the dynamic properties of the bridge on the flutter onset velocity, the use of an empiric *aerodynamic stability performance index*, dependent only on the geometric characteristics of the bridge, has already been tried [39]. However, such a method does not provide any information about the importance each aerodynamic derivative has separately on the flutter generation mechanism. Based on that, different methods should be used for that purpose.

Matsumoto et al. [4] proposed the *Step-By-Step Analysis* (SBS Analysis), an iterative flutter analysis method claimed to clarify the role each aerodynamic derivative plays for

the genesis of flutter instability. Basically, in this method the interactions between heaving and torsional modes are analyzed through the application of a forced vibration in one of the modes, which in turn induces the vibration in the other mode. Then, this consequent induced vibration affects the vibration in the mode excited previously, and so the iteration is kept until the convergence condition is reached.

By using this method [4, 10, 32, 78, 79], it was identified that A_2^*, A_1^* and H_3^* play major roles in the stabilization of the torsional branch and H_1^*, A_1^* and H_3^* in the heaving branch. As a result, an optimal scenario for coupled flutter stability in terms of aerodynamic derivatives can be delineated, as shown in Table 3.1. Moreover, considering the dependence between these aerodynamic derivatives (see Section 2.3.2), Matsumoto et al. [78] isolated A_1^* as the most relevant aerodynamic derivative in terms of impact on the onset velocity.

Table 3.1: Role of the aerodynamic derivatives in coupled flutter, according to *Step-by-step Analysis*

Derivative	**Stabilization**	**Destabilization**
A_1^*	*low absolute values*	*high absolute values*
A_2^*	*negative values*	*positive values*
A_3^*	*low absolute values*	*high absolute values*
H_1^*	*negative values*	*positive values, low absolute values*
H_3^*	*low absolute values*	*high absolute values*
A_1^* x H_3^*	*negative values*	*positive values*

A point of concern in the scenario of Table 3.1 might be related to the exact frontiers for terms like *low absolute values* and *high absolute values*, as well as the range of values of aerodynamic derivatives for which the conclusions still hold. Since the coupled flutter is a phenomenon associated to slender cross-sections, which present similarities in terms of aerodynamic derivatives to a flat plate, a good starting point for the establishment of these frontiers might be the derivatives obtained through Theodorsen function [47].

Although Selberg's formula is recognized to provide accurate results for a flat plate, its provisions are considered usually conservative in terms of coupled flutter [80]. In the search for better estimations for this instability, Nakamura [42] in 1978 came to an equation, whose aerodynamic coefficient was calculated based on a relationship between the aerodynamic derivatives, very similar to the Selberg's formula. In fact, when the aerodynamic derivatives calculated for a flat plate in a high frequency of oscillation were used, the aerodynamic index of Nakamura‘s formulation differed from the Selberg's formula‘s, i.e. 0.44, only slightly.

In the same line, considering cross-sections of long span bridges prone to coupled flutter and assuming well-separated eigen-frequencies, Chen [8] presented a closed-form solution, Eq.3.1, also similar to the one suggested by Selberg [81], Eq.3.2. This formulation was claimed to be an analytical basis for Selberg's formula, serving as an extension to bridges with generic bluff deck sections.

$$U_{cr} = \gamma_{chen}.\omega_{\varphi}.b\sqrt{\left(1 - \left(\frac{\omega_{\eta}}{\omega_{\varphi}}\right)^{2}\right).\left(\frac{m_{chen}.r}{\rho.b^{3}}\right)} \tag{3.1}$$

where: U_{cr} is the flutter onset velocity; γ_{chen} is an aerodynamic index, dependent on the aerodynamic derivatives; ω_{φ} is the torsional natural frequency; b is the half-width of the deck; ω_{η} is the heaving natural frequency; m_{chen} is the mass coefficient; r is the radius of gyration.

$$U_{cr} = 0.44.\omega_{\varphi}.b\sqrt{\left(1 - \left(\frac{\omega_{\eta}}{\omega_{\varphi}}\right)^{2}\right).\frac{\sqrt{2}w.r_{m}}{\pi.\rho.b^{3}}} \tag{3.2}$$

where: w is the weight of the bridge; r_m is the mass radius of gyration.

In Chen's formulation, the onset velocity is computed by considering the influences of the dynamic properties separately from the influences of the geometric characteristics, which assume the form of an aerodynamic index composed by a relationship between A_1^*, A_2^*, A_3^* and H_3^*. Here, differently from the formulation proposed in [39], this aerodynamic index is a direct consequence of a relationship between aerodynamic derivatives, providing an insight on their contributions for the coupled flutter generation mechanism.

Through a sensitivity analysis using that closed form solution, the influences of those four aerodynamic derivatives on the flutter onset velocity of a box girder bridge deck were identified. The bridge deck investigated presented aerodynamic derivatives similar to a flat plate and the method used in the analysis was based on individually impacting by factors of *0.5* and *2.0* (*50%* and *200%* of the original values) each one of the four aerodynamic derivatives - A_1^*, A_2^*, A_3^*, H_3^* -, evaluating subsequently the onset velocity of each new combination. The results are summarized in Table 3.2, presenting the impact in percentage on

the original flutter onset velocity of each arrangement, showing a good agreement with the scenario proposed in Table 3.1.

Table 3.2: Impact on the onset velocity through sensitivity analysis considering closed form solution proposed by Chen[8]

Derivative	**50%**	**200%**
A_1^*	*+11%*	*-36%*
A_2^*	*-36%*	*+14%*
A_3^*	*+13%*	*-16%*
H_3^*	*+14%*	*-36%*

Of course such a sensitivity analysis lacks the sense of reality, since the independent manipulation of the aerodynamic derivatives still represents a challenge, due to their inherent inter-relation (see Section 2.3.2). However, it provides some useful information about the role each aerodynamic derivative plays individually for the coupled flutter destabilization, pointing directions for its stabilization process.

3.3 Unsteady Pressure Characteristics

Since the aerodynamic derivatives are numerical indices derived from a physical reality, i.e. the unsteady pressure characteristics along the bridge deck, it seems to be logical to face the problem of stability of bridges by looking directly on these unsteady pressure characteristics, instead of focusing solely on the aerodynamic derivatives.

In this section the relationships between flutter stability and aerodynamic derivatives are extended to the level of the unsteady pressure characteristics, represented by $\tilde{C}_p(x^*)$ and $\psi(x^*)$, so that the conclusions drawn in Section 3.2 can be *translated* into this perspective. By doing so, optimal scenarios of unsteady pressure characteristics are delineated, which can turn to be a valuable resource in the proposition of better schemes of flutter stabilization through the *manipulation* of these unsteady pressure characteristics, by the insertion of *geometric singularities* along the bridge deck.

Understanding the impacts these *geometric singularities* may have on the unsteady

pressure characteristics along bridge decks is a key point in the mainstream of this thesis, and subsequent chapters will discuss this theme.

3.3.1 Qualitatively Analysis

In terms of the equations related to the pressure distribution, each aerodynamic derivative is compounded by a summation of forces or moments along the bridge deck, which are given by the integrals of the Eq.2.52 to Eq.2.59. Because of the orientation of the normalized coordinate system, the pressure components of the derivatives related to the pitching moment (A_1^*, A_2^*, A_3^*, A_4^*) take negative sign for the upwind half of the cross-section and positive sign for its downwind half, Fig.3.1. The pressure components related to the aerodynamic derivatives related to the lift forces (H_1^*, H_2^*, H_3^*, H_4^*) are not affected by their location x^* on the deck, being dependent only on the unsteady pressure characteristics themselves.

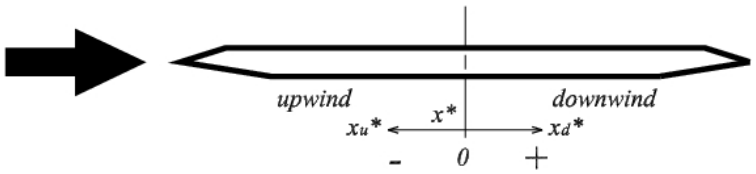

Figure 3.1: Orientation of the normalized coordinate system

It is worth drawing the attention to the fact that even though Fig.3.1 is representing a single and symmetric bridge deck, these considerations about the influences of the normalized coordinate system on the values of the aerodynamic derivatives can be extended to any geometry and arrangement of deck, considering only the location of the rotational pivot of the whole structure.

From a simplistic point of view, it can be said that in order to bring the values of A_1^*, A_2^*, A_3^*, A_4^* to the negative side, the upwind side pressure components of these derivatives should be greater than their downwind side pressure components in Eq.2.52 to Eq.2.59. For the same reasons, in order to bring them to positive values their downwind side components should be greater than their upwind side components, and in order to make them zero valued both upwind and downwind side components should be equivalents. In the case of H_1^*, H_2^*, H_3^* and H_4^* , since they are not affected by x^*, considerations about side are not necessary.

In the equations for the aerodynamic derivatives, Eq.2.52 to Eq.2.59 in Section 2.3, the

role played by the unsteady pressure amplitude $\tilde{C}_p(x^*)$ is associated to the modulus of the integrands, which means that the signs of the derivatives are defined by the value of *sin* or *cos* of the phase difference, accordingly. So the control of the aerodynamic derivatives from an unsteady pressure characteristics point of view can be obtained by providing suitable values of phase difference to locations along the cross-section where the amplitude exerts a major influence, considering in the case of A_1^*, A_2^*, A_3^* and A_4^* the effects of the normalized coordinate system as well.

Assuming, as a simplification, constant values of amplitude $\tilde{C}_p(x^*)$ along the whole deck and proposing configurations of phase difference distribution $\psi(x^*)$ convenient for coupled flutter stabilization, the influences of $\psi(x^*)$ in this process can be emphasized and then better understood.

In the case of A_2^*, which is considered to be one of the most important aerodynamic derivatives in terms of flutter stabilization, negative values should be pursued. In order to satisfy this condition through the control of the phase difference $\psi(x^*)$, the torsional system must exhibit values situated in the range of $0 < \psi(x_u^*) < +\pi$ for the upwind side of the deck and in the range of $0 > \psi(x_d^*) > -\pi$ for its downwind side. This may be a first requirement for a bridge deck design from an unsteady pressure characteristics perspective, and locations where this requirement is not satisfied must be somehow counterbalanced with measures in other locations of the bridge deck, whether by increasing the weight of $\tilde{C}_p(x^*)$ in *stable zones* or by leading $\psi(x^*)$ to more suitable values. Moreover, considering the fact that this aerodynamic derivative is also dependent on the normalized coordinate x^*, it should be kept in mind that locations near the edges play greater roles for the definition of its value, in comparison to locations near the center.

According to the set of aerodynamic derivatives presented in Table 3.1, H_3^* has also to be taken in consideration in the torsional system. This derivative should have *low absolute values* and the values of phase difference $\psi(x^*)$ which minimize this aerodynamic derivative are situated around $+\pi/2$ and $-\pi/2$ for the whole deck. However, this requirement is also fulfilled for a combination of $-\pi/2 \leq \psi(x_u^*) \leq +\pi/2$ in the upwind half with its nearly antisymmetric distribution $+\pi/2 \geq \psi(x_d^*) \geq -\pi/2$ in the downwind half of the deck, or *vice-versa*.

Also, A_3^* plays relevant role for the stability of the torsional branch, and in order to bring this derivative to the safety side the phase difference distribution $\psi(x^*)$ should have constant values in modulus along the whole deck.

Considering these 3 aerodynamic derivatives, a possible configuration for phase difference distribution that fulfills the requirements proposed in Table 3.1 would be any antisymmetric configuration with values in the range of $0 \leq \psi(x_u^*) \leq +\pi/2$ for the upwind side and in the range of $0 \geq \psi(x_d^*) \geq -\pi/2$ for the downwind side of the deck, according to Fig. 3.2.

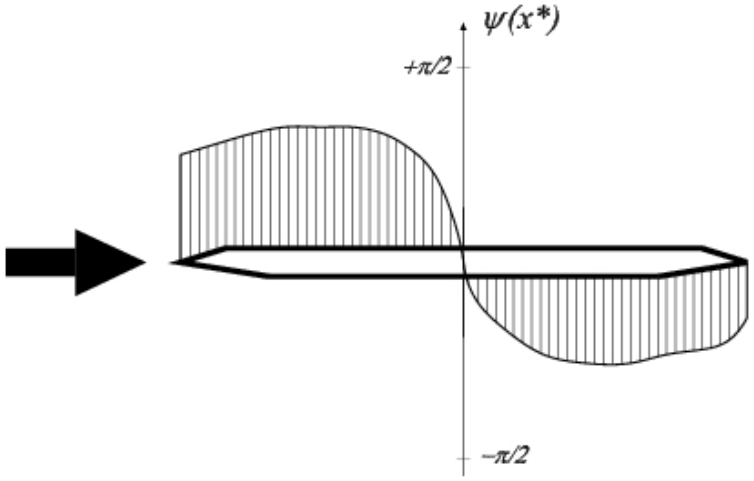

Figure 3.2: Stable phase difference $\psi(x^*)$ distribution for the torsional system, assuming constant $\tilde{C}_p(x^*)$ along the body

It is important to keep in mind that this configuration would be the target if the amplitude $\tilde{C}_p(x^*)$ of the unsteady pressure characteristics could be maintained constant throughout the whole deck, which does not occur in real bridges. So the real influences of the proposed configuration of phase difference distribution $\psi(x^*)$ will be strongly related to the values of unsteady pressure amplitude $\tilde{C}_p(x^*)$ at each position x^* of the deck, resulting in that many other possible configurations might be delineated.

Still following the conditions established in Table 3.1, the heaving branch, represented by A_1^* and H_1^*, has also to be considered. By conducting an analysis similar to the one performed for the torsional system, optimal configurations for the unsteady pressure characteristics of the heaving system can also be obtained. In these configurations, A_1^* requires a pattern similar to the one required by A_3^*, and H_1^* requires values in the range of $-\pi/2 \leq \psi(x^*) \leq +\pi/2$ for the whole deck.

Combining these 2 conditions, the result is any antisymmetric distribution which presents values in the range of $-\pi/2 \leq \psi(x^*) \leq +\pi/2$ along the whole deck. Fig.3.3 illustrates some examples.

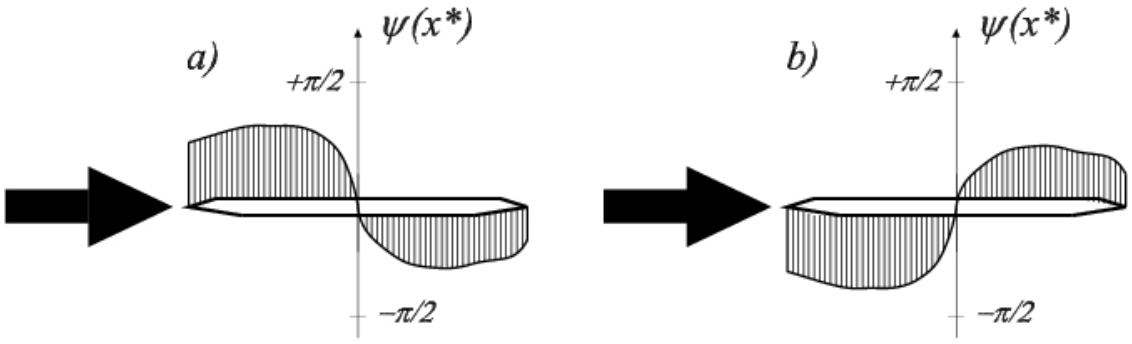

Figure 3.3: Some stable phase difference $\psi(x^*)$ distributions for the heaving system, assuming constant $\tilde{C}_p(x^*)$ along the body

The targets for the aerodynamic derivatives can be obtained by several independent combinations of amplitude $\tilde{C}_p(x^*)$ and phase difference $\psi(x^*)$ in each system. However, since the conclusions presented in Table 3.1 are strongly based on the assumption of the aerodynamic interdependence (section 2.3.2), the optimal configuration for the unsteady pressure characteristics of the heaving system must be somehow similar to the one proposed for the torsional system. Due to the intrinsic relationship between the unsteady pressure characteristics of both systems [82], responsible for the aerodynamic derivatives dependence, totally independent scenarios can not be easily obtained; and this should be taken into account during the design phase of bridge decks.

Integrating the results above into a common solution, it is possible to propose as an optimal scenario in terms of unsteady pressure characteristics common for both systems the one proposed for the torsional branch, Fig.3.2, which also stabilizes the heaving branch, Fig.3.3-a.

3.3.2 Quantitatively Analysis

In order to verify the optimal configurations proposed in this study, flutter analyses were conducted by combining 3 different values of $\tilde{C}_p(x^*)$ i.e. *0.1*, *0.5* and *1.0*, constant along the whole deck, with values of phase difference $\psi(x^*)$ varying within the limits of the intervals proposed previously: in the range of $0 \leq \psi(x_u^*) \leq +\pi/2$ for the upwind side and in the range of $0 \geq \psi(x_d^*) \geq -\pi/2$ for the downwind side of the deck. By doing so, the limits for the qualitatively analysis done in Section 3.3.1 can be verified.

Initially, for each value of $\tilde{C}_p(x^*)$, two different approaches were taken. In the first one, same values in modulus with opposite signs for $\psi(x^*)$ were adopted along each side of the deck, keeping the antisymmetry of the distribution ($\psi(x_d^*) = -\psi(x_u^*)$), Fig.3.4. In the second approach, for each different value of phase difference $\psi(x_u^*)$ presented in the upwind side, the whole range of phase difference $\psi(x_d^*)$ of the downwind side of the deck was tested, Fig.3.5-a, and vice-versa, Fig.3.5-b.

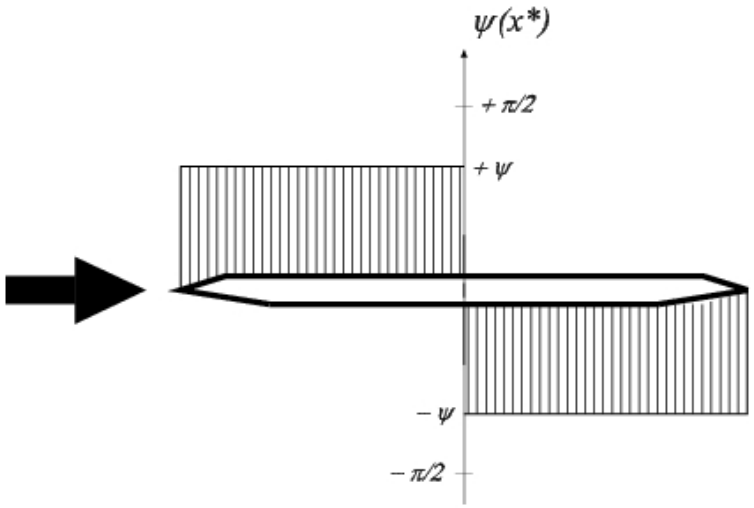

Figure 3.4: First approach: antisymmetric distribution

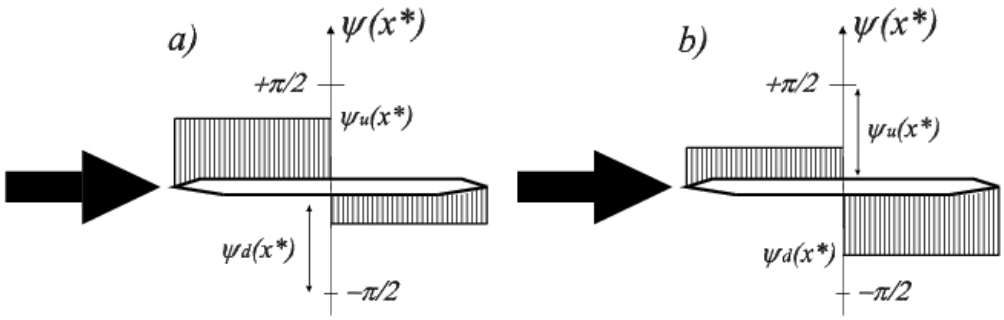

Figure 3.5: Second approach: independent values for each side

A preliminary analysis pointed out that the values of $\psi(x^*)$ which contribute for flutter destabilization were located near the boundaries of the proposed intervals. So near the boundaries a more refined resolution was adopted, by giving steps of 1° in the $\psi(x^*)$. Steps of 10° were adopted in the intermediate range of values, in order to save analysis effort.

The unsteady pressure characteristics adopted for both heaving and torsional systems were the same, which leads to the maintenance of the aerodynamic derivatives interdependence. The flutter stability was checked until the wind velocity of *100 m/s* by using the *Complex Eigenvalue Analysis*, considering a rectangular cylinder with width *B=0.30 m*, mass *m=2.42 kg/m*, mass moment of inertia *I=0.0181 Kg.m*^{2}*/m*, torsional natural frequency f_φ=5.2 Hz, heaving natural frequency f_η=4.0 Hz and null structural damping. For comparison purposes, the onset velocity for a flat plate (through Theodorsen function) with the same structural properties was also evaluated, resulting in a value around *10 m/s*.

For the first approach, 48 different combinations of unsteady characteristics were analyzed, Table 3.3, revealing flutter instability only on the boundaries of the proposed intervals of phase difference $\psi(x^*)$. For $\psi(x^*)$=0° flutter was trigged by the torsional branch and for $\psi(x_u^*)$=90° combined with $\psi(x_d^*)$=-90° by the heaving branch, Fig.3.6.

Table 3.3: First approach - antisymmetric distribution of $\psi(x^*)$

$\psi(x_u^*)$	$\psi(x_d^*)$	$\tilde{C}_p(x^*)$=0.1	$\tilde{C}_p(x^*)$=0.5	$\tilde{C}_p(x^*)$=1.0
0°	0°	*unstable*	*unstable*	*unstable*
1°	-1°	-	-	-
2°	-2°	-	-	-
3°	-3°	-	-	-
10°	-10°	-	-	-
20°	-20°	-	-	-
⋮	⋮	⋮	⋮	⋮
70°	-70°	-	-	-
80°	-80°	-	-	-
87°	-87°	-	-	-
88°	-88°	-	-	-
89°	-89°	-	-	-
90°	-90°	*unstable*	*unstable*	*unstable*

The antisymmetry in the phase difference $\psi(x^*)$ distribution contributes for the re-

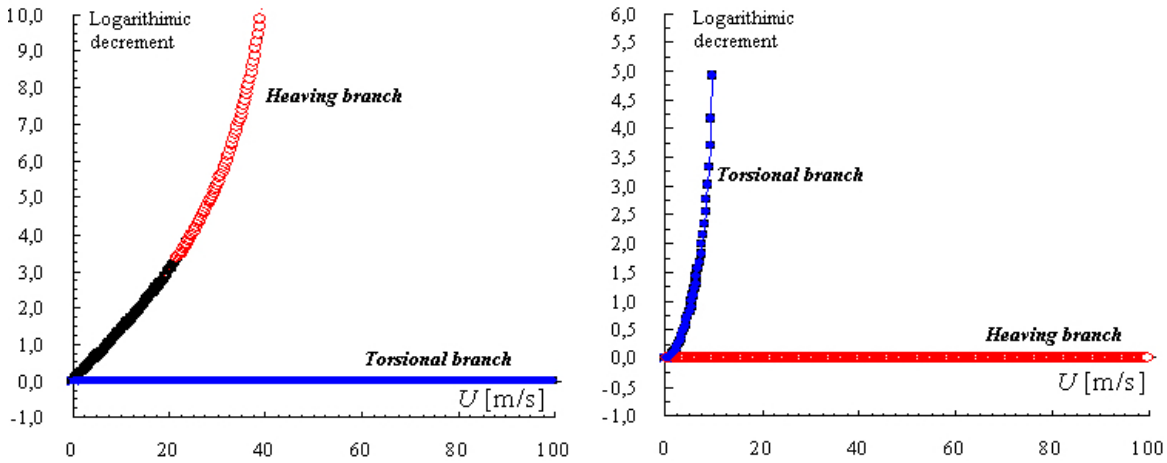

(a) by torsional branch (b) by heaving branch

Figure 3.6: Flutter destabilization

duction of the absolute values of A_1^* and A_3^*, which brings stabilizing effects in terms of flutter. However, the variation imposed on $\psi(x^*)$ induces a high oscillation in the values of A_2^* and H_3^*, which are also important components in this process, highlighting the whole these aerodynamic derivatives play for flutter instability.

In the second approach, the number of combinations of unsteady pressure characteristics analyzed was 972, and some of them are illustrated in Table 3.4.

At this time, a more complete panorama is represented, since the aerodynamic derivatives assume a wider range of values. In concordance with the previous approach, the boundaries of the intervals, represented by the combinations of $\psi(x_u^*)$=0° with $\psi(x_d^*)$=0° and $\psi(x_u^*)$=90° with $\psi(x_d^*)$=-90°, showed themselves prone to flutter. However, now some additional conclusions can be extracted from the results, which showed flutter instability also for combinations of low values of $\psi(x_u^*)$ with high values of $\psi(x_d^*)$ and *vice versa*, associated to higher values of $\tilde{C}_p(x^*)$. By visual analysis of Table 3.4, it is noticeable that flutter onset gets higher when the phase difference $\psi(x^*)$ distribution approaches the antisymmetry, and this effect is even reinforced with the increase of the values of $\tilde{C}_p(x^*)$. From an opposite point of view, it can be said that the higher the degree of non-antisymmetry, the lower the onset velocity.

Since in the range of phase difference $\psi(x^*)$ distributions verified in this analysis the

Table 3.4: Second approach: independent distributions of $\psi(x_u^*)$ and $\psi(x_d^*)$

		$\psi(x_d^*)$									
$\psi(x_u^*)$	$\tilde{C}_p(x^*)$	0°	−10°	−20°	−30°	−40°	−50°	−60°	−70°	−80°	−90°
	0.1	*10.0 m/s*	-	-	-	-	-	-	-	-	-
0°	*0.5*	*4.5 m/s*	-	-	-	*77.5 m/s*	*65.0 m/s*	*57.0 m/s*	*52.5 m/s*	*49.5 m/s*	*48.5 m/s*
	1.0	*12.5 m/s*	-	*68.5 m/s*	*50.5 m/s*	*41.0 m/s*	*34.5 m/s*	*30.0 m/s*	*27.5 m/s*	*26.0 m/s*	*25.0 m/s*
	0.1	-	-	-	-	-	-	-	-	-	-
10°	*0.5*	-	-	-	-	-	*82.0 m/s*	*70.0 m/s*	*63.0 m/s*	*59.5 m/s*	*58.0 m/s*
	1.0	*50.5 m/s*	-	*92.0 m/s*	*76.5 m/s*	*53.5 m/s*	*42.5 m/s*	*36.5 m/s*	*32.5 m/s*	*30.5 m/s*	*30.0 m/s*
	0.1	-	-	-	-	-	-	-	-	-	-
20°	*0.5*	-	-	-	-	-	-	*91.0 m/s*	*79.5 m/s*	*74.0 m/s*	*72.0 m/s*
	1.0	*33.5 m/s*	-	-	-	*80.5 m/s*	*57.5 m/s*	*46.5 m/s*	*41.0 m/s*	*38.0 m/s*	*37.0 m/s*
	0.1	-	-	-	-	-	-	-	-	-	-
30°	*0.5*	-	-	-	-	-	-	-	-	*97.0 m/s*	*94.0 m/s*
	1.0	*28.0 m/s*	-	-	-	-	*89.5 m/s*	*65.5 m/s*	*54.5 m/s*	*49.0 m/s*	*47.5 m/s*
	0.1	-	-	-	-	-	-	-	-	-	-
40°	*0.5*	-	-	-	-	-	-	-	-	-	-
	1.0	*25.5 m/s*	*40.5 m/s*	-	-	-	-	-	*79.5 m/s*	*69.0 m/s*	*66.0 m/s*
	0.1	-	-	-	-	-	-	-	-	-	-
50°	*0.5*	*53.5 m/s*	-	-	-	-	-	-	-	-	-
	1.0	*24.0 m/s*	*32.5 m/s*	-	-	-	-	-	-	-	-
	0.1	-	-	-	-	-	-	-	-	-	-
60°	*0.5*	*48.5 m/s*	*63.0 m/s*	-	-	-	-	-	-	-	-
	1.0	*24.0 m/s*	*28.0 m/s*	-	-	-	-	-	-	-	-
	0.1	-	-	-	-	-	-	-	-	-	-
70°	*0.5*	*46.0 m/s*	*58.5 m/s*	-	-	-	-	-	-	-	-
	1.0	*24.0 m/s*	*26.0 m/s*	*36.0 m/s*	-	-	-	-	-	-	-
	0.1	-	-	-	-	-	-	-	-	-	-
80°	*0.5*	*45.0 m/s*	*55.5 m/s*	*70.5 m/s*	-	-	-	-	-	-	-
	1.0	*25.0 m/s*	*26.0 m/s*	*33.5 m/s*	-	-	-	-	-	-	-
	0.1	-	-	-	-	-	-	-	-	-	*0.5 m/s*
90°	*0.5*	*45.0 m/s*	*55.0 m/s*	*69.5 m/s*	-	-	-	-	-	-	*0.5 m/s*
	1.0	*26.5 m/s*	*26.0 m/s*	*34.0 m/s*	*45.5 m/s*	-	-	-	-	-	*0.5 m/s*

aerodynamic derivatives A_2^* and H_3^* are kept in their stabilizing zone, the instability associated to non-antisymmetric distributions of $\psi(x^*)$ can be regarded to the effects of the high absolute values assumed by A_1^* and A_3^* in these configurations, which contribute for flutter destabilization. By keeping the antisymmetry of the phase difference $\psi(x^*)$ distribution, the absolute values of A_1^* and A_3^* decrease, creating stabilizing conditions for flutter.

These two approaches, even not being realistic, confirm that flutter stability can be obtained by keeping the values of phase difference within the limits proposed in Fig.3.2 in both systems. This is not guaranteed for all combinations that may result from that

condition, but serves as a guideline in the proposition of configurations of unsteady pressure characteristics for flutter proof bridge decks.

Since it was assumed a constant and continuous distribution for $\tilde{C}_p(x^*)$ throughout the whole deck, nothing can be said about the importance of the location of the peaks in the unsteady pressure amplitude $\tilde{C}_p(x^*)$ distribution. This situation is commonly presented in real bridge decks and impacts substantially on the values of the aerodynamic derivatives. In order to check for that, a third and a fourth approaches were taken, in which the unsteady pressure amplitude $\tilde{C}_p(x^*)$ assumed a *discretized distribution* as a *singleton* at different locations along the deck, assuming a value of $\tilde{C}_p(x^*)$=1.0 spanned for a normalized width of Δx^*_{cp}= 0.25b, according to Fig.3.7.

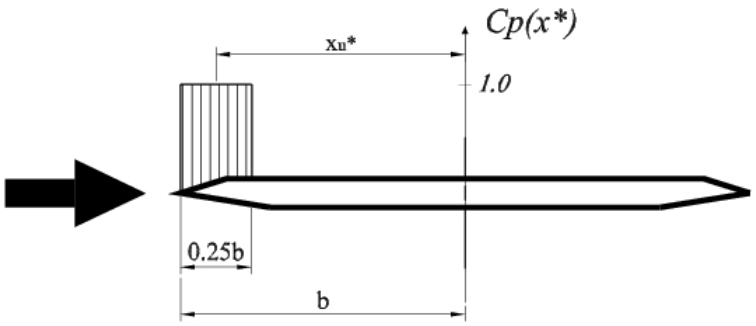

Figure 3.7: $C_p(x*)$ as a singleton

In the first of these two additional propositions, called herein *Third Approach*, the peaks of unsteady pressure amplitude were limited to only one location whether in the upwind side, x^*_u=-0.875, x^*_u=-0.625, x^*_u=-0.375 and x^*_u=-0.125, or in the downwind side, x^*_d=+0.125, x^*_d=+0.375, x^*_d=+0.625 and x^*_u=+0.875, combined with the values of phase difference proper to each side of the cross-section, $0 \leq \psi(x^*_u) \leq +\pi/2$ and $0 \geq \psi(x^*_d) \geq -\pi/2$, varying in steps of 10°. The number of combinations analyzed was 88, showed in Table 3.5 and Table 3.6 with their resulting flutter onset.

The results show that the flutter onset increases as the peak moves towards the trailing edge, for all values of phase difference $\psi(x^*)$. This effect is maximized in the situation in which the peak is located in the downwind side of the deck, Table 3.6, in which flutter could not be detected. This tendency is related to the decreasing of the values of A^*_1 and A^*_3, which turn negative when the peak is located in the downwind side. The signs of the derivatives H^*_2 and H^*_3 are also impacted by the side of the section in which the peak is located, since they are also dependent on the values of phase difference $\psi(x^*)$ of each side, which are in different

Table 3.5: Third approach - peak in the upwind side

x_u^*	$\psi(x_u^*)$ 0°	10°	20°	30°	40°	45°	50°	60°	70°	80°	90°
-0.875	*0.5 m/s*	*6 m/s*	*7.5 m/s*	*8 m/s*	*8 m/s*	*7.5 m/s*	*7.5 m/s*	*6.5 m/s*	*5.5 m/s*	*4 m/s*	*0.5 m/s*
-0.625	*0.5 m/s*	*6.5 m/s*	*8.5 m/s*	*9 m/s*	*9 m/s*	*8.5 m/s*	*8.5 m/s*	*7.5 m/s*	*6.5 m/s*	*5 m/s*	*0.5 m/s*
-0.375	*0.5 m/s*	*7 m/s*	*10 m/s*	*11 m/s*	*11 m/s*	*11 m/s*	*10.5 m/s*	*9.5 m/s*	*8 m/s*	*6 m/s*	*0.5 m/s*
-0.125	*0.5 m/s*	*8 m/s*	*13 m/s*	*15.5 m/s*	*16.5 m/s*	*16.5 m/s*	*16.5 m/s*	*15 m/s*	*13 m/s*	*11 m/s*	*0.5 m/s*

Table 3.6: Third approach - peak in the downwind side

x_d^*	$\psi(x_d^*)$ 0°	−10°	−20°	−30°	−40°	−45°	−50°	−60°	−70°	−80°	−90°
+0.125	-	-	-	-	-	-	-	-	-	-	-
+0.375	-	-	-	-	-	-	-	-	-	-	-
+0.625	-	-	-	-	-	-	-	-	-	-	-
+0.875	-	-	-	-	-	-	-	-	-	-	-

ranges; however, the influences of their signs on flutter have not been proved relevant.

When the peak is located in the upwind side, the same tendency of destabilization near the extremities of the interval, 0° and 90°, observed in the previous analyses is repeated. On the other hand, intermediate values of $\psi(x_u^*)$ presented higher onset velocities.

For the *Fourth Approach*, two peaks in the unsteady pressure amplitude distribution $C_p(x*)$ were adopted, one in each side of the deck. The same four locations for the upwind side of the deck, x_u^*=-0.875, x_u^*=-0.625, x_u^*=-0.375 and x_u^*=-0.125, were combined one by one with the same four symmetric locations in the downwind side of the deck, x_u^*=+0.125, x_u^*=+0.375, x_u^*=+0.625 and x_u^*=+0.875. Also, the same intervals of phase difference distribution $\psi(x_u^*)$ and $\psi(x_d^*)$ used in the previous analyses were adopted, totalizing 1600 different combinations, Table 3.7 to Table 3.10.

Again, combinations near the boundaries of the intervals showed themselves prone to flutter and symmetric arrangements, this time not only in terms of values of $\psi(x^*)$ but also in terms of location of peaks in the amplitude $\tilde{C}_p(x^*)$ distribution, presented the most stable configurations.

Table 3.7: Fourth approach - downwind x_d^*=+0.125

		$\psi(x_d^*)$									
$\psi(x_u^*)$	x_u^*	0°	−10°	−20°	−30°	−40°	−50°	−60°	−70°	−80°	−90°
0°	-0.875	0.5 m/s	1 m/s	1.5 m/s	2.5 m/s	3 m/s	3.5 m/s	4.5 m/s	5 m/s	5.5 m/s	6 m/s
	-0.625	0.5 m/s	1.5 m/s	2.5 m/s	3.5 m/s	4.5 m/s	5 m/s	6 m/s	7 m/s	7.5 m/s	8.5 m/s
	-0.375	0.5 m/s	2.5 m/s	4.5 m/s	6 m/s	8 m/s	9.5 m/s	10.5 m/s	11.5 m/s	12.5 m/s	13.5 m/s
	-0.125	19 m/s	-	-	-	-	-	-	-	-	-
10°	-0.875	4.5 m/s	5 m/s	5.5 m/s	6 m/s	6.5 m/s	7 m/s	7.5 m/s	8 m/s	9 m/s	9.5 m/s
	-0.625	5 m/s	6 m/s	6.5 m/s	7.5 m/s	8 m/s	9 m/s	9.5 m/s	10 m/s	11 m/s	11.5 m/s
	-0.375	6 m/s	8 m/s	9.5 m/s	10.5 m/s	12 m/s	13 m/s	14 m/s	15 m/s	15.5 m/s	16.5 m/s
	-0.125	-	-	-	-	-	-	-	-	-	-
20°	-0.875	7 m/s	7 m/s	7.5 m/s	8 m/s	8.5 m/s	9 m/s	9.5 m/s	10 m/s	10.5 m/s	11 m/s
	-0.625	8 m/s	8.5 m/s	9 m/s	9.5 m/s	10 m/s	11 m/s	11.5 m/s	12 m/s	13 m/s	13.5 m/s
	-0.375	10 m/s	11 m/s	12.5 m/s	13.5 m/s	14.5 m/s	15.5 m/s	16.5 m/s	17 m/s	18 m/s	19.5 m/s
	-0.125	-	-	-	-	-	-	-	-	-	-
30°	-0.875	8 m/s	8.5 m/s	8.5 m/s	9 m/s	9.5 m/s	10 m/s	10.5 m/s	11.5 m/s	12 m/s	13 m/s
	-0.625	9.5 m/s	10 m/s	10.5 m/s	11 m/s	11.5 m/s	12.5 m/s	13 m/s	14 m/s	14.5 m/s	15.5 m/s
	-0.375	12 m/s	13 m/s	14 m/s	15 m/s	16 m/s	17 m/s	18 m/s	19.5 m/s	20.5 m/s	22 m/s
	-0.125	-	-	-	-	-	-	-	-	-	-
40°	-0.875	8.5 m/s	9 m/s	9.5 m/s	10 m/s	10.5 m/s	11 m/s	12 m/s	12.5 m/s	13.5 m/s	14.5 m/s
	-0.625	10 m/s	10.5 m/s	11.5 m/s	12 m/s	12.5 m/s	13.5 m/s	14.5 m/s	15.5 m/s	16.5 m/s	18 m/s
	-0.375	13.5 m/s	14.5 m/s	15.5 m/s	16.5 m/s	17.5 m/s	19 m/s	20 m/s	21.5 m/s	23 m/s	25 m/s
	-0.125	-	-	-	-	-	-	-	-	-	-
50°	-0.875	9 m/s	9.5 m/s	10 m/s	10.5 m/s	11.5 m/s	12 m/s	13 m/s	14 m/s	15 m/s	17 m/s
	-0.625	10.5 m/s	11.5 m/s	12 m/s	13 m/s	13.5 m/s	14.5 m/s	15.5 m/s	17 m/s	18.5 m/s	20.5 m/s
	-0.375	14.5 m/s	15.5 m/s	16.5 m/s	18 m/s	19 m/s	20.5 m/s	22 m/s	24 m/s	26 m/s	29 m/s
	-0.125	-	-	-	-	-	-	-	-	-	-
60°	-0.875	9.5 m/s	10 m/s	10.5 m/s	11.5 m/s	12 m/s	13 m/s	14 m/s	15.5 m/s	17.5 m/s	20 m/s
	-0.625	11 m/s	12 m/s	12.5 m/s	13.5 m/s	14.5 m/s	16 m/s	17 m/s	19 m/s	21 m/s	24 m/s
	-0.375	15 m/s	16.5 m/s	17.5 m/s	19.5 m/s	20.5 m/s	22 m/s	24 m/s	26.5 m/s	29.5 m/s	34 m/s
	-0.125	95 m/s	-	-	-	-	-	-	-	-	-
70°	-0.875	9.5 m/s	10 m/s	11 m/s	12 m/s	13 m/s	14 m/s	15.5 m/s	17.5 m/s	20 m/s	24.5 m/s
	-0.625	11.5 m/s	12.5 m/s	13.5 m/s	14.5 m/s	15.5 m/s	17 m/s	19 m/s	21.5 m/s	24.5 m/s	30 m/s
	-0.375	15.5 m/s	17 m/s	18.5 m/s	20 m/s	22 m/s	24 m/s	26.5 m/s	30 m/s	34.5 m/s	42.5 m/s
	-0.125	96 m/s	-	-	-	-	-	-	-	-	-
80°	-0.875	9.5 m/s	10.5 m/s	11.5 m/s	12.5 m/s	14 m/s	15.5 m/s	17.5 m/s	20 m/s	25 m/s	35 m/s
	-0.625	11.5 m/s	12.5 m/s	14 m/s	15 m/s	16.5 m/s	18.5 m/s	21 m/s	24 m/s	30.5 m/s	43 m/s
	-0.375	16 m/s	17.5 m/s	19.5 m/s	21 m/s	23.5 m/s	26 m/s	29.5 m/s	34.5 m/s	42.5 m/s	60.5 m/s
	-0.125	99 m/s	-	-	-	-	-	-	-	-	-
90°	-0.875	10 m/s	11 m/s	12 m/s	13.5 m/s	15 m/s	17 m/s	20 m/s	24.5 m/s	35 m/s	0.5 m/s
	-0.625	12 m/s	13 m/s	14.5 m/s	16 m/s	18 m/s	20.5 m/s	24 m/s	30 m/s	43 m/s	0.5 m/s
	-0.375	16.5 m/s	18 m/s	20 m/s	22.5 m/s	26 m/s	29 m/s	34 m/s	42.5 m/s	60.5 m/s	1 m/s
	-0.125	-	-	-	-	-	-	-	-	-	0.5 m/s

Table 3.8: Fourth approach - downwind x_d^*=+0.375

$\psi(x_u^*)$	x_u^*	$\psi(x_d^*)$ 0°	−10°	−20°	−30°	−40°	−50°	−60°	−70°	−80°	−90°
0°	-0.875	0.5 m/s	3.5 m/s	5.5 m/s	7.5 m/s	8.5 m/s	9.5 m/s	10 m/s	10.5 m/s	11 m/s	11 m/s
	-0.625	0.5 m/s	6 m/s	10 m/s	12 m/s	13.5 m/s	14.5 m/s	15 m/s	15.5 m/s	16 m/s	16.5 m/s
	-0.375	15.5 m/s	-	-	-	-	-	-	-	97.5 m/s	95.5 m/s
	-0.125	-	-	-	-	-	-	-	-	-	-
10°	-0.875	6.5 m/s	8 m/s	9 m/s	10 m/s	10.5 m/s	11 m/s	11.5 m/s	12 m/s	12.5 m/s	13 m/s
	-0.625	9 m/s	11.5 m/s	13.5 m/s	14.5 m/s	15.5 m/s	16.5 m/s	17 m/s	17.5 m/s	18 m/s	18.5 m/s
	-0.375	84 m/s	-	-	-	-	-	-	-	-	-
	-0.125	-	-	-	-	-	-	-	-	-	-
20°	-0.875	9 m/s	10 m/s	10.5 m/s	11 m/s	11.5 m/s	12.5 m/s	13 m/s	13.5 m/s	14 m/s	14.5 m/s
	-0.625	12.5 m/s	14 m/s	15.5 m/s	16 m/s	17 m/s	17.5 m/s	18.5 m/s	19 m/s	20 m/s	20.5 m/s
	-0.375	-	-	-	-	-	-	-	-	-	-
	-0.125	-	-	-	-	-	-	-	-	-	-
30°	-0.875	10 m/s	11 m/s	11.5 m/s	12 m/s	12.5 m/s	13.5 m/s	14 m/s	14.5 m/s	15.5 m/s	16 m/s
	-0.625	14.5 m/s	15.5 m/s	16.5 m/s	17.5 m/s	18 m/s	19 m/s	20 m/s	20.5 m/s	22 m/s	23 m/s
	-0.375	-	-	-	-	-	-	-	-	-	-
	-0.125	-	-	90 m/s	-	-	-	-	-	-	-
40°	-0.875	11 m/s	11.5 m/s	12 m/s	13 m/s	13.5 m/s	14 m/s	15 m/s	16 m/s	17 m/s	18.5 m/s
	-0.625	15.5 m/s	16.5 m/s	17.5 m/s	18 m/s	19 m/s	20 m/s	21.5 m/s	22.5 m/s	24 m/s	26 m/s
	-0.375	-	-	-	-	-	-	-	-	-	-
	-0.125	-	-	86.5 m/s	-	-	-	-	-	-	-
50°	-0.875	11.5 m/s	12 m/s	12.5 m/s	13.5 m/s	14.5 m/s	15 m/s	16 m/s	17.5 m/s	19 m/s	21 m/s
	-0.625	16 m/s	17 m/s	18 m/s	19 m/s	20 m/s	21.5 m/s	23 m/s	24.5 m/s	26.5 m/s	29.5 m/s
	-0.375	-	-	-	-	-	-	-	-	-	-
	-0.125	-	-	85.5 m/s	-	-	-	-	-	-	-
60°	-0.875	11.5 m/s	12.5 m/s	13 m/s	14 m/s	15 m/s	16 m/s	17.5 m/s	19 m/s	21.5 m/s	24.5 m/s
	-0.625	16.5 m/s	17.5 m/s	18.5 m/s	20 m/s	21.5 m/s	23 m/s	25 m/s	27 m/s	30 m/s	34.5 m/s
	-0.375	-	-	-	-	-	-	-	-	-	-
	-0.125	-	-	87 m/s	-	-	-	-	-	-	-
70°	-0.875	12 m/s	12.5 m/s	13.5 m/s	15 m/s	16 m/s	17.5 m/s	19 m/s	21.5 m/s	25 m/s	30 m/s
	-0.625	16.5 m/s	18 m/s	19.5 m/s	21 m/s	22.5 m/s	24.5 m/s	27 m/s	30.5 m/s	35 m/s	42.5 m/s
	-0.375	94.5 m/s	-	-	-	-	-	-	-	-	-
	-0.125	-	-	90.5 m/s	-	-	-	-	-	-	-
80°	-0.875	12 m/s	13 m/s	14 m/s	15.5 m/s	17 m/s	19 m/s	21.5 m/s	25 m/s	30.5 m/s	43 m/s
	-0.625	17 m/s	18.5 m/s	20 m/s	22 m/s	24 m/s	26.5 m/s	30 m/s	35 m/s	43 m/s	61 m/s
	-0.375	91.5 m/s	-	-	-	-	-	-	-	-	-
	-0.125	-	-	96 m/s	-	-	-	-	-	-	-
90°	-0.875	12 m/s	13.5 m/s	15 m/s	16.5 m/s	18.5 m/s	21 m/s	24.5 m/s	30 m/s	43 m/s	0.5 m/s
	-0.625	17 m/s	19 m/s	21 m/s	23.5 m/s	26 m/s	29.5 m/s	34.5 m/s	42.5 m/s	60.5 m/s	0.5 m/s
	-0.375	91 m/s	-	-	-	-	-	-	-	-	1 m/s
	-0.125	-	-	-	-	-	-	-	-	-	1.5 m/s

Table 3.9: Fourth approach - downwind x_d^*=+0.625

$\psi(x_u^*)$	x_u^*	$\psi(x_d^*)$ 0°	−10°	−20°	−30°	−40°	−50°	−60°	−70°	−80°	−90°
0°	-0.875	0.5 m/s	9 m/s	12.5 m/s	14.5 m/s	16.5 m/s	16 m/s	16.5 m/s	16.5 m/s	17 m/s	17 m/s
	-0.625	15.5 m/s	-	-	-	-	-	-	-	95.5 m/s	94.5 m/s
	-0.375	-	-	-	-	-	-	-	-	-	-
	-0.125	-	-	-	-	-	-	-	-	-	-
10°	-0.875	11 m/s	13.5 m/s	15 m/s	16 m/s	16.5 m/s	17 m/s	17.5 m/s	18 m/s	18.5 m/s	19 m/s
	-0.625	-	-	-	-	-	-	-	-	-	-
	-0.375	-	95 m/s	97.5 m/s	-	-	-	-	-	-	-
	-0.125	-	-	-	-	-	-	-	-	-	-
20°	-0.875	14 m/s	15.5 m/s	16.5 m/s	17 m/s	18 m/s	18.5 m/s	19 m/s	19.5 m/s	20 m/s	21 m/s
	-0.625	-	-	-	-	-	-	-	-	-	-
	-0.375	-	82.5 m/s	97.5 m/s	-	-	-	-	-	-	-
	-0.125	-	-	-	-	-	-	-	-	-	-
30°	-0.875	15.5 m/s	16.5 m/s	17 m/s	18 m/s	18.5 m/s	19.5 m/s	20.5 m/s	21 m/s	22 m/s	23.5 m/s
	-0.625	-	-	-	-	-	-	-	-	-	-
	-0.375	92 m/s	80 m/s	99.5 m/s	-	-	-	-	-	-	-
	-0.125	-	-	-	-	-	-	-	-	-	-
40°	-0.875	16 m/s	17 m/s	18 m/s	19 m/s	19.5 m/s	20.5 m/s	21.5 m/s	23 m/s	24.5 m/s	26 m/s
	-0.625	-	-	-	-	-	-	-	-	-	-
	-0.375	76 m/s	80 m/s	-	-	-	-	-	-	-	-
	-0.125	-	-	93.5 m/s	-	-	-	-	-	-	-
50°	-0.875	16.5 m/s	17.5 m/s	18.5 m/s	19.5 m/s	20.5 m/s	22 m/s	23 m/s	25 m/s	27 m/s	29.5 m/s
	-0.625	-	-	-	-	-	-	-	-	-	-
	-0.375	69.5 m/s	81 m/s	-	-	-	-	-	-	-	-
	-0.125	-	-	90 m/s	-	-	-	-	-	-	-
60°	-0.875	17 m/s	18 m/s	19 m/s	20.5 m/s	21.5 m/s	23 m/s	25 m/s	27.5 m/s	30.5 m/s	34.5 m/s
	-0.625	-	-	-	-	-	-	-	-	-	-
	-0.375	70.5 m/s	82.5 m/s	-	-	-	-	-	-	-	-
	-0.125	-	-	89 m/s	-	-	-	-	-	-	-
70°	-0.875	17 m/s	18.5 m/s	19.5 m/s	21 m/s	23 m/s	25 m/s	27.5 m/s	30.5 m/s	35 m/s	42.5 m/s
	-0.625	97 m/s	-	-	-	-	-	-	-	-	-
	-0.375	72 m/s	85 m/s	-	-	-	-	-	-	-	-
	-0.125	-	-	91 m/s	-	-	-	-	-	-	-
80°	-0.875	17.5 m/s	18.5 m/s	21 m/s	22 m/s	24.5 m/s	27 m/s	30.5 m/s	35 m/s	43 m/s	60.5 m/s
	-0.625	93 m/s	-	-	-	-	-	-	-	-	-
	-0.375	74.5 m/s	88 m/s	-	-	-	-	-	-	-	-
	-0.125	-	-	95.5 m/s	-	-	-	-	-	-	-
90°	-0.875	17.5 m/s	19 m/s	26 m/s	23.5 m/s	26 m/s	29.5 m/s	34.5 m/s	42.5 m/s	60.5 m/s	1.5 m/s
	-0.625	92 m/s	-	-	-	-	-	-	-	-	0.5 m/s
	-0.375	78 m/s	93 m/s	-	-	-	-	-	-	-	0.5 m/s
	-0.125	-	-	-	-	-	-	-	-	-	0.5 m/s

Table 3.10: Fourth approach - downwind x_d^*=+0.875

$\psi(x_u^*)$	x_u^*	$\psi(x_d^*)$ 0°	−10°	−20°	−30°	−40°	−50°	−60°	−70°	−80°	−90°
0°	*-0.875*	*19 m/s*	-	-	-	-	-	-	-	*95.5 m/s*	*94 m/s*
	-0.625	-	-	-	-	-	-	-	-	-	-
	-0.375	-	-	-	-	-	-	-	-	-	-
	-0.125	-	-	-	-	-	-	-	-	-	-
10°	*-0.875*	-	-	-	-	-	-	-	-	-	-
	-0.625	-	*87 m/s*	-	-	-	-	-	-	-	-
	-0.375	-	-	-	-	-	-	-	-	-	-
	-0.125	-	-	-	-	-	-	-	-	-	-
20°	*-0.875*	-	-	-	-	-	-	-	-	-	-
	-0.625	*76 m/s*	*87 m/s*	-	-	-	-	-	-	-	-
	-0.375	-	*96.5 m/s*	*96 m/s*	-	-	-	-	-	-	-
	-0.125	-	-	-	-	-	-	-	-	-	-
30°	*-0.875*	-	-	-	-	-	-	-	-	-	-
	-0.625	*72.5 m/s*	*90 m/s*	-	-	-	-	-	-	-	-
	-0.375	-	*85 m/s*	*91.5 m/s*	-	-	-	-	-	-	-
	-0.125	-	-	-	-	-	-	-	-	-	-
40°	*-0.875*	-	-	-	-	-	-	-	-	-	-
	-0.625	*73 m/s*	*91.5 m/s*	-	-	-	-	-	-	-	-
	-0.375	-	*80 m/s*	*90 m/s*	-	-	-	-	-	-	-
	-0.125	-	-	*98 m/s*	-	-	-	-	-	-	-
50°	*-0.875*	-	-	-	-	-	-	-	-	-	-
	-0.625	*74.5 m/s*	*91.5 m/s*	-	-	-	-	-	-	-	-
	-0.375	*87 m/s*	*78 m/s*	*90.5 m/s*	-	-	-	-	-	-	-
	-0.125	-	-	*93 m/s*	-	-	-	-	-	-	-
60°	*-0.875*	-	-	-	-	-	-	-	-	-	-
	-0.625	*75 m/s*	*91.5 m/s*	-	-	-	-	-	-	-	-
	-0.375	*80 m/s*	*78.5 m/s*	*92.5 m/s*	-	-	-	-	-	-	-
	-0.125	-	-	*91.5 m/s*	-	-	-	-	-	-	-
70°	*-0.875*	-	-	-	-	-	-	-	-	-	-
	-0.625	*76.5 m/s*	*92.5 m/s*	-	-	-	-	-	-	-	-
	-0.375	*76.5 m/s*	*80.5 m/s*	*95.5 m/s*	-	-	-	-	-	-	-
	-0.125	-	-	*92.5 m/s*	-	-	-	-	-	-	-
80°	*-0.875*	-	-	-	-	-	-	-	-	-	-
	-0.625	*78.5 m/s*	*94 m/s*	-	-	-	-	-	-	-	-
	-0.375	*76 m/s*	*83.5 m/s*	-	-	-	-	-	-	-	-
	-0.125	-	-	*96 m/s*	-	-	-	-	-	-	-
90°	*-0.875*	*92.5 m/s*	-	-	-	-	-	-	-	-	*2.5 m/s*
	-0.625	*81.5 m/s*	*97.5 m/s*	-	-	-	-	-	-	-	*0.5 m/s*
	-0.375	*77.5 m/s*	*89 m/s*	-	-	-	-	-	-	-	*0.5 m/s*
	-0.125	-	-	-	-	-	-	-	-	-	*0.5 m/s*

Comparing the onset velocities obtained through this approach with the results reported in Table 3.5 and Table 3.6, it can be perceived that the existence of two peaks of unsteady pressure amplitude, one in each side of the cross-section, has a great impact on the stabilization of flutter. While only one peak in the upwind side conducts to flutter onset velocities comparable to the one presented by the theoretical flat plate case, around *10 m/s*, the addition of one more peak in the downwind half of the deck brings beneficial effects to the system, increasing considerably the value of the onset velocity. However, from a contrary perspective, the presence of a peak in the upwind side brings destabilizing effects to configurations with only one peak in the downwind side.

It should be reminded that these configurations are hypothetical situations; however, they draw the attention to the potential stabilizing effects of peaks in the downwind side and destabilizing effects of peaks in the upwind side.

Putting the focus on the location of the peak of the amplitude $\tilde{C}_p(x^*)$ distribution of the upwind side, it is perceived from the results that the stability is increased as the peak moves towards the center of the cross-section, and that the usual configuration with a peak near the leading edge is more susceptible to flutter. In order to stabilize this configuration, the peak in the downwind half of the deck should be located as close as possible to the trailing edge, resulting in symmetric locations for the peaks. This tendency is presented for all combinations of $\psi(x_u^*)$ and $\psi(x_d^*)$, showing stabilizing effects as their absolute values increase.

If the focus is changed to the position of the peak of $\tilde{C}_p(x^*)$ of the downwind half of the deck, this behavior is partially confirmed. Although as a general tendency flutter stability is increased as the peak moves towards the trailing edge, and this stability seems to be even more prominent when the peak in the upwind half moves to the center, in the middle range of $\psi(x^*)$ the tendency is that the more symmetrical the locations of the peaks, the higher the onset velocity. This result confirms that the symmetry of both location of peaks of amplitude $\tilde{C}_p(x^*)$ and absolute values of phase difference $\psi(x^*)$, provided they are in the "safe range", improves the flutter stability.

Analyzing the results from an aerodynamic derivatives point of view, nothing can be said about the effects related to the values of H_1^* and H_3^*, since the variation of the location of peaks of $C_p(x*)$ along each half of the cross-section has no influence on them. However, this symmetry has a major impact on the values of A_1^* and A_3^*, tending to minimize their absolute values. For configurations with the peak of $\tilde{C}_p(x^*)$ near the leading edge in the upwind side

and near the center of the cross-section in the downwind side, this symmetry is lost and the values of these two aerodynamic derivatives tend to become positive. As a consequence, the stabilizing effects of the negative values presented by A_2^* seem to be overcome, and flutter tends to arise at lower wind velocities. As the peak of the upwind side moves to the center and the peak of the downwind side moves to the trailing edge, the signs of A_1^* and A_3^* turn negative, resulting in stabilizing effects for flutter.

3.4 Concluding Remarks

The proposition of this chapter was to study the flutter stabilization problem from an unsteady pressure characteristics perspective, instead of the usually adopted aerodynamic derivatives point of view. By considering the influences of each aerodynamic derivative on the flutter onset, it was possible to identify patterns of unsteady pressure characteristics that contribute for the stabilization of flutter in bridge decks, i.e. *optimal unsteady pressure characteristics*.

The configurations presented in this study are extreme situations and some of them can not be obtained in practical terms. However, they provide valuable hints for the definition of stable patterns of unsteady pressure characteristics along the deck and can be a guideline in the definition of the cross-sections.

Based on analysis results, some guidelines could be proposed in terms of unsteady pressure characteristics, as the antisymmetric distribution of phase difference $\psi(x^*)$, which should be kept within the limits of $0 \leq \psi(x_u^*) \leq +\pi/2$ for the upwind side of the deck and $0 \geq \psi(x_d^*) \geq -\pi/2$ for its downwind side. Also, moving the peaks of unsteady pressure amplitude $\tilde{C}_p(x^*)$ to downstream was found to provide more stable configurations, and in an extreme situation, in which only one peak is presented in the downwind side of the deck flutter, is not developed. These considerations are valid not only for single box girders, but also for any kind of arrangement, like multi-box girders, grating girders, etc.

The important role played by the aerodynamic A_1^* could be verified, since the destabilization was always associated to the impacts of the unsteady pressure characteristics on this derivative. As a consequence, since the derivatives dependence was kept, variations in the value of A_3^* could also be related to the occurrence of flutter. However, it should be

reminded that the sensitivity of flutter on these two aerodynamic derivatives is dependent on the maintenance of negatives values for A_2^*.

The aerodynamic derivatives interdependence holds for streamlined cross-sections; however, as already discussed in Chapter 2, it can not be fully verified for all kinds of geometry, which means that some of the "stability boundaries" proposed in this chapter can be relaxed, considering independently the torsional and heaving systems. The approach presented in this chapter assumes a full interdependence with the objective of simplifying the development of the concept. Further investigations are necessary in order to cover the cases in which the aerodynamic derivatives interdependence is not completely held, as it usually occurs when *geometric singularities* are installed along the deck. In the following chapters it will be shown that the use of *geometric singularities* indeed deforms this interdependence, and how this deformation can be used in advantage for flutter stabilization is an issue that remains to be addressed.

In this sense, strategies for the control of the unsteady pressure characteristics along bridge deck surfaces are valuable and the next step in the present research should be the identification of methods for obtaining these patterns in real bridge decks, through the control with the use of *geometric singularities*. The following chapters will discuss that in more details, so that the influences of the geometry of the bridge deck and its relationship with the oncoming flow on its inherent unsteady pressure characteristics can be addressed. The objective is to provide tools for bridge designers to properly manipulate the amplitude $\tilde{C}_p(x^*)$ and phase difference distribution $\psi(x^*)$ along the deck, through the proposition of proper geometric configurations, aiming flutter stabilization.

Chapter 4

Unsteady Pressure Characteristics of Modified Rectangular Cylinders

4.1 Introduction

Changing the focus from the aerodynamic derivatives to the unsteady pressure characteristics in bridge decks, as proposed in the introduction of this thesis, brings the need for a better understanding of the mechanisms involved in the definition of these characteristics, including the way they are related to the oncoming flow and to the geometric properties of the bridge deck itself. By exerting control over the combination of amplitude and phase difference of the unsteady pressure field around the bridge deck, a more rational control over the aerodynamic derivatives can be obtained, which undoubtedly leads to better schemes of flutter stabilization.

Although no conclusive study considering the relationships between geometric characteristics of bridge decks and their intrinsic unsteady pressure characteristics has been published by the date, theories based on the analyses done independently by Theodorsen [47] and Küssner [83], who solved the problem of unsteady pressure characteristics for a thin flat plate submitted to incompressible and inviscid two-dimensional flow, and also on the analyses of this kind of problem done by Kàrmàn & Sears [84] have been used as starting points for more refined mathematical models concerning the unsteady pressure characteristics of

airfoils [85, 86, 87, 88, 89, 90, 91, 92]. Through those studies, the concepts of circulatory and non-circulatory flows, potential flow and their applicability for such cross-sections have been expanded and extended to more general cases, serving as base for investigations on bridge decks [93, 94].

Among those works, based on a simplified method for the calculation of the pressure distribution around steady airfoils presented by Allen [95] in 1939, McCroskey [96] developed a method to evaluate the flow field around unsteady airfoils considering thickness and camber, proposing the use of a "modified Theodorsen function", which was validated through pressure measurements. Moreover, the author related the dynamic delay in the laminar boundary-layer separation on oscillating airfoils to the phase difference presented at the leading edge.

Concerning the phase difference, Yoshiki et al. [97], by using a static airfoil submitted to a periodically fluctuating air flow in wind tunnel tests, pointed out that the values of phase difference between pressure and flow velocity fluctuations could not be well predicted by thin flat plate theories [47, 84], not even for airfoils. The reasons for that were found to be related to the thickness inherent to those bodies. However, it was verified that for great values of reduced frequency k there was a tendency towards a convergence between the theoretically predictable through flat plate theory and the experimentally verifiable for airfoils, with the influence of this parameter increasing with the increase of the angle of attack.

For the estimation of the unsteady pressure characteristics distribution of bridge decks, it should be considered the development of special methods, focusing on small values of reduced frequency k and taking into account the inherent bluffness and possible *geometric singularities* (flow separation points, gaps, gratings, etc) such a kind of bluff body may have. The approaches for such studies should be based mostly on wind tunnel experiments and on CFD simulations, searching for relationships between geometry and unsteady pressure characteristics, so that an insight on the flow field around the structure can be obtained. Alternative techniques such as neural networks had already been successfully tried with other kinds of structures [98, 99] and may also provide good results for the case of bridges. From assumptions based on that knowledge it may be possible to propose extensions of the classical flat plate theories to be used with bridge decks.

In general lines, Matsumoto et al. [82] have suggested a model for an equivalent Theodorsen function based on an "inverse analysis" approach, by using rectangular cylinders. Although no consideration about the calculation of the coefficients of such equation was

provided, this framework might serve as starting point for the development of a generic equivalent Theodorsen function to be used with bridge decks. Nevertheless, such a kind of approximation may incur in errors in the modeling of the aerodynamic forces [12].

In this chapter, through a study based on wind tunnel experiments conducted with B/D=20 rectangular cylinders as base geometry, a calculation framework to be used in the estimation of the unsteady pressure characteristics of bluff bodies is proposed. In this initial stage, the framework is restricted to the reproduction of the unsteady pressure characteristics of rectangular cylinders. It consists of predefined equations whose variable parameters, dependent on geometric characteristics, are isolated in empirical coefficients and related to the aerodynamic characteristics of the system body-flow. In the following chapters the approach will be better investigated, by considering the impacts on the unsteady pressure characteristics of *geometric singularities* along the cylinders, such as detachments points and slots.

By using such a framework in a more advanced stage of development and already adapted to generic cross-sections, the aerodynamic derivatives can be evaluated by using coefficients obtained analytically, so that the flutter analysis can be performed, making possible a preliminary assessment of the feasibility of some proposed geometry of bridge deck. So possessing this tool, *a priori*, the bridge deck designer would be able to have an insight on the tendency of a proposed bridge deck geometry to present flutter or not, and make the necessary geometric improvements before going to wind tunnel tests.

In order to achieve that stage, a first step should be given, by proposing the framework and proving it efficient in reproducing known unsteady pressure characteristics; and that is the objective of this chapter. Future extensions are expected, which means that this study is not a closed subject, but it is introduced as a novel approach for the problem of the flutter stability assessment.

4.2 Some background

Differently from aerodynamic cross-sections, i.e. airfoils, in which the flow follows the contours of the body, bluff bodies exhibit a separation of boundary layer, whose characteristics are highly related to the Reynold‘s number of the local flow conditions, Fig.4.1. This sep-

aration occurs when the velocity of the boundary layer approaches zero and the wind flow detaches itself from the surface of the body, originating vortices that will interact with the free layer flow.

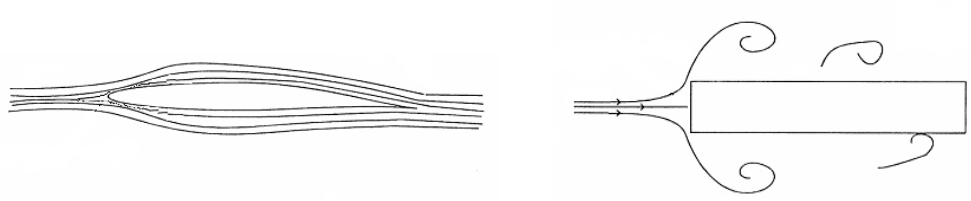

(a) Airfoil (b) Bluff Body

Figure 4.1: Flow field around bodies - boundary layer

The contours of the flow field are usually defined by a flow stagnation point in the front, a shear layer separation and a possible reattachment on the side surface [100], Fig.4.2. As important consequences of such a pattern, there is an increasing in the drag forces, due to a small pressure recovery region usually presented in the afterbody [100], and the arising of the Kàrmàn vortices, which will be shed periodically into the wake, Fig.4.3, in a frequency that leads to resonance in case it is close to the natural frequency of the body. The characteristics of this vortex shedding are dependent on the Reynold's number of the fluid [101] and keeps the balance of the change of the fluid momentum along the body surface, affecting the aerodynamic loads of the whole body [102].

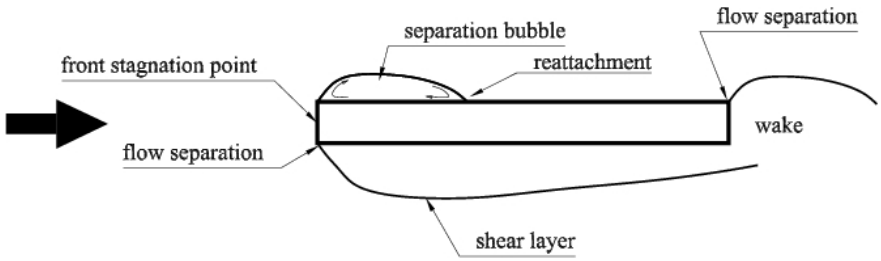

Figure 4.2: Flow field around bluff body

Such a phenomenon may take the forms of very complex equations when brought to the mathematical reality. Techniques of flow visualization, as the use of smoke and oil misty, allied to measurements of the unsteady pressure distribution around the oscillating bodies, help in tracing relationships between separated shear flow and aerodynamic forces [45], providing good insights on the physics around bluff bodies.

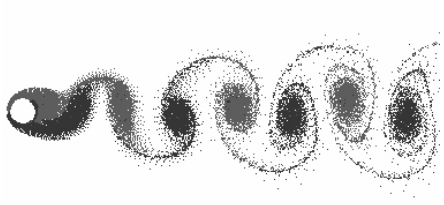

Figure 4.3: Kàrmàn street

The whole process is strongly influenced by the turbulence characteristics of the flow, which changes considerably the aerodynamic forces imposed on the body. Depending on the shape of the body, both stabilizing and destabilizing effects may occur, through a transfer of energy between modes which is dependent on the turbulence correlation length [103]. However, since this study is conducted by considering smooth flow, the turbulence effects will not be discussed extensively herein.

One important feature of such a fluid-body interaction, in terms of unsteady pressure characteristics, is that flow separation points induce an amplification on the amplitude of the fluctuating pressure, imposing modifications on the phase difference, which becomes smaller (goes to the "negative direction", in the notation of the present study) in accelerating regions and larger in decelerating regions in the chord direction [104]. Primarily, the phase difference is considered independent of the fluctuating amplitudes and is recognized to be responsible for the aerodynamic instabilities the structures may experience, mainly when small values are assumed by it [29].

Depending on the flow conditions and on the body length, the flow may reattach or not, in a distance from the leading edge, x_R in Fig.4.4, that oscillates along the time around an average position on the body‘s surface. In smooth flows this position coincides with the maximum RMS pressure levels [105] and with a positive peak in the skewness distribution [106], found to be around $4.4D$ (where D is the thickness of the plate) in experiments with flat plates. In the separation bubble, upstream the reattachment point, the mean pressures present high negative values, experiencing the largest peak pressures.

For rectangular cylinders, the comparison between the unsteady pressure characteristics obtained through heaving and torsional forced oscillations in terms of unit angle of attack shows a high degree of similarity and the unsteady pressure characteristics of both systems can be considered almost identical [3]. In the case of bridge decks, the degree of similarity

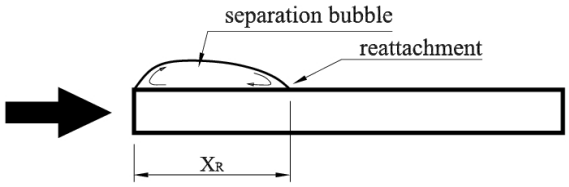

Figure 4.4: Separation bubble and reattachment point

will depend on the shape of the cross-section of the bridge in study, and by observing the wind tunnel tests results reported in [4, 32, 107] it is noticeable that the more complex the geometry is, in terms of presence of *geometric singularities* as flow separation points, presence of fairings and slots, the less similar the unsteady pressure characteristics are.

Since the aerodynamic derivatives interdependence is related to these similarities, a good approach for breaking the former must be related to strategies for deforming the latter. So a key point in this process is the understanding of the geometric factors in bridge decks which can make that feasible.

The unsteady pressure characteristics related to rectangular cylinders seem to follow a pattern of distribution that can be considered independent of the width of the body, appearing to be more related to the detachment point than to the body itself. Downstream the flow separation point provided by the leading edge, the unsteady pressure characteristics develop themselves regardless the width they still have to span along the cross-section, resulting in that the unsteady pressure characteristics of rectangular cylinders with different side ratios can be superimposed from the leading edge, as shown in Fig.4.5.

By observing Fig.4.5, it is possible to verify that the distance from the peak of the unsteady pressure amplitude $\tilde{C}_p(x^*)$ to the leading edge barely changes with the increase of the side ratio B/D. Based on that, it is natural to conclude that the upstream side of the cross-section gains importance in the definition of the aerodynamic derivatives of rectangular cylinders, which are illustrated in Fig.4.6, as their side ratios increase.

In order to illustrate this feature, the aerodynamic derivatives obtained from torsional motion are examined and the results are reported in Fig.4.7, which was constructed by using the data obtained from [4]. In this figure, the vertical axes represent in percentage values the contribution of the upwind side of the cross-section for the definition of each aerodynamic derivative at every wind reduced velocity (horizontal axes). As expected, with the increase

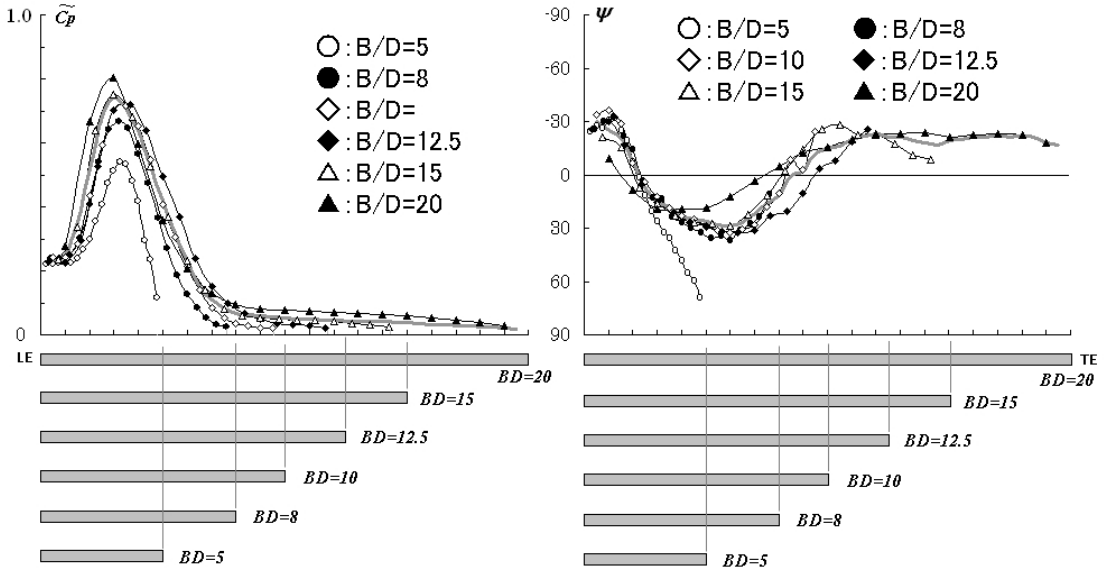

Figure 4.5: Unsteady pressure characteristics of rectangular cross-sections in torsional motion with different side ratios B/D at 10 m/s, U/f.B=18.7 (adapted from [3])

of the side ratio the contribution of the upwind side also increases, and in the limit of an infinite side ratio B/D, all derivatives show the tendency to be defined solely by the upwind side of the cross-section; this is concluded by checking that the contribution approaches 100% as the side ratio increases. In the quasi-steady limit there seems to be stabilization at a different value for every different side ratio, which results in that the larger the side ratio becomes the higher the contribution of the upwind side will be. The same investigation was also performed for the heaving motion, leading to similar conclusions.

The relationships between this polarization and the side ratio B/D, in terms of resulting values of aerodynamic derivatives, will depend on the phase difference $\psi(x^*)$ and on the magnitude of the peak of the amplitude $\tilde{C}_p(x^*)$ near the leading edge, which are thought to be highly dependent on the characteristics of the leading edge itself. In the case of the A_i^* aerodynamic derivatives, the effects of the normalized coordinate x^*, which is also affected by the increasing of the side ratio, should be taken into account in such analyses.

As already mentioned, flow separation points induce a peak in $\tilde{C}_p(x^*)$ causing a reduction (becoming more negative) in the phase difference $\psi(x^*)$ due to the accelerating flow. Because of that, the importance of the leading edge in the definition of the unsteady pressure

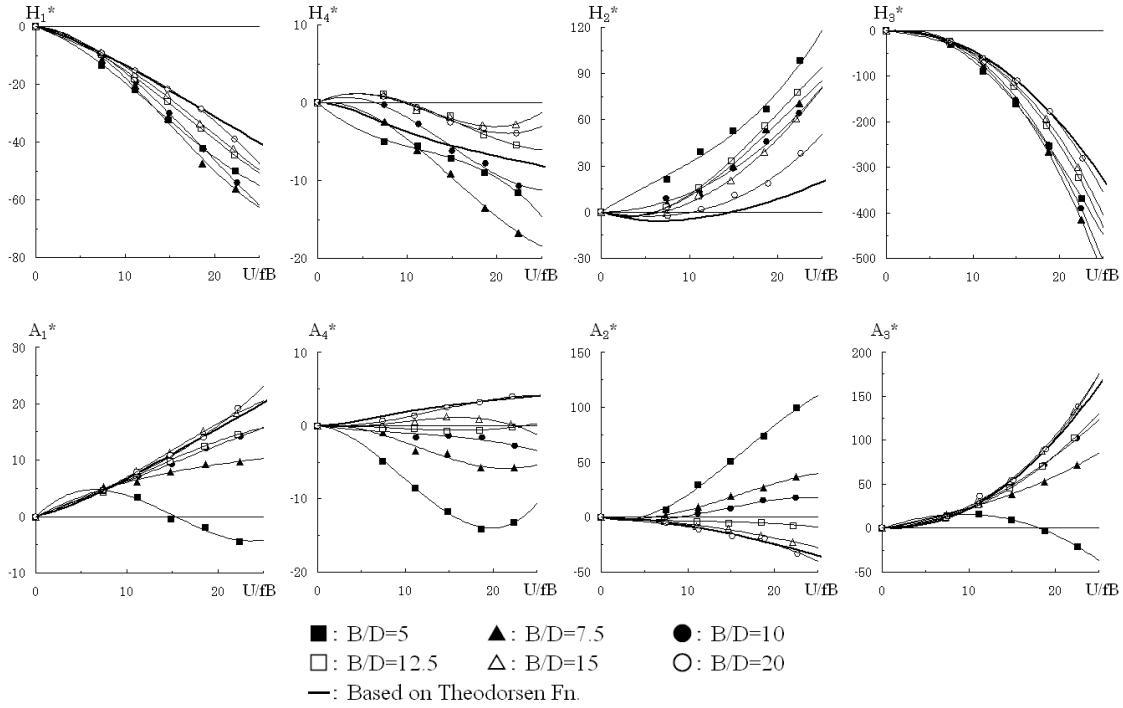

Figure 4.6: Aerodynamic derivatives for rectangular cylinders with side ratio B/D=5 to 20 (adapted from [4])

characteristics and, consequently, of the aerodynamic derivatives of rectangular cylinders is emphasized.

Modifications in the leading edge of bridge decks, as the attachment of fairings, have been recognized to be a good strategy for flutter stabilization, when they are able to reduce the flow separation and consequently lead to a prevention of the growth of the separation bubble responsible for producing exciting forces for flutter [108]. Different leading edges have been proved to have different effects on the streamlines around the bridge deck [109] and the efficiency of such a device in mitigating aerodynamic instabilities was found to be dependent on the original cross-section of the deck. Triangular fairings became very popular, but other geometries, as elliptical and circular shapes, have also provided good results [110] in flutter stabilization. However, a deterministic and optimal solution could not be established yet.

The visualization of the differences imposed by the different possibilities of leading edges through the resulting unsteady pressure characteristics of the deck may lead to a

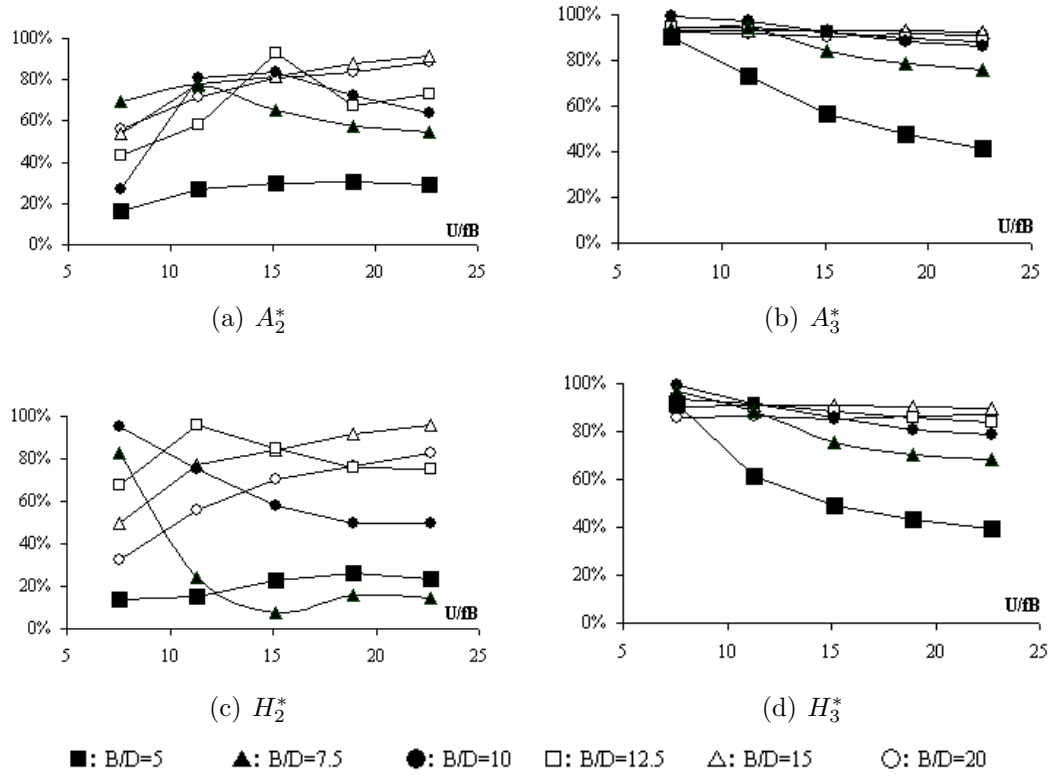

Figure 4.7: Contribution of the upwind side of the cross-section for the definition of the aerodynamic derivatives (adapted from [4])

better understanding of the relationships between leading edges, bridge geometry and flutter stabilization. Many research works already tried to trace some of these dependences [108, 109, 110, 111, 112], as showing for example that the adjustment of the separation of the flow, turning the cross-section to be a more streamlined shape, is better attained when the edge of the fairing coincides with the stagnation point of the original cross-section [109], and this can be a guideline in the design of the fairings.

In the context of the this research, the different configurations of unsteady pressure characteristics obtained by using different leading edges can be used in advantage. By changing only one parameter per turn, i.e. the leading edge, and keeping the same base cross-section, i.e. rectangular cylinders, it is possible to compare the resulting unsteady pressure characteristics and identify the common patterns inherent to the flow field around the base cross section, so that they can be isolated in a basic formulation. The parameters

of this formulation should be related to each different type of leading edge, which modifies the equations to mimic the behavior of a particular configuration of leading edge. The understanding of the factors involved in the definition of the basic formulation should provide information to be used in the development of the common framework proposed herein.

The following sections of this chapter will be developed considering that feature, with the main purpose of investigating the relationships concerning unsteady pressure characteristics in different geometries of bluff bodies, without the pretension of solving the problems related to leading edges. However, some parameters related to each leading edge investigated herein will be generated, and these parameters can be considered a starting point for an effort to be developed in the future, focused on gathering such parameters for a wider range of types of leading edges, as an extension of the current research.

4.3 The Approach

The investigations were carried out based on wind tunnel test results, which were conducted by using a rectangular cylinder with side ratio B/D=20 in four different configurations: no fairing in the leading edge (NF), *corner up* leading edge (CU), *corner down* leading edge (CD) and semi-circular leading edge (SC), Fig.4.8. The procedures adopted for the wind tunnel tests are described in Appendix A and the models are identified by the code of their leading edges (NF, CU, CD and SC) throughout this study.

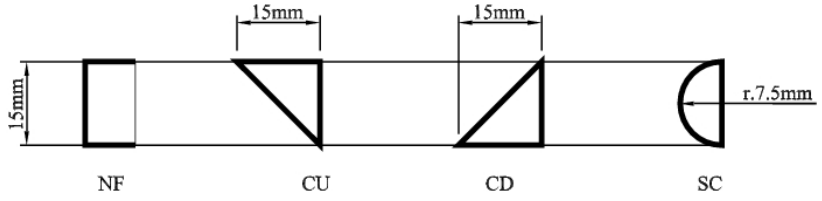

Figure 4.8: Leading edges

The analyses are performed with the objective of identifying patterns among the results, concerning the unsteady pressure characteristics of the models. These patterns are separated into two main classes: the ones related to the base cross-section, i.e. B/D=20 rectangular cylinders, and the ones related to each different leading edge. The former set of patterns should be expected to be similar throughout all configurations of models (with different

leading edges), resulting in that generic formulations to be used in the estimation of the unsteady pressure characteristics along bluff bodies can be proposed.

These generic formulations are designed to account for the influences of the different leading edges through coefficients obtained empirically from the latter set of patterns. At this moment, the objective is the proposition of the equations themselves, that should be proved efficient in the reproduction of known unsteady pressure characteristics, obtained in this study through wind tunnel tests.

The empirical coefficients are used with the purpose of abbreviating the process of the proposition of the formulation, fitting the estimations provided by it to the experimental data. As a consequence, an initial set of values is generated, which should be used as base for the proposition of analytical formulations for their estimation. The similarities between them can be used for the classification of the leading edges, helping in the development of the proposed framework.

The main purpose of using different leading edges at this time is to obtain different patterns to be analyzed. In this sense, the fact that the cases *CD* and *CU* induce different unsteady pressure characteristics in the upper and in the lower surfaces of the models, due to the asymmetry of the leading edges, can be neglected.

In Fig.4.10 the unsteady pressure characteristics of the rectangular cylinder without fairing (NF) are given, while the configurations with fairings are reported in Fig.4.11 to Fig.4.13. From a qualitatively point of view, it is possible to confirm that all configurations follow similar patterns, more or less "deformed" according to the leading edge and to the reduced wind velocity; also, in a major extent, similarities between torsional and heaving systems can be identified.

Although the focus of this investigation is on the unsteady pressure characteristics, the aerodynamic derivatives related to each case were evaluated according to Section 2.3.1 and are reported in Fig.4.9. The results are not intended to be conclusive in terms of influences of the leading edge on the aerodynamic derivatives, but they show differences, confirming the importance of understanding their effects.

The variations presented in the results highlight the differences existent in terms of aerodynamics and a deeper investigation considering them can provide valuable information about the aerodynamic phenomena in bluff bodies. In this sense, it is perceived that not

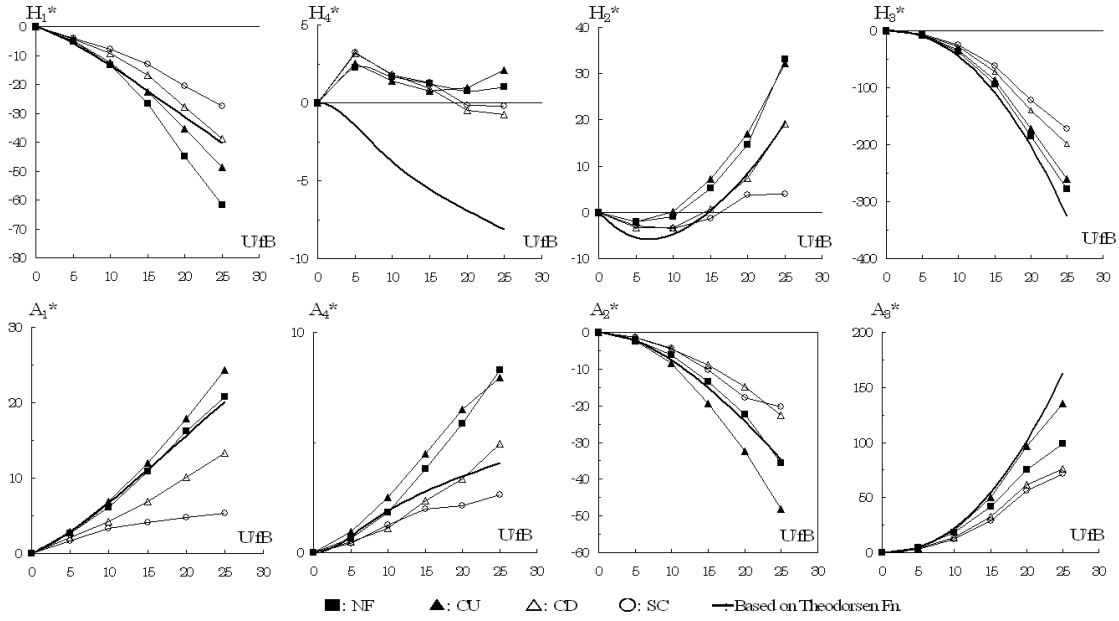

Figure 4.9: Aerodynamic derivatives of B/D=20 rectangular cylinders with different leading edges

only the separation of the flow near the leading edge is affected by the presence of different fairings, but also the whole development of the unsteady pressure characteristics along the body is. The detachment of the flow provided by the leading edge generates a perturbation around the body, inducing pressure fluctuations. The energy regarding this perturbation can be directly related to the characteristics of the unsteady pressures amplitude $\tilde{C}_p(x^*)$ distribution, represented by the magnitude and location of its peak, and to the characteristics of the phase difference $\psi(x^*)$ distribution.

By visual analysis, it is possible to confirm that the location of the peak in the amplitude $\tilde{C}_p(x^*)$ distribution is somehow interconnected with the location of the first inflection point in the positive zone of the phase difference $\psi(x^*)$ distribution. With the increase of the reduced wind velocity, there is a broadening of the base of the $\tilde{C}_p(x^*)$ and $\psi(x^*)$ distributions, which can be related to the size of the waves developed along the body‘s surface and finally regarded to the energy involved in the interactions.

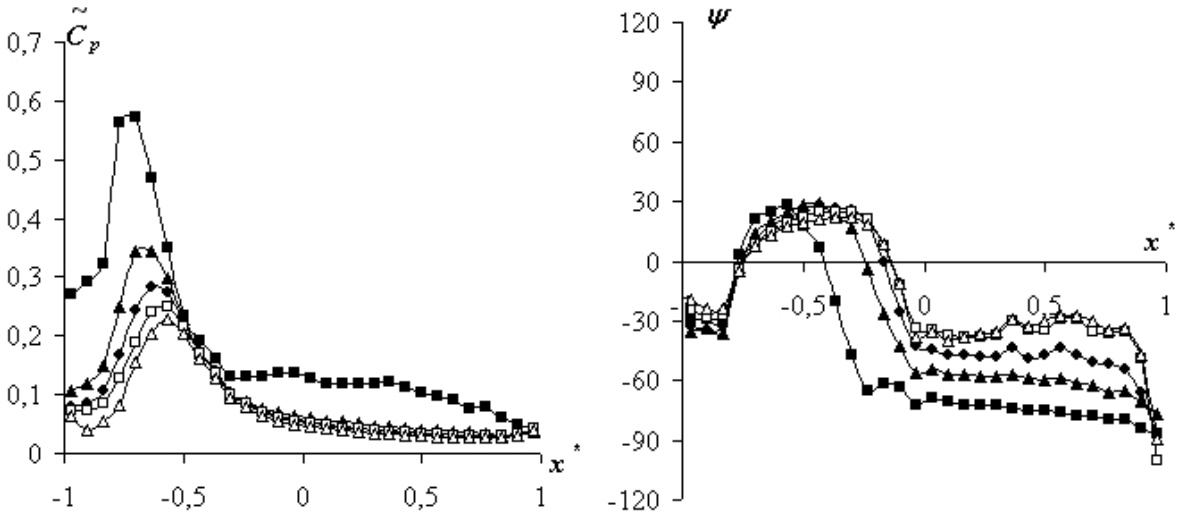

(a) Heaving

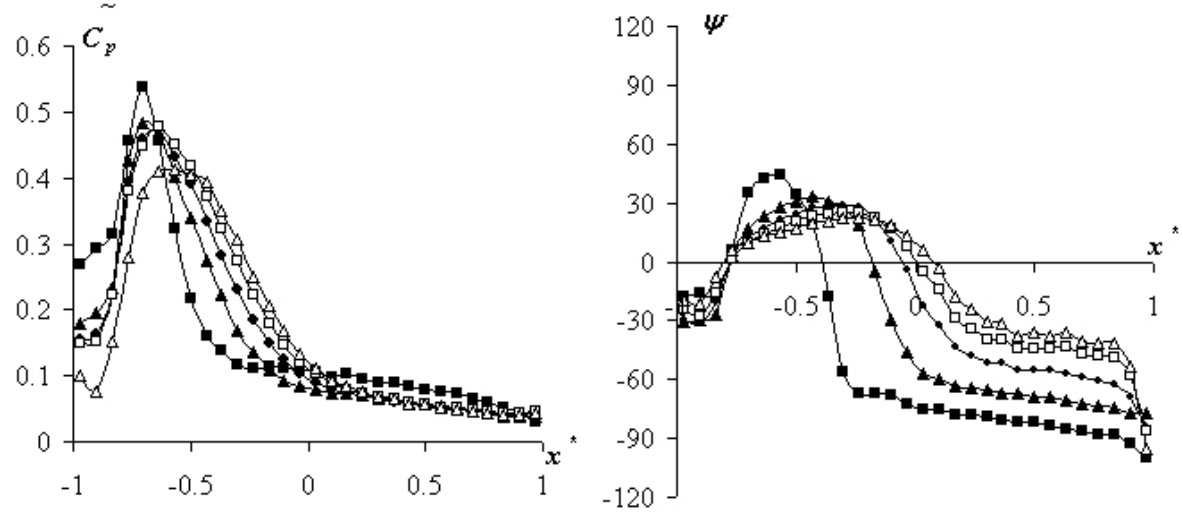

(b) Torsion

■: Uf/B=5 ▲: Uf/B=10 ●: Uf/B=15 □: Uf/B=20 △: Uf/B=25

Figure 4.10: Unsteady pressure characteristics of B/D=20 rectangular cylinders

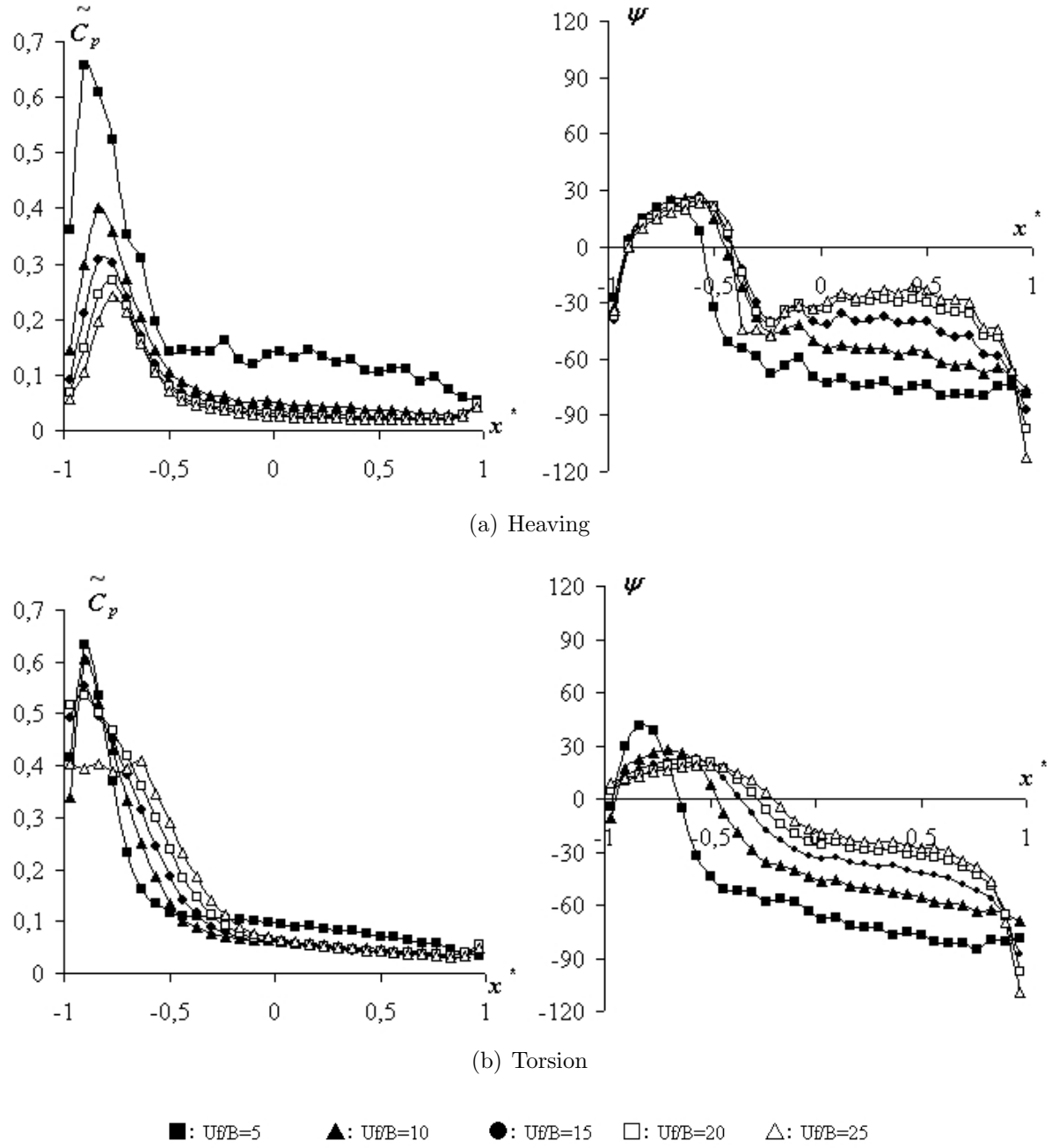

Figure 4.11: Unsteady pressure characteristics of B/D=20 rectangular cylinders with *CU* fairing

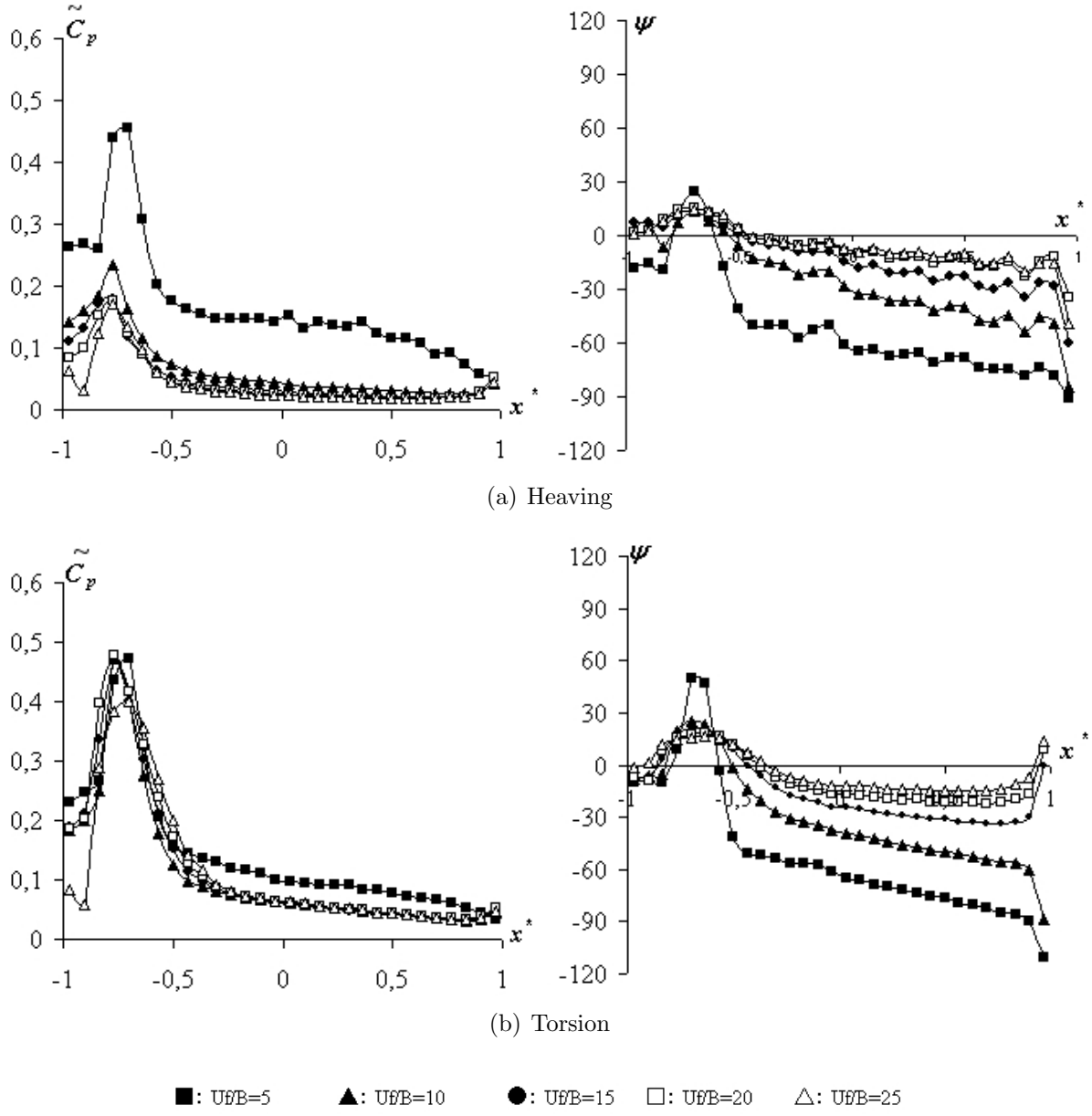

Figure 4.12: Unsteady pressure characteristics of B/D=20 rectangular cylinders with *CD* fairing

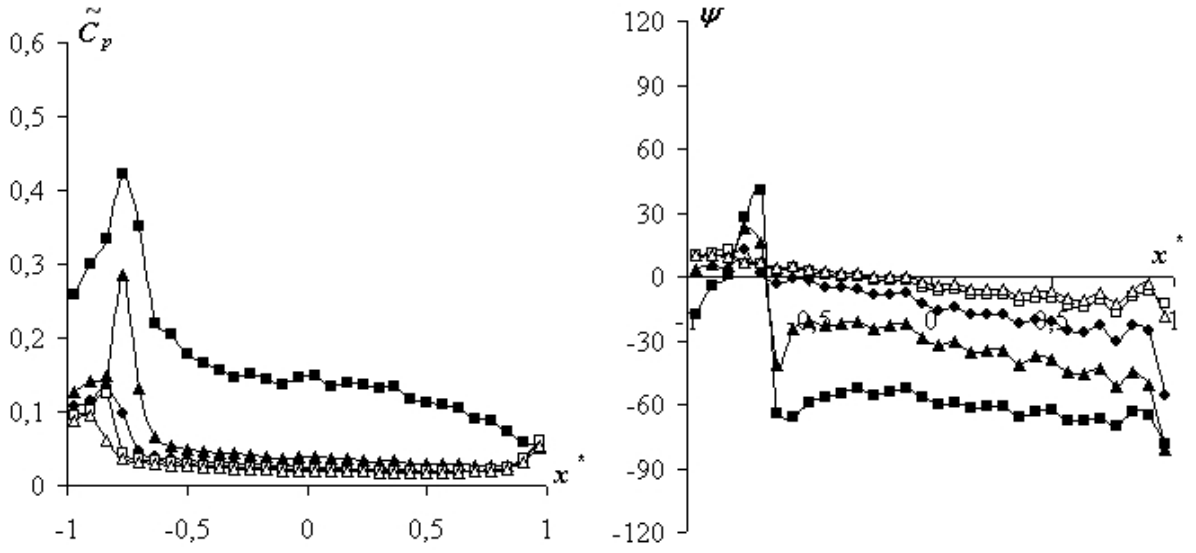

(a) Heaving

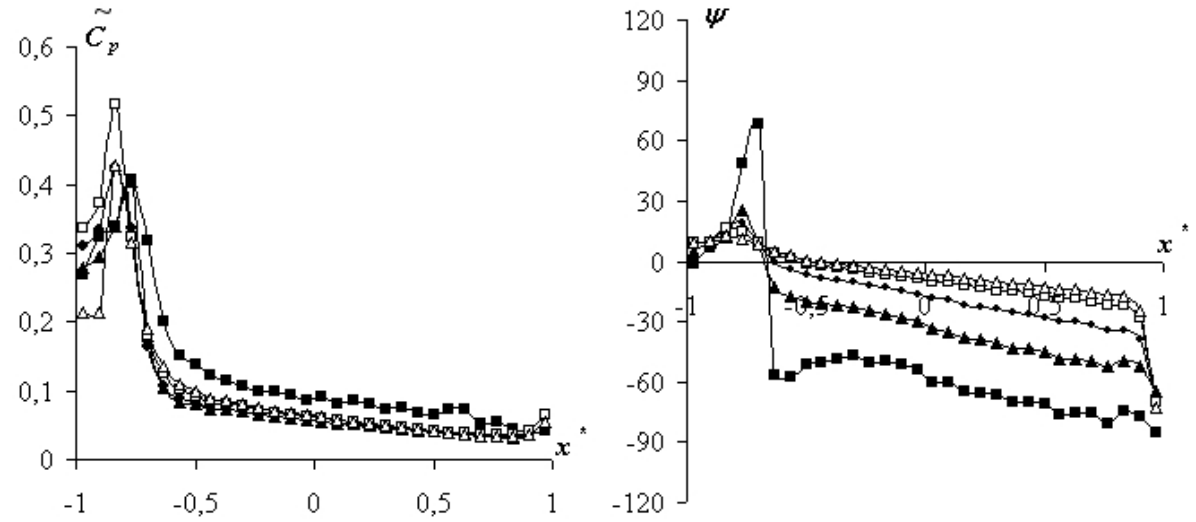

(b) Torsion

■: U/B=5 ▲: U/B=10 ●: U/B=15 □: U/B=20 △: U/B=25

Figure 4.13: Unsteady pressure characteristics of B/D=20 rectangular cylinders with *SC* fairing

From the assumptions above, it seems to be logical to build relationships between leading edge and unsteady pressure characteristics, defined by phase difference $\psi(x^*)$ and amplitude $\tilde{C}_p(x^*)$ distributions, developed along the afterbody. The discussions about this theme can include formulations based on *Navier-Stokes*, visualization of flow and complex theories and propositions, which still can not predict completely these interactions in a simple way. However, in this study the focus will be put on simple direct relationships between geometry and unsteady pressure characteristics, taking into account of course the fundaments of fluid mechanics. Mathematical considerations will be abbreviated and, by using the data corresponding to Fig.4.10 to Fig.4.13, the following sections will deal with the proposition of semi-empirical formulations to be used in the estimation of both phase difference $\psi(x^*)$ and amplitude $\tilde{C}_p(x^*)$ distributions along the surface of bluff bodies, using a rectangular cylinder as a base geometry. The purpose of this proposition is to provide an initial framework to be extended to cover generic bridge cross-sections, towards the development of a basic framework to be used during the design phase of long span bridges, based on the manipulation of the aerodynamic derivatives through the control of the unsteady pressure characteristics along the bridge deck.

4.3.1 Phase Difference Distribution

Concerning the phase difference $\psi(x^*)$ distribution and starting from model *NF*, Fig.4.10, some patterns can be identified. Following the development of the curve from leading edge to trailing edge, a negative peak is observed near the leading edge, so the values start to grow towards the positive direction crossing the x axis at a specific x_1^* location. After crossing the x axis a positive peak is reached, at approximately the same absolute value observed in the negative zone. The tendency is inverted and the values cross the x axis one more time, at x_2^*, reaching a second peak in the negative side that approaches the previous peaks in modulus as the wind velocity increases. After that second peak, the curves tend to remain in that value, developing themselves almost steadily. This behavior can also be observed in Fig.4.11 to Fig.4.13.

A classification for the phase difference distribution had already been proposed by dividing it into three main regions [5]: *near constant phase*, before x_1^*; *rapidly increasing phase*, between x_1^* and x_2^*; and *slowly changing phase*, after x_2^*. It was also reported in the same reference that the region of *rapidly increasing phase* is related to the expansion and contraction of the separation bubble while the body is in motion, Fig.4.14.

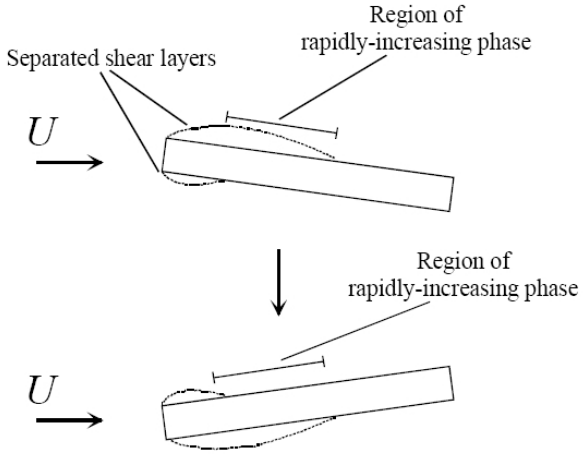

Figure 4.14: region of *rapidly increasing phase*, adapted from [5]

In this study, in order to better describe the behavior of the curves of phase difference distribution, it was thought to be convenient to split them into two main branches: a *curvy* branch, which can be approximated by a sinusoidal equation, Eq.4.1, and a *steady* branch, which presents constant values along its development.

$$\psi(x^*) = -A_\psi.cos\,[\omega_\psi.(x^* + 1) + \phi_\psi] \tag{4.1}$$

where $\psi(x^*)$ is the value of phase difference at a specific x^* non-dimensional (normalized by half-width b) location; A_ψ is the *amplitude* of the phase difference distribution; ω_ψ is the *circular wave number* of the phase difference distribution; ϕ_ψ is the *phase difference* of the distribution; "+1" is necessary to account for the coordinate transformation.

Eq.4.1 can be transformed into Eq.4.2.

$$\psi(x^*) = -A_\psi.cos\,[\omega_\psi.x^* + \omega_\psi + \phi_\psi] \tag{4.2}$$

By a visual analysis of Fig.4.10 to Fig.4.13, it is possible to identify a dependence of the parameters A_ψ and ϕ_ψ on the characteristics of the leading edge, since they change

among different configurations of leading edges; the same way, ω_ψ is strongly influenced by variations of wind velocity.

For a flat plate, the theoretical wave length in the wake is described by the relationship $2.\pi.b/k$ [113], which becomes numerically equivalent to the reduced wind velocity U_r=$U/f.b$ when normalized by the deck half-width b, i.e. λ_b. In addition, Kubo & Hirata [114] experimentally accounted for the existence of a relationship between the phase difference and the traveling time of the vortices on the body‘s surface. That relationship was found to be independent of both the amplitude of vibration (in the range of amplitudes tested by them, i.e. small amplitudes) and of the wind flow velocity. Based on their findings, it can be concluded that in harmonically oscillating bodies the traveling time between two subsequent points on the body‘s surface that present the same value of phase difference $\psi(x^*)$, e.g. x_1^* and x_2^*, must be equal among all wind velocities. The locations with the same phase difference $\psi(x^*)$ may be different for every wind velocity, but the traveling time between them is always the same, independently of the wind velocity.

Moreover, the flow structure around rectangular cylinders is two-dimensionalized and the vortices shed from the leading edge are controlled by its motion, presenting lock-on patterns under particular conditions [115], taking exactly one natural period to travel from leading edge to trailing edge [116]

The assumptions above were verified by dividing the wind velocities related to each phase difference distribution of Fig.4.10 to Fig.4.13 by the normalized (by the half length b) distance between the points where the curves intercept the x axis, which gives a unity of *normalized frequency* that would represent in the last instance the wave half-length $\lambda/2$. For the curves in which the first intercepting point was missed, a graphical interpolation was performed.

The results were compared with the theoretical wave half-length $\pi.b/k$, bold line in Fig.4.15, showing similarities that suggest that the value of $2.\pi.b/k$ might have a strong relationship with the wave length also in bluff bodies.

Since ω_ψ represents the *circular wave number* $2.\pi.f$ in Eq.4.2, the multiplication of the value of the normalized wave half-length by $2.\pi$ with a subsequent division by the wind velocity should provide the value of ω_ψ of Eq.4.2. This relationship is given by Eq.4.3.

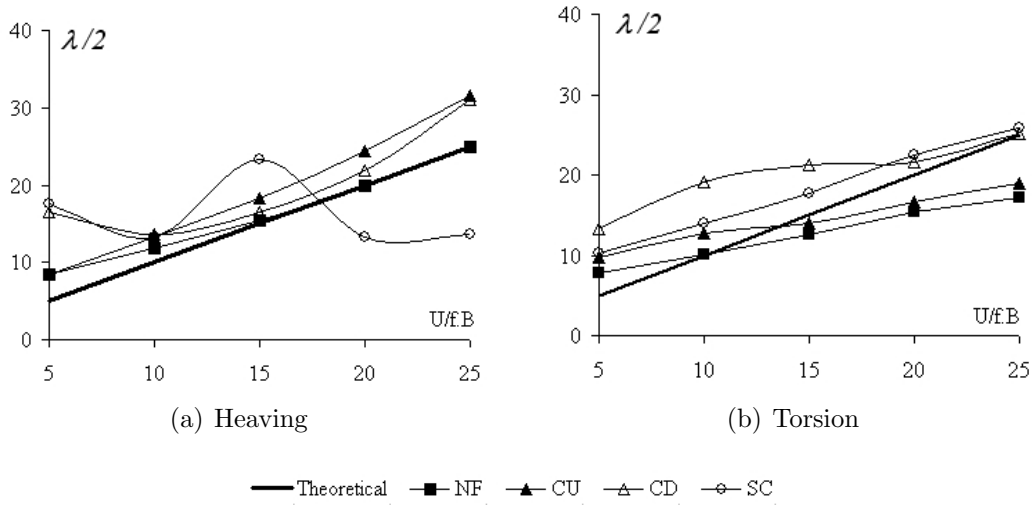

(a) Heaving (b) Torsion

Figure 4.15: Wave half-length $\lambda/2$

$$\omega_\psi = \frac{2.\pi}{\Delta x^*_\psi} \tag{4.3}$$

where Δx^*_ψ is the wave half-length $\lambda/2$ normalized by b, given by the distance between x^*_1 and x^*_2.

In the theoretical case, the value of ω_ψ can be calculated through Eq.4.4, leading to constant values throughout all the velocity range. In Fig.4.16 a comparison between this theoretical value and the ones obtained for the cases of Fig.4.10 to Fig.4.13 through Eq.4.3 shows that the agreement between the results obtained from Eq.4.3 and Eq.4.4 increases with the increase of the wind velocity, appearing to be equivalents in the quasi-steady state.

$$\omega_\psi = \frac{\pi}{b.f} \tag{4.4}$$

where f is the oscillation frequency.

The tendencies presented herein point to the necessity of a deeper study on the influences of different types of leading edges on the values of ω_ψ, based on the characteristics of

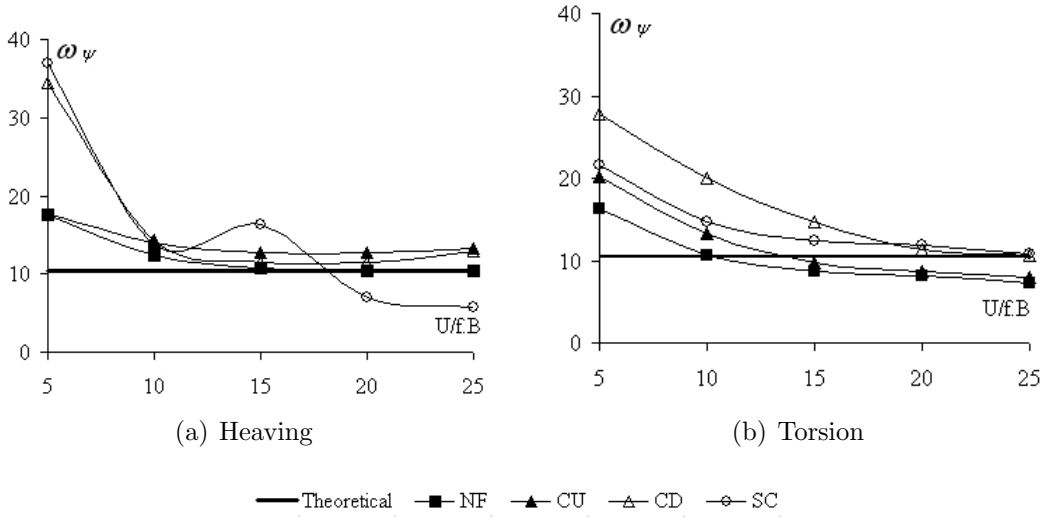

Figure 4.16: Circular wave number ω_ψ

the flow separation and on the fluid dynamics generated due to this detachment, so that deterministic approaches can be established for the estimation of ω_ψ. That is not the objective of this study, which is restricted only to point out the existence of such relationships and to the establishment of semi-empirical formulations to describe them, which can be obtained at this point of the study through Fig.4.16.

Although the curves obtained for the torsional system in Fig.4.16 tend to be better defined, the general tendency is that both systems show similar behaviors, and as an attempt towards an empirical formulation for ω_ψ, Fig.4.17 shows the results of polynomial interpolations for the curves in the torsional system.

Since such a kind of study could not be found by the author in the technical literature, no comparison parameters could be established at this point, so the discrepancies observed in Fig.4.16 could not be related neither to inaccuracies in the acquisition of the data nor to inherent characteristics of the leading edges. Further studies should be conducted for the clarification of these relationships.

In the case of the *amplitude* A_ψ of the phase difference distribution, the average of the absolute values at the inflection points were taken, also through graphical interpolation for those distributions in which one of the peaks is missed. Table 4.1 summarizes the values for

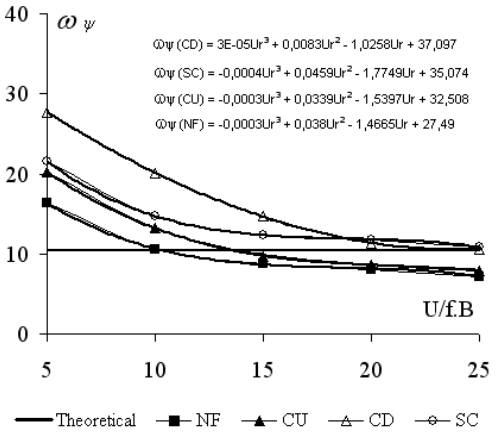

Figure 4.17: Tentative Equations for ω_ψ in the torsional system

the four cases presented herein and Fig.4.18 provides a graphical representation for them.

Table 4.1: Amplitude A_ψ

$U/f.B$	5	10	15	20	25
NF torsion	31°	32°	30°	27°	22°
NF heaving	30°	33°	31°	27°	23°
CU torsion	47°	28°	23°	20°	19°
CU heaving	26°	30°	33°	31°	28°
CD torsion	50°	29°	20°	17°	13°
CD heaving	24°	18°	14°	14°	13°
SC torsion	64°	30°	19°	16°	13°
SC heaving	53°	22°	12°	12°	10°

Both torsional and heaving systems show similar tendencies, especially for model NF,

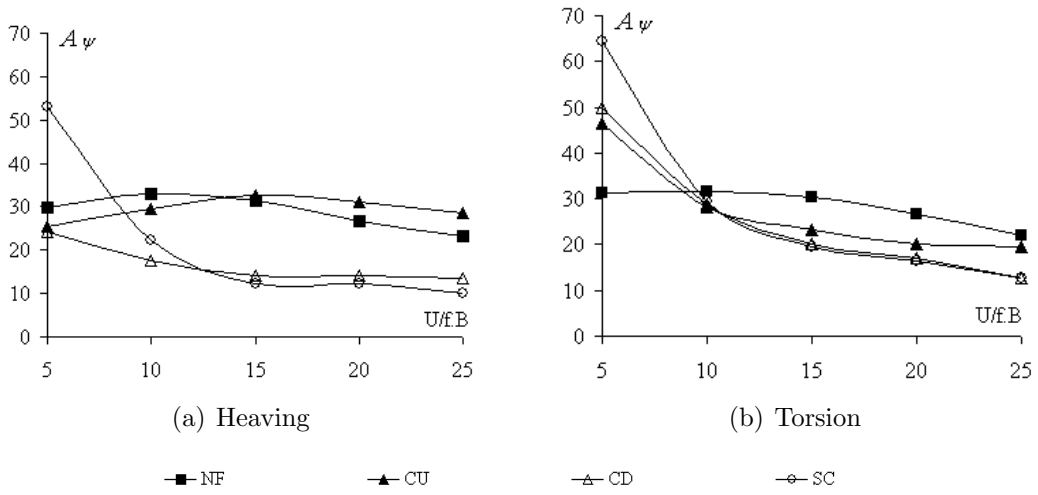

Figure 4.18: Amplitude A_ψ

which presents almost the same values in both systems throughout the entire range of reduced wind velocities. However, the proportionality relationships between the values obtained from each motion for every leading edge (values and development of the curves between Fig.4.18(a) and Fig.4.18(b)) are different for all types of fairing, and this fact introduces a manner of breaking the strong aerodynamic derivatives dependence discussed in Section 2.3.2 related to model NF (B/D=20 rectangular cylinder with no fairing). With the increase of the reduced wind velocity the values seem to asymptotically approach an equilibrium state, which can be regarded as a characteristic value for each type of leading edge.

For the parameter ϕ_ψ, the calculation was conducted by evaluating the relationship between Δx^*_ψ and x^*_1, considering x^*_1 as a reference for ϕ_ψ= 90°. The results are reported in Table 4.2 and in Fig.4.19.

This parameter showed a high sensitivity to the leading edge. Although the general tendencies of both torsional and heaving systems are the same, the values assumed are different for all configurations of leading edges. Each curve is developed in a very particular range, without sharing values among themselves, looking for stabilization also in different values.

Although the use of ϕ_ψ is suitable for Eq.4.2, it may also be convenient to evaluate the position ψ^*_0 of the inflection point in the positive side of the phase difference $\psi(x^*)$

Table 4.2: Phase Lag ϕ_ψ

$U/f.B$	5	10	15	20	25
NF torsion	$-12°$	$21°$	$33°$	$37°$	$48°$
NF heaving	$-25°$	$3°$	$14°$	$14°$	$12°$
CU torsion	$66°$	$68°$	$90°$	$90°$	$90°$
CU heaving	$42°$	$50°$	$55°$	$54°$	$50°$
CD torsion	$-71°$	$-14°$	$30°$	$69°$	$70°$
CD heaving	$-117°$	$82°$	$101°$	$90°$	$65°$
SC torsion	$62°$	$132°$	$142°$	$113°$	$100°$
SC heaving	$-75°$	$143°$	$121°$	$130°$	$123°$

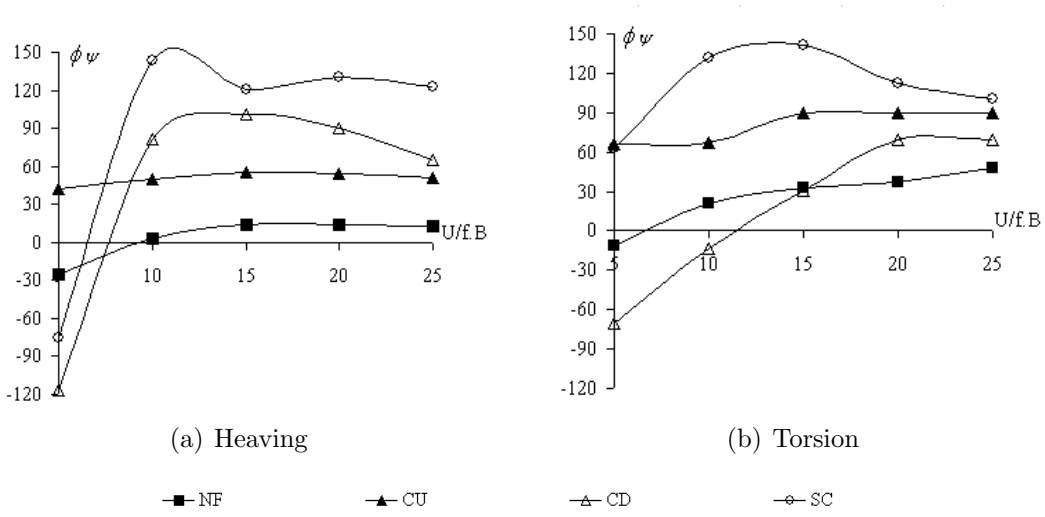

(a) Heaving (b) Torsion

Figure 4.19: Phase Lag ϕ_ψ

distribution, Fig.4.20, which can be associated to the position of the peak in the amplitude $\tilde{C}_p(x^*)$ distribution, pointed out in Section 4.3.2.

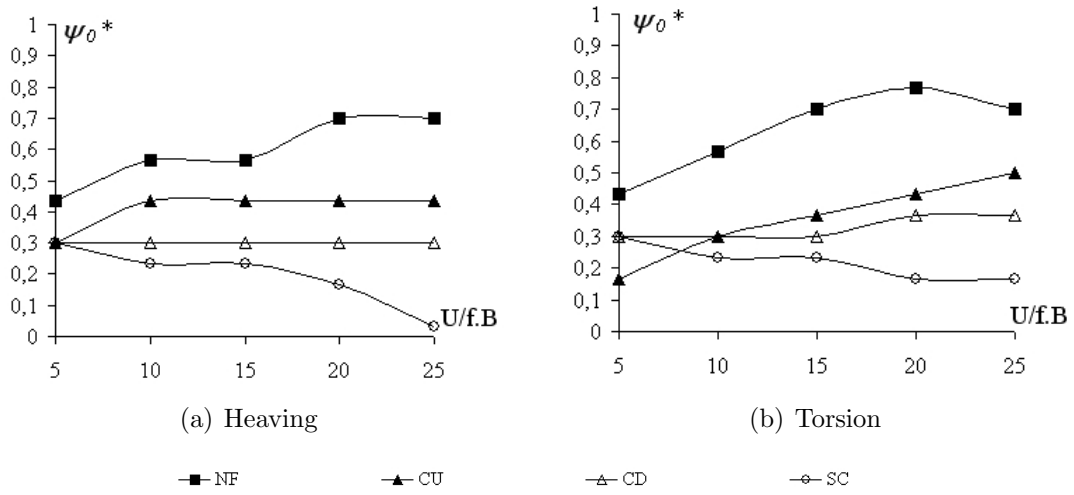

Figure 4.20: Location of the inflection point of the phase difference $\psi(x^*)$ distribution

In order to check for the "efficiency" of the formulation proposed in this section to reproduce the phase difference distributions, the aerodynamic derivatives of the four cases were recalculated by using the phase difference $\psi(x^*)$ distributions obtained through Eq.4.2, considering Eq.4.3 and the parameters reported in Table 4.1 and Table 4.2. The real amplitude $\tilde{C}_p(x^*)$ of the unsteady pressure characteristics was used in the calculations and the results are provided in Fig.4.21.

The results show good agreement between wind tunnel tests data (continuous line) and the approximations through Eq.4.2 (dashed line), with only some minor discrepancies in the *sin* related derivatives, which showed a tendency to approach the Theodorsen function.

This can be understood as an indicative that Eq.4.2 can lead to reasonable approximations for the aerodynamic derivatives, provided the right coefficients are used. At a first moment an effort should be put in the acquisition of these coefficients for different types of leading edges so that in a second instance the physical phenomena behind these coefficients can be understood, and mechanisms to obtain them for new geometries of leading edges in a deterministic fashion can be developed.

The objective of this study is to propose a systematization to be used in the repro-

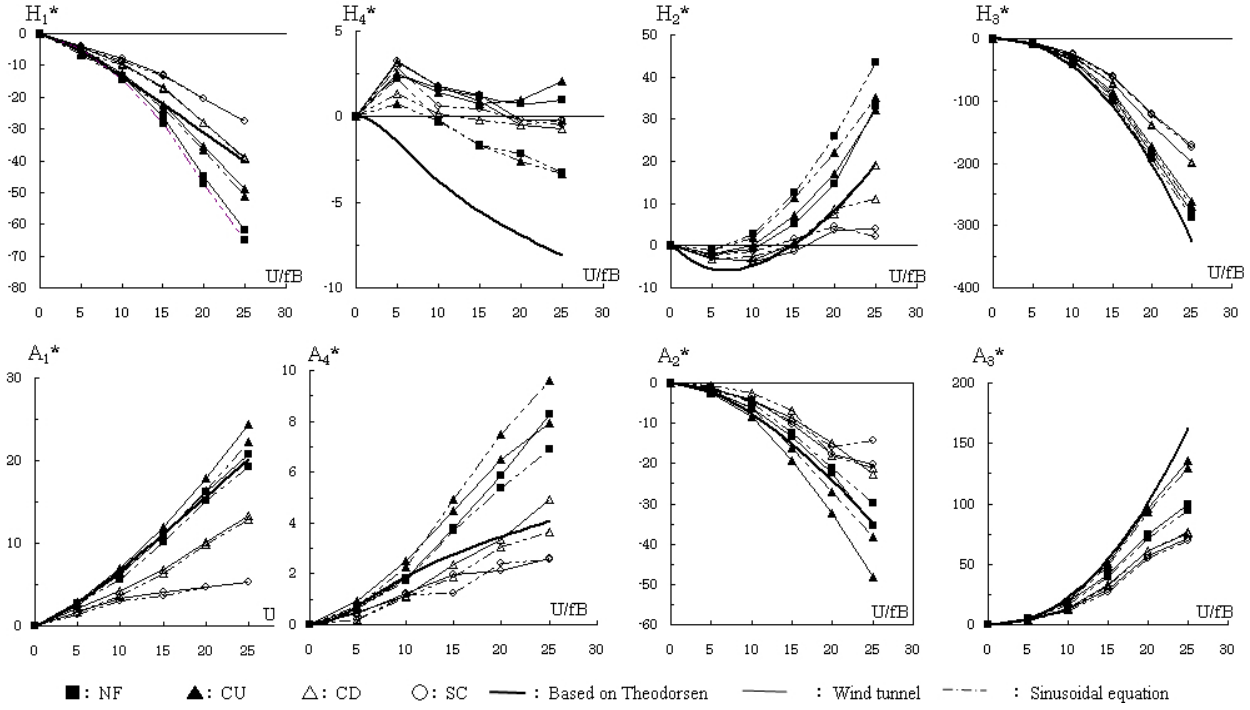

Figure 4.21: Derivatives - wind tunnel *versus* Eq.4.2 combined with original $\tilde{C}_p(x^*)$ distribution

duction of the phase difference $\psi(x^*)$ distribution, and to prove it feasible, not focusing at this time in finding ways to obtain the coefficients analytically. Future works are expected in this sense.

4.3.2 Amplitude Distribution

The amplitude of the unsteady pressure characteristics is a function of the amplitude of vibration and of the wind velocity, among other factors; and when normalized by the dynamic pressure $1/2.\rho.U^2$, where ρ is the air density and U is the wind velocity, provides non-dimensional values comparable along the entire range of wind velocities. Since it is a representation of pressure fluctuations along the body surface, the area under its curve might be treated as a measure of part of the external work done by the fluid along one cycle of vibration and carries meaningful information about the aerodynamics around bodies in

harmonic motion.

For the four cases of leading edges treated in the this chapter – NF, CU, CD and SC –, the areas under the curves of the unsteady pressure characteristic's amplitude were calculated for each different wind velocity through Riemann's integral method and normalized by the maximum angle of attack. In Fig.4.22, the y axis displays this normalized area and the x axis corresponds to the maximum angle of attack for which each area was obtained.

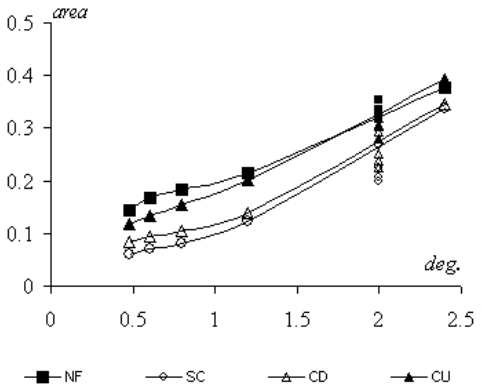

Figure 4.22: Normalized areas for amplitude $\tilde{C}_p(x^*)$ distribution

It is shown in Fig.4.22 that every type of leading edge shows a proportional relationship between area and maximum angle of attack, which is better illustrated in the heaving system (inclined lines), since for every different wind velocity different angles of attack and areas are presented. Because in the torsional motion the maximum angle of attack was kept constant throughout all wind velocities tested (2°), the areas are accumulated in a vertical line in $x = 2$, showing concordance with the values observed in the heaving motion in $x = 2$.

Matsumoto [3] had already accounted for the existence of a relationship between the peak of the $\tilde{C}_p(x^*)$ distribution, $\tilde{C}_{pmax}$, and the maximum angle of attack for both motions. This relationship was also verified for the four cases studied herein, Fig.4.23, showing a pattern very similar to the one obtained in Fig.4.22.

As an attempt to isolate the similarities between Fig.4.22 and Fig.4.23, the areas of Fig.4.22 were normalized by the peak values of $\tilde{C}_p(x^*)$ obtained for every wind velocity, y axis in Fig.4.23. The results are reproduced in Fig.4.24, showing a tendency to present

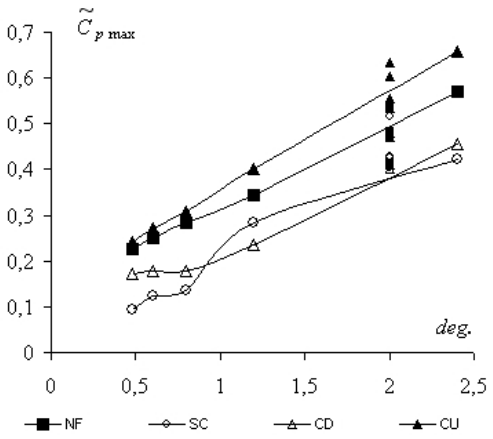

Figure 4.23: Relationship between maximum angle of attack and maximum $\tilde{C}_p(x^*)$, i.e. $\tilde{C}_{pmax}$

results restricted to a limited range (between 0.4 and 0.8) and developing themselves almost constantly throughout the whole range of wind velocities. This can be considered as a characteristic imposed by the leading edge on the amplitude $\tilde{C}_p(x^*)$ distribution and might be a starting point for the verification of relationships for the unsteady pressures amplitude $\tilde{C}_p(x^*)$ distribution. Based on that, it was thought to be convenient to normalize the distributions by their peak values in the search of these relationships, generating the $\tilde{C}_pN(x^*)$ distributions of Fig.4.25 and Fig.4.26.

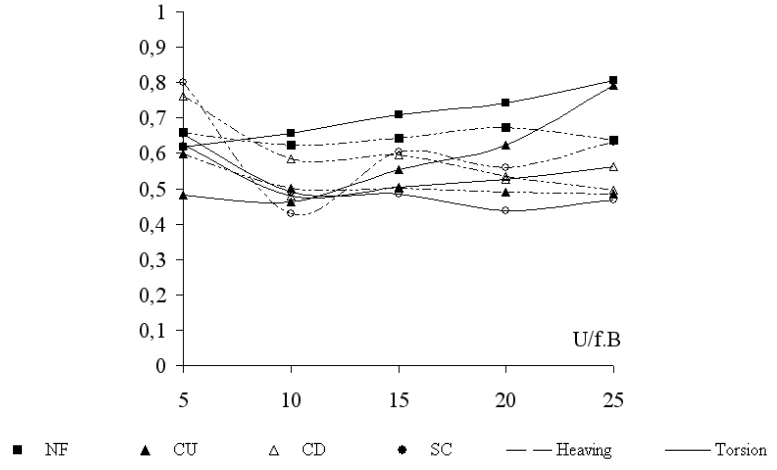

Figure 4.24: Area under $\tilde{C}_p(x^*)$ distribution normalized by its peak value $\tilde{C}_{pmax}$

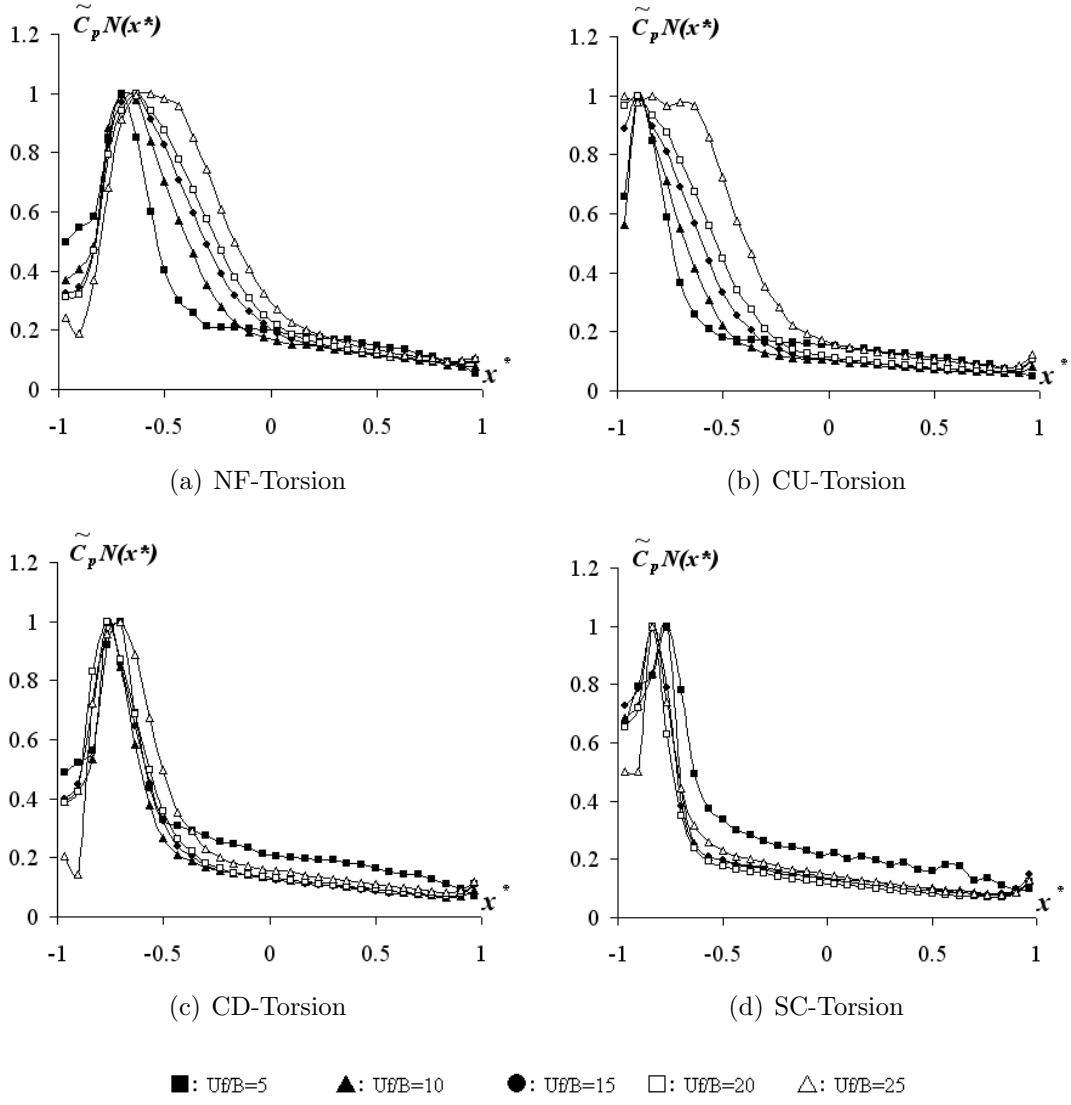

(a) NF-Torsion

(b) CU-Torsion

(c) CD-Torsion

(d) SC-Torsion

Figure 4.25: Normalized amplitude $\tilde{C}_p(x^*)$ distributions for torsional system

A visual analysis of Fig.4.25 and Fig.4.26, in comparison with the phase difference $\psi(x^*)$ distributions of Fig.4.10 to Fig.4.13, reveals that the peaks of $\tilde{C}_pN(x^*)$ distributions are located upwards the peaks of the $\psi(x^*)$ distributions in almost the totality of the samples. Also, the broadening of the base of the $\tilde{C}_pN(x^*)$ distributions with the increase of wind velocity is an important factor to be considered, which must be somehow related to the size

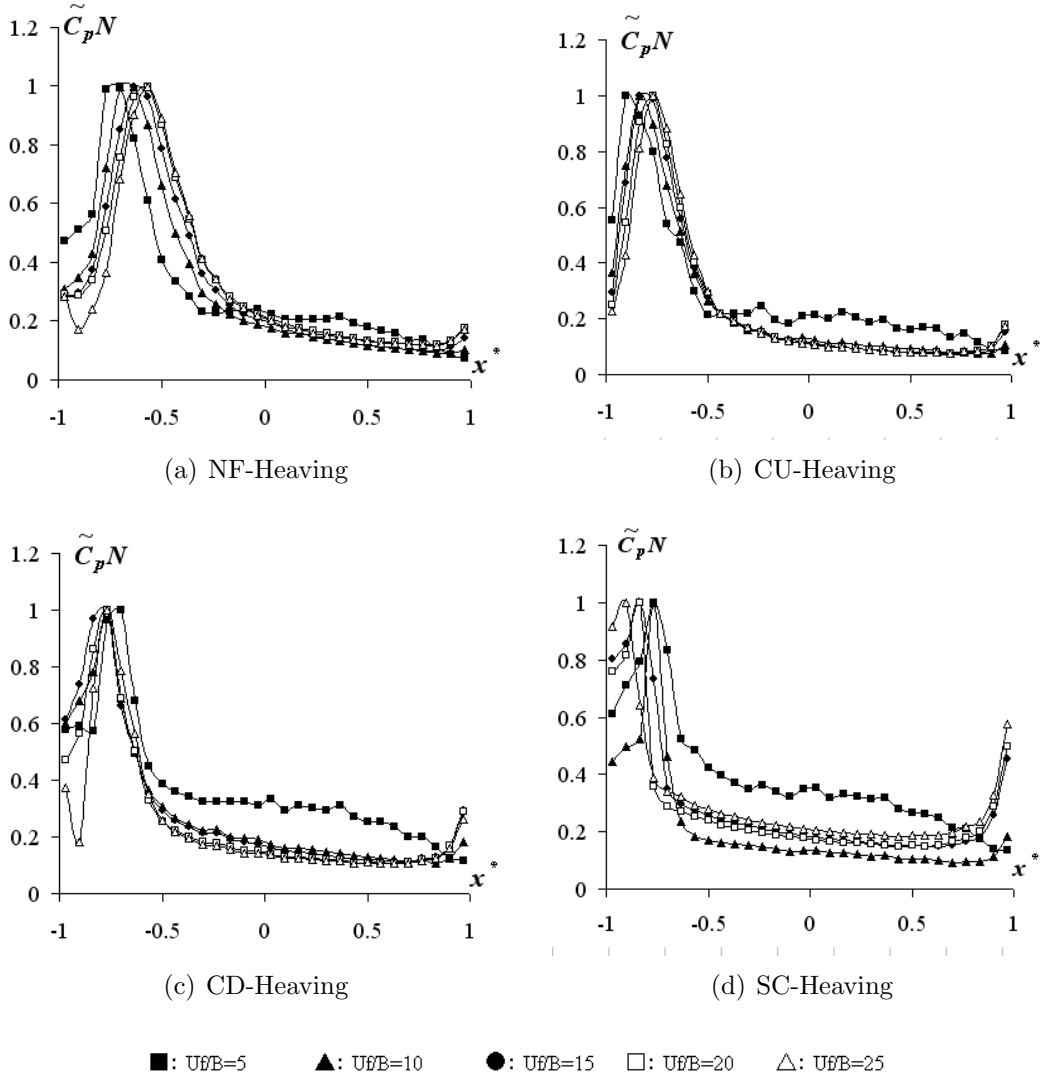

Figure 4.26: Normalized amplitude $\tilde{C}_p(x^*)$ distributions for heaving system

of separation bubble originated in the leading edge.

As for the location of the peaks in the $\tilde{C}_pN(x^*)$ distributions, x_0^*, the values induced by different leading edges show different relationships with the variation of the reduced wind velocity, Fig.4.27. In the case of NF and CU, the increase of $U/f.B$ promotes a displacement of the location of the peak towards downstream, for CD the values are kept almost constant

throughout all the velocities and for SC the peak is moved upstream with the increase of the wind velocity.

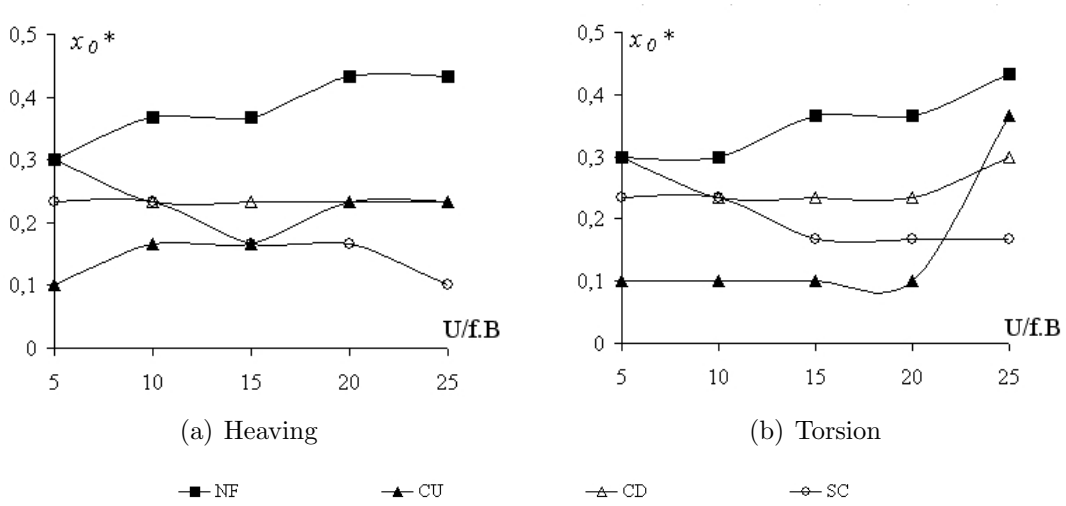

Figure 4.27: Location of the peak x_0^* in the normalized amplitude distribution $\tilde{C}_p N(x^*)$

As mentioned previously in Section 4.2, techniques of flow visualization combined with pressure measurements pointed out that the location of the peak of the fluctuating pressures is strongly related to the reattachment point of the separated flow, exposing the dimension of the separation bubble, and this can be finally regarded to the energy involved in the aerodynamics of the system body-flow. In this sense, it is expected that, in comparison to bluffer leading edges, less bluff leading edges promote lower levels of modification in the energy associated to the flow, producing smaller separation bubbles and inducing consequently peaks closer to the leading edge.

Also already mentioned previously, the point where the flow reattachment occurs in rectangular cross-sections that present afterbody long enough to promote this reattachment was found to be located in a distance around $4.4D$ from the leading edge [105], where D is the thickness of the cross-section, which in normalized dimension corresponds to x_R= 0.44 and in normalized coordinates to x^*= -0.56. Considering the bluffness of the leading edge used in that original reference [105], this value can be regarded as a superior limit and as a reference for the ones presented in Fig.4.27. As it can be noticed in that figure, all the values are situated below that limit, which is reached only by model NF, in the highest reduced wind velocity ($U/f.B = 25$).

The equivalent of x_0^* in the phase difference distribution is the *phase difference* ϕ_ψ, which can also be related to the location of the inflection point of that distribution, Fig.4.20. So comparing these two sets of values, Fig.4.20 and Fig.4.27, it can be noticed that similar patterns are presented, suggesting the existence of a relationship between them, which in terms of angular difference can be expressed by Fig.4.28.

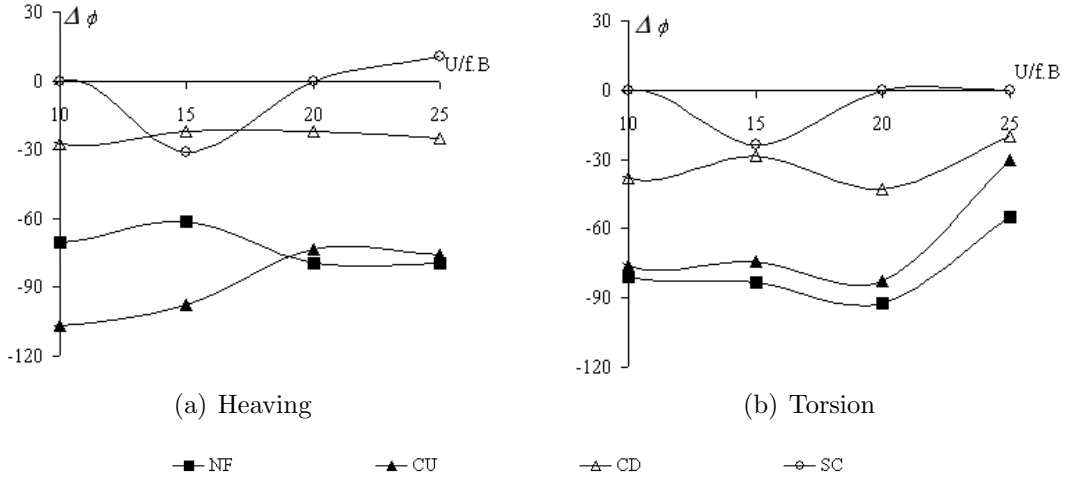

Figure 4.28: Phase difference between peaks of normalized amplitude $\tilde{C}_p N(x^*)$ and phase difference $\psi(x^*)$ distributions

For the interpolation of the values related to the distributions of Fig.4.25 and Fig.4.26, it is proposed the use of an equation in the form of a *Weibull distribution*, Eq.4.5, impacted by a *bias* value, $\tilde{C}_{p0}$, and normalized by its maximum value. The *bias* value is necessary to account for the residue of the decaying of the amplitude of fluctuation of the unsteady pressures, adjusting the curve to its minimum level.

$$C_p N(x^*) = \left[\frac{\gamma_{cp}}{\alpha_{cp}} . \left(\frac{x_{cp}}{\alpha_{cp}} \right)^{\gamma_{cp}-1} . e^{-\left(\frac{x_{cp}}{\alpha_{cp}}\right)^{\gamma_{cp}}} + \tilde{C}_{p\,0} \right]_{max=1} \tag{4.5}$$

where: γ_{cp} is the shape parameter; α_{cp} is the scale parameter; x_{cp} is the x coordinate defined by $x_{cp}= x^*+ 1$; e is the base of the natural logarithm.

The use of Eq.4.5 demands the definition of the parameters γ_{cp}, α_{cp} and the *bias* value $\tilde{C}_{p0}$. These parameters can be estimated in the same fashion it was done for the phase

difference distribution in Section 4.3.1, by considering the wind tunnel tests results reported in Fig.4.10 to Fig.4.13 and the normalized amplitude $\tilde{C}_p(x^*)$ distributions $\tilde{C}_pN(x^*)$ reported in Fig.4.25 and Fig.4.26.

The calculations should be conducted through an iterative procedure, getting the values of the parameters refined after each iteration, until the error of the approximations, calculated through least squares method, is minimized. In a second moment, not covered in this thesis, rational formulations for the calculation of the parameters obtained herein empirically should be proposed based on fluid dynamics concepts.

The parameter $\tilde{C}_{p0}$ is calculated by considering the relationship between the value of the peak and the minimum level of pressure fluctuation of the $\tilde{C}_pN(x^*)$ distribution. After the peak, the amplitude decreases following Eq.4.5 until an inferior level defined by $\tilde{C}_{p0}$ is reached , so after that point the decreasing rate is changed and the curve is developed around the value of the $\tilde{C}_{p0}$. In order to estimate a value for $\tilde{C}_{p0}$, this last part of the curve should be considered; and resorting to the results presented in Fig.4.25 and Fig.4.26, through a weighted mean among the values assumed after the last inflection point, the value of *0.1* is assumed as a initial value for the *bias* $\tilde{C}_{p0}$.

Considering this *bias* value in the normalized distributions of those figures and after some cycles of iteration, it is possible to evaluate the shape parameter γ_{cp} of all configurations, through *Maximum Likelihood Estimation* method. So by applying the calculated shape parameter γ_{cp} into Eq.4.5, the values for the scale parameter α_{cp} are obtained. The results of the last iteration are reported in Table 4.3 and in Fig.4.29 and Fig.4.30.

(a) γ_{cp}

$U/f.B$	5	10	15	20	25
NF torsion	3	2.2	2.15	2.2	2.2
NF heaving	2.85	2.7	2.8	2.9	3
CU torsion	1.9	1.55	1.3	1.3	1.6
CU heaving	1.8	1.8	1.95	2	2.2
CD torsion	3.8	3	2.3	2.1	2.2
CD heaving	3.7	2.5	2.1	2.1	2.2
SC torsion	3	2.05	2	2.2	2.1
SC heaving	3.5	2.3	2.5	2.3	1.5

(b) α_{cp}

$U/f.B$	5	10	15	20	25
NF torsion	0.34	0.43	0.48	0.53	0.6
NF heaving	0.32	0.42	0.47	0.5	0.55
CU torsion	0.17	0.2	0.27	0.32	0.39
CU heaving	0.2	0.26	0.29	0.3	0.32
CD torsion	0.3	0.28	0.3	0.33	0.38
CD heaving	0.3	0.3	0.3	0.29	0.32
SC torsion	0.26	0.25	0.24	0.2	0.24
SC heaving	0.26	0.21	0.19	0.17	0.14

Table 4.3: Parameters for Eq.4.5

The figures show that for both parameters each geometry shows similar patterns in both

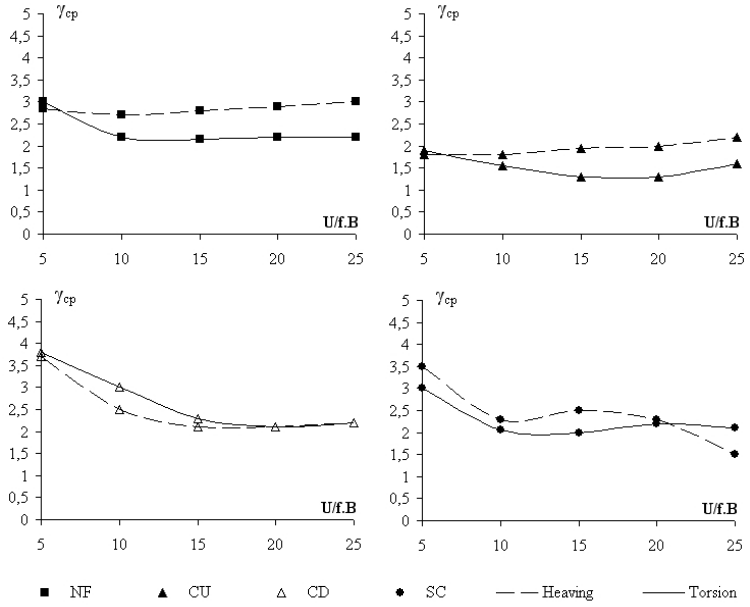

Figure 4.29: Parameter γ_{cp} for Eq.4.5

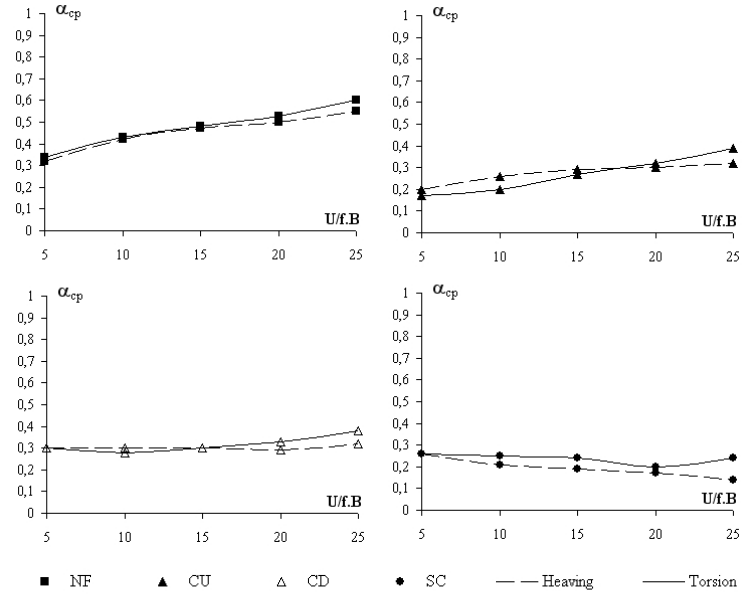

Figure 4.30: Parameter α_{cp} for Eq.4.5

torsional and heaving systems, especially the scale parameter α_{cp}. The shape parameter γ_{cp} presents some discrepancies among systems and with the increase of the wind velocity all configurations tend to oscillate in a range around the value of *2*, which defines the *Rayleigh distribution*. Considering as a extrapolation that the unsteady pressures amplitude would behave as a Rayleigh distribution (γ_{cp}= 2) in B/D=20 rectangular cylinders, the scale parameter α_{cp} would be regarded as the one that characterizes each leading edge in terms of unsteady pressure amplitude distribution.

Since the shape parameter γ_{cp} is related to the shape of the amplitude $\tilde{C}_p(x^*)$ distribution, the "size" of the curve, which is dependent on the size of the separation bubble and presents consequently a direct dependence on the thickness D and an indirect dependence on the side ratio B/D, must be dependent on the parameter α_{cp}. So, for the development of an analytical systematization to be used in the estimation of γ_{cp} and α_{cp}, those relationships must be considered, by making use of models with different side ratios and leading edges.

By comparing the superposition of the different distributions at the same reduced wind velocity provided by Fig.4.5, it is noted that the relative size of the $\tilde{C}_p(x^*)$ distributions in relation to the side ratio changes with the side ratio by keeping the same absolute sizes and shapes, which leads to the conclusion that the parameter α_{cp} must have a different value for every different side ratio, as stated above. As for the parameter γ_{cp}, which is related to the shape of the distributions, it must be mostly dependent on the characteristics of the separation point, since it barely changes among the configurations found in that figure, that kept the same leading edge. However, these assumptions remain to be better investigated, as stated in the previous paragraph, and in Chapter 5, additional information will be brought to scene.

The efficiency of Eq.4.5 in reproducing the amplitude $\tilde{C}_p(x^*)$ distributions can be verified by recalculating the aerodynamic derivatives of the four cases studied throughout this chapter by using the distributions produced through it and comparing the results with the real values, calculated with wind tunnel tests data. Fig.4.31 presents the $\tilde{C}_p(x^*)$ distributions obtained with Eq.4.5 for NF in torsion oscillation and Fig.4.32 the aerodynamic derivatives obtained for the 4 cases, compared with both the real values and Theodorsen function. The good agreement obtained in the comparisons provided by Fig.4.31 and Fig.4.32 confirms that Eq.4.5 is able to provide reasonable results, if the proper parameters are used.

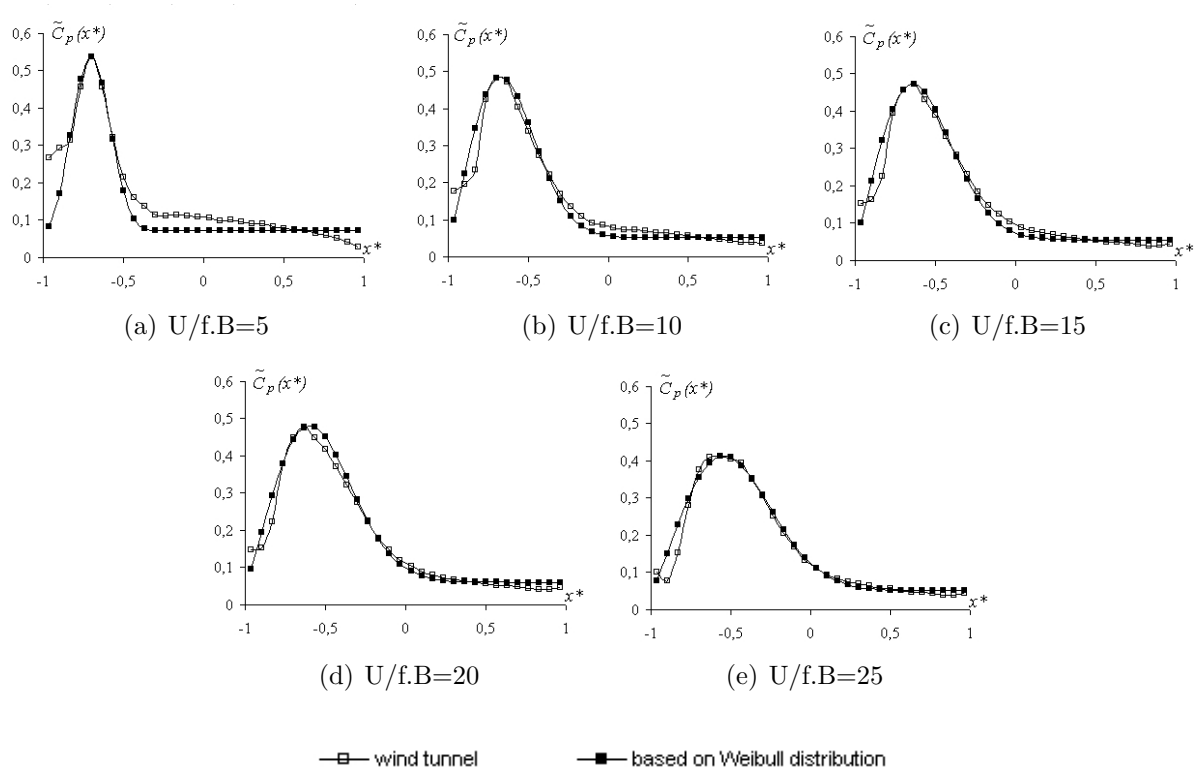

(a) U/f.B=5 (b) U/f.B=10 (c) U/f.B=15

(d) U/f.B=20 (e) U/f.B=25

Figure 4.31: Unsteady pressure amplitude $\tilde{C}_p(x^*)$ distribution for NF in torsion obtained with Eq.4.5 and compared with wind tunnel test data

4.3.3 Combining Phase Difference and Amplitude Distributions

In *Weibull distributions* the scale parameter α_{cp} has the same unit as x_{cp} (as an analogy to [117]), which in Eq.4.5 refers to the normalized location x^*. Comparing the empirical parameters obtained for Eq.4.2 and Eq.4.5, it is noticed that with the increase of the reduced wind velocity both the normalized wave half-length $\lambda/2$, which is given by the relation $2.\pi/\omega_\psi$in Eq.4.2, and α_{cp} of Eq.4.5 show similar tendencies. Both parameters provide a *scaling effect* on the distributions. A comparison between the inverse of their values (hereafter called "scale factor"), obtained for the 4 geometries of leading edges in all reduced wind velocities, can be seen in Fig.4.33 and Fig.4.34.

The comparisons indicate that both parameters follow indeed similar tendencies. Be-

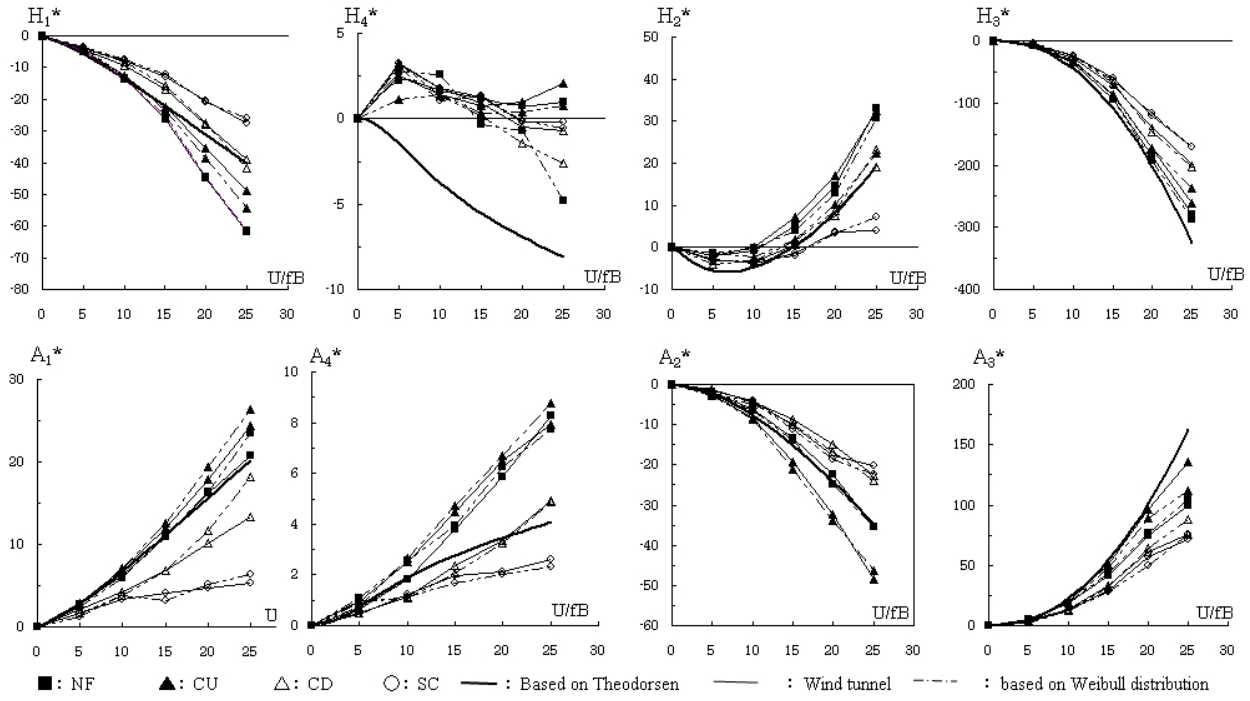

Figure 4.32: Derivatives - wind tunnel *versus* Eq.4.5 combined with original phase difference distribution

cause of that, it seems to be natural to search for relationships between them, through a "proportionality relationship".

In the search for this "proportionality relationship" the ratio between both values was evaluated for all configurations, showing a tendency towards the unity as γ_{cp} approaches π. Based on that, a further comparison can be established by taking the index $\gamma_{cp}/\ \alpha_{cp}$ of Eq.4.5 multiplied by 2 and the value of ω_ψ, obtained from the phase difference distribution. Both can be regarded as "wave number factor" and the results are shown in Fig.4.35 and Fig.4.36.

With the exception of model *SC*, the agreement of this further comparison is very good, pointing to a strong relationship between phase difference $\psi(x^*)$ and amplitude $\tilde{C}_p(x^*)$ distributions. This relationship is associated to the wave length and can be understood in the calculation framework proposed herein as an index inherent to each type of leading edge, which in the quasi-steady state might be approximated by analytical approaches.

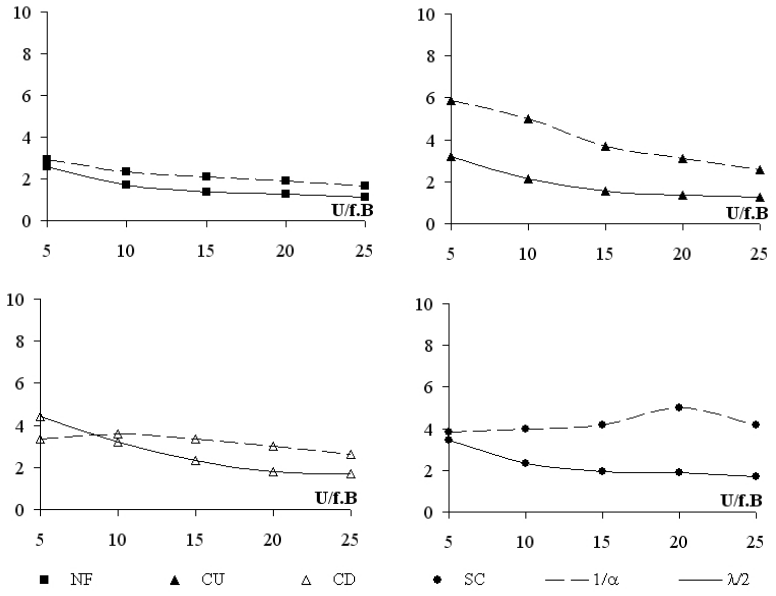

Figure 4.33: Scale factor for torsional system

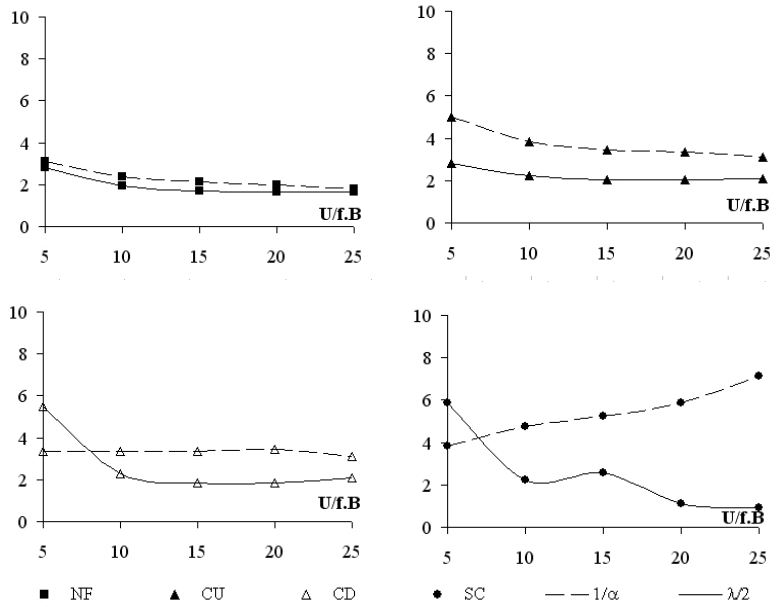

Figure 4.34: Scale factor for heaving system

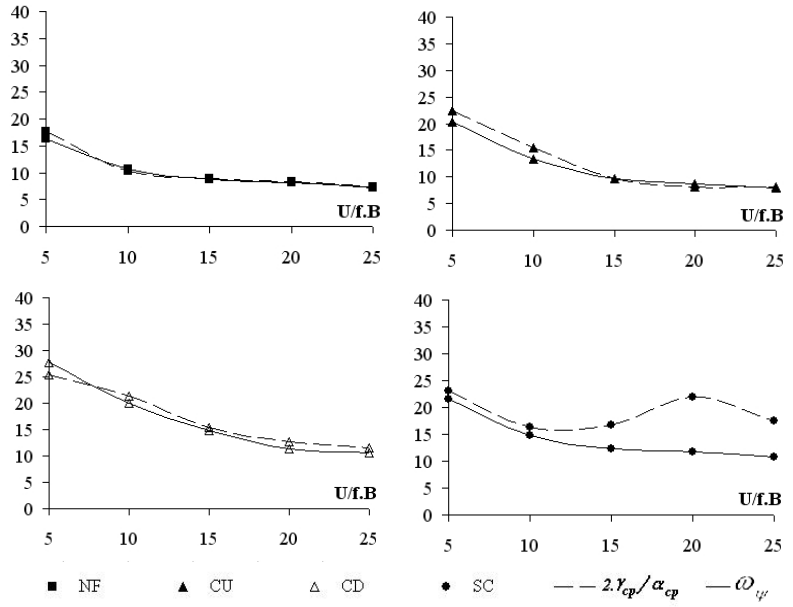

Figure 4.35: wave number factor for torsional system

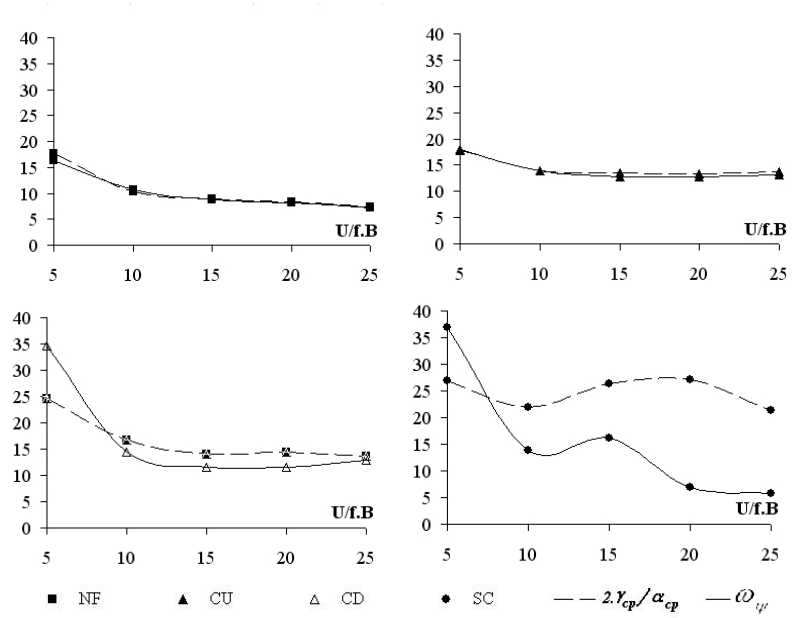

Figure 4.36: wave number factor for heaving system

The aerodynamic derivatives were also evaluated by considering both the phase difference and the unsteady pressure distributions calculated through the approach proposed in this chapter, by using Eq.4.2 and Eq.4.5. The results can be found in Fig.4.37, showing also a good agreement with the real values for all aerodynamic derivatives, with the exception of some discrepancies in the approximations obtained for H_4^* derivative. The tendency presented by H_4^* in the approximations was to approach the Theodorsen function, and this behavior is somehow expected for such a cross-section, having been already reported in other references, Fig.4.6.

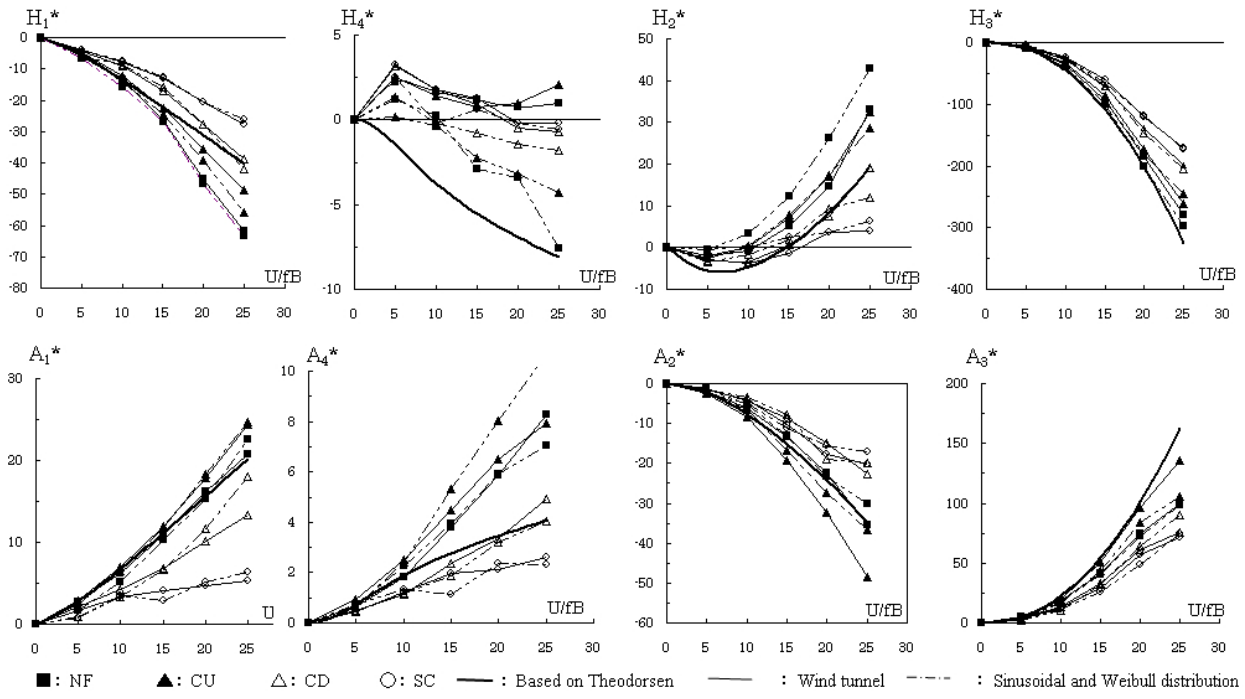

Figure 4.37: Derivatives - wind tunnel *versus* Eq.4.5 combined with Eq.4.2

4.4 Concluding Remarks

This chapter dealt with the proposition of a calculation framework to be used in the reproduction and the estimation of the unsteady pressure characteristics of rectangular cylinders submitted to smooth flow. It was demonstrated that these characteristics follow pre-established

patterns, identifiable through common equations whose parameters can be related to the characteristics of each cross-section.

The phase difference distribution was found to follow a sinusoidal equation, while the pressure fluctuation along the body surface tended to be distributed according a *Weibull distribution*. For both equations, the wave length developed along the body plays a very important role in the definition of their parameters, providing an interconnection between phase difference and amplitude distributions.

For all cases, the *Weibull distribution* tended to behave as a Rayleigh distribution (γ_{cp}= 2) in higher reduced wind velocities; however, this must not be treated as a final conclusion, since only few cases were tested, but as an inherent characteristic of the types of models investigated, i.e. B/D=20 rectangular cylinders. The scale parameter α_{cp}, regarded as the responsible for the definition of the "size" of the distributions, was related to the wave length developed along the body. Since this wave length is dependent on the leading edge and on the side ratio B/D, this parameter is thought to be the result of the combination of the influence of both factors, associated also to the effects of the wind velocity.

Through the analysis of wind tunnel tests results, characteristic parameters were obtained for a B/D=20 rectangular cylinder, with four different configurations of leading edges. However, the number of cases analyzed is small and can not be considered representative. So, an extension of this study should be conducted by acquiring the characteristic parameters for a wider range of leading edges and cross-sections, so that a picture of the phenomena can be obtained.

The experiments contain uncertainties, so the results provided by the formulations should be considered based on the "tendency" of reproducing the test results, not on the "exactness" of their provisions. The objective of this chapter was the proposition of the formulations and to prove them feasible, providing also the characteristic parameters regarding every geometry investigated, in an empirical basis, not focusing at this time in finding ways to obtain them analytically. Since the equations are established, the work from this point on should be the refinement of the framework and the proposition of strategies for obtaining the characteristic parameters through an analytical approach, by considering the concepts of fluid dynamics and wind engineering.

A rationalization about the unsteady pressure characteristics of bridge decks can be obtained with the extension of the investigations reported in this chapter, and the subsequent

step towards the development of a design framework to be used with long span bridges is the development of strategies to control and "manipulate" the unsteady pressure characteristics along the bridge deck. In this context, the idea of *geometric singularities* was proposed, referring to the insertion of "geometric accidents" (flow separation points, slots and gratings) along the deck, in proper locations, with the objective of leading both phase difference and amplitude distributions to assume values suitable for flutter stabilization, according to the optimal conditions discussed in Chapter 3.

This concept will be approached in the sequence of this thesis as well as the influences of such *geometric singularities* on the unsteady pressure characteristics. Their impacts on the characteristic parameters of the equations proposed in this chapter will be discussed and rationalized.

Chapter 5

Effects of Vertical Plates on the Unsteady Pressure Characteristics of Modified Rectangular Cylinders

5.1 Introduction

As suggested in the previous chapters, a more rational control over flutter instability in long span bridges can be obtained through the *manipulation* of the unsteady pressure characteristics developed along their decks, which can be obtained by disposing *geometric singularities* along their surfaces.

Although a framework to be used in the calculation of these unsteady pressure characteristics through the use of closed formulations and empirical coefficients was proposed in Chapter 4, those equations did not take in consideration the impacts of such *geometric singularities* on their coefficients. So in this chapter the framework proposed in that chapter is revisited by considering the introduction of flow separation points along the cylinder‘s surface, provided by the use of vertical plates.

Wind tunnel tests were conducted by using B/D=20 rectangular cylinders with 4 dif-

ferent geometries of leading edges, combined with vertical plates of 2 different sizes disposed in 7 different arrangements on the upper side surface of the cylinders. So the effects of location and size combined with the inherent unsteady pressure distributions induced by the different leading edges could be investigated.

The pressures measurement system and the configurations of leading edges were the same used in the previous chapter, as well as the configuration of the wind tunnel, i.e. Appendix A. The *runs* are identified by the leading edges code – NF, CU, CD, SC – followed by the vertical plate code, which is formed by a *location code* (Fig.5.1) and a *size code* ("A" for height=D/2 and "B" for height=D). In the configurations IV, V and VI, the vertical plates are located at the middle of the half-width.

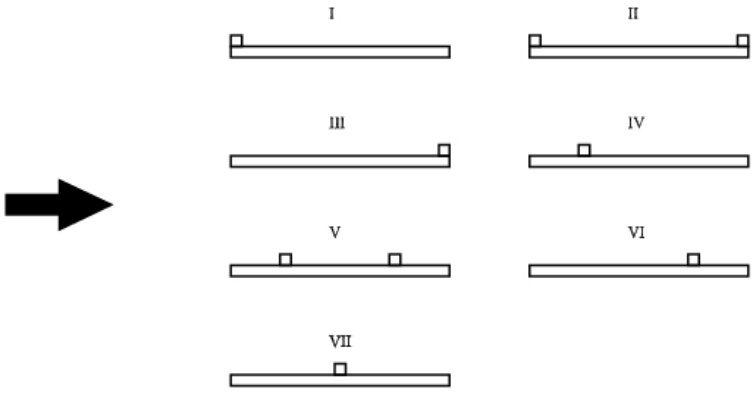

Figure 5.1: Vertical plates location code

The results of the investigations are reported in the following sections, considering the arrangement of the vertical plates. They are accompanied by considerations on the relationships of size and position of the vertical plates along the cylinder's surface with the resulting values of phase difference $\psi(x^*)$ and amplitude distributions $\tilde{C}_p(x^*)$, and should be interpretated by considering the discussions around the *optimal unsteady pressure characteristics* obtained in Chapter 3.

5.2 Vertical plate at the leading edge

Some of the influences of vertical plates installed near the leading edge, Fig.5.6, will be analyzed by considering the results reported in Fig.5.2 to Fig.5.5.

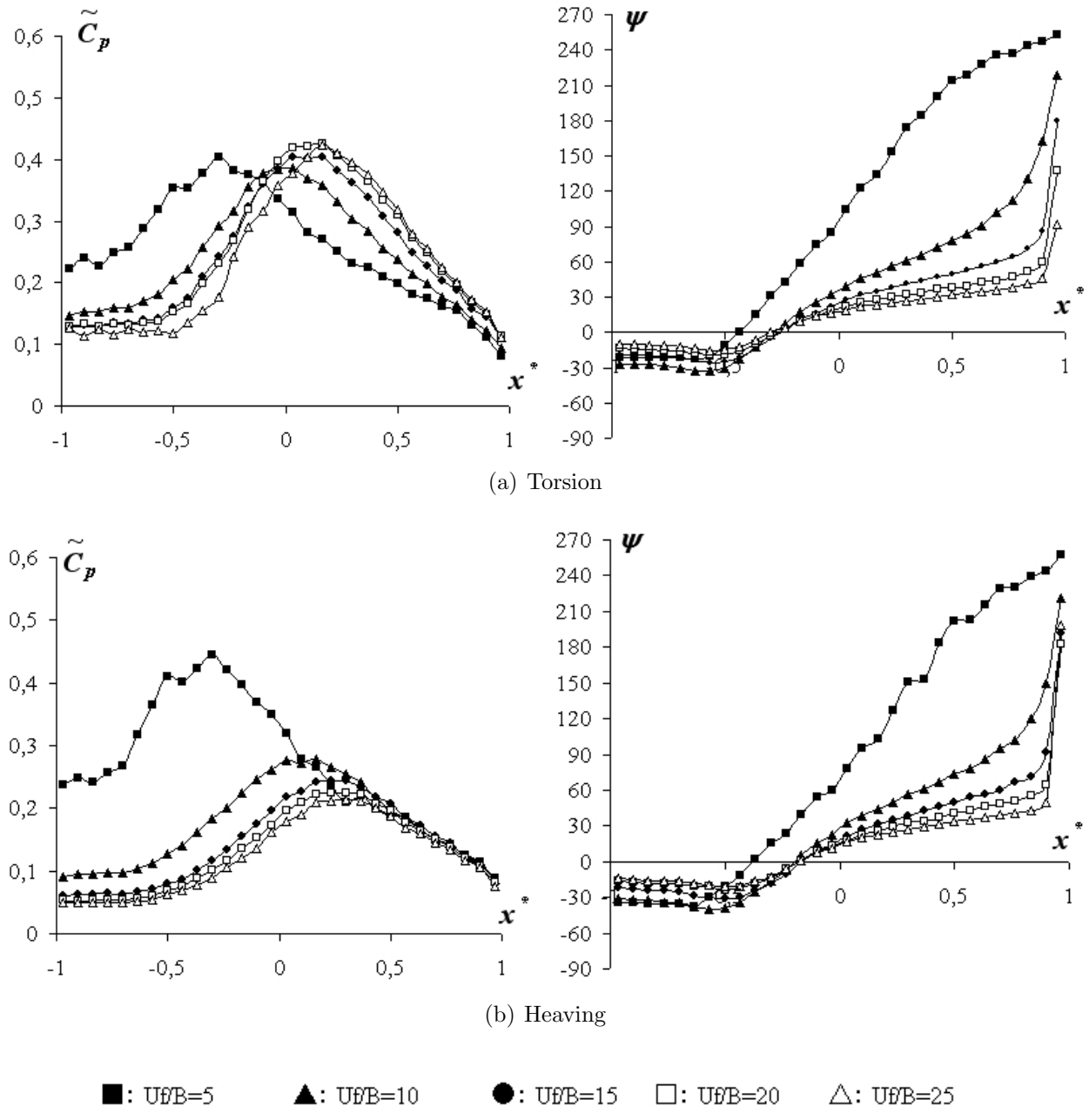

Figure 5.2: Unsteady pressure characteristics of case NF-I-A

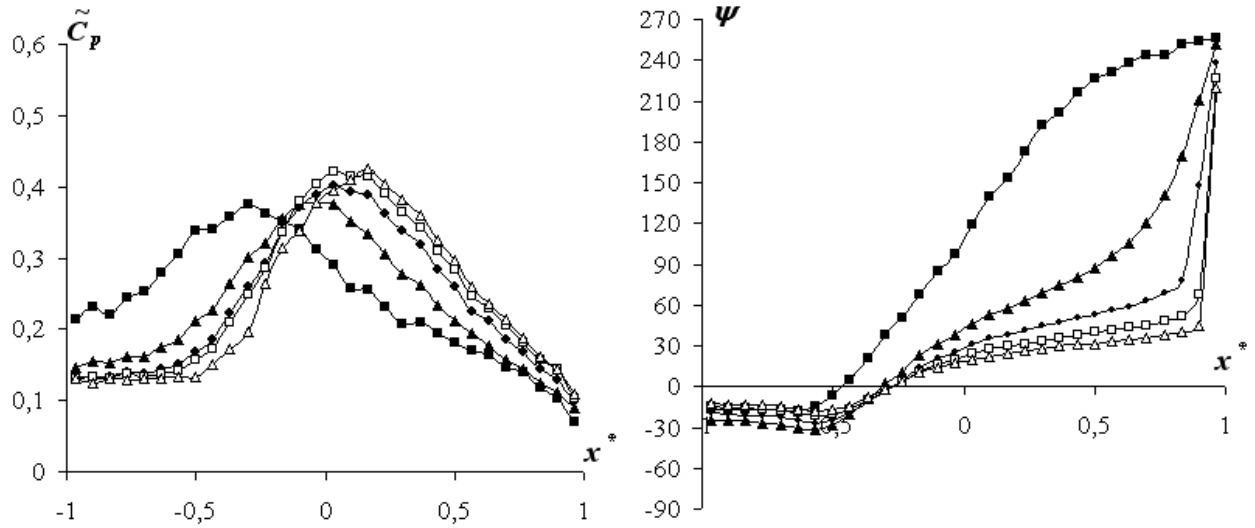

(a) Torsion

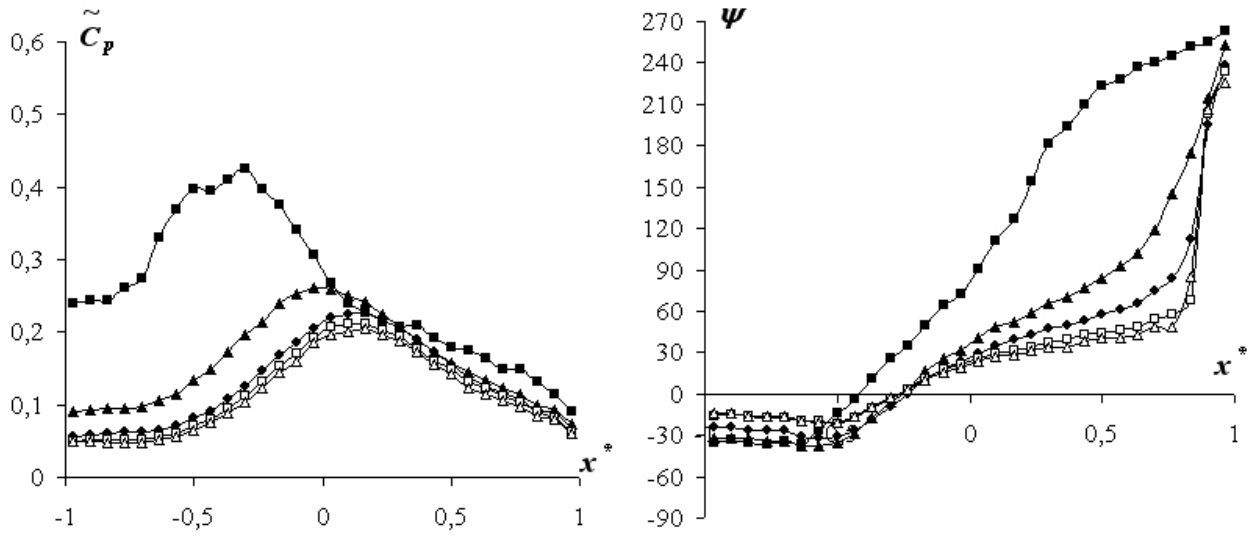

(b) Heaving

■: U∞B=5 ▲: U∞B=10 ●: U∞B=15 □: U∞B=20 △: U∞B=25

Figure 5.3: Unsteady pressure characteristics of case SC-I-A

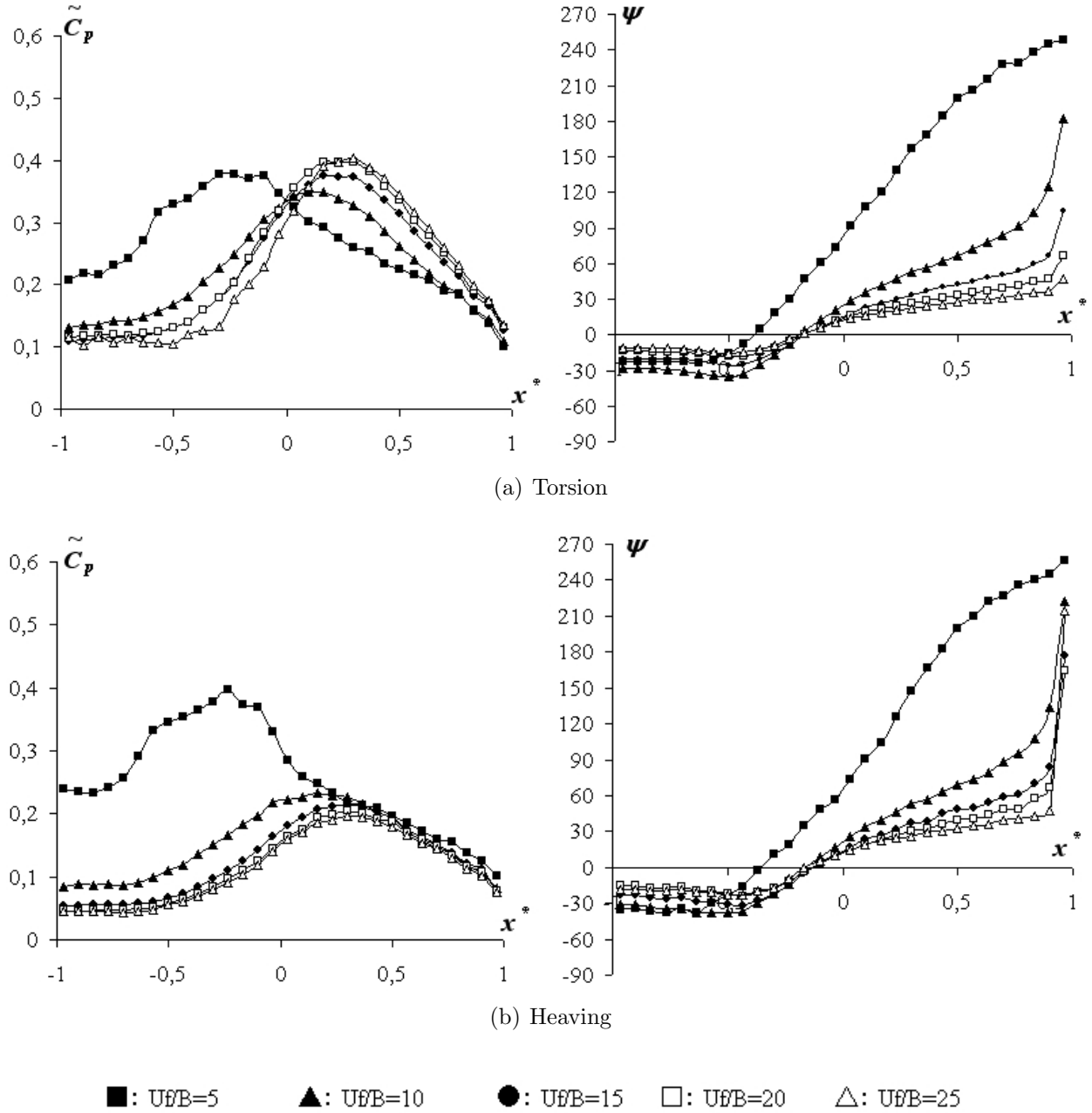

(a) Torsion

(b) Heaving

Figure 5.4: Unsteady pressure characteristics of case CD-I-A

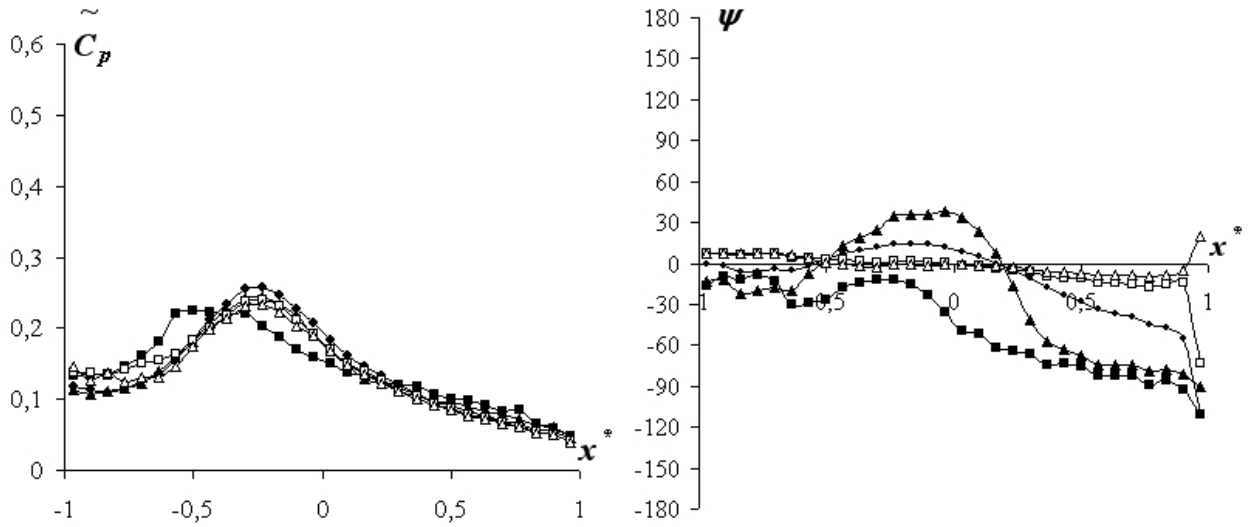

(a) Torsion

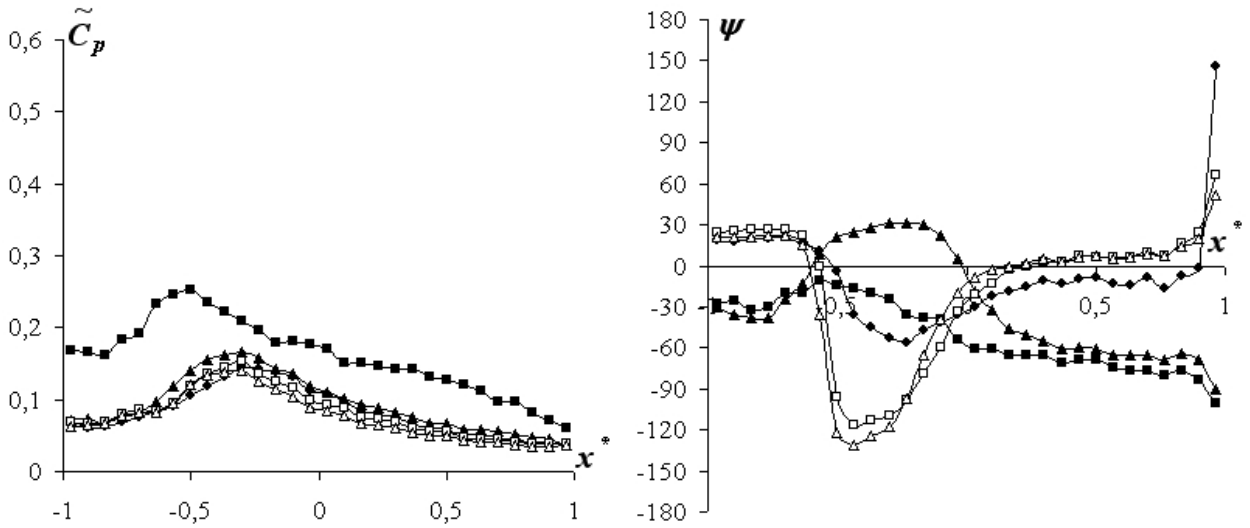

(b) Heaving

■: U∞/B=5 ▲: U∞/B=10 ●: U∞/B=15 □: U∞/B=20 △: U∞/B=25

Figure 5.5: Unsteady pressure characteristics of case CU-I-A

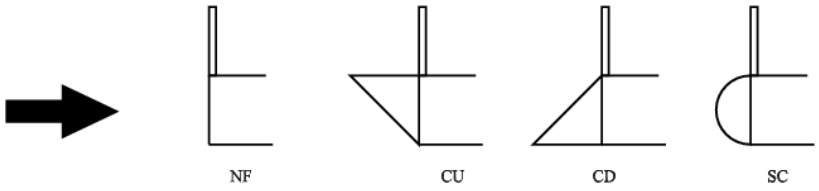

Figure 5.6: Vertical plate at the leading edge

With the exception of CU-I-A, regardless the unsteady pressure characteristics of the original cross-section (NF, CD and SC), all the resulting distributions of $\tilde{C}_p(x^*)$ and $\psi(x^*)$ are lead to similar configurations. Comparing the amplitude $\tilde{C}_p(x^*)$ distributions in terms of maximum angle of attack, as proposed in Section 4.3.2, with the results obtained for the B/D=20 rectangular cylinder, as shown in Fig.5.7, it can be seen that although the $\tilde{C}_{pmax}$ peaks get attenuated, the normalized areas under the curves of the amplitude $\tilde{C}_p(x^*)$ distributions are increased. This increase is related to a broadening of the base of the distributions and must have relationship with the size of the vortices generated at the leading edge, due to the vertical plate, in this case.

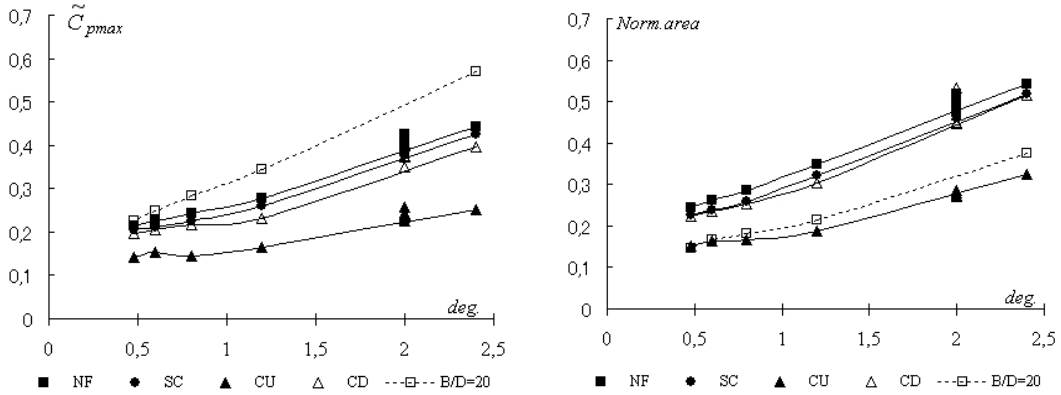

(a) $\tilde{C}_{pmax}$ - Maximum $\tilde{C}_p(x^*)$ (b) Area normalized by $\tilde{C}_{pmax}$

Figure 5.7: Comparison in terms of maximum angle of attack

The confirmation of the broadening of the $\tilde{C}_p(x^*)$ distributions is obtained by evaluating their areas normalized by their $\tilde{C}_p(x^*)$ peak values $\tilde{C}_{pmax}$, Fig.5.8. The results show higher values when compared with the B/D=20 rectangular cylinder. All configurations presented similar patterns, including CU-I-A.

Resorting to the method proposed in Section 4.3.2, the amplitude $\tilde{C}_p(x^*)$ distributions

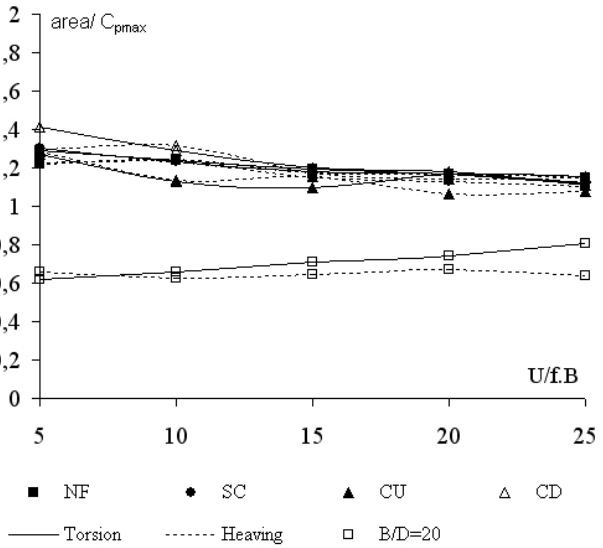

Figure 5.8: Area under $\tilde{C}_p(x^*)$ distribution normalized by its peak value $\tilde{C}_{pmax}$

of the 4 cases studied in this section were rebuilt, and the parameters obtained for Eq.4.5 in this process are listed in Table 5.1. All interpolations showed good agreement with the wind tunnel test data; as an example, the distributions obtained for NF-I-A in torsional motion are reproduced in Fig.5.9.

Installing a vertical plate near the leading edge promoted an increase in the level of the *bias* $\tilde{C}_{p0}$ for all distributions, which now oscillate around *0.3*, and this is a consequence of the new relationships between normalized areas and peaks, Fig.5.7.

The ratio $\gamma_{cp}/\ \alpha_{cp}$ also showed itself more stable, in comparison with model NF of Chapter 4 (B/D=20 rectangular cylinder), Fig.5.10. Although the shapes of the amplitude $\tilde{C}_p(x^*)$ distributions of all cases can be considered similar to regular rectangular cylinders, a shift downstream in the location of the peak is an important feature of the resulting distributions discussed in this chapter.

As already mentioned in Chapter 4, the location x_0^* of the peak $\tilde{C}_{pmax}$ of the unsteady pressure amplitude distributions can be related to the reattachment of the flow in the surface of the body, and finally regarded to the size of the vortices developed due to the flow separation at the leading edge. Based on that, the relationship $x_0^*= 4.4.D$ was investigated

Table 5.1: Parameters obtained through Eq.4.5 for modified rectangular cylinders with vertical plate of height=D/2 near the leading edge

		Torsion				Heaving			
U/f.B		NF-I-A	SC-I	CD-I	CU-I	NF-I-A	SC-I	CD-I	CU-I
5	γ	2.8	3.0	3.0	3.2	2.8	2.8	2.8	2.9
	α	0.85	0.83	0.9	0.65	0.82	0.75	0.85	0.6
	α/γ	3.29	3.61	3.33	4.92	3.41	3.73	3.29	4.83
	$\tilde{C}_{p0}$	0.44	0.52	0.59	0.54	0.33	0.36	0.38	0.55
10	γ	3.7	3.7	4.0	4.1	4.0	3.7	3.9	3.8
	α	1.1	1.07	1.25	0.8	1.22	1.1	1.25	0.75
	α/γ	3.36	3.46	3.2	5.13	3.28	3.36	3.12	5.07
	$\tilde{C}_{p0}$	0.38	0.39	0.39	0.46	0.34	0.34	0.37	0.44
15	γ	3.9	4.0	4.4	4.1	4.2	4.2	4.3	4.0
	α	1.2	1.15	1.35	0.81	1.35	1.22	1.35	0.85
	α/γ	3.25	3.48	3.26	5.06	3.11	3.44	3.19	4.71
	$\tilde{C}_{p0}$	0.32	0.32	0.3	0.47	0.24	0.26	0.23	0.42
20	γ	4.2	4.2	4.4	4.2	4.3	4.2	4.3	4.0
	α	1.25	1.2	1.32	0.8	1.35	1.25	1.4	0.75
	α/γ	3.36	3.5	3.33	5.25	3.19	3.36	3.07	5.33
	$\tilde{C}_{p0}$	0.29	0.3	0.28	0.55	0.22	0.25	0.21	0.4
25	γ	4.5	4.4	4.6	4.5	4.4	4.4	4.3	4.0
	α	1.3	1.22	1.4	0.8	1.4	1.25	1.4	0.73
	α/γ	3.46	3.61	3.29	5.63	3.14	3.52	3.07	5.48
	$\tilde{C}_{p0}$	0.24	0.28	0.25	0.52	0.23	0.24	0.23	0.43

for all cases, by getting the position x_0^* of the peaks in the distributions of Fig.5.2 to Fig.5.5 and evaluating an *equivalent thickness* D_{eq} for all cross-sections, i.e. values of D that satisfy the equality. By using this *equivalent thickness* D_{eq} and considering that the results are in normalized dimensions for a B/D=20 rectangular cylinder in which a normalized thickness *D=0.1* is expected for a normalized width B=2 (since it is normalized by the half-width b), an *equivalent side ratio* BD_{eq} can be obtained for all cases. This *equivalent side ratio* is calculated through the relationship $BD_{eq}= 2/D_{eq}$ and can be understood as "the side ratio of rectangular cross-section that would generate the same amplitude distribution". Thanks to the similarities presented by the amplitude $\tilde{C}_p(x^*)$ distributions, a comparison link can be established between the modified rectangular cylinders (with a vertical plate near the leading edge) and basic rectangular cylinders. The results are reported in Table 5.2.

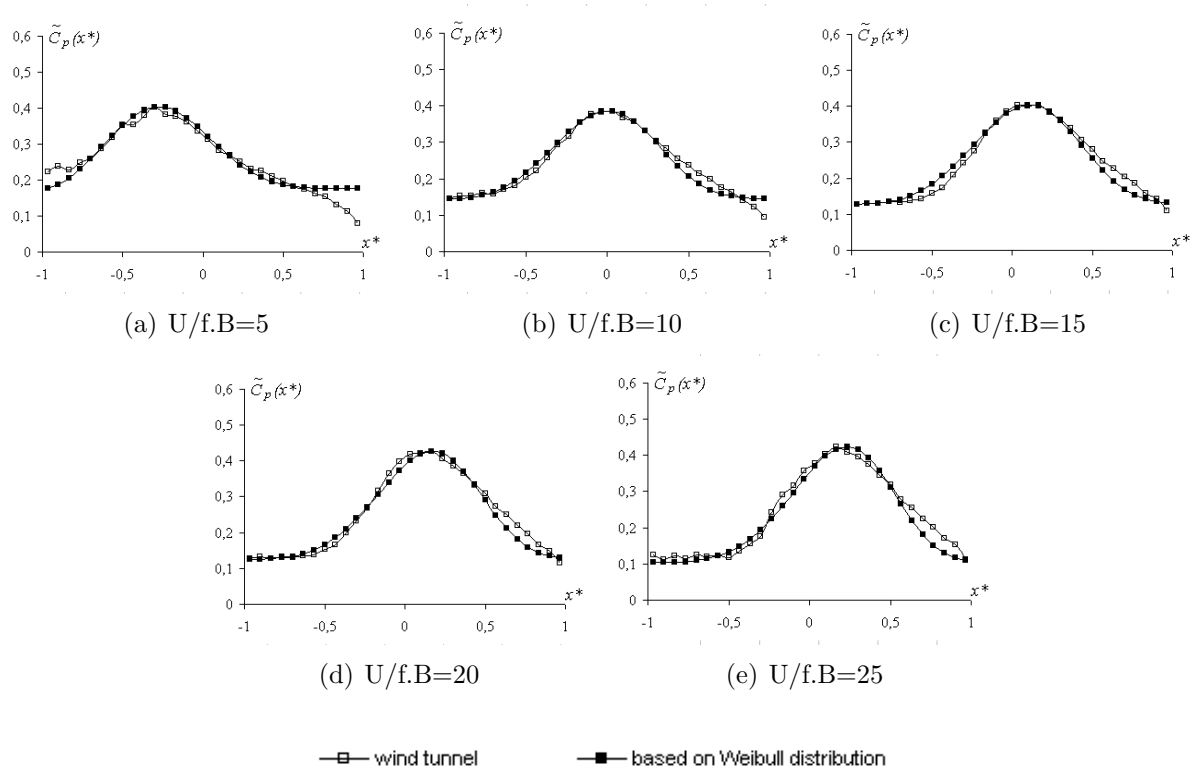

(a) U/f.B=5 (b) U/f.B=10 (c) U/f.B=15

(d) U/f.B=20 (e) U/f.B=25

Figure 5.9: Unsteady pressure amplitude $\tilde{C}_p(x^*)$ distribution for NF-I-A in torsion, obtained with Eq.4.5 and compared with wind tunnel test data

According to the results expressed in Table 5.2, with the increase of the reduced wind velocity the *equivalent side ratios* BD_{eq} of the models SC, CD and NF tend to a value around 7. Comparing in terms of values and shapes the amplitude $\tilde{C}_p(x^*)$ distributions of these cases with the wind tunnel test data used to produce Fig.4.5, and also observing the relationship $x_0^*= 4.4D$ obtained at higher reduced wind velocities, it can be verified that the distributions obtained for SC-I-A, CD-I-A and NF-I-A present indeed an intermediate configuration between rectangular cylinders with side ratios B/D=5 and B/D=7.5, as can be seen Fig.5.11.

It happens that the introduction of a vertical plate of height=D/2 at the leading edge changes the *apparent side ratio* of the models to $(B/D)_{ap} = 13.3$. This *apparent side ratio* is calculated by considering the relationship between the width B of the rectangular cross-section and a value of thickness formed by the summation of the real thickness D of the

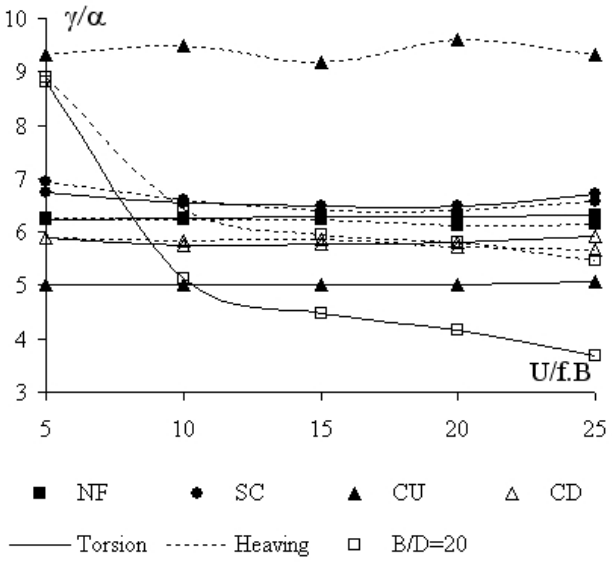

Figure 5.10: Ratio $\frac{\gamma_{cp}}{\alpha_{cp}}$ for configurations with vertical plate near the leading edge

Table 5.2: Equivalent side ratio and equivalent thickness for modified rectangular cylinders (vertical plate $height = D/2$ in the leading edge), calculated through x_0^*= $4.4D_{eq}$

U/f.B	5		10		15		20		25	
	D_{eq}	BD_{eq}	D_{eq}	BD_{eq}	D_{eq}	BD_{eq}	D_{eq}	BD_{eq}	D_{eq}	BD_{eq}
NF in torsion	0.16	12.57	0.23	8.52	0.23	8.52	0.27	7.54	0.27	7.54
NF in heaving	0.16	12.57	0.27	7.54	0.30	6.77	0.30	6.77	0.30	6.77
SC in torsion	0.16	12.57	0.22	9.10	0.23	8.52	0.23	8.52	0.27	7.54
SC in heaving	0.16	12.57	0.22	9.10	0.27	7.54	0.27	7.54	0.27	7.54
CD in torsion	0.16	12.57	0.27	7.54	0.27	7.54	0.27	7.54	0.30	6.77
CD in heaving	0.17	11.48	0.27	7.54	0.30	6.77	0.30	6.77	0.30	6.77
CU in torsion	0.11	17.60	0.17	11.48	0.17	11.48	0.17	11.48	0.17	11.48
CU in heaving	0.11	17.60	0.16	12.57	0.16	12.57	0.16	12.57	0.16	12.57

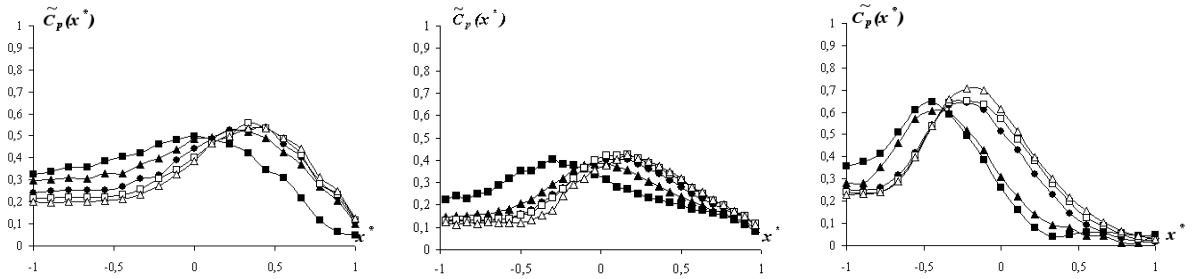

(a) B/D=5 in torsion,(adapted from [3])

(b) NF-I-A in torsion

(c) B/D=7.5 in torsion,(adapted from [3])

Figure 5.11: Comparison between amplitude $\tilde{C}_p(x^*)$ distributions of rectangular cylinders with side ratios B/D=5, B/D=7.5 and the NF-I-A case, in torsion

cylinder and the height of the vertical plate ($D/2$ in this case), i.e. cross-flow dimension. This resulting number is the double of the values of the *equivalent side ratio* BD_{eq} presented by models SC-I-A, CD-I-A and NF-I-A in Table 5.2.

In search for logical relationships for that effect, a further experiment was conducted by installing a vertical plate with double of the size of the previous one, i.e. same as the thickness of the model (D), at the leading edge of the model NF. This new arrangement led to the unsteady pressure distributions of Fig.5.12 and is hereafter referred to as NF-I-B.

The same calculation approach was applied and, similarly to model NF-I-A, the *equivalent side ratio* BD_{eq} of this new arrangement resulted in a value around two times the expected one, considering the *apparent side ratio* of NF-I-B. Table 5.3 shows the values of D_{eq} and BD_{eq} for all reduced wind velocities, and comparing the values of BD_{eq} obtained for $U/f.B = 25$ with the *apparent side ratio* $(B/D)_{ap} = 10$ of model NF-I-B, the previous statement can be verified.

As a preliminary conclusion, it can be thought that when a vertical plate installed near the leading edge is able to cancel the influences of this leading edge, the amplitude $\tilde{C}_p(x^*)$ distribution behaves as a regular rectangular cylinder whose side ratio is induced to present an *equivalent side ratio* 50% smaller than the expected *apparent side ratio*.

As for model CU-I-A, the shapes of the resulting unsteady pressure amplitude $\tilde{C}_p(x^*)$ distributions also assumed the characteristics of a *Weibull distribution*, able to be reproduced

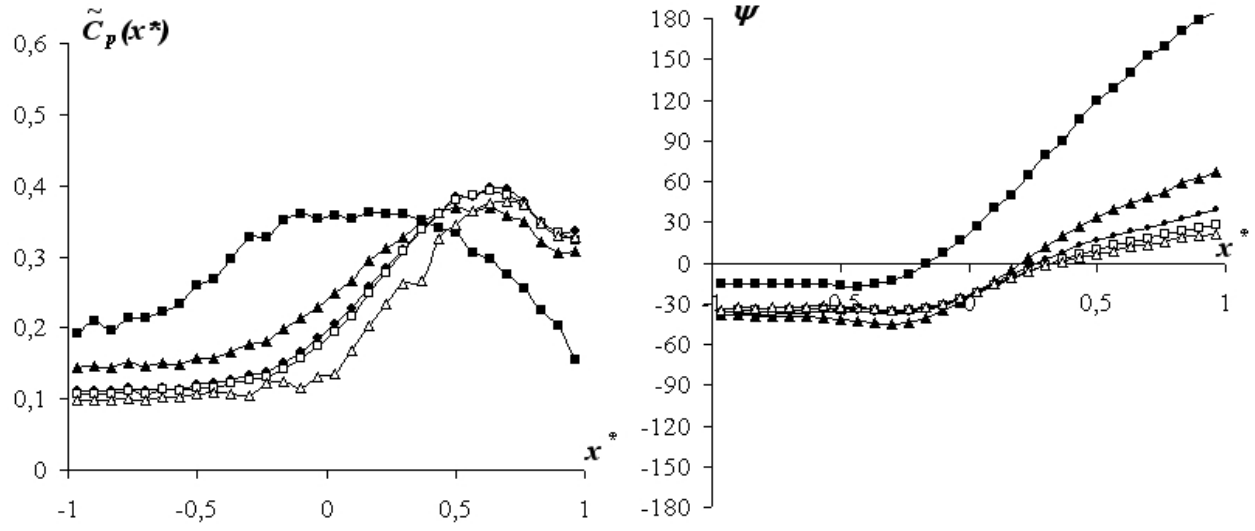

(a) Torsion

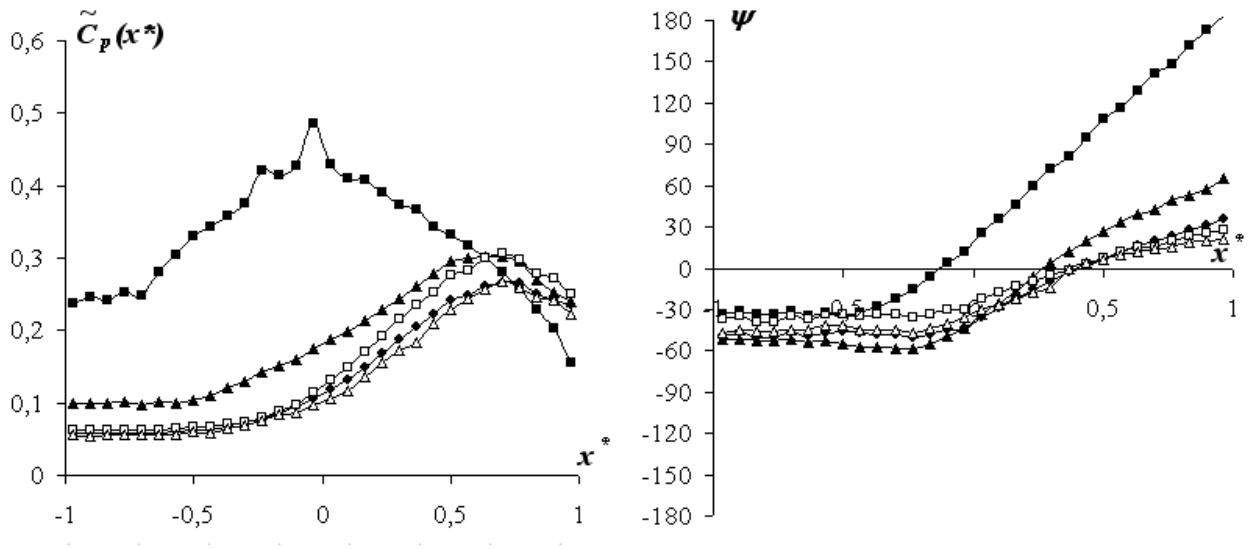

(b) Heaving

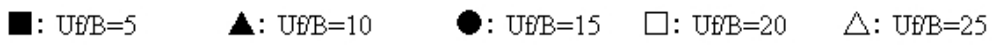

Figure 5.12: Unsteady pressure characteristics of case NF-I-B

Table 5.3: Equivalent side ratio and equivalent thickness for modified rectangular cylinders (vertical plate *height* = D in the leading edge), calculated through x_0^*= $4.4D_{eq}$

U/f.B	5		10		15		20		25	
	D_{eq}	BD_{eq}	D_{eq}	BD_{eq}	D_{eq}	BD_{eq}	D_{eq}	BD_{eq}	D_{eq}	BD_{eq}
NF in torsion	0.27	7.54	0.34	5.87	0.37	5.39	0.37	5.39	0.39	5.18
NF in heaving	0.22	9.10	0.37	5.39	0.39	5.18	0.39	5.18	0.39	5.18

with Eq.4.5; however, the parameters γ_{cp} and α_{cp} did not show concordance with the other 3 cases. Also differently from the other 3 cases, the *equivalent side ratio* assumed values close to the expected *apparent side ratio.*

These differences are related to the interactions between the flow and the separation points. Actually, the flow separated at the CU leading edge does not encounter space enough to be completely developed before reaching the vertical plate, where an additional separation point is provided. So the characteristics imposed on the unsteady pressure characteristics are more related to the topics discussed in Section 5.3 than to this section. However, the results of the calculations concerning this leading edge are also showed in this section, for comparison purposes.

As already discussed in Section 4.3, the normalized wave length λ_b is expected to have the same numerical value of the reduced wind velocity $U/f.b$, Eq.5.1, and this relationship can be used to check if the *equivalent side ratio* calculated previously in this section can also be used in the evaluation of the phase difference $\psi(x^*)$ distributions.

$$\lambda_b = \frac{2.\pi.b_{eq}}{k.b} = \frac{U}{f.b} \tag{5.1}$$

where b_{eq} is the *equivalent* half-width, which in the regular rectangular cylinders is equal to b.

Considering the values reported in Fig.5.10 and applying the relationship between

Eq.4.2 and Eq.4.5 proposed in Section 4.3, given by $\gamma_{cp}/\ \alpha_{cp}= \omega_\psi/2$, an *equivalent* value for ω_ψ is obtained for every reduced wind velocity. Assuming the reverse of the approach taken to obtain ω_ψ in that section, values of λ_{beq} can be calculated for all velocities, using the notation λ_{beq} to emphasize that the values of b_{eq} of Eq.5.1 are *equivalent* values and may vary according to the velocity. Since the wave length was related to the width of the cross-section, variations in the value of λ_b can be associated to different values of *equivalent* half-width b_{eq}, if the real values of the other parameters of Eq.5.1 are used.

The comparison between the values of λ_{beq} obtained for each velocity with the ones that would be expected, i.e. λ_b, which are numerically equivalent to the reduced wind velocity $U/f.b$, can be done by dividing the former by the later, which also provides the relationship between b_{eq} and b. So the value of the *equivalent* half-width b_{eq} of each reduced wind velocity can be isolated. By using this value, the *equivalent side ratio* BD_{eq} for all cases can be calculated, and some steps of this process are described in Table 5.4.

Table 5.4: Equivalent side ratios for modified rectangular cylinders (vertical plate with $height = D/2$), calculated through ω_ψ

		Torsion				Heaving			
U/f.B		NF-I-A	SC-I-A	CD-I-A	CU-I-A	NF-I-A	SC-I-A	CD-I-A	CU-I-A
5	λ_{beq}	3.15	3.45	3.18	4.7	3.26	3.57	3.15	4.62
	b_{eq}/b	0.31	0.35	0.32	0.47	0.33	0.36	0.31	0.46
	BD_{eq}	6.29	6.90	6.37	9.4	6.52	7.13	6.29	9.23
10	λ_{beq}	6.42	6.6	6.11	9.79	6.26	6.42	5.96	9.68
	b_{eq}/b	0.32	0.33	0.31	0.49	0.31	0.32	0.30	0.48
	BD_{eq}	6.42	6.6	6.11	9.79	6.26	6.42	5.96	9.68
15	λ_{beq}	9.31	9.96	9.34	14.5	8.91	9.86	9.12	13.48
	b_{eq}/b	0.31	0.33	0.31	0.48	0.30	0.33	0.30	0.45
	BD_{eq}	6.21	6.64	6.22	9.67	5.94	6.57	6.08	8.99
20	λ_{beq}	12.83	13.37	9.34	20.05	12.17	12.83	11.73	20.37
	b_{eq}/b	0.32	0.33	0.32	0.50	0.30	0.32	0.29	0.51
	BD_{eq}	6.42	6.68	6.37	10.03	6.08	6.42	5.87	10.19
25	λ_{beq}	16.53	17.22	15.69	26.86	15.01	16.81	14.66	26.16
	b_{eq}/b	0.33	0.34	0.31	0.54	0.30	0.34	0.29	0.52
	BD_{eq}	6.61	6.89	6.28	10.74	6.00	6.72	5.87	10.46

With the increase of the reduced wind velocity, the values of BD_{eq} of Table 5.2 ap-

proach the values of Table 5.4, which show themselves more stable throughout the entire velocity range. This tendency of agreement that even for the modified cross sections investigated in this section the relationship between amplitude $\tilde{C}_p(x^*)$ and phase difference $\psi(x^*)$ distributions through the wave length still holds, becoming an important information to be used in the manipulation of the unsteady pressure characteristics of bridge decks.

Analyzing graphically the shapes of the phase difference $\psi(x^*)$ distributions of Fig.5.2 to Fig.5.5, it can be said that as a general tendency the vertical plate at the leading edge induces a kind of *scale amplification* on them, as if magnifying lens were being used near the leading edge. Comparing them to the cases without vertical plate, Fig.4.10 to Fig.4.13 in Section 4.3, the same *amplitude* A_ψ (vide Section 4.3.1) is kept; however, the lengths in which the curves are developed are elongated, which implies in transferring the crossing point x_1^* to downstream. In terms of Eq.4.2, this phenomenon can be obtained through a reduction of the value of ω_ψ, confirming the conclusions of Table 5.4, and through an adjustment of ϕ_ψ to a suitable value, which is discussed in the next lines.

For NF-I-A, SC-I-A and CD-I-A, in which the same size of vertical plate was used (Fig.5.2, Fig.5.3 and Fig.5.4), the impacts of the vertical plate on the phase difference distribution were very similar. Similarly to the comparison between the amplitude $\tilde{C}_p(x^*)$ distributions of rectangular cylinders with side ratios B/D=5 and B/D=7.5 and the ones provided by the NF-I-A in torsion, as shown in Fig.5.11, the phase difference $\psi(x^*)$ distributions of the same models also indicate similarities, as shown in Fig.5.13. It is shown that the phase difference distributions of NF-I-A is comparable to a rectangular cylinder with side ratio B/D between 6 and 7, which is nearly the same result obtained for the $\tilde{C}_p(x^*)$ distribution.

With the values of A_ψ and ω_ψ already checked, only ϕ_ψ of Eq.4.2 remains to be defined. Consulting the phase difference $\psi(x^*)$ distributions of model NF, Fig.4.10, it is observed that all curves cross the x axis almost at the same point x_1^*, which is around $\Delta x^*= 0.22$ from the leading edge in the torsional system and around $\Delta x^*= 0.25$ from the leading edge in the heaving system. For NF-I-A, with the exception of the lowest wind reduced velocity (U/f.B=5), all curves also cross the x axis almost at the same point x_1^*, around $\Delta x^*= 0.70$ in the torsional system and around $\Delta x^*= 0.80$ in the heaving system. These values keep the same 1/3 proportionality presented between the *equivalent side ratio* and the actual side ratio. From these assumptions and considering the crossing point x_1^* as a reference for 90° and the value of ω_ψ, the values for ϕ_ψ can be calculated.

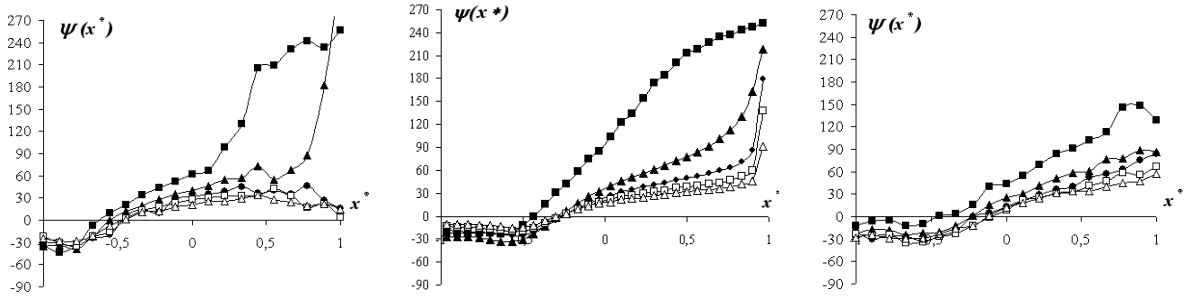

(a) B/D=5 in torsion,(adapted from [3])

(b) NF-I-A in torsion

(c) B/D=7.5 in torsion,(adapted from [3])

Figure 5.13: Comparison between phase difference $\psi(x^*)$ distributions of rectangular cylinders with side ratios B/D=5, B/D=7.5 and the NF-I-A case in torsion

Checking the same assumptions for NF-I-B, whose vertical plate has the double of the size of NF-I-A, the conclusions are similar; even though the *apparent side ratio* is $(B/D)_{ap} = 10$, the *equivalent side ratio* is induced to present half of this value, Table 5.5.

Table 5.5: Equivalent side ratios for modified rectangular cylinders (vertical plate with $height = D$), calculated through ω_ψ

U/f.B		Torsion	Heaving
5	λ_{beq}	2.50	2.52
	b_{eq}/b	0.25	0.25
	BD_{eq}	5.00	5.04
10	λ_{beq}	5.09	4.94
	b_{eq}/b	0.25	0.25
	BD_{eq}	5.09	4.94
15	λ_{beq}	7.86	7.56
	b_{eq}/b	0.26	0.25
	BD_{eq}	5.24	5.04
20	λ_{beq}	10.26	9.97
	b_{eq}/b	0.26	0.25
	BD_{eq}	5.13	4.99
25	λ_{beq}	12.73	12.56
	b_{eq}/b	0.25	0.25
	BD_{eq}	5.09	5.03

From a simplistic point of view, the approaching flow "sees" the shape of the leading edge of NF-I-A and NF-I-B the same way it would "see" a regular rectangular cylinder, since only a vertical surface is found in its trajectory, composed by the thickness of the cylinder plus the height of the vertical plate. However, after the separation point, the flow encounters a void space between this separation point and the upper surface of the model, and this void space is responsible for changing the whole flow structure of the afterbody.

A vertical plate installed at the leading edge of a rectangular cylinder is responsible for changing the wave length of the flow around this body, which is "understood" by the wind as a rectangular cylinder with different side ratio. In the cases studied in this section, this *equivalent side ratio* is the result of an *apparent side ratio* divided by 2, and this relationship proved itself to be very consistent in terms of unsteady pressure characteristics, which were able to be fully reproduced with the formulation proposed in Section 4.3. Based on that, a way towards the control of the unsteady pressure characteristics of bridge decks through the control and manipulation of the wave length developed along its surface may be pointed out.

5.3 Vertical plates along the chord direction

In order to evaluate the effects of separation points and blockages along the chord direction, vertical plates were installed at different locations – IV, VI and VII according to Fig.5.1 – on the model‘s upper surface. The unsteady pressure characteristics of the rectangular cylinders with different leading edges submitted to forced torsional and heaving harmonic oscillations were measured, Fig.5.14 to Fig.5.25, and compared with the cases studied in Chapter 4 (rectangular cross-sections without vertical plate).

Although the locations of the inflection points of the distributions vary among the different configurations of models, the impacts of the vertical plate on the unsteady pressure characteristics of each model, in terms of shape and general tendencies, were similar in both heaving and torsional systems, for all configurations.

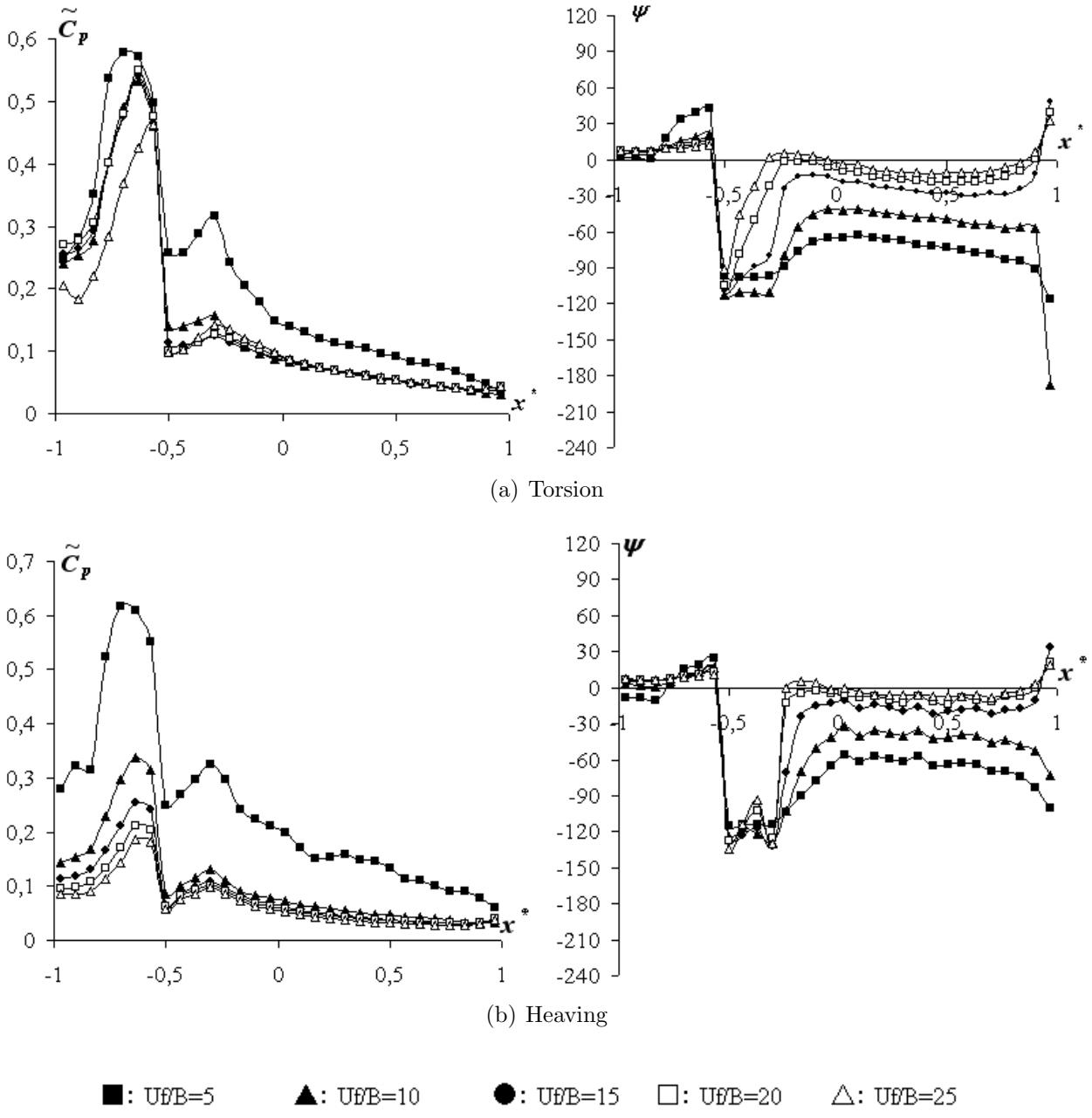

Figure 5.14: Unsteady pressure characteristics of case NF-IV-A

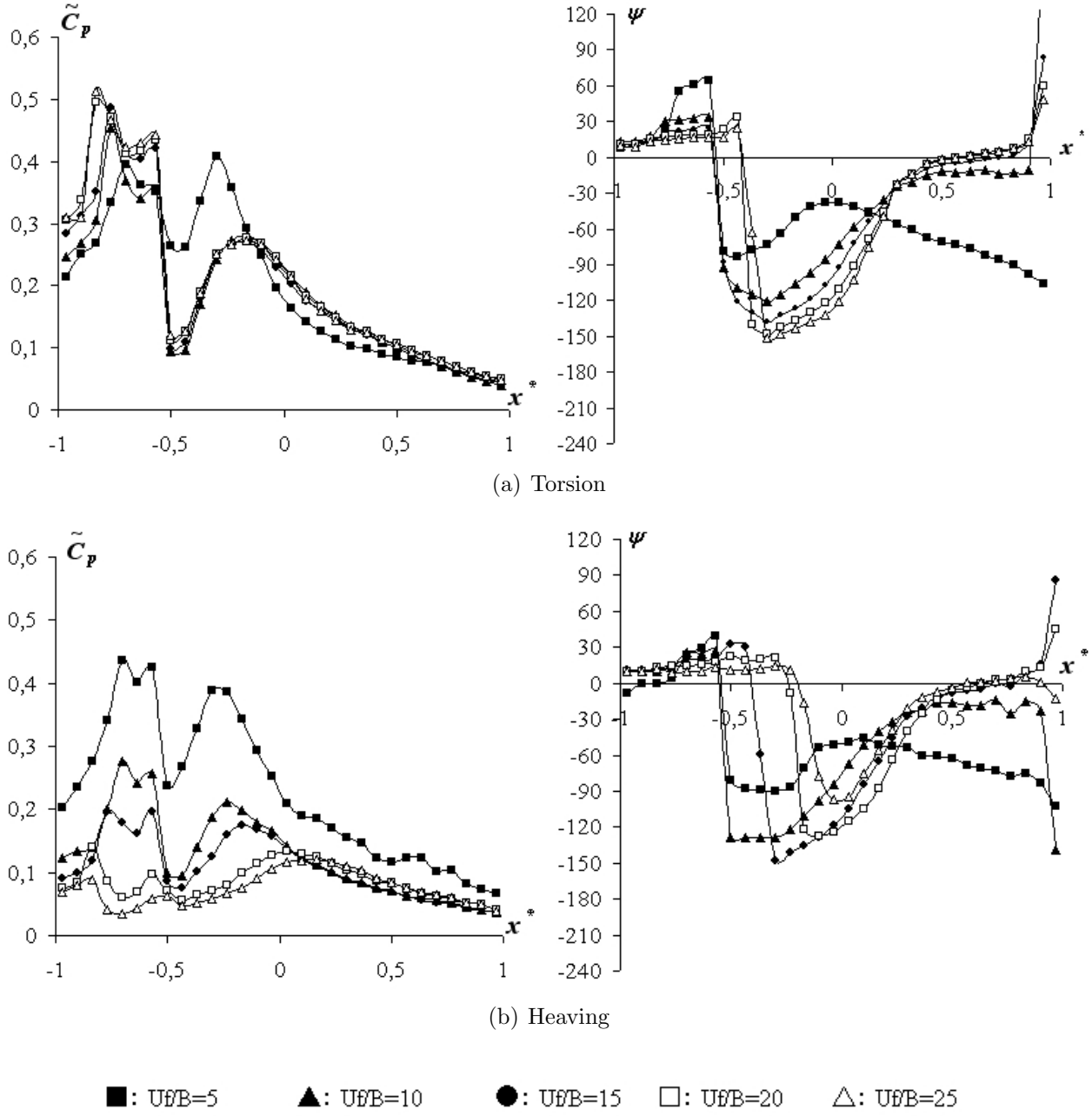

Figure 5.15: Unsteady pressure characteristics of case SC-IV-A

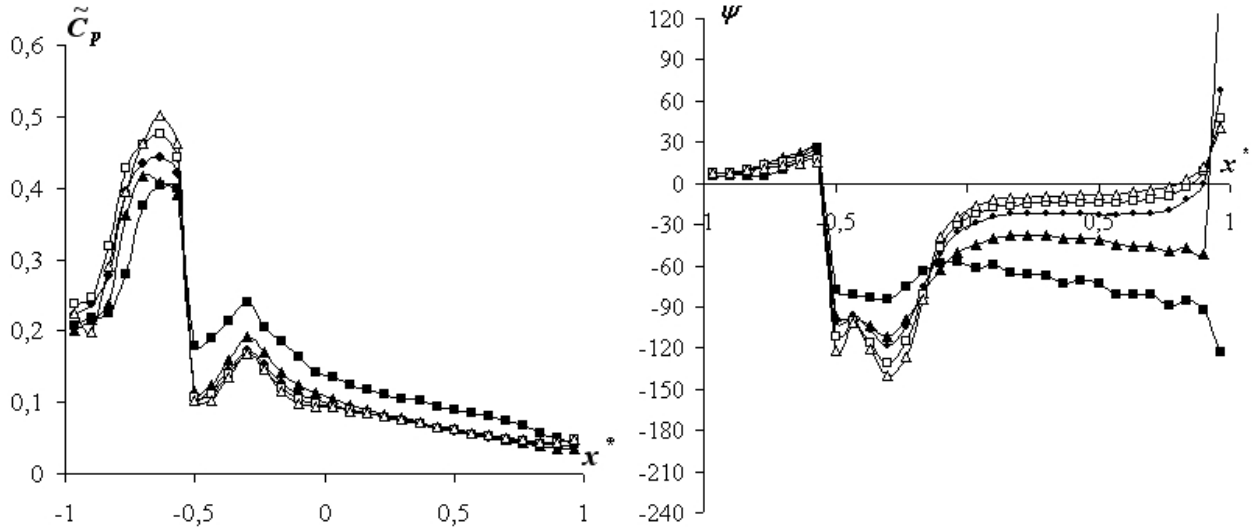

(a) Torsion

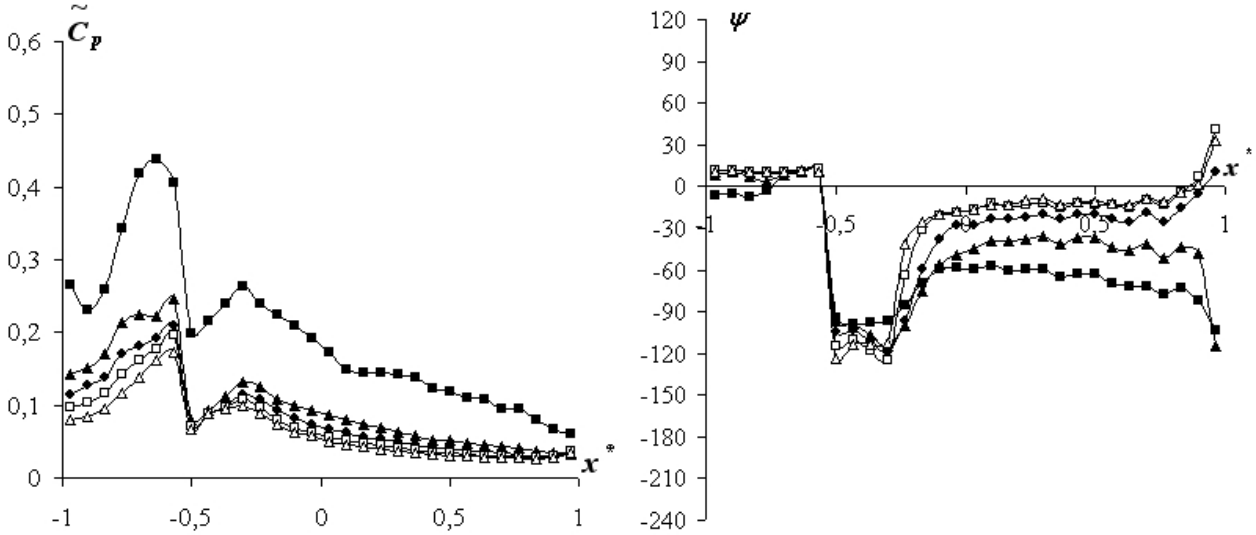

(b) Heaving

■: U/fB=5 ▲: U/fB=10 ●: U/fB=15 □: U/fB=20 △: U/fB=25

Figure 5.16: Unsteady pressure characteristics of case CD-IV-A

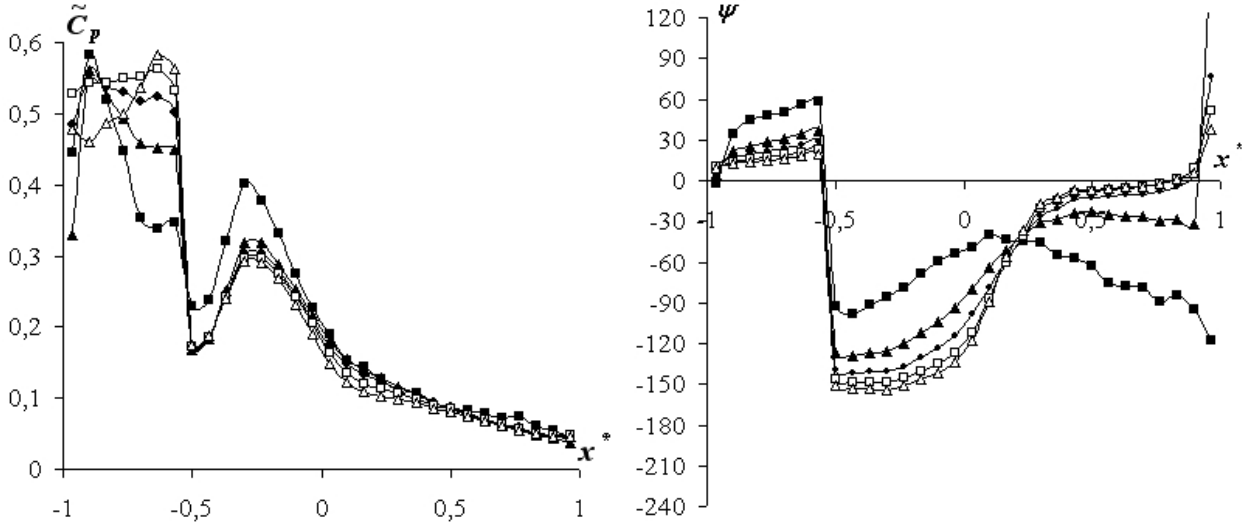

(a) Torsion

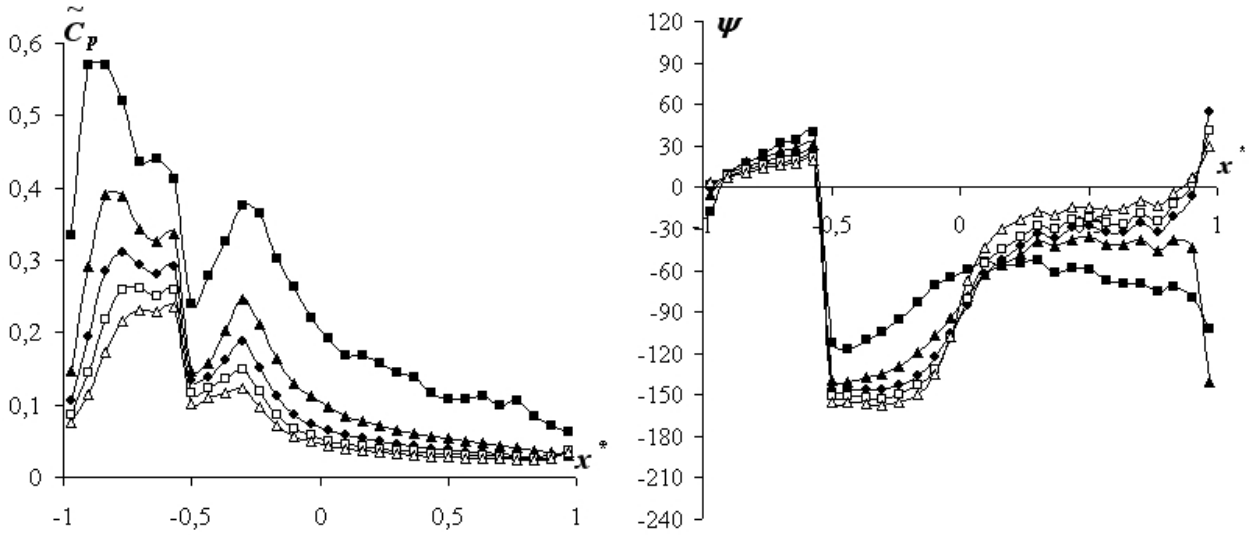

(b) Heaving

■: U/B=5 ▲: U/B=10 ●: U/B=15 □: U/B=20 △: U/B=25

Figure 5.17: Unsteady pressure characteristics of case CU-IV-A

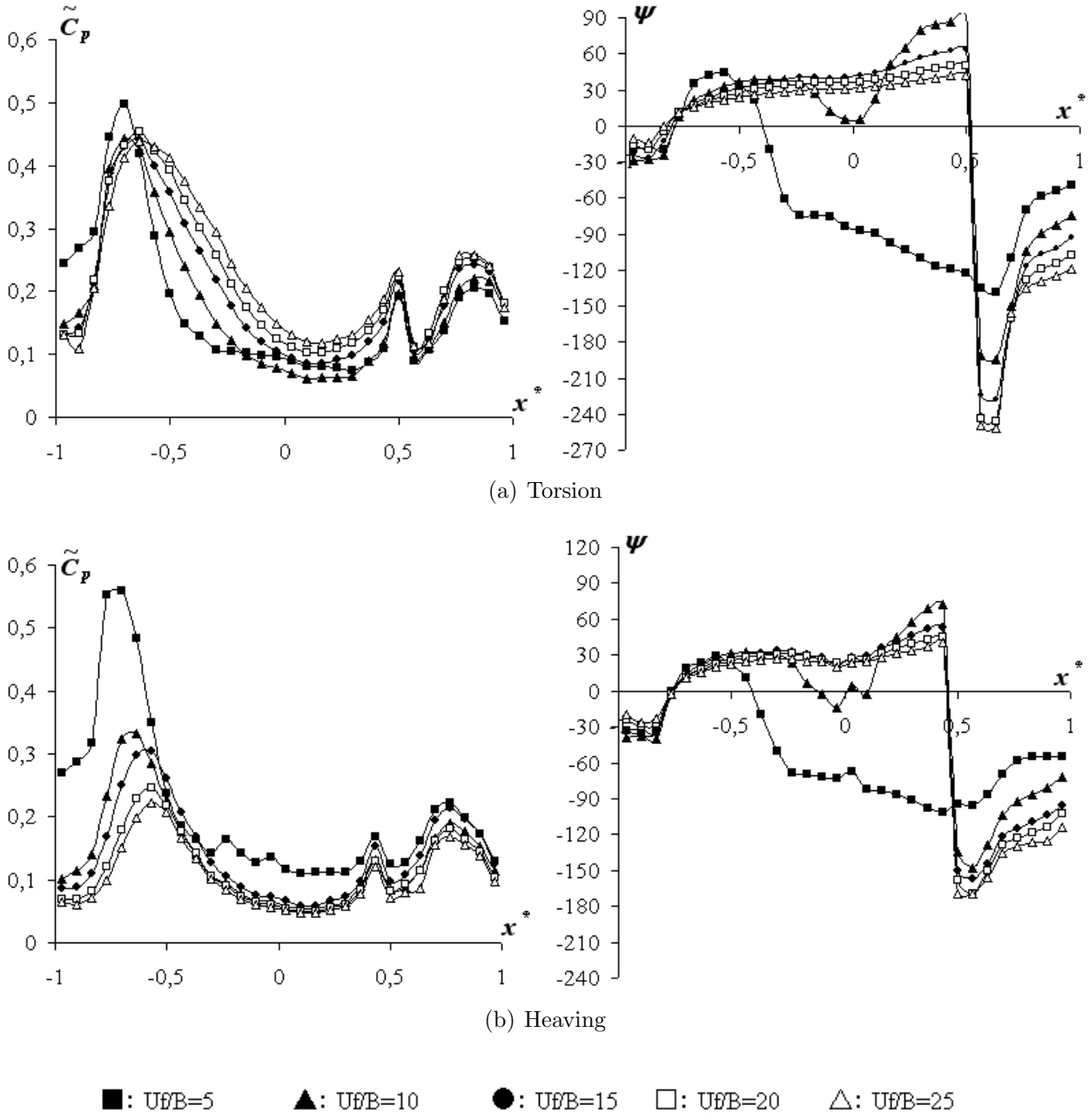

Figure 5.18: Unsteady pressure characteristics of case NF-VI-A

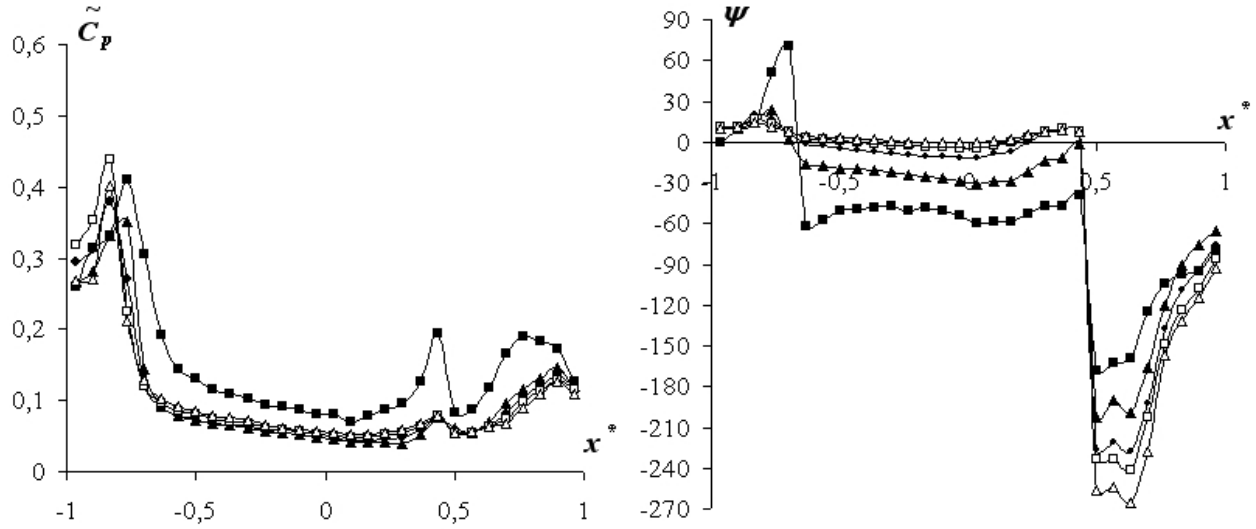

(a) Torsion

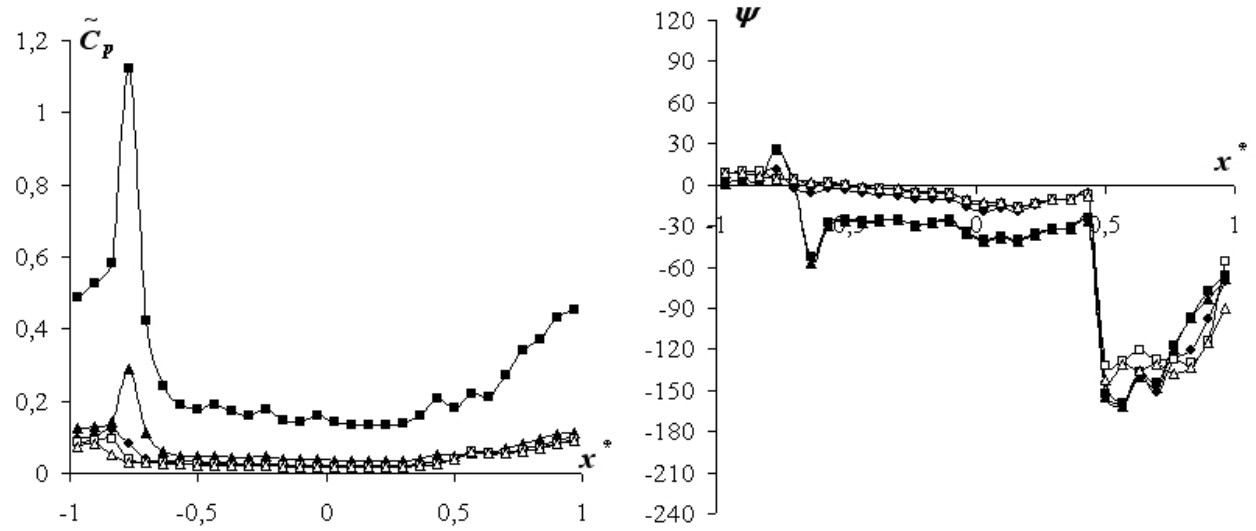

(b) Heaving

■: Uf/B=5 ▲: Uf/B=10 ●: Uf/B=15 □: Uf/B=20 △: Uf/B=25

Figure 5.19: Unsteady pressure characteristics of case SC-VI-A

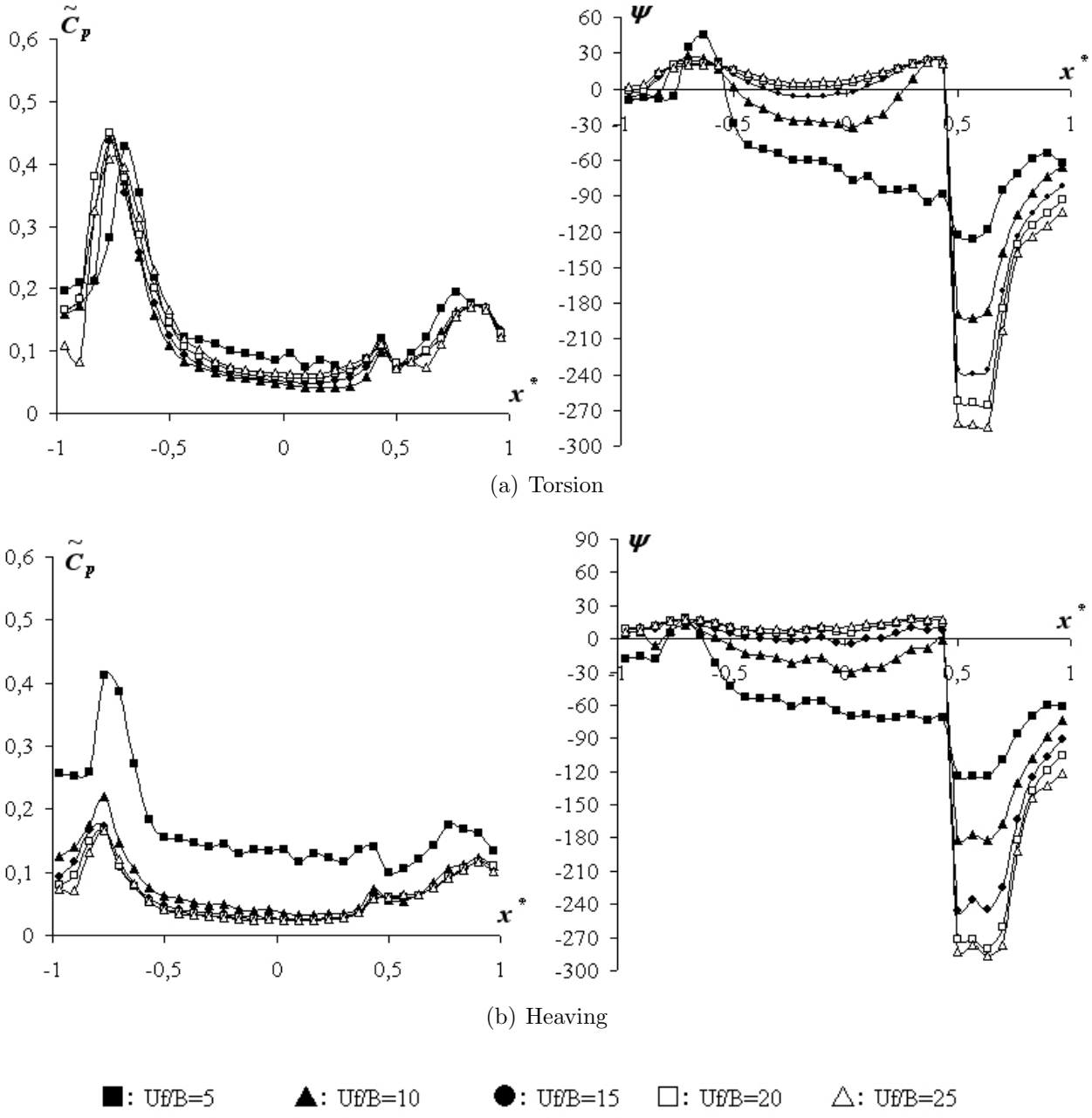

Figure 5.20: Unsteady pressure characteristics of case CD-VI-A

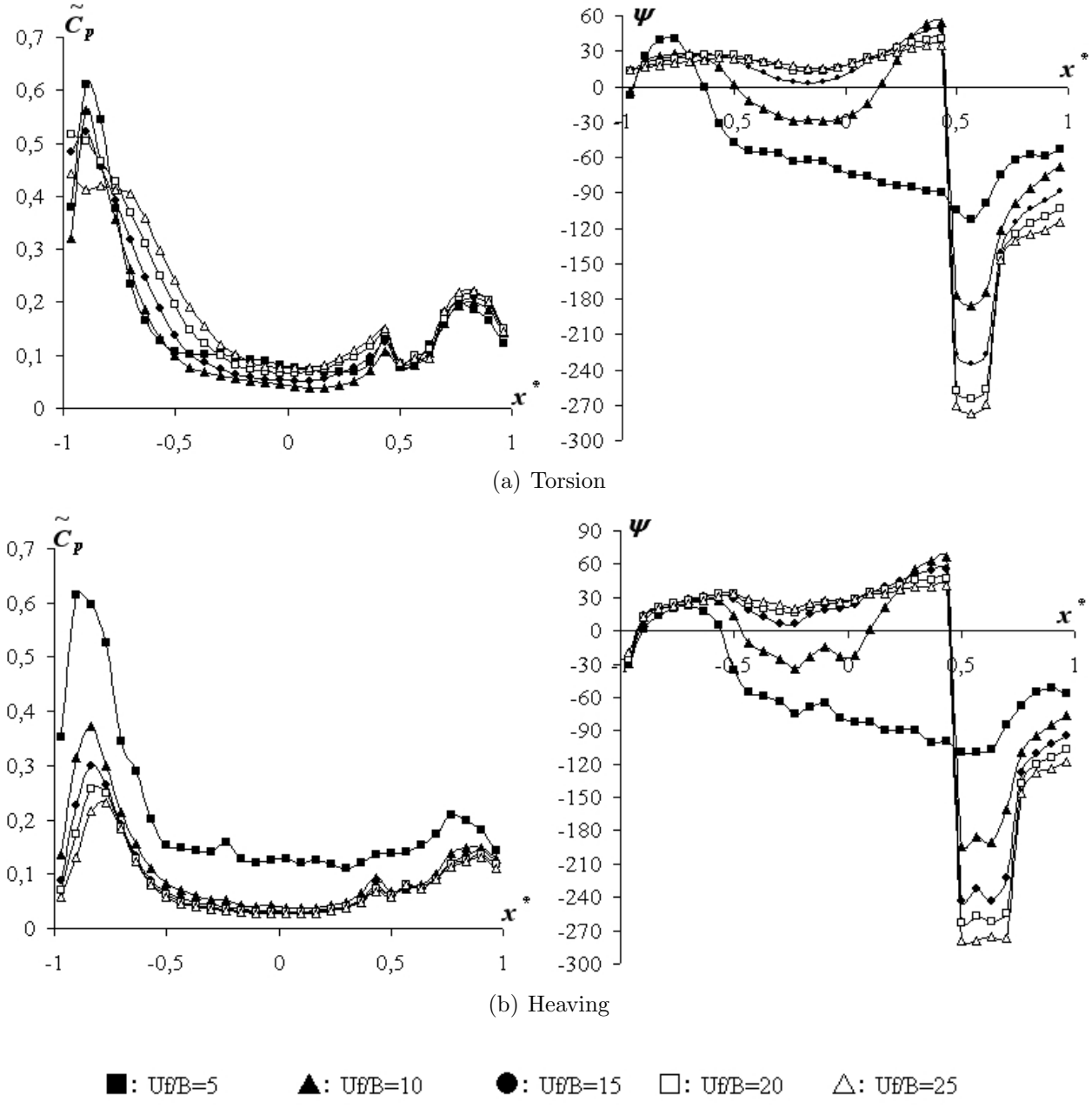

(a) Torsion

(b) Heaving

Figure 5.21: Unsteady pressure characteristics of case CU-VI-A

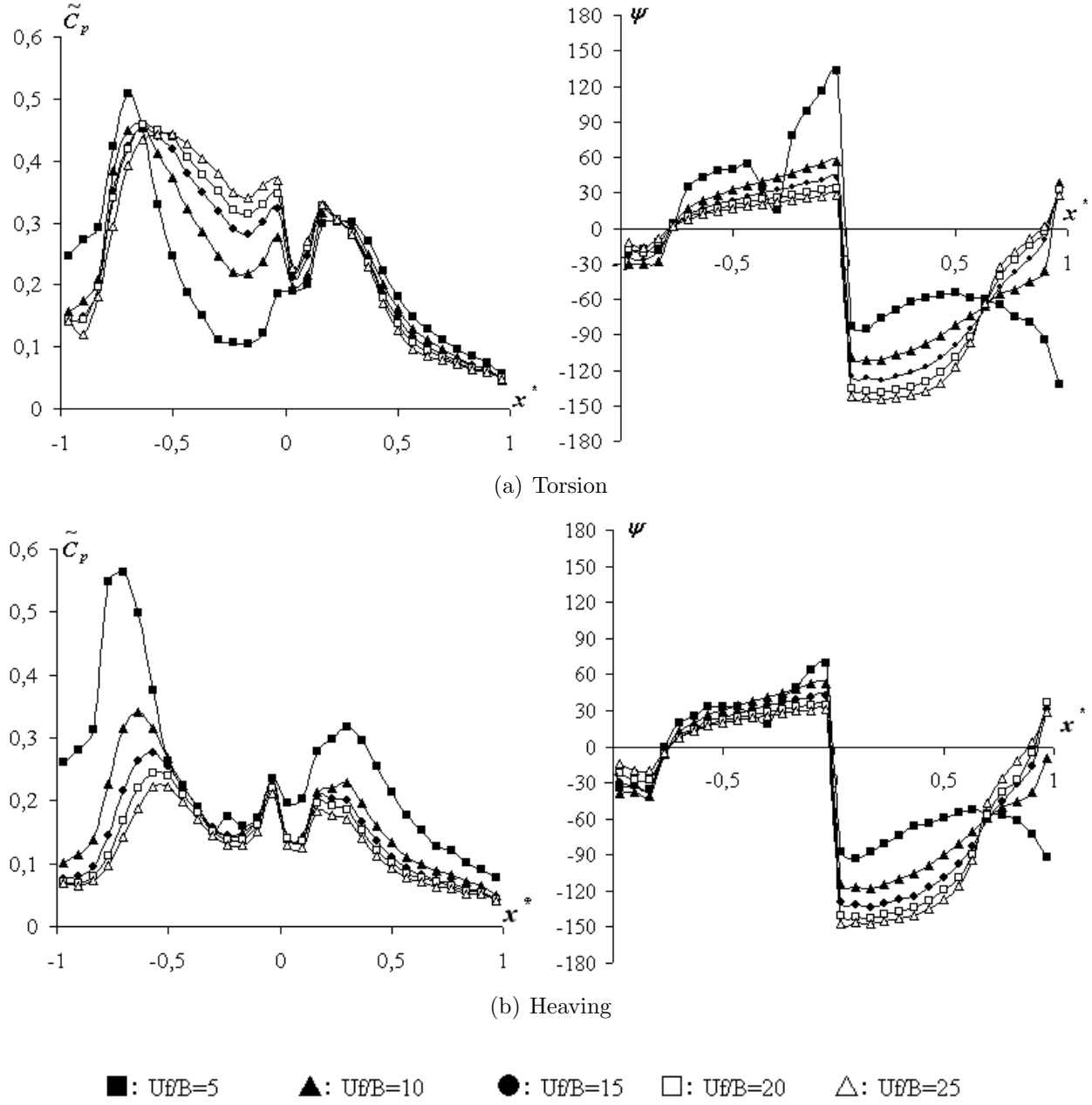

Figure 5.22: Unsteady pressure characteristics of case NF-VII-A

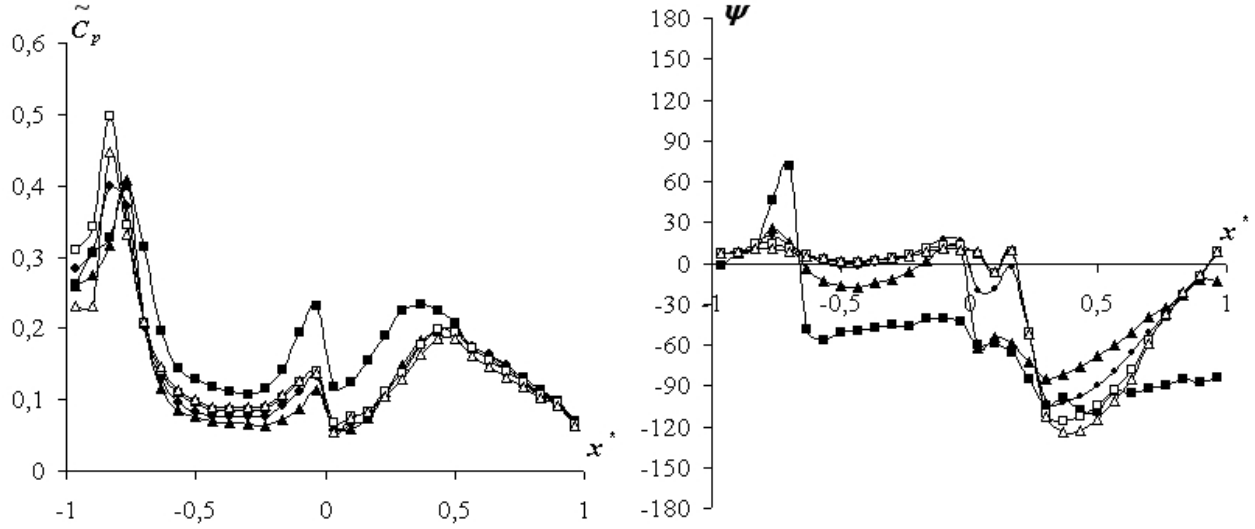

(a) Torsion

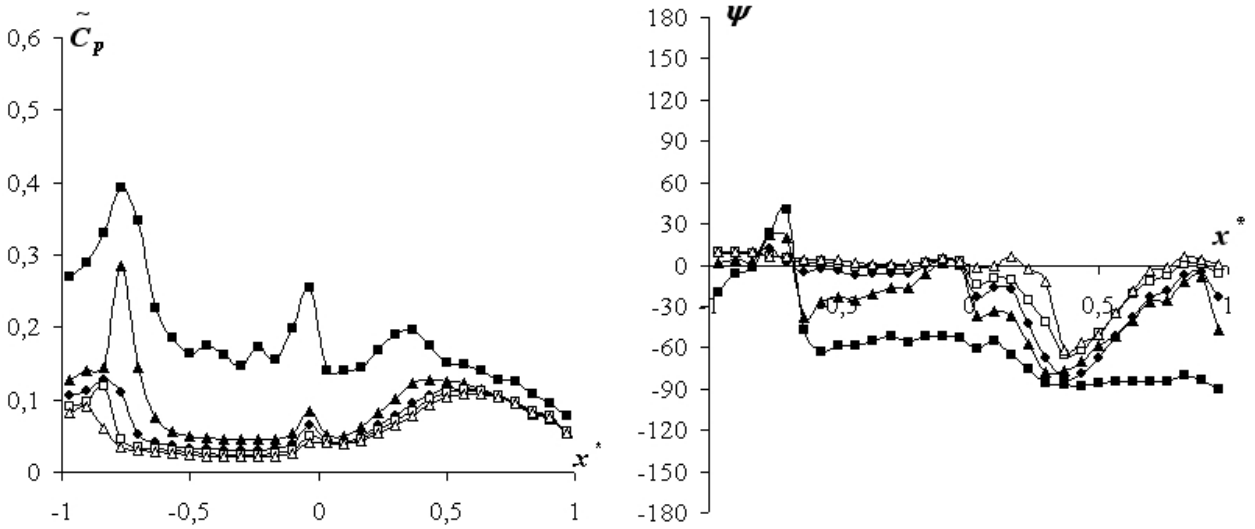

(b) Heaving

■: Uf/B=5 ▲: Uf/B=10 ●: Uf/B=15 □: Uf/B=20 △: Uf/B=25

Figure 5.23: Unsteady pressure characteristics of case SC-VII-A

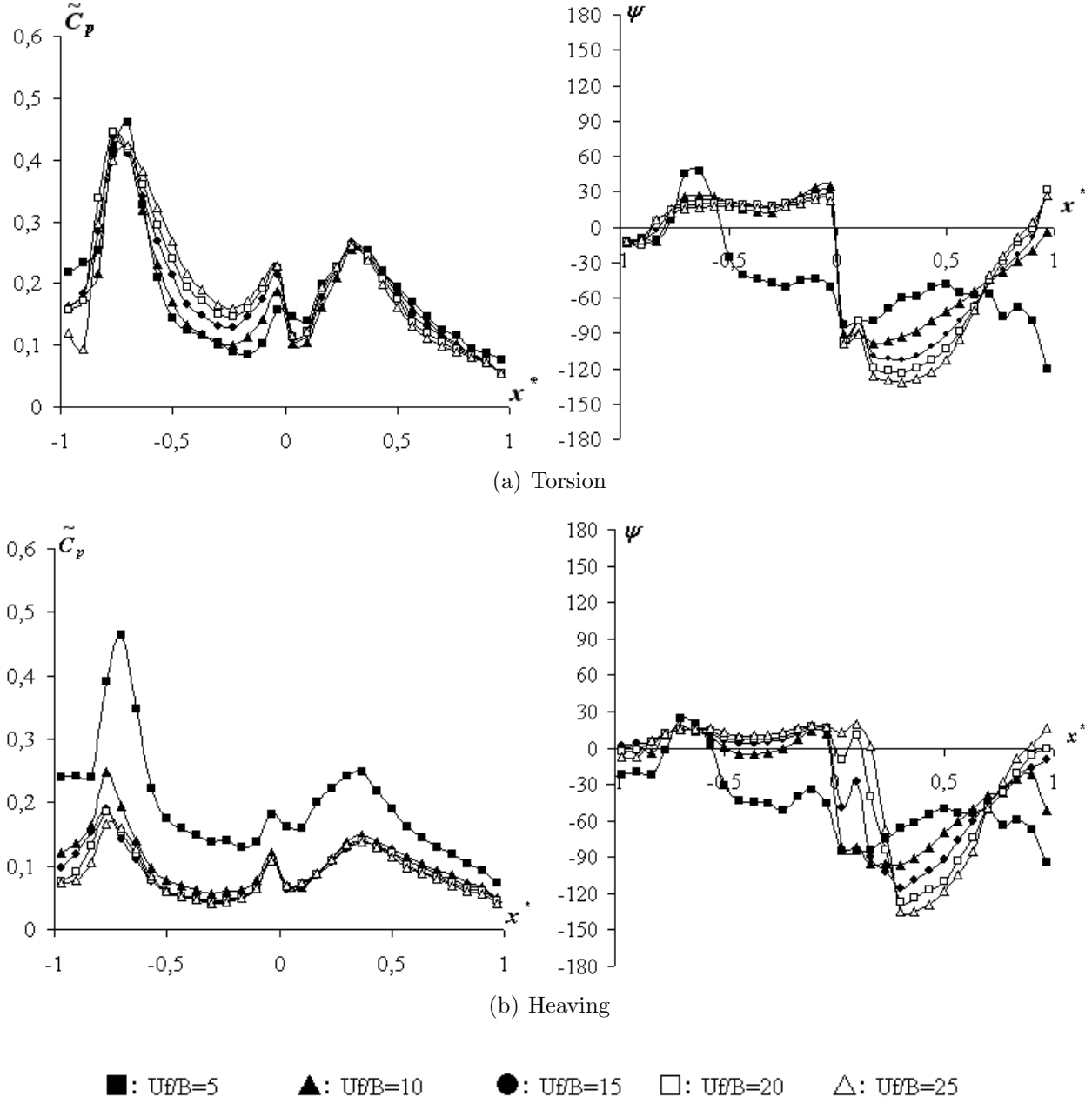

Figure 5.24: Unsteady pressure characteristics of case CD-VII-A

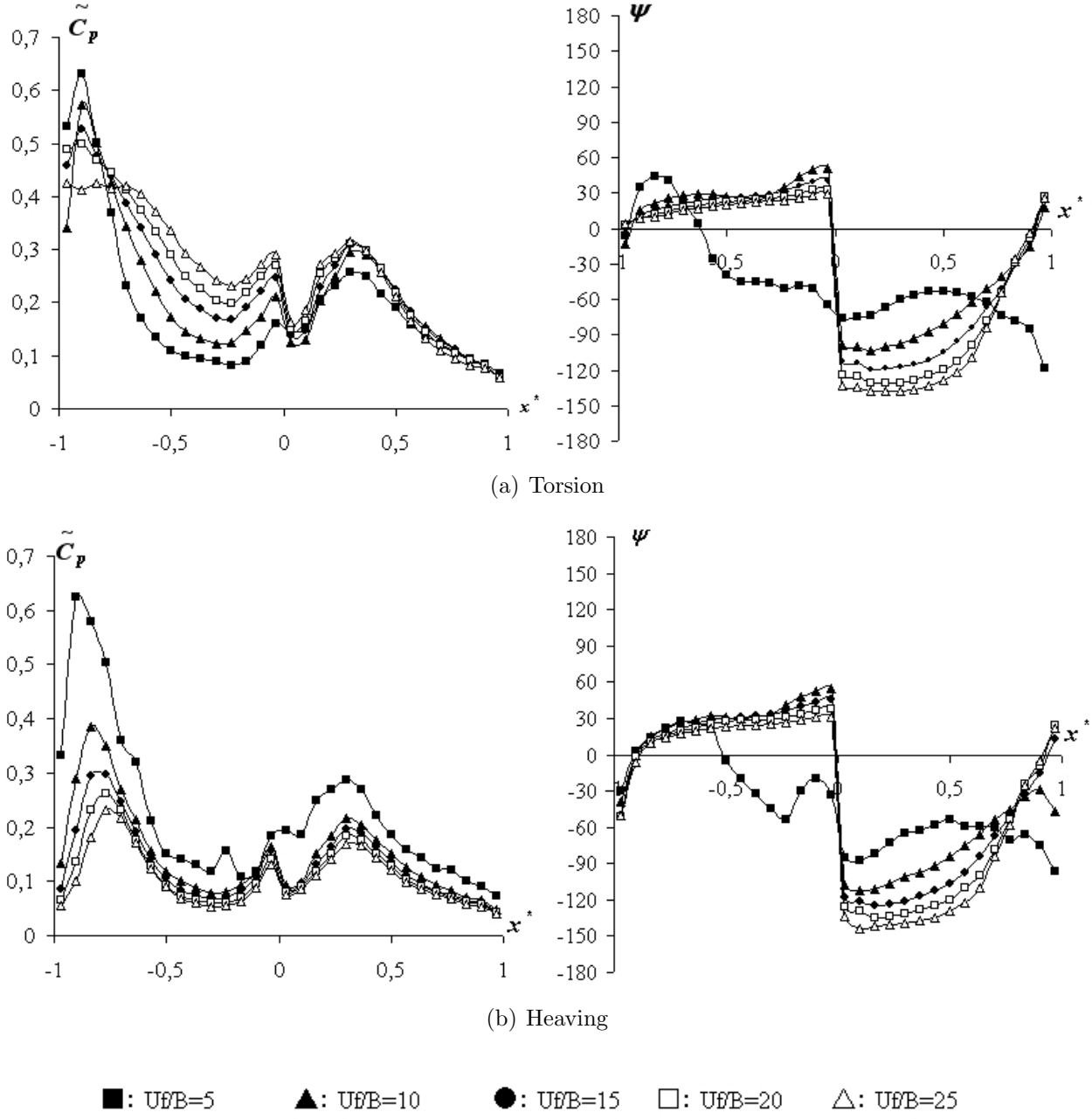

Figure 5.25: Unsteady pressure characteristics of case CU-VII-A

The presence of vertical plates on the upper surface of the models was "felt" both upstream and downstream their locations, mostly by the phase difference $\psi(x^*)$ distributions, with higher impacts on their downstream region due to the flow separation caused by their presence. Upstream the vertical plate the flow is blocked, and the recirculation created by this blockage increases the level of the fluctuating components of the pressure signal, being translated into a broadening of the amplitude $\tilde{C}_p(x^*)$ distributions, which is emphasized with the increase of the wind velocity.

The effects of the vertical plate on the amplitude $\tilde{C}_p(x^*)$ distribution can be summarized by the presence of 2 peaks: one at the location of the vertical plate and another downstream its location. From the upstream side, before reaching the first peak, the curves of the amplitude $\tilde{C}_p(x^*)$ distributions radically invert their decaying tendencies as they approach the vertical plate, and start going up towards the first peak. This is the first *symptom* of the existence of the vertical plate, caused by the blockage of the flow which is forced to recirculate (circulatory flow). This effect showed itself to be more prominent in models that had vertical plates installed far away enough from the reattachment of the flow separated at the leading edge, i.e. cases VI and VII. So the flow is separated at the vertical plate, inducing a valley followed by a recovering of the ascendant tendency until finally reaching the second peak, with a value of $\tilde{C}_p(x^*)$ that, despite being dependent on the position of the vertical plate, is always larger than the peak produced in the separation point provided by the vertical plate.

Comparing the distributions obtained with models VI and VII (Fig.5.18 to Fig.5.25) with their corresponding configurations without vertical plate (Fig.4.10 to Fig.4.13) and assuming the location of the vertical plate as the reference point, it is noticed that the amplitude $\tilde{C}_p(x^*)$ distributions start the inversion of the decaying tendency (upstream the vertical plate) at a position nearly symmetric to the location of the peak induced downstream the vertical plate. This last peak can be associated to the reattachment of the flow separated by the vertical plate and both distances vary among the models, showing a dependence on the flow conditions at the location where the plate is installed. The distances in the heaving system tend to be longer than the ones of the torsional system, but in average they are around $\Delta x^* = 0.3$ in non-dimensional units for cases VII and $\Delta x^* = 0.4$ for cases VI.

When the vertical plate is installed near the reattachment point of the flow separated by the leading edge, i.e. case IV, the behavior is different; the peak upstream the vertical plate is superimposed to the peak induced by the leading edge, enhancing its effects, and the peak downstream is weaker and located at a shorter distance from the vertical plate,

compared to the previous cases, VI and VII. This is a consequence of the high vorticity existent in that region, in a scale larger than the size of the vertical plate, so the influences of the vertical plate get proportionally reduced.

As a general tendency, the potentiality of a vertical plate of inducing peaks on the unsteady pressure amplitude $\tilde{C}_p(x^*)$ distribution showed itself to be directly related to the conditions of the flow in its upstream, in terms of proximity to reattachment points and levels of $\tilde{C}_p(x^*)$. A visual analysis of Fig.5.14 to Fig.5.25 shows that the values of $\tilde{C}_p(x^*)$ reached by the peaks promoted by the vertical plate are inside an envelope that follows a decaying tendency with the increase of the distance from the leading edge, resulting in that the farther away the vertical plate is from the leading edge, the weaker the peak is, but always showing a difference between peaks and valleys in the range of $\Delta\tilde{C}_p$ from *0.1* to *0.2*.

In the case of the phase difference $\psi(x^*)$ distribution, the presence of the vertical plate is "felt" more upstream than the amplitude distribution does, at a distance around 70% longer from the vertical plate. The deceleration of flow caused by the blockage is translated into the maintenance of the positive values, which are forced to become even more positive as if a *bias* was introduced into the distribution.

Downstream the separation point the flow is accelerated, and this acceleration is translated into a "jump" to the negative side in the phase difference $\psi(x^*)$ distribution. The magnitude of this jump varies among the configurations and presents an increasing tendency with the increase of both reduced wind velocity and distance from the leading edge. The approximate values for each case studied in this section are summarized in Table 5.6.

Downstream the negative peak promoted by the jump, the phase difference $\psi(x^*)$ distribution shows the tendency to gradually recover its positive values.

Similar phenomenon has already been observed in more complex cross-sections, as the case of two-box girders with a vertical plate in the middle of the gap [6], Fig.5.26. In reference [6] the vertical plate had a height of $D/2$ from the upper surface of the model and, similarly to cases VII and VI, was located outside the separation bubble induced by the leading edge. The cross-section was composed by two $B^*/D = 5$ rectangular cylinders, i.e. two-box cross-sections, modified by triangular fairings in both leading and trailing edges of the resulting cross-section, with a gap length equivalent to $0.5B^*$, where B^* is the width of each individual cylinder.

Table 5.6: "Jump" in phase difference $\psi(x^*)$ distribution induced by vertical plate with height=D/2

U/f.B	5		10		15		20		25	
	Torsion	Heaving	Torsion	Heaving	Torsion	Heaving	Torsion	Heaving	Torsion	Heaving
NF-IV	140°	140°	134°	141°	126°	143°	118°	141°	104°	146°
NF-VII	216°	157°	166°	167°	167°	172°	169°	175°	171°	178°
NF-VI	−−°	−−°	284°	207°	288°	202°	293°	203°	292°	210°
SC-IV	148°	110°	143°	153°	145°	179°	181°	144°	176°	89°
SC-VII	−−°	37°	96°	61°	99°	83°	119°	67°	122°	54°
SC-VI	129°	129°	201°	128°	234°	138°	241°	125°	264°	134°
CU-IV	151°	153°	163°	171°	168°	172°	169°	173°	170°	175°
CU-VII	−−°	−−°	150°	162°	154°	163°	157°	164°	162°	165°
CU-VI	22°	−−°	231°	261°	274°	299°	298°	311°	305°	321°
CD-IV	104°	107°	121°	108°	123°	117°	130°	128°	138°	133°
CD-VII	−−°	39°	125°	94°	122°	62°	124°	80°	121°	131°
CD-VI	35°	53°	214°	182°	260°	254°	283°	286°	301°	300°

Despite the fact that the aerodynamic conditions generated at the surroundings of the vertical plate in that model are expected to be fairly different from the ones in the vicinities of the vertical plates of the cases studied in this section, the effects on the phase difference $\psi(x^*)$ distribution were similar, characterized by a jump to the negative side with a magnitude similar to the cases of Table 5.6, associated to a recovering tendency downstream the jump. The impacts, however, were different comparing torsional and heaving systems, what was explained by the effects of the torsional velocity of the vertical plate on the flow field in the torsional motion, which does not happen in the heaving motion.

From the results above, it is concluded that the influences of the vertical plate depend on the characteristics of the flow in its upstream, and this dependence seems to get reduced with the increase of the reduced wind velocity. In order to have an insight on the dependence of these influences on the size of the vertical plate, a plate with double of the size, i.e. D,

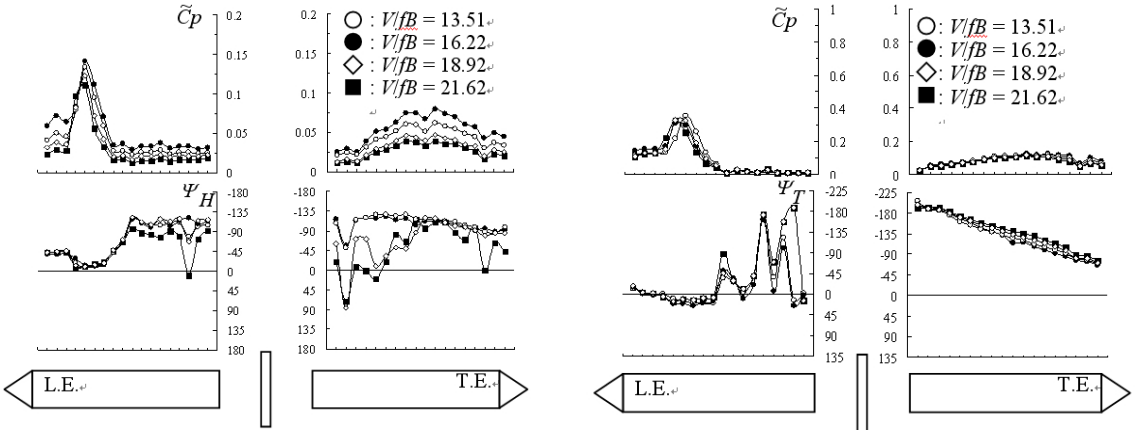

(a) Heaving (b) Torsion

Figure 5.26: Vertical plate in the gap, extracted from [6]

was installed in the model NF at the locations IV, VI and VII and the resulting unsteady pressure characteristics (Fig.5.27 to Fig.5.29) were analyzed by comparing them with the previous cases.

Although some dependence on the location of the vertical plate can be noticed, the results show the same general tendencies of the models with vertical plate of size A. In comparison with models NF-IV-A and NF-VII-A, models NF-IV-B and NF-VII-B exhibited an enhancement of the effects of the vertical plate; the inflection points located downstream the vertical plates in the unsteady pressure amplitude $\tilde{C}_p(x^*)$ distributions were moved to locations around the double of the distance in comparison with the cases with vertical plate of size A, showing a direct proportionality between size of vertical plate and location of peaks. Also, a slight increase on the values of the peaks $\tilde{C}_{pmax}$ is noticed. Upstream the vertical plate, although the effects were hidden by the peak originated at the separation point provided by the leading edge, an enhancement of the effects is also noticed, with a broadening of the distributions associated to the increasing of the reduced wind velocity.

In the phase difference $\psi(x^*)$ distribution, the "jump" was also slightly increased, accompanied by a increasing in the distance where the influence of the vertical plates starts to be felt upstream. Downstream the vertical plate, the recovering tendency is softened, and the negative values induced by the vertical plate are kept for a longer distance.

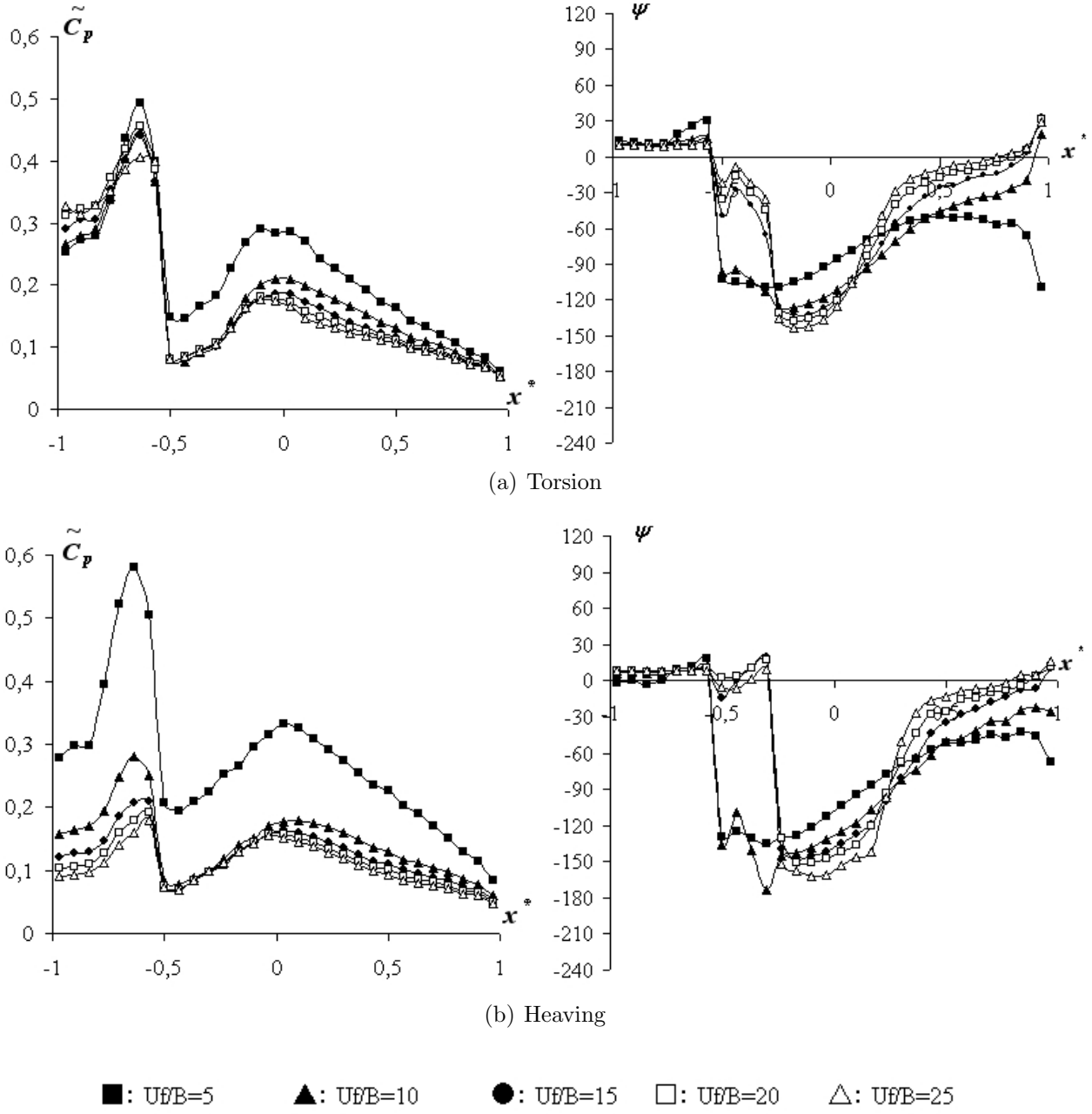

Figure 5.27: Unsteady pressure characteristics of case NF-IV-B

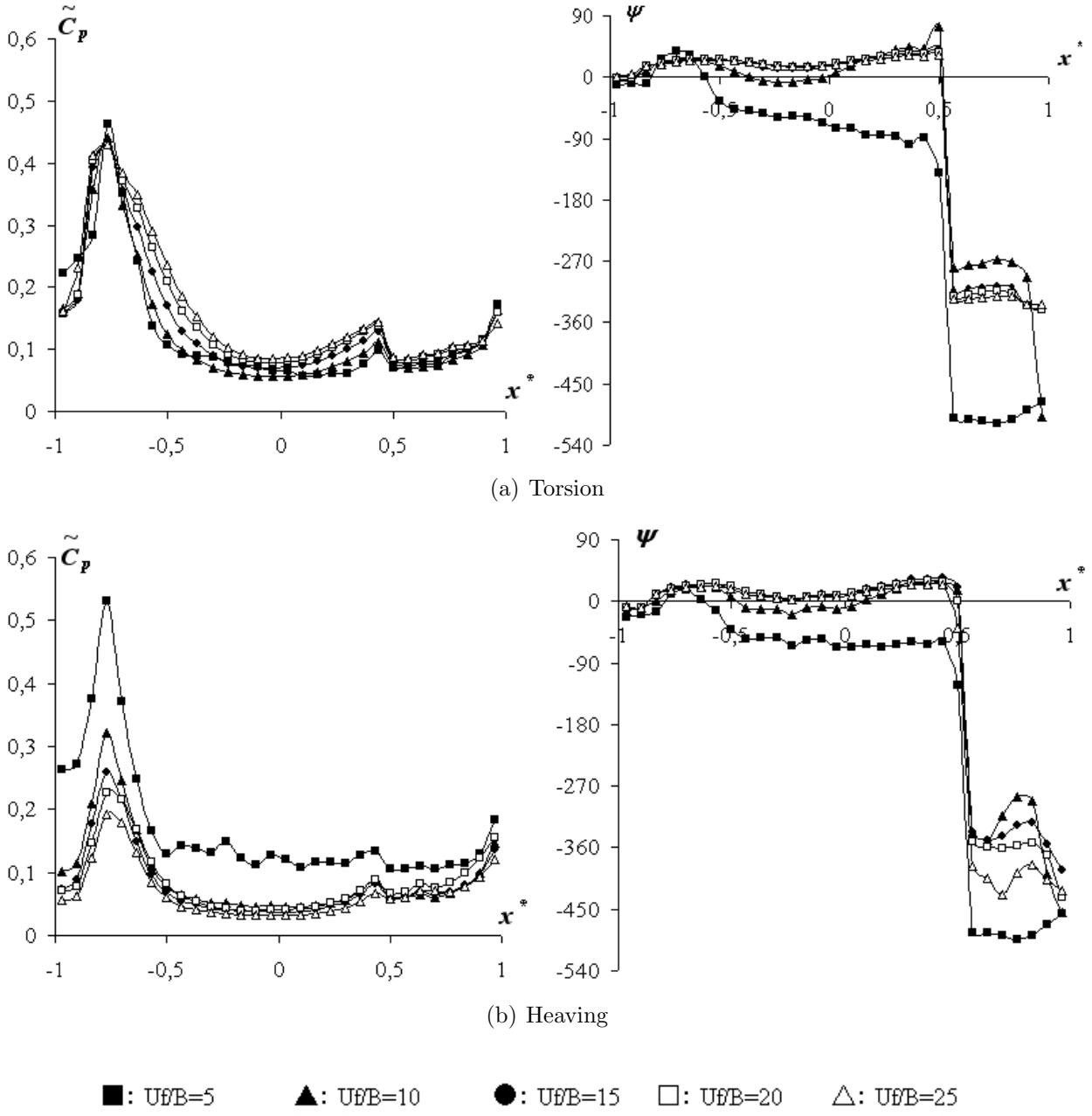

(a) Torsion

(b) Heaving

Figure 5.28: Unsteady pressure characteristics of case NF-VI-B

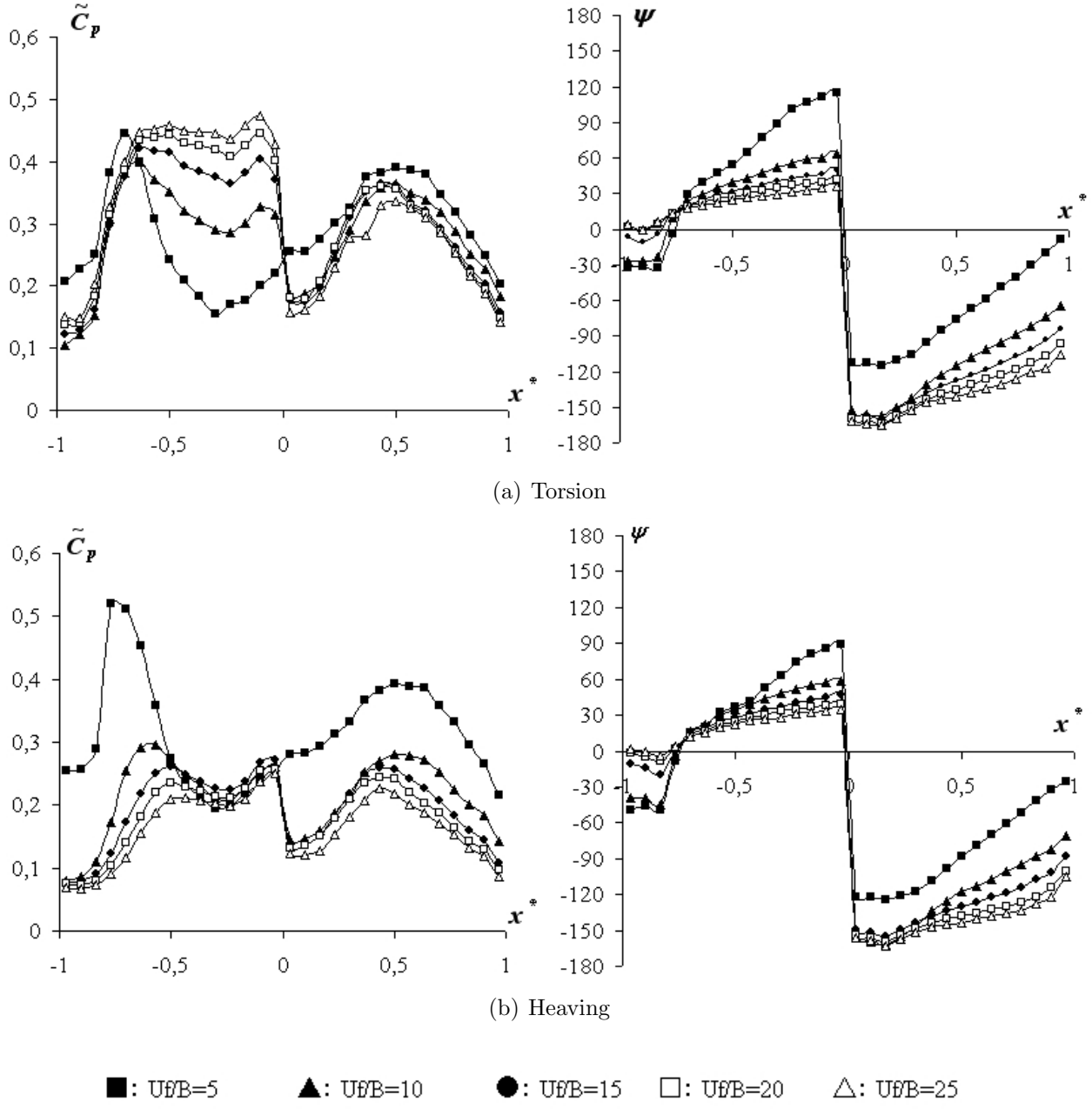

Figure 5.29: Unsteady pressure characteristics of case NF-VII-B

However, in case NF-VI-B, which presents the larger distance from the leading edge and is represented by Fig.5.28, although the effects of the vertical plate on the phase difference $\psi(x^*)$ distribution were quite prominent, with a "jump" of around 360°, its effects on the amplitude $\tilde{C}_p(x^*)$ distribution were weaker, in comparison with the vertical plate of size A.

Based on that, it is confirmed that the influences of the vertical plate on the amplitude $\tilde{C}_p(x^*)$ distribution is decreased with the increasing of the distance from the leading edge, contrarily to what is observed for the phase difference $\psi(x^*)$ distribution; and the increasing of the size of the vertical plate enhances this disparity.

An additional comparison can be established by checking the effects of 2 vertical plates of same size installed along the chord direction, for heights of $D/2$ and D, Fig.5.30 and Fig.5.31 respectively.

For both sizes, the effects on the unsteady pressure characteristics were a kind of *non cumulative superposition of effects* of cases NF-IV and NF-VI. Upstream the vertical plate corresponding to position VI, both amplitude $\tilde{C}_p(x^*)$ and phase difference $\psi(x^*)$ distributions behave essentially as they do for case NF-IV (Fig.5.14 and Fig.5.27), and with the addition of the vertical plate in the location VI, the unsteady pressure characteristics downstream that point behaves as case VI (Fig.5.18 and Fig.5.28). As a result, the configurations of unsteady pressure characteristics of cases V become the composition of the effects of cases IV and VI, as both configurations were obtained separately.

The vertical plate of size A starts to exert its influences only downstream its location, which means that the effects of plate VI on its upstream are practically imperceptible. In the case of vertical plate of size B, the effects upstream are more appreciable, through the increasing of the values of amplitude $\tilde{C}_p(x^*)$ and the maintenance of the positive values of $\psi(x^*)$ caused by the blockage effect; however, in its downstream the effects are essentially the same as those observed in case NF-VI-B, Fig.5.28.

This is an important feature of the composition of vertical plates along the body‘s surface. There seems not to exist an interaction between the individual effects of each vertical plate, and the unsteady pressure characteristics downstream the vertical plate are influenced basically by only that vertical plate itself, regardless what exists in its upstream. However, this should not be treated as a generalization, since only few cases were investigated, and although this assumption holds for the cases covered herein, it may present different effects for different sizes of vertical plates and different *geometric singularities*.

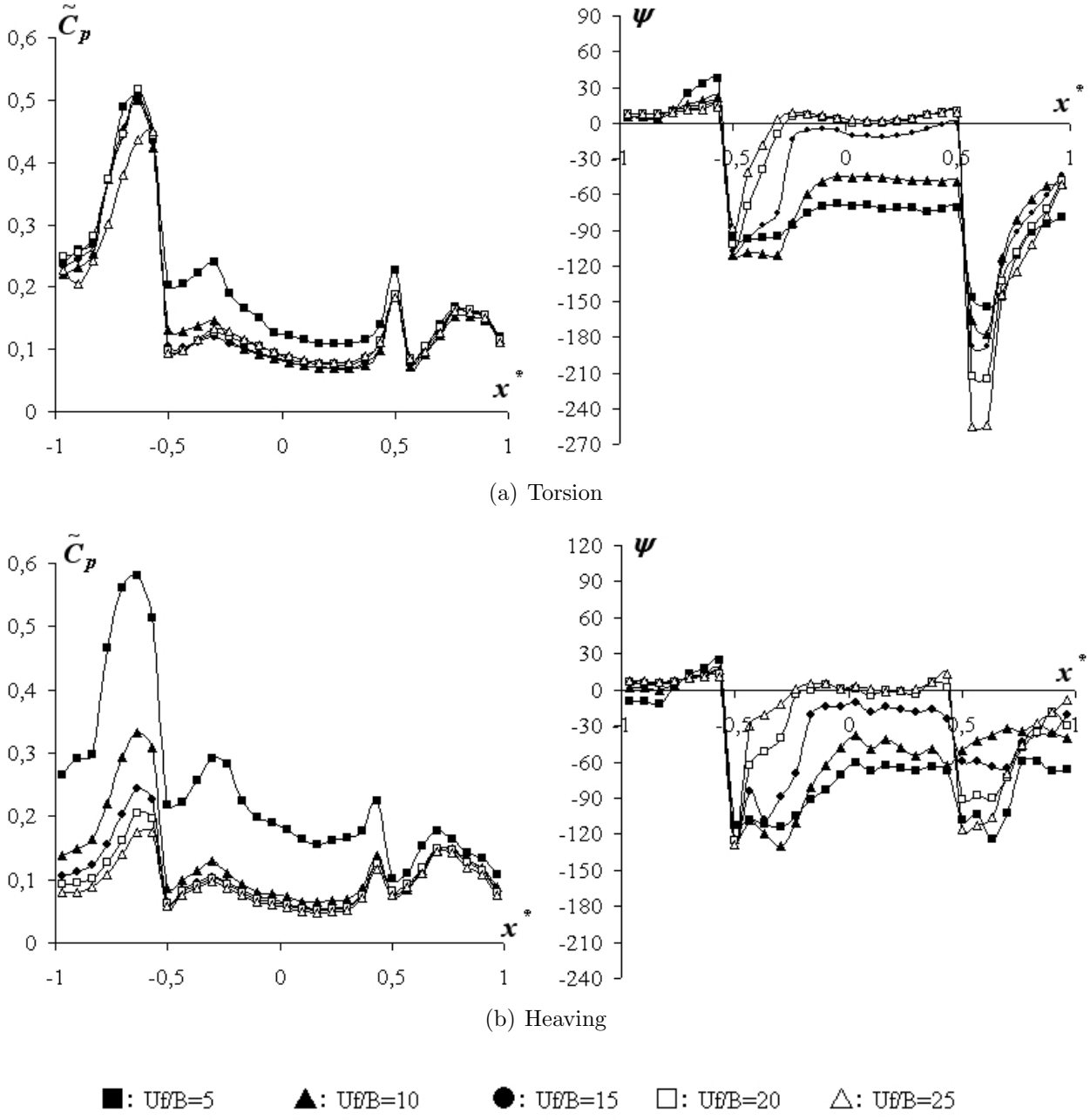

Figure 5.30: Unsteady pressure characteristics of case NF-V-A

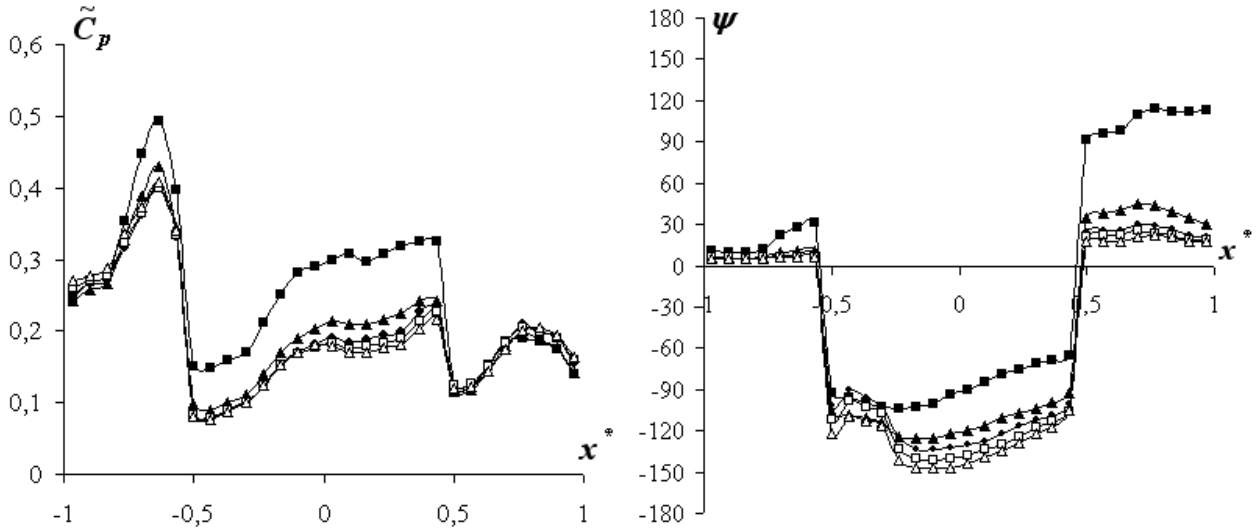

(a) Torsion

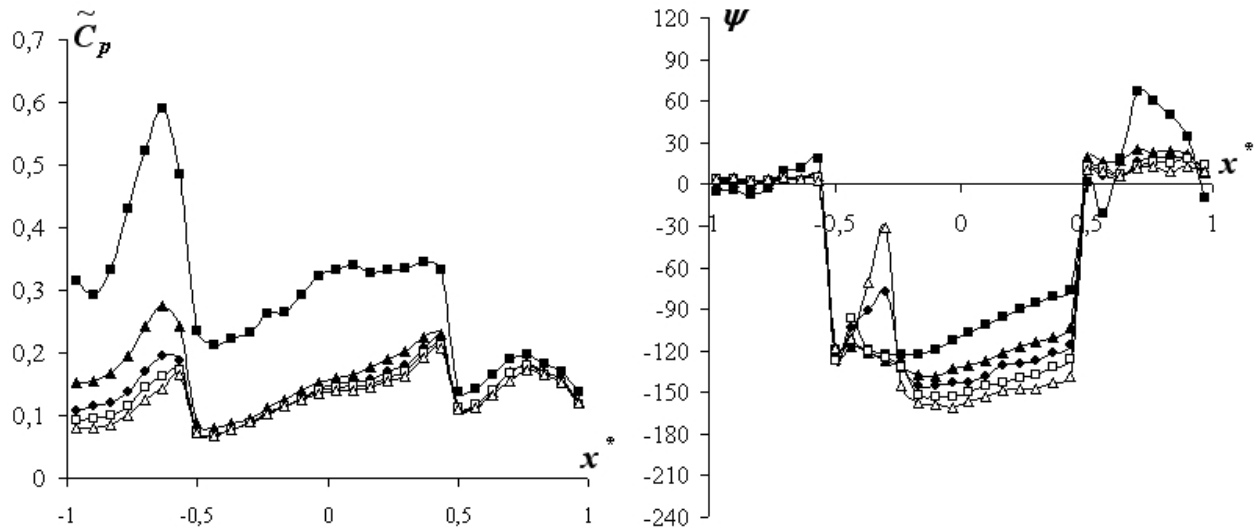

(b) Heaving

■: Uf/B=5 ▲: Uf/B=10 ●: Uf/B=15 □: Uf/B=20 △: Uf/B=25

Figure 5.31: Unsteady pressure characteristics of case NF-V-B

Concerning model CU, introduced in Section 5.2, there seems to exist a mixture between the influences of the cases with vertical plate installed at the leading edge, i.e. Section 5.2, and the cases with vertical plate installed along the chord direction, i.e. Section 5.3. The amplitude $\tilde{C}_p(x^*)$ distribution presents a behavior between both situations for all velocities tested and the phase difference $\psi(x^*)$ distribution seems to be dominated by the effects of a vertical plate at the leading edge in the lower velocity range, assuming a configuration similar to the ones induced by a vertical plate along the chord direction in the higher reduced wind velocity.

5.4 Vertical plate at the trailing edge

By installing a vertical plate at the trailing edge, the conclusions about the effects in its upstream can be better assessed. The results of the wind tunnel tests are reported in Fig.5.32 to Fig.5.35.

For all cases, the effects are quite similar in both heaving and torsional systems. Comparing case NF-III-A, Fig.5.34, with the model without vertical plate, i.e. NF in Fig.4.10, it is noticed that a vertical plate installed at the trailing edge can exert its influence on both amplitude $\tilde{C}_p(x^*)$ and phase difference $\psi(x^*)$ distributions even at locations as far away as the leading edge. The distributions seem to be compressed and this can be understood as a reduction of the wave length developed along the body, leading the unsteady pressure characteristics of the model to behave as it had a greater side ratio B/D. This effect is even enhanced when a vertical plate of type B is used, in the case of model NF-III-B in Fig.5.35.

However, when there already exists a vertical plate at the leading edge, i.e. cases NF-I-A and NF-I-B, the equivalent bluffness of the body is increased, as already discussed in section 5.2, and the addition of a vertical plate at the trailing edge. i.e. cases NF-II-A and NF-II-B, does not have a major impact on the unsteady pressure characteristics of the models, being restricted to the same influences related to the blockage effect perceived in the cases of Section 5.3. The effects are felt mostly in the amplitude $\tilde{C}_p(x^*)$ distribution and it is possible to infer that the same phenomena observed in the cases with 2 vertical plates installed along the body surface, i.e. NF-V-A and NF-V-B, also take place in cases NF-II-A and NF-II-B, and their resulting unsteady pressure characteristics are the resultant of a *non cumulative superposition of effects*.

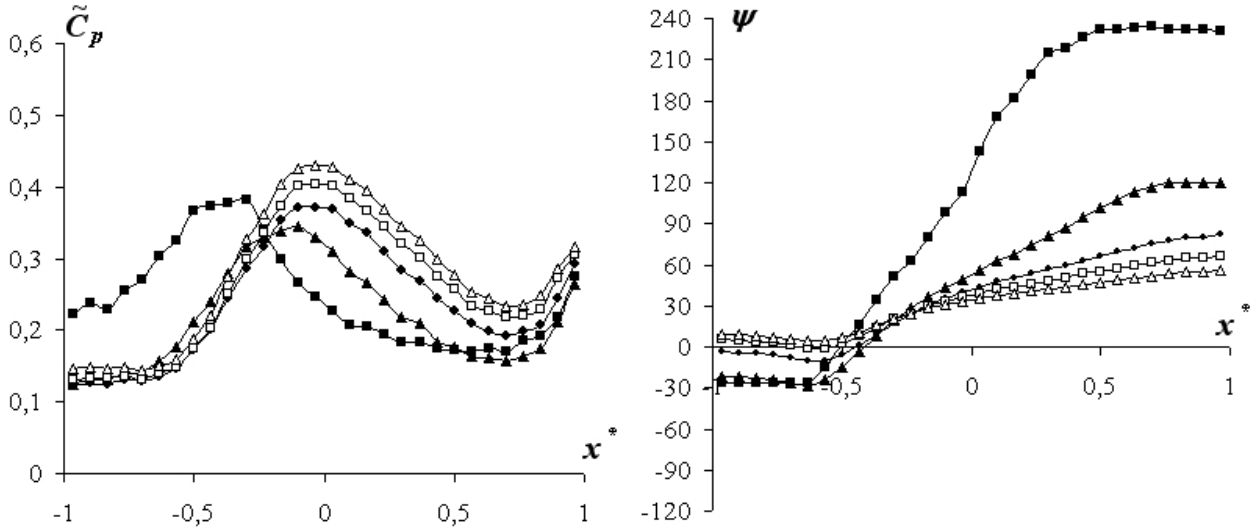

(a) Torsion

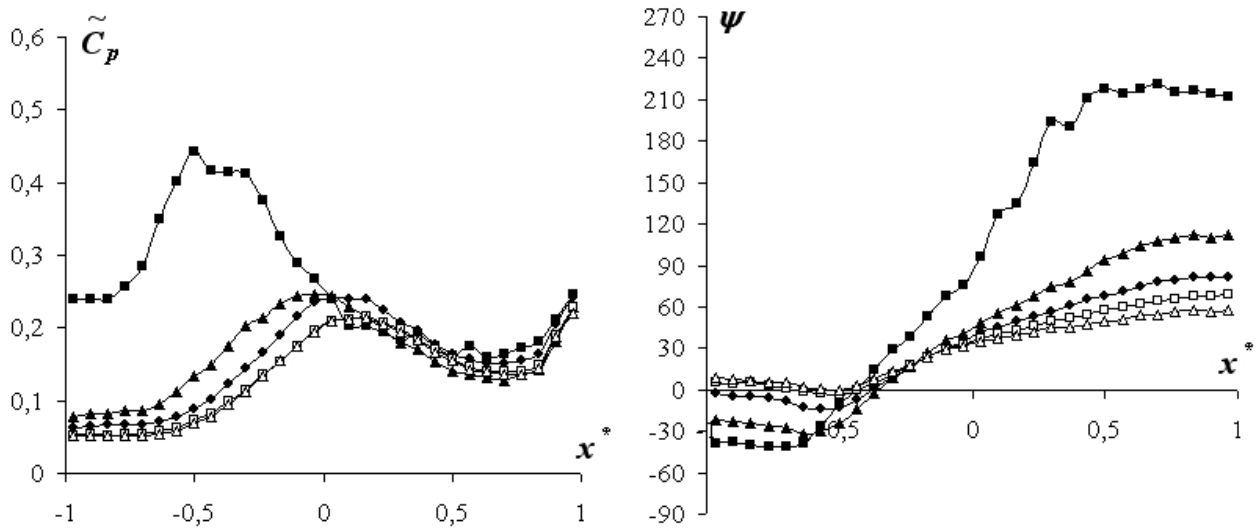

(b) Heaving

■: U/fB=5 ▲: U/fB=10 ●: U/fB=15 □: U/fB=20 △: U/fB=25

Figure 5.32: Unsteady pressure characteristics of case NF-II-A

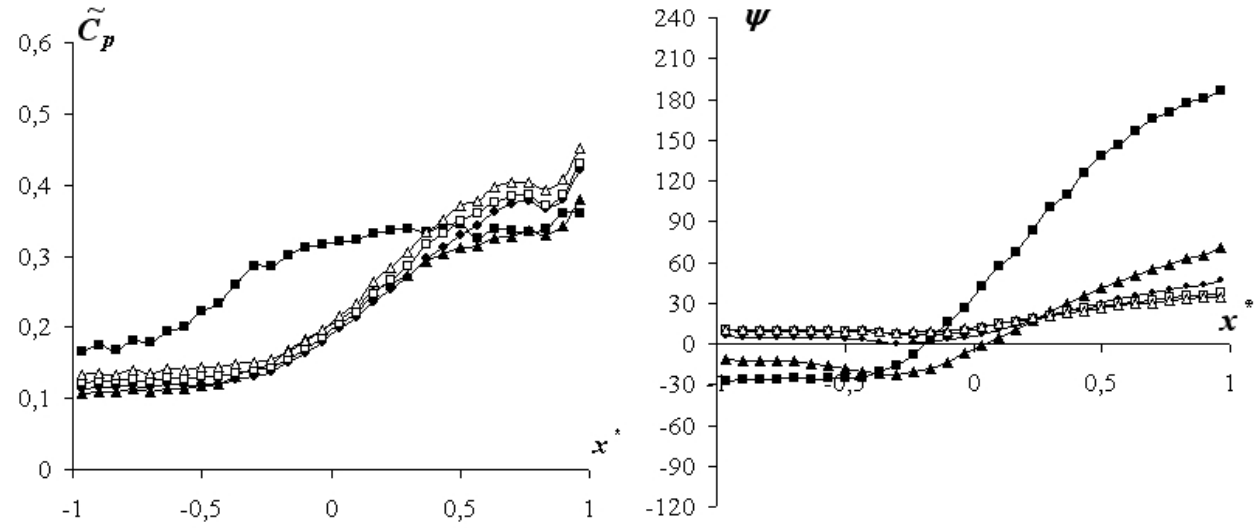

(a) Torsion

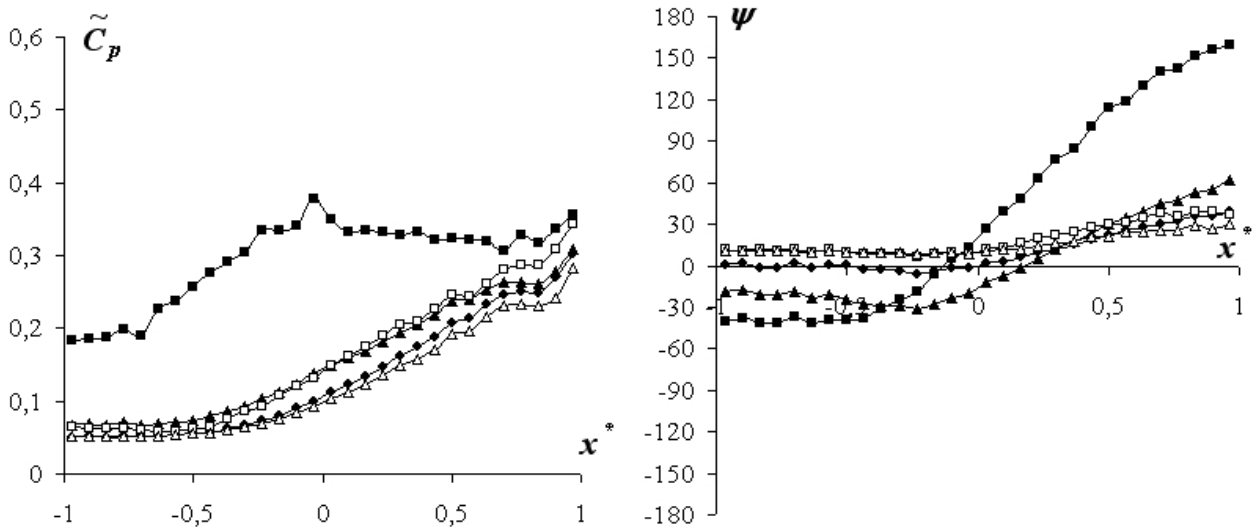

(b) Heaving

■: Uf/B=5 ▲: Uf/B=10 ●: Uf/B=15 □: Uf/B=20 △: Uf/B=25

Figure 5.33: Unsteady pressure characteristics of case NF-II-B

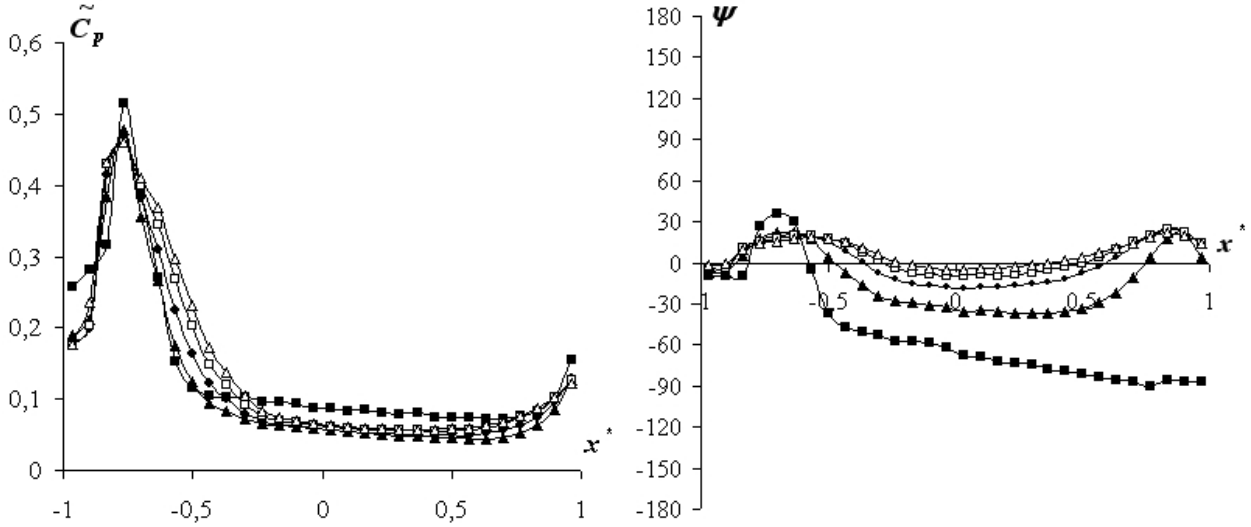

(a) Torsion

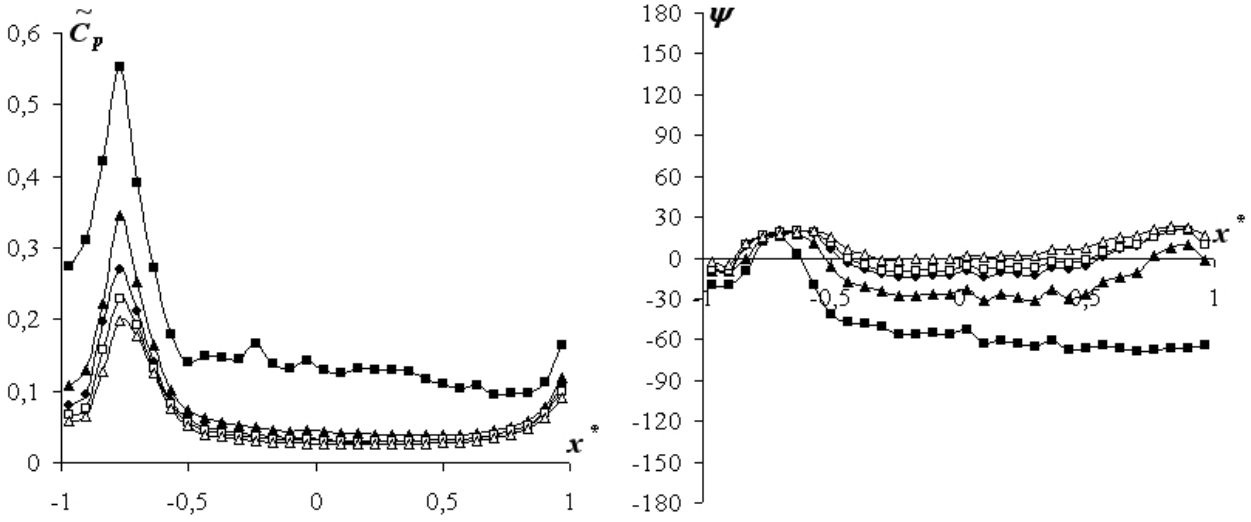

(b) Heaving

■: U/B=5 ▲: U/B=10 ●: U/B=15 □: U/B=20 △: U/B=25

Figure 5.34: Unsteady pressure characteristics of case NF-III-A

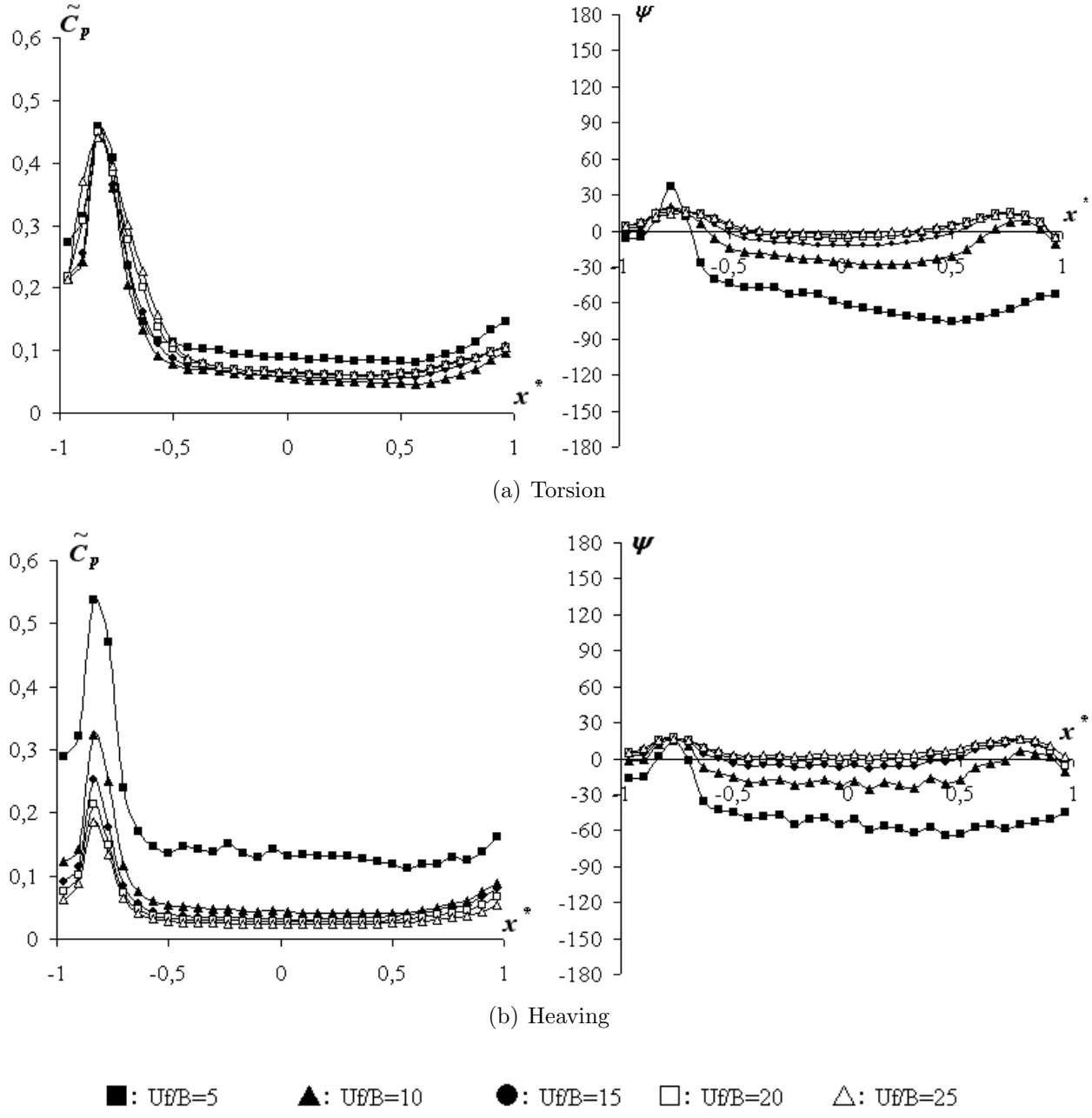

(a) Torsion

(b) Heaving

Figure 5.35: Unsteady pressure characteristics of case NF-III-B

Finally, it seems that the effects of the vertical plate at the trailing edge are better perceived in bodies with larger side ratios, being useful for the increasing of the equivalent side ratio.

5.5 Concluding Remarks

This chapter provided an overview of the effects of vertical plates installed along the upper surface of rectangular cylinders on their unsteady pressure characteristics, through the analysis of the impacts on the equations proposed in Chapter 4 and on the shapes of the resulting distributions themselves. As a basic conclusion, vertical plates were proved to be good devices for the manipulation of the unsteady pressure characteristics of rectangular cylinders, since their effects were quite prominent and measurable, and it is assumed as a generalization that they are also of great value in any geometry of cross-section.

Vertical plates installed near the leading edge led the resulting unsteady pressure characteristics of the rectangular cylinders to assume configurations similar to those obtained with rectangular cylinders with a lower side ratio. The *equivalent side ratio* differed from the *apparent side ratio* by a factor of 0.5 and showed itself to keep a close relationship with the size of the vertical plate, being finally regarded to the wave length developed along the body‘s surface. These effects could be caught by the equations proposed in Chapter 4, provided the necessary arrangements in their parameters considering this reduction of side ratio were performed, and can be surely used in advantage for the manipulation of the unsteady pressure characteristics towards flutter stabilization.

Since the increasing of the "apparent" bluffness of the body (reduction of the *apparent side ratio*) may impact negatively on the flutter stability, vertical plates near the leading edge may need to be associated to other *geometric singularities* along the body‘s surface to provide stable configurations of unsteady pressure characteristics, according to the conclusions of Chapter 3. Because the effects of vertical plates were proved to be closely related to their size, their use in the manipulation of the unsteady pressure characteristics should be associated to the judicious adjustment of this key parameter.

Vertical plates installed along the chord direction presented a quite different impact on the unsteady pressure characteristics, by promoting a peak in the amplitude $\tilde{C}_p(x^*)$

distribution and a "jump" in the phase difference $\psi(x^*)$ distribution. The location of the peak in the amplitude $\tilde{C}_p(x^*)$ distribution was found to be directly related to the size of the vertical plate; however the "jump" in the phase difference $\psi(x^*)$ distribution was always located at the vertical plate position. The influences of the vertical plate on the peak values $\tilde{C}_{pmax}$ promoted in the amplitude $\tilde{C}_p(x^*)$ distribution decreased with the increasing of the distance from the leading edge, contrarily to what was observed for the phase difference $\psi(x^*)$ distribution, and the increasing of the size of the vertical plate enhanced this relationship.

This leads to a non-linear relationship between size and location of vertical plates and aerodynamic derivatives, which can be rationalized only by considering the impacts of the vertical plates individually on the amplitude and on the phase difference distributions. So the importance and the applicability of the information presented in this chapter is highlighted and corroborated, since the impacts of the vertical plates on the unsteady pressure characteristics showed themselves quite measurable and able to be put in the forms of equations. Further investigations are required for the improvement of these relationships, and are expected as future works.

By using the relationships between the jump in the phase difference $\psi(x^*)$ distribution, the location of the peak in the amplitude distribution and the size of the vertical plate, an optimal size that makes the phase difference to fit in the *stable* zone can be easily defined. In the vertical plates investigated herein, i.e. height $D/2$ and height D, the jumps were quite big. Because of that, smaller vertical plates should be preferred. This optimal size should be associated to a proper position. In the case of a B/D=20 rectangular cylinder, this position would be in the middle of the cross-section (position VII), since it induces a pattern in the phase difference distribution proper for flutter stabilization (according to Chapter 3). However, other shapes or even rectangular cylinders with different side ratios may require different positions and sizes.

The influences of single vertical plates were found to be dependent on the characteristics of the flow upstream their locations, which were reduced with the increase of the reduced wind velocity. Because of that, the potentiality of inducing peaks in the $\tilde{C}_p(x^*)$ distribution is directly related to the conditions of the oncoming flow before reaching the vertical plate, in terms of proximity to reattachment points and levels of $\tilde{C}_p(x^*)$, which enhances the role played by the leading edge plays in this process. However, in compositions with two vertical plates, there seemed not to exist an interaction between the individual effects of each vertical plate. As a result, the unsteady pressure characteristics downstream the second vertical plate are influenced basically by only that vertical plate itself, regardless the configuration in its

upstream. However, this should not be treated as a generalization, since only few cases were investigated, and although this assumption holds for the cases covered herein, it may present different effects for different sizes of vertical plates and different *geometric singularities*.

The differences in terms of impacts of the vertical plate in the torsional system and in the heaving system showed some dependence on the leading edge and in this sense the semi-circular leading edge, i.e. SC, showed itself a good device for breaking the aerodynamic derivatives interdependence, since considerably different arrangements between torsional and heaving systems could be obtained for the unsteady pressures characteristics. This might have some relationship with the Reynold‘s number effect and deserves deeper investigations.

The vertical plates investigated in this chapter exerted their effects not only downstream their location, but also upstream, due to a recirculation of the flow caused by the blockage effect. This does not mean that all *geometric singularities* will have the same effect, and even vertical plates with smaller sizes may not present effects upstream. The effects in terms of distance of the peaks from the vertical plate, both upstream and downstream, and also the values of the peaks, were found to be proportional to the size of the vertical plates, in the range of sizes investigated.

Finally, it seems that the effects of the vertical plate at the trailing edge are better perceived in bodies with larger side ratios, being associated to increasing even more the *equivalent side ratio*, contrarily to what can be observed for vertical plates installed near the leading edge, which were found to promote a reduction of the *equivalent side ratio*.

Chapter 6

Effects of the Gap on the Unsteady Pressure Characteristics of Two-Box Cross-Sections

6.1 Introduction

Bridge cross-sections composed by two single boxes separated by a void space (air gap) have been referred in the technical literature by different terms, e.g. slotted box girder, two-box girder, twin-box girder, 2-box girder, separated box girder, etc. However, all definitions point to the same concept, recognized to provide stable solutions for long span bridges and resulting in considerably lighter structures compared to opaque decks, which makes them economically attractive.

The presence of the gap is recognized to play major role for this attractiveness, and this has been extensively reported in the technical literature [15, 16, 17, 18, 118, 119], with positive associations between the benefits of increasing the gap length and the flutter stability of the bridge. The details of the mechanisms of aerodynamic stabilization provided by such a kind of cross-section are still not fully clarified [6]; however, the reduction on the relative density of the deck provided by the existence of open spaces is an important factor in the maintenance of values of total torsional damping in a level high enough, which can also be

associated to the ratio between gap length and deck width [38]. In addition, openings in the deck reduce the destabilizing pitching moment originated by the twist [38] and the quasi-static coefficients of aerodynamic resistance to torque and lift [35], increasing the flutter onset speed.

Nevertheless, the existence of open spaces along the deck is not beneficial in terms of flutter stability in all circumstances. Depending on the location and on the opening ratio, the flutter onset may also be decreased, even for two box girders (with a central gap) [120]. Associations with the characteristics of the single box were attempted by Yang et al. [121], leading also to the conclusion that central-slotting is not always able to improve the stability, which will depend on the aerodynamic characteristics of the original cross-section and on the gap length. In addition, associations with the effects of grating have shown dependency on the Reynold‘s number [16, 122, 123]. Based on all above, it is recognized that for every cross-section and characteristic of gap different general behaviors may be expected.

Usually, it is assumed that both boxes behave as a rigid body, which is guaranteed by transverse beams rigid enough to prevent the two decks to twist independently, i.e. beyond an acceptable value. Another structural aspect is that the torsional stiffness necessary to prevent flutter increases with the increase of the span, impacting substantially on the cost of the construction. So reducing or even eliminating the need of torsional stiffness is a good strategy for reducing the costs, which can be acquired through aerodynamic improvements.

The values of gap length have been usually referred as a ratio to the width B^* of one single box, and studies conducted on slotted girders have already accounted for the good aerodynamic stability of cross-sections with gap length $> 0.25B^*$[120]. However, because the costs increase with the increase of the gap length, the shorter the gap, the better. Usual values have been limited to not longer than $1.0B^*$, as Stonecutters Bridge in Hong Kong with gap length of $0.73B^*$ and the proposed Kitan Straits bridge in Japan with gap length of $0.34B^*$ [18].

In this chapter, the gap will be faced as a *geometric singularity*. So its influences on the unsteady pressure characteristics of two-box cross-sections will be investigated through wind tunnel tests, by considering the studies performed in the previous chapters. A wide range of gap lengths will be tested, with the presence of grating and vertical plates in some configurations. The interactions of these additional *geometric singularities* with the gap in terms of resulting impacts on the unsteady pressure characteristics will also be investigated, providing additional information concerning the subjects addressed in Chapter 4 and in

Chapter 5.

6.2 Wind Tunnel Tests

The wind tunnel experiments of this chapter were conducted by focusing on the influences of the gap length on the unsteady pressure characteristics of two-box cross-sections. Also, the impacts of some geometric modifications, as gratings and vertical plates, on the overall aerodynamic characteristics of the models were investigated.

The techniques used for the measurement of the pressures along the models are described in Appendix B and are basically the same used in the previous chapters. The two-box cross-sections are formed by 2 rectangular cylinders with side ratio B^*/D=20 each, separated by different values of gap length – $0B^*$, $0.1B^*$, $0.25B^*$, $0.5B^*$, $1.0B^*$, $1.5B^*$, $2.0B^*$, $3.0B^*$– with the rotational pivot fixed at the midpoint of both cylinders. Gratings with 35% of permeability and vertical plates with $height = D$ located at the middle of the chord direction of the upstream box (case VL) and of both boxes (case VB) were installed in the models with gap length $1.0B^*$ and $2.0B^*$. The results are presented considering the reduced wind velocity U_r defined by Eq.6.1.

$$U_r = \frac{U}{f.B^*} \tag{6.1}$$

where: B^* is the width of a single box

The *runs* are identified throughout this study by a code composed by the gap length and the motion code (H for heaving and T for torsion). In the case of grating (models $1.0B^*$ and $2.0B^*$), an additional code G is used; for the cases with vertical plate in the upstream box the code VL is used and for vertical plate in both boxes VB is added to the code of the respective *runs*.

The results are reported in Fig.6.1 to Fig.6.14, in terms of unsteady pressure characteristics.

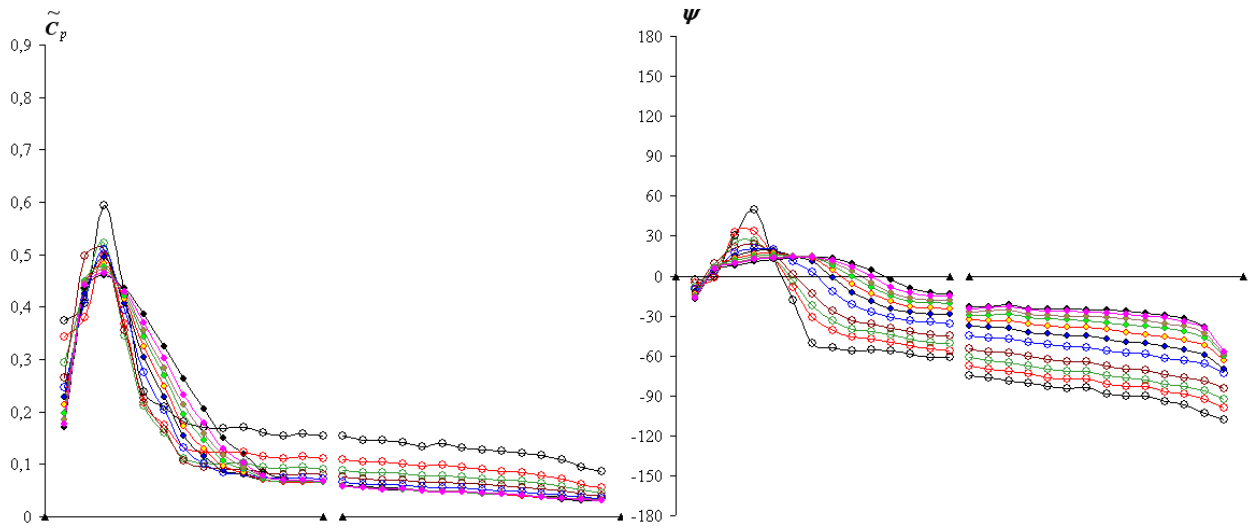

(a) Torsion

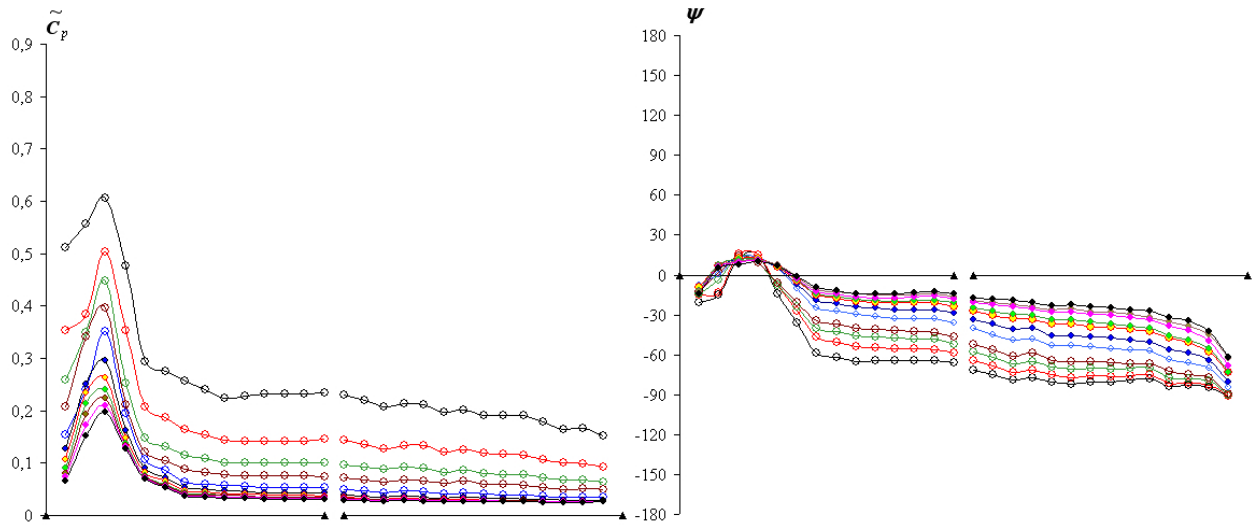

(b) Heaving

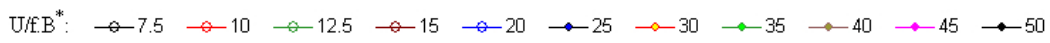

Figure 6.1: case $0B^*$: two-box B^*/D=20 with gap=0

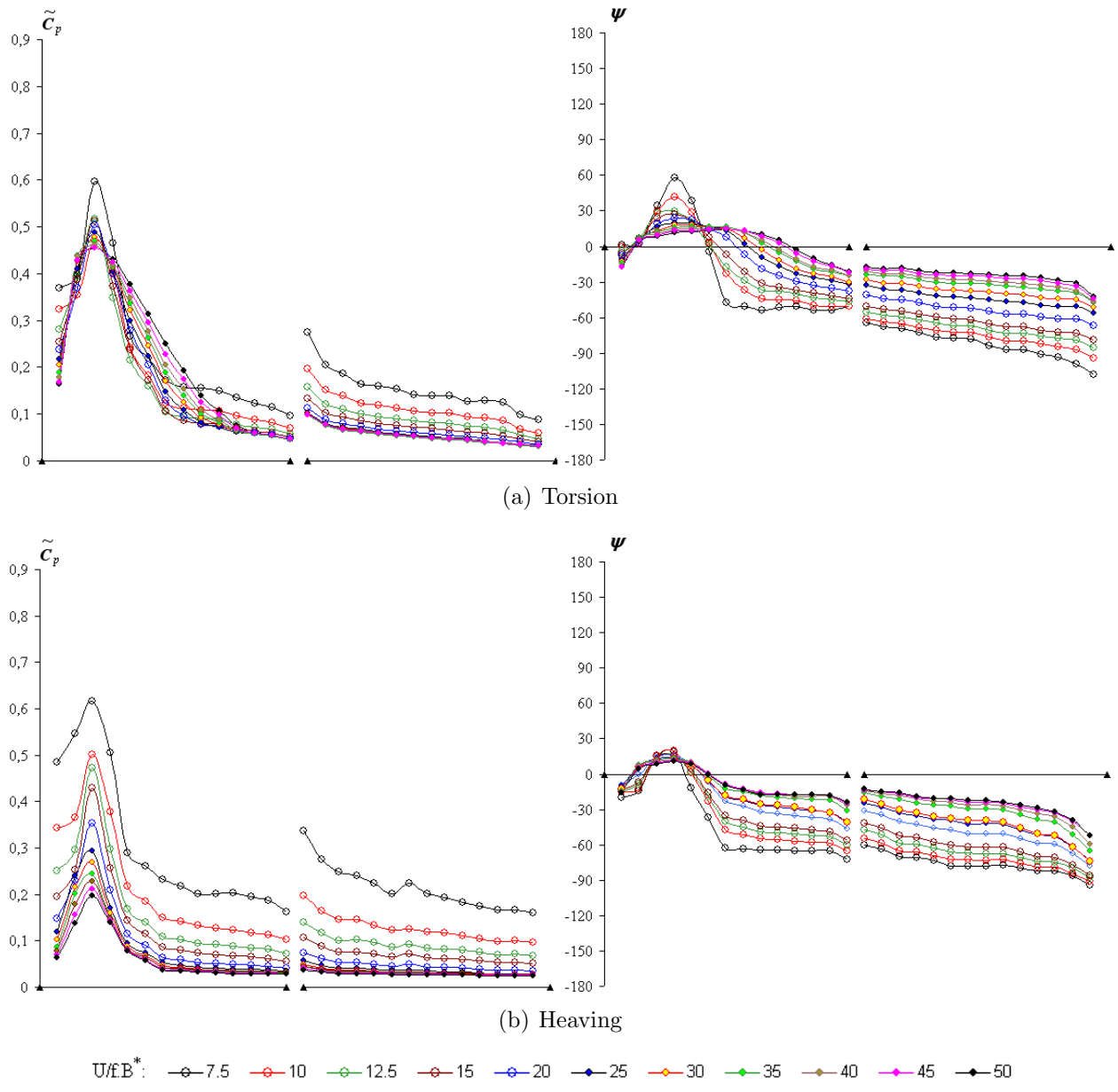

(a) Torsion

(b) Heaving

Figure 6.2: case $0.1B^*$: two-box B^*/D=20 with gap=$0.1B^*$

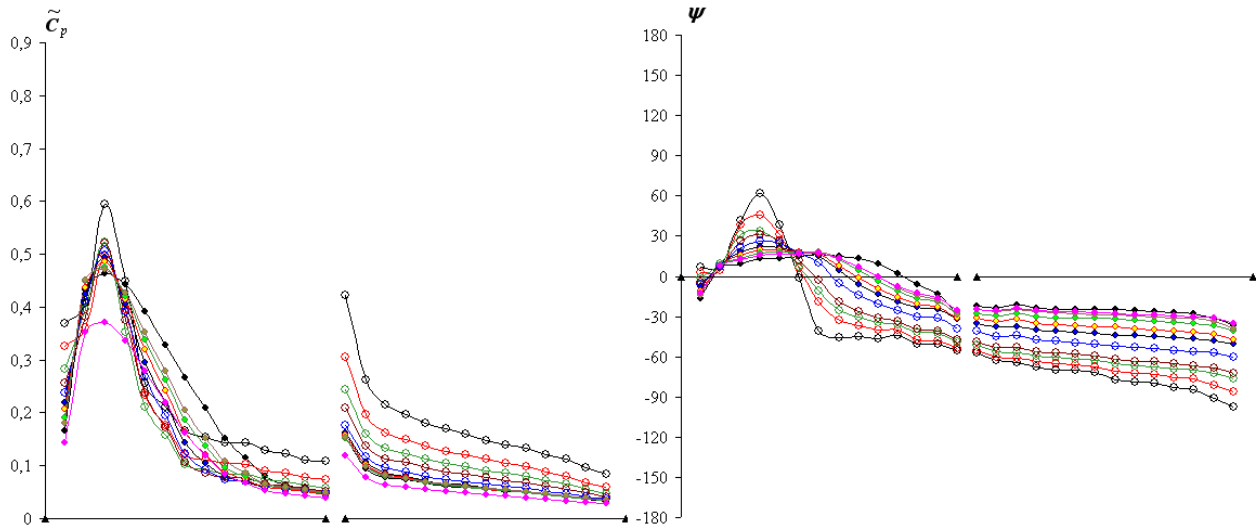

(a) Torsion

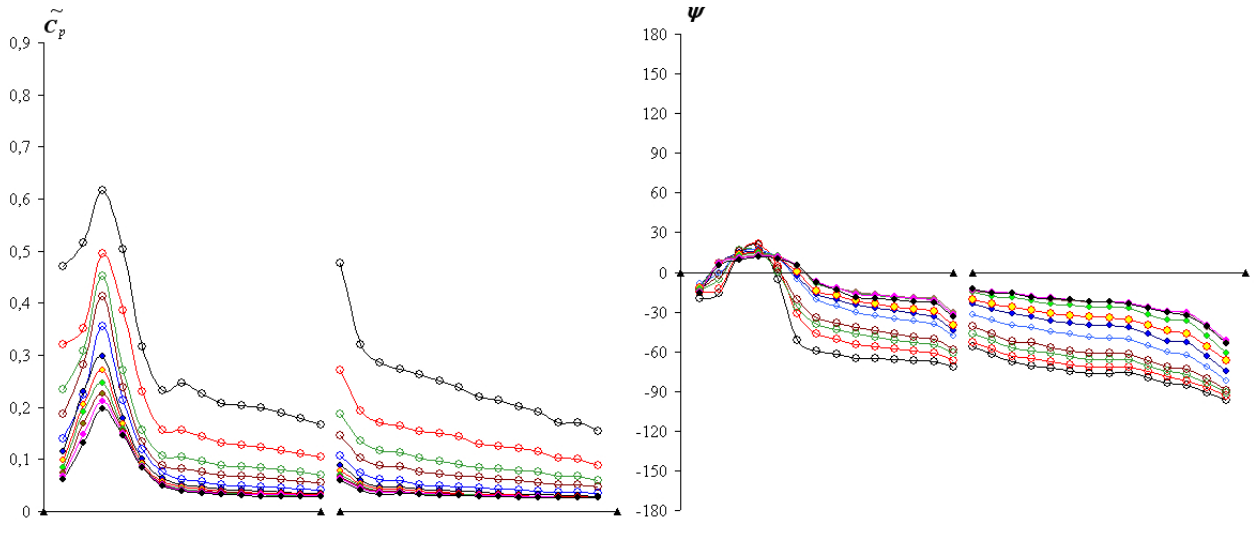

(b) Heaving

Figure 6.3: case $0.25B^*$: two-box B^*/D=20 with gap=$0.25B^*$

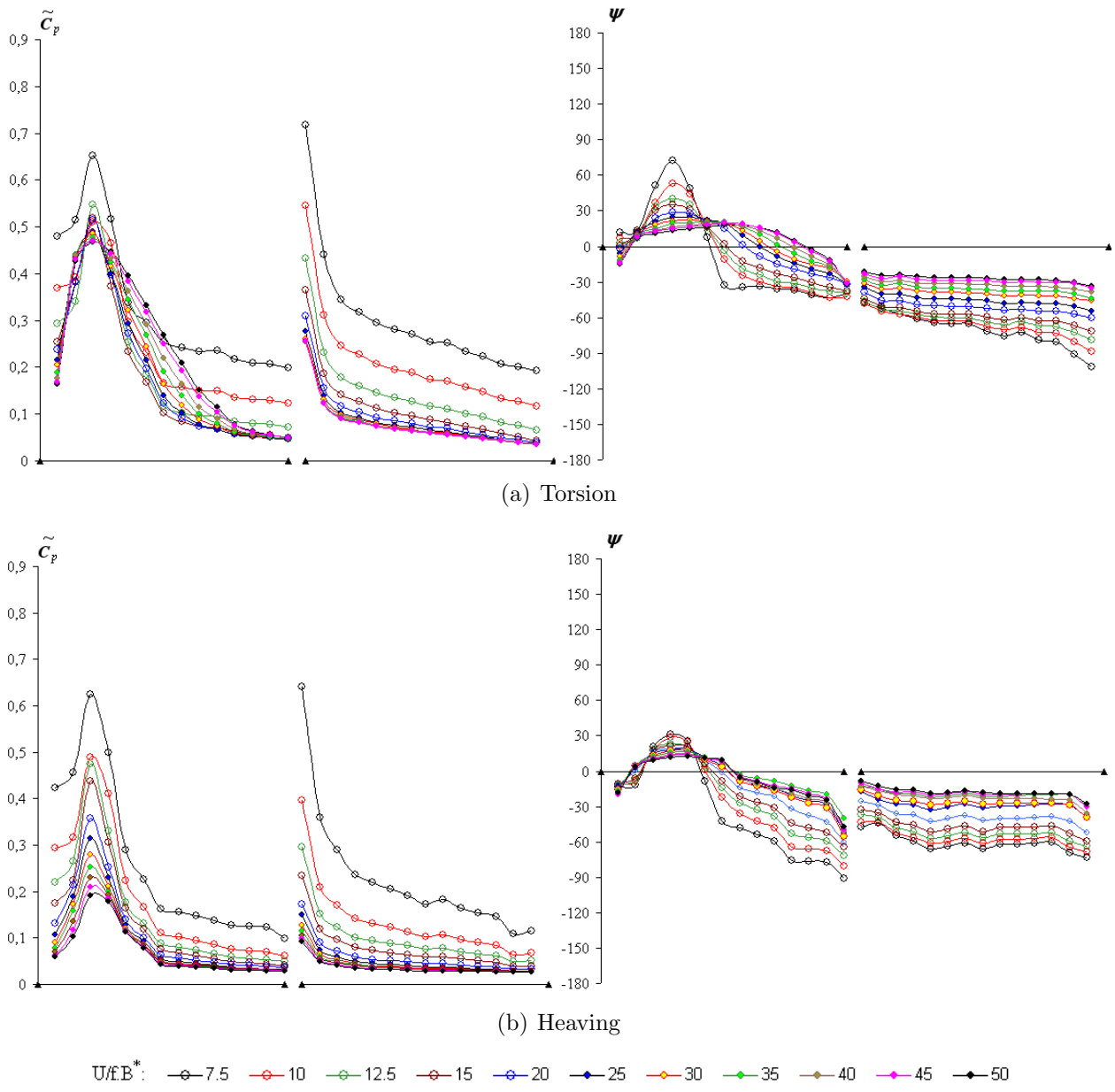

(a) Torsion

(b) Heaving

Figure 6.4: case $0.5B^*$: two-box B^*/D=20 with gap=$0.5B^*$

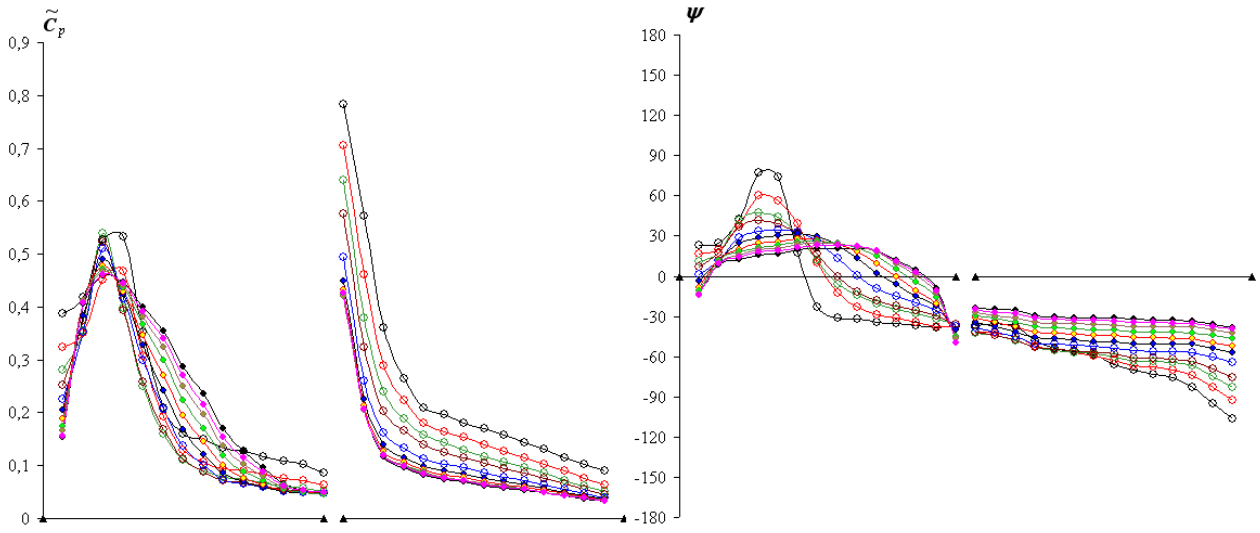

(a) Torsion

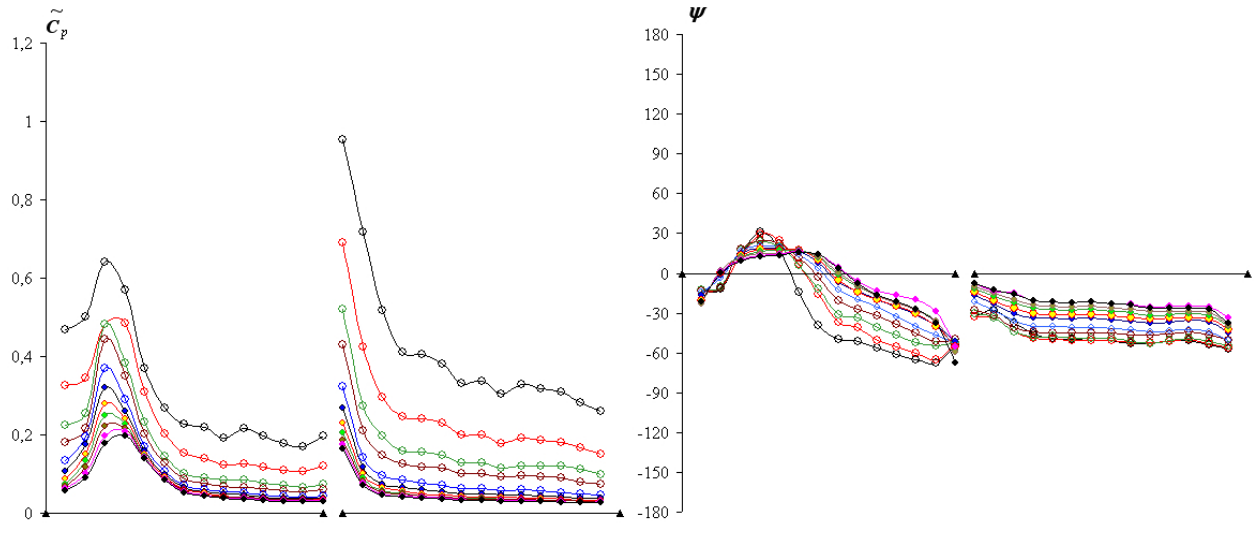

(b) Heaving

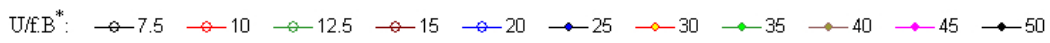

Figure 6.5: case $1.0B^*$: two-box B^*/D=20 with gap=$1.0B^*$

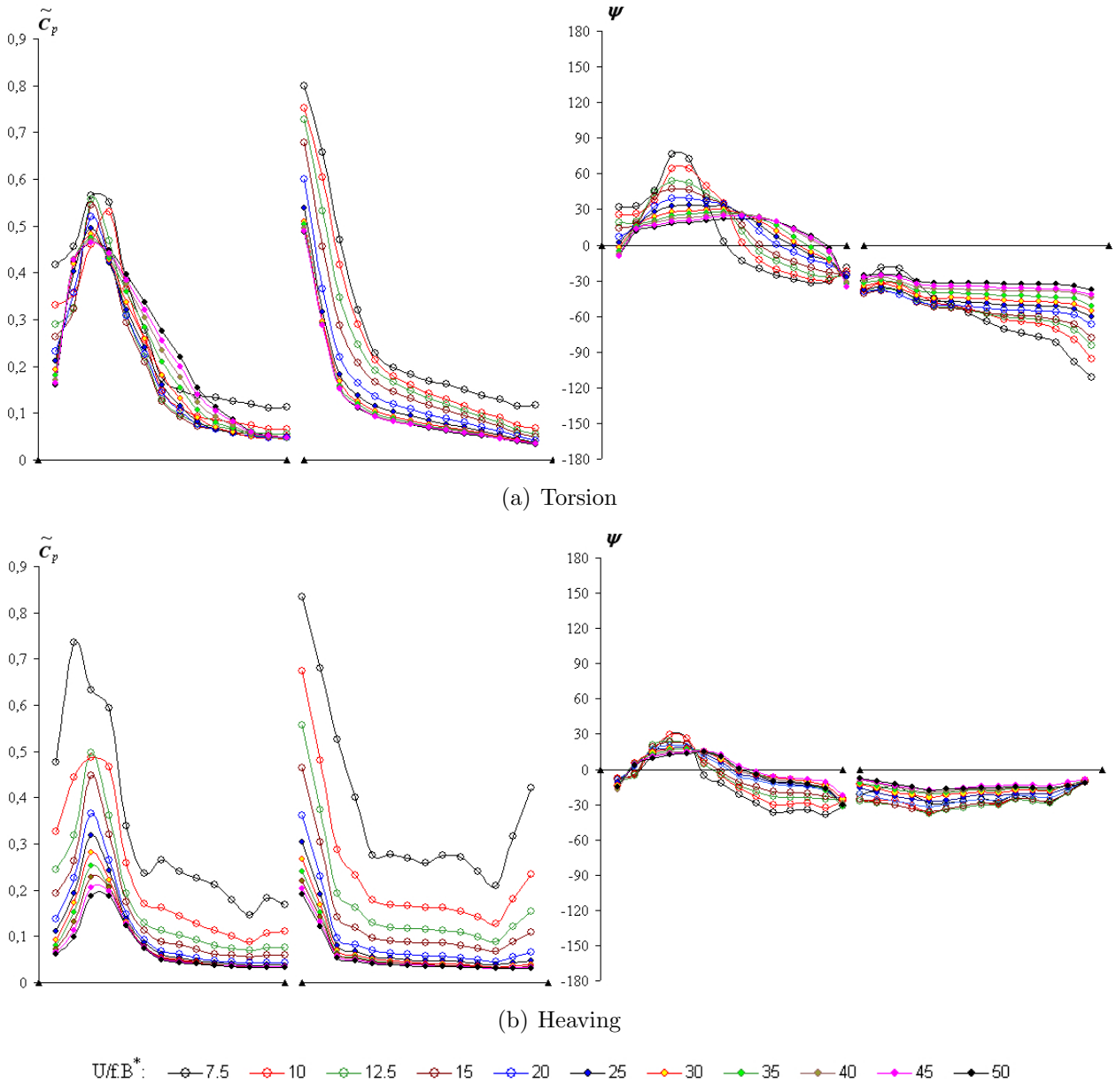

(a) Torsion

(b) Heaving

Figure 6.6: case $1.5B^*$: two-box B^*/D=20 with gap=$1.5B^*$

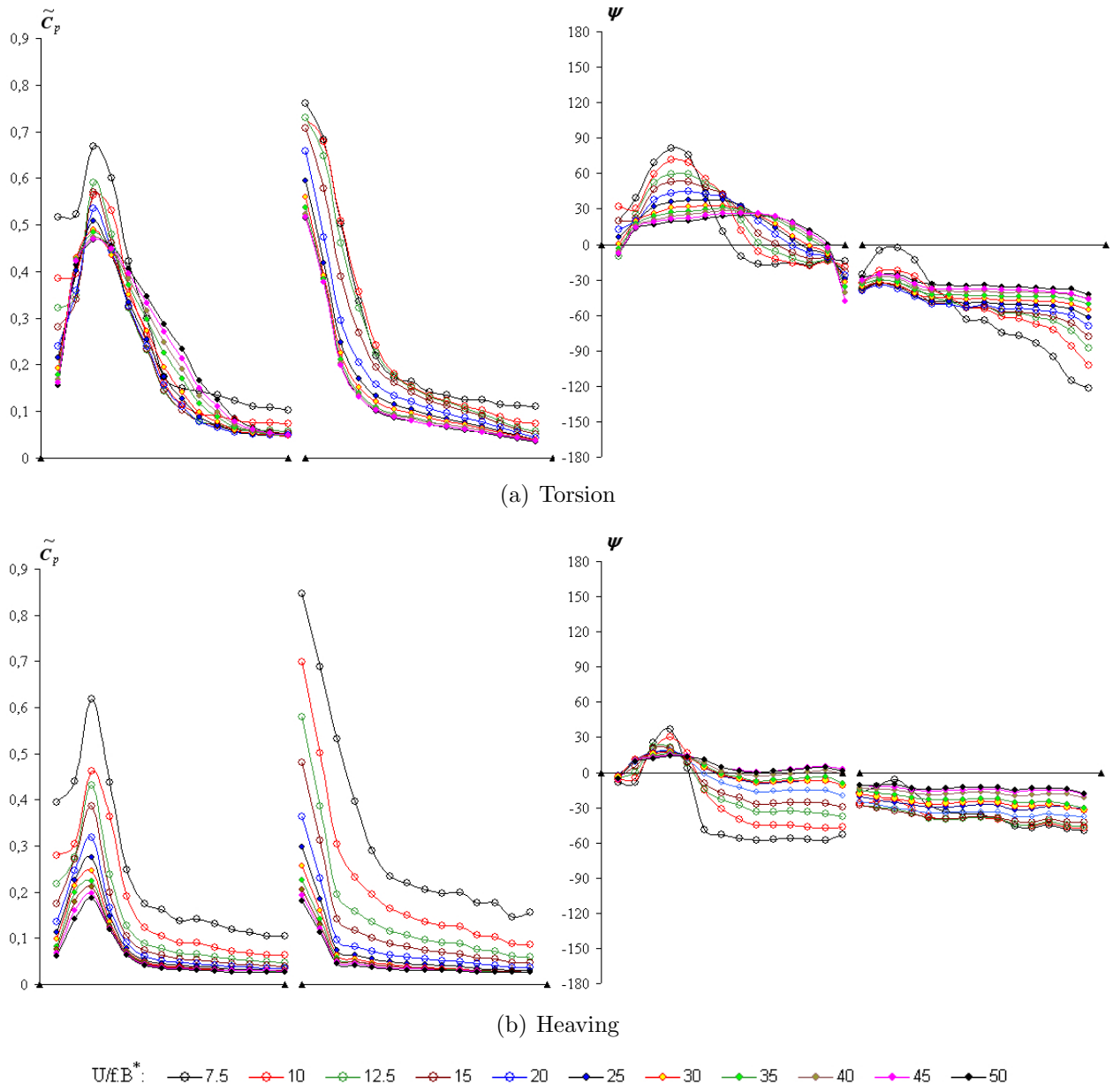

(a) Torsion

(b) Heaving

Figure 6.7: case $2.0B^*$: two-box B^*/D=20 with gap=$2.0B^*$

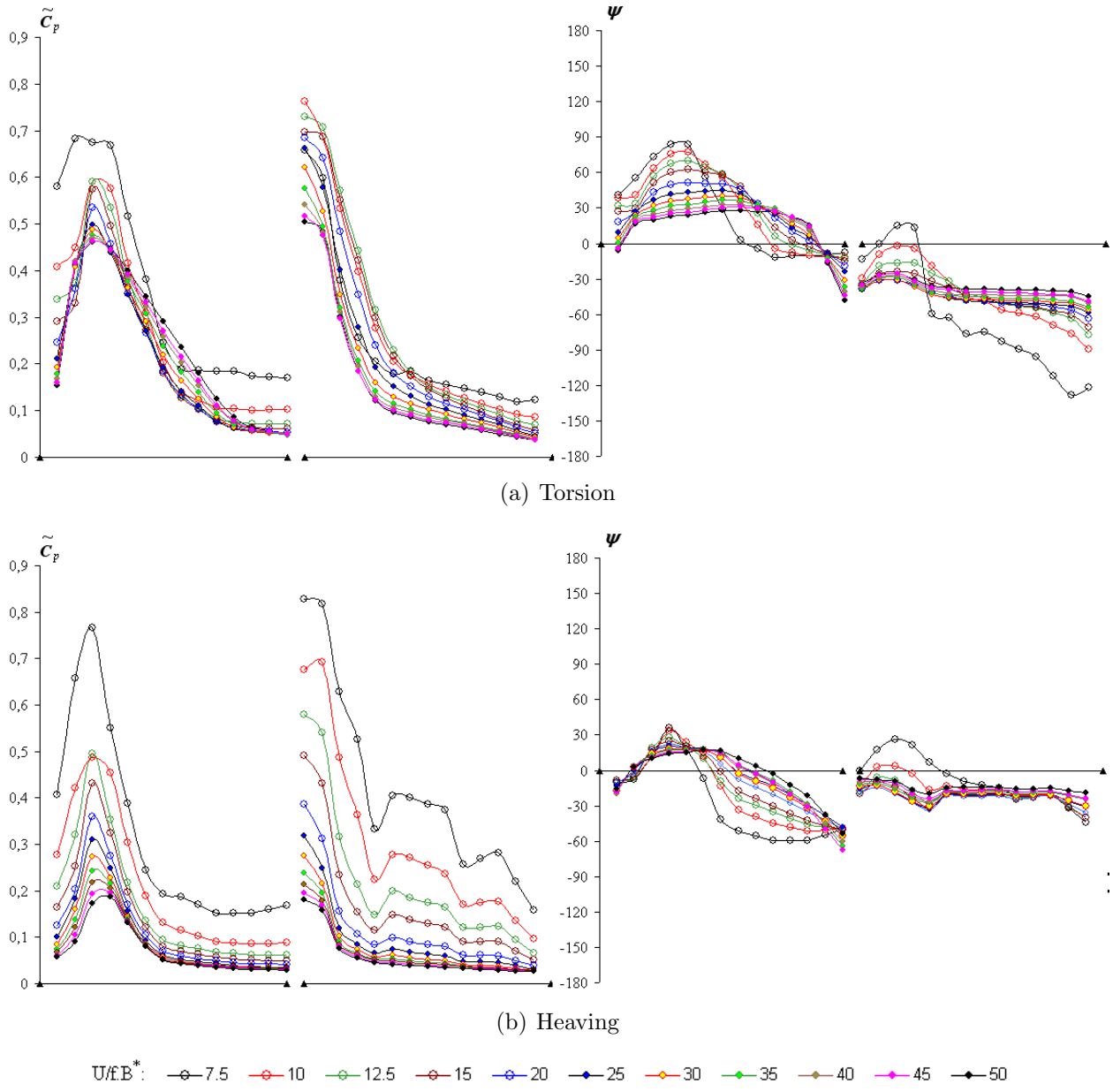

(a) Torsion

(b) Heaving

Figure 6.8: case $3.0B^*$: two-box B^*/D=20 with gap=$3.0B^*$

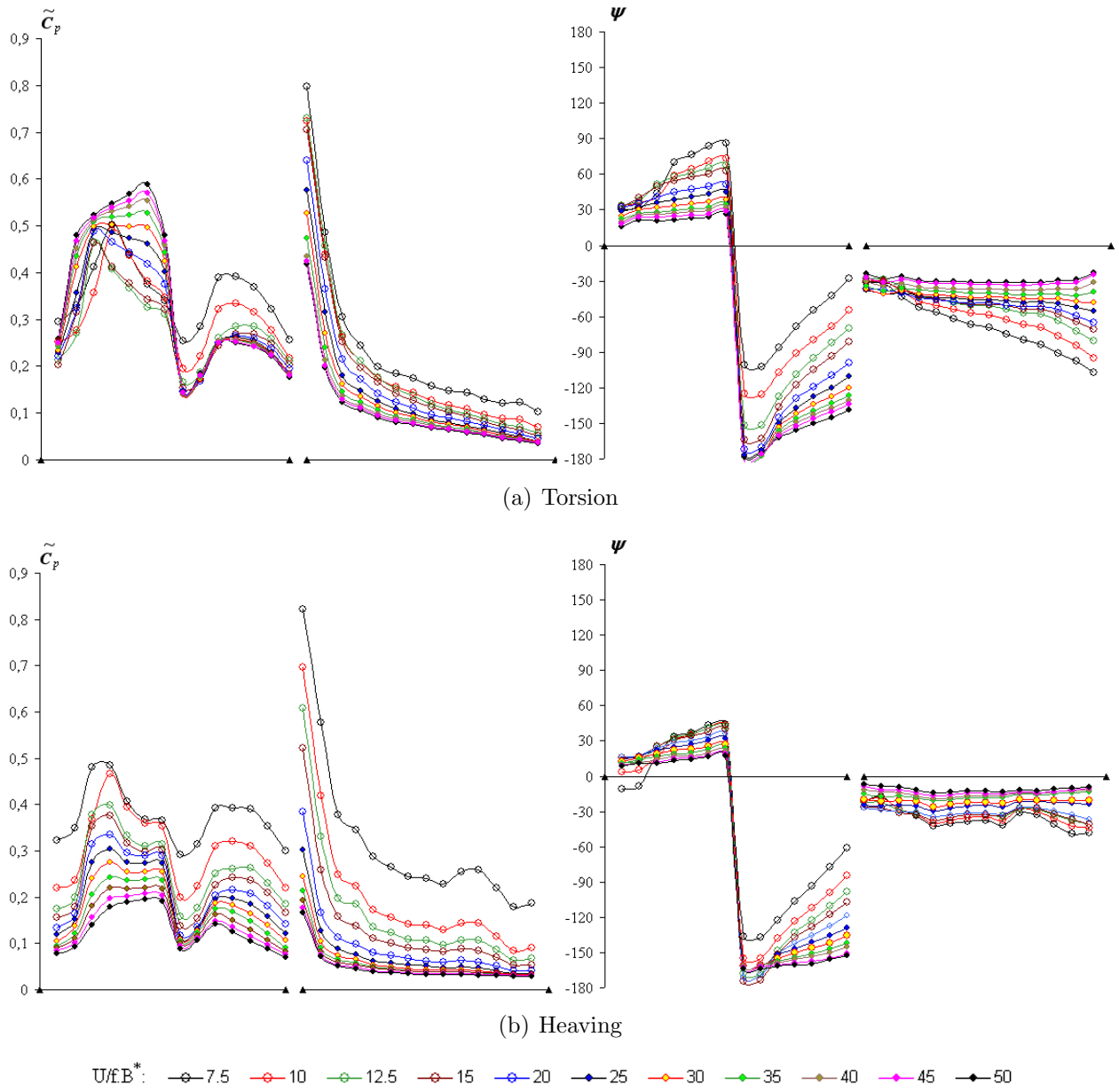

(a) Torsion

(b) Heaving

Figure 6.9: case $1.0B^*$_VL: two-box B^*/D=20 with gap=$1.0B^*$ and vertical plate in the leeward box

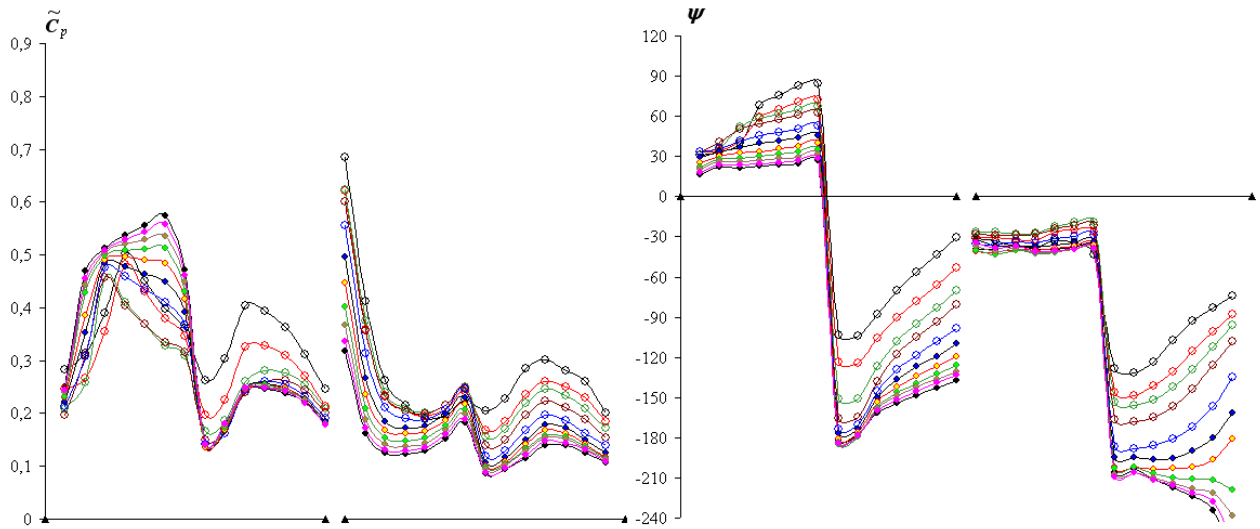

(a) Torsion

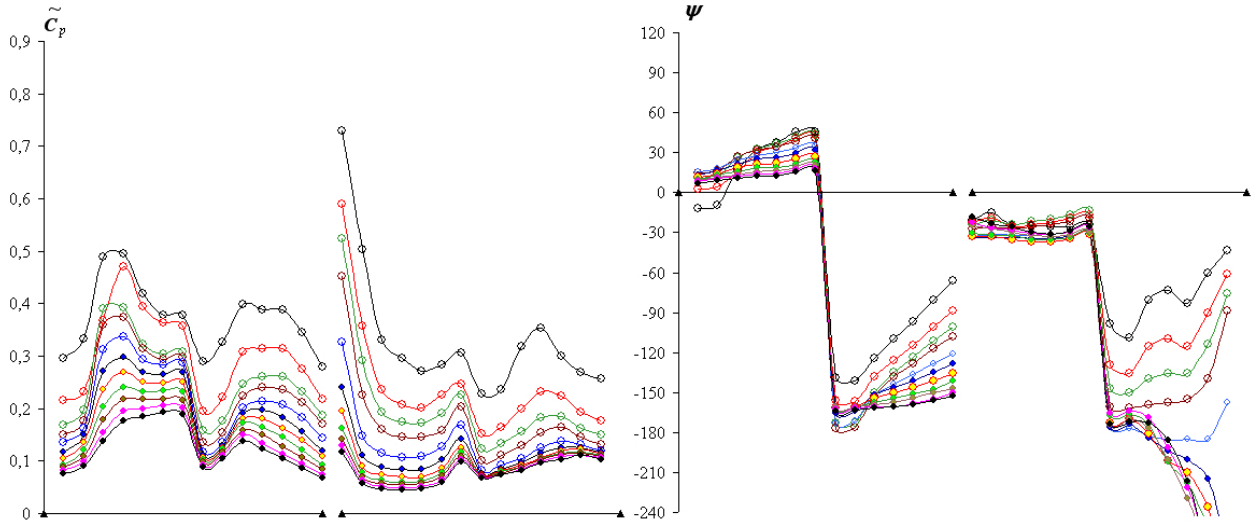

(b) Heaving

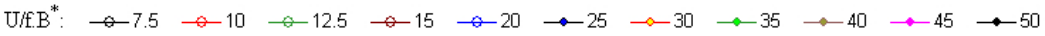

Figure 6.10: case $1.0B^*$_VB: two-box B^*/D=20 with gap=$1.0B^*$ and vertical plate in the both boxes

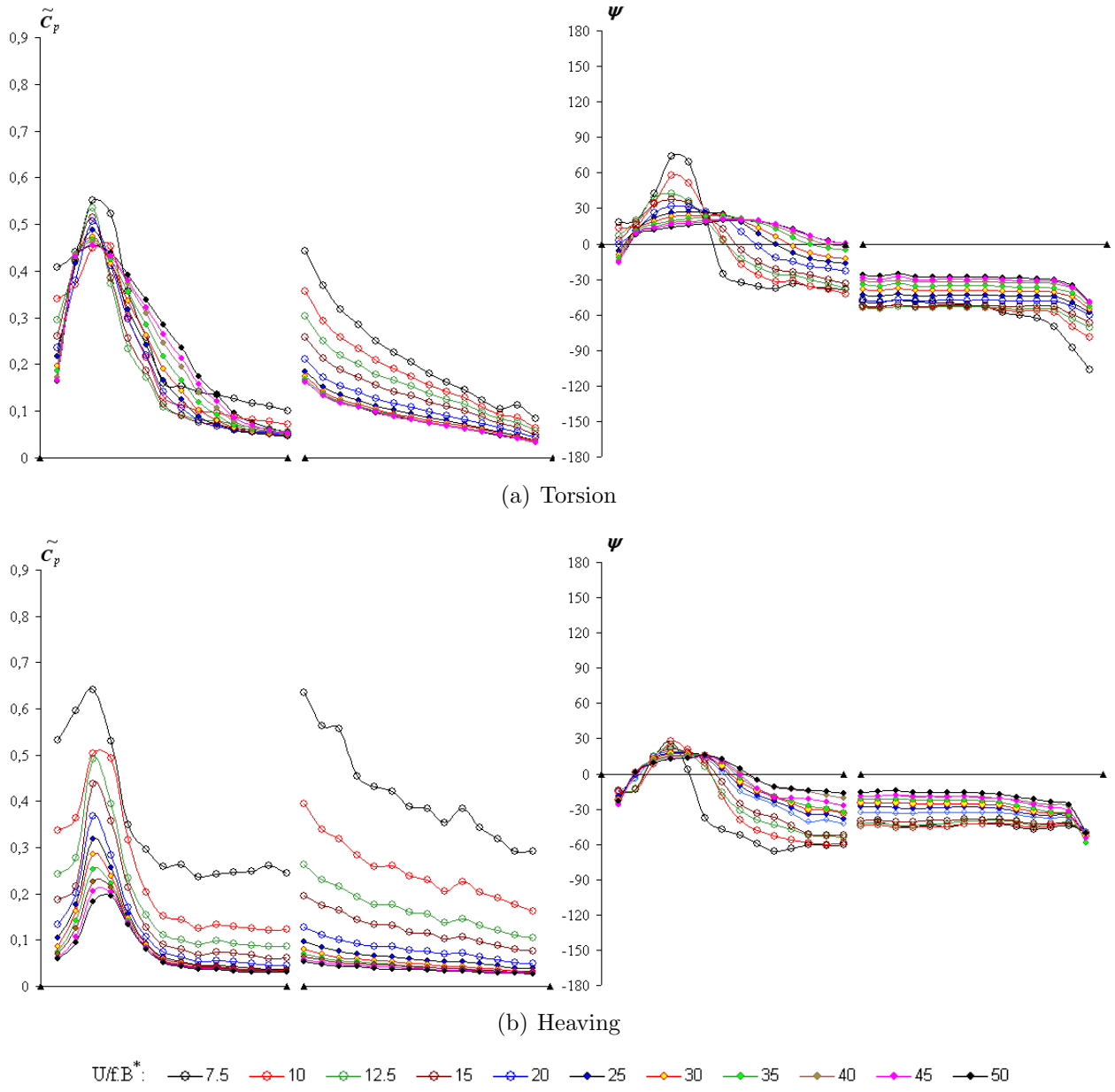

(a) Torsion

(b) Heaving

Figure 6.11: case $1.0B^*$_G: two-box B^*/D=20 with gap=$1.0B^*$ and grating

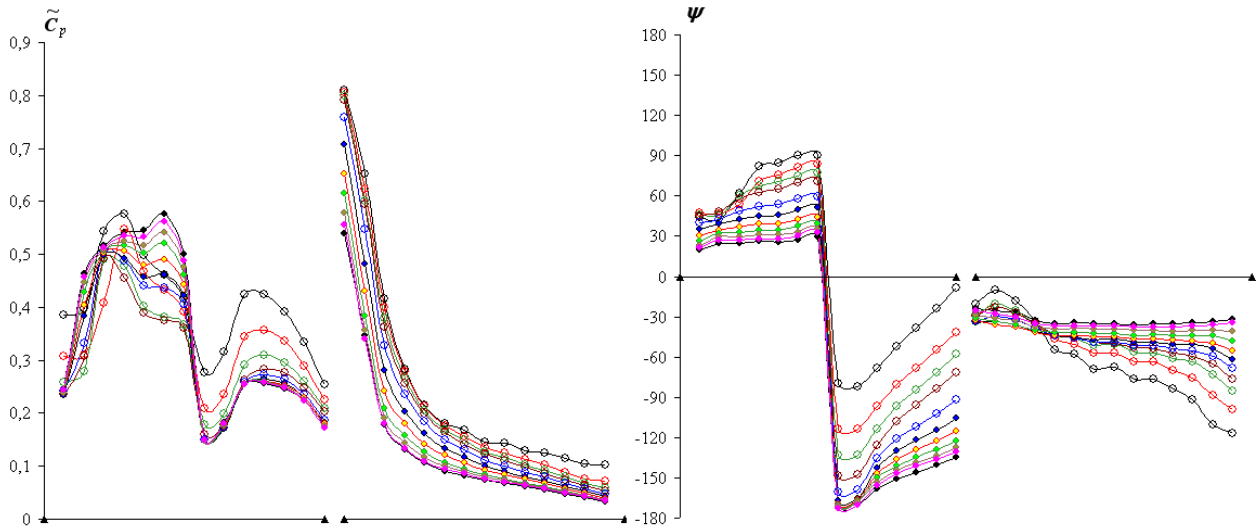

(a) Torsion

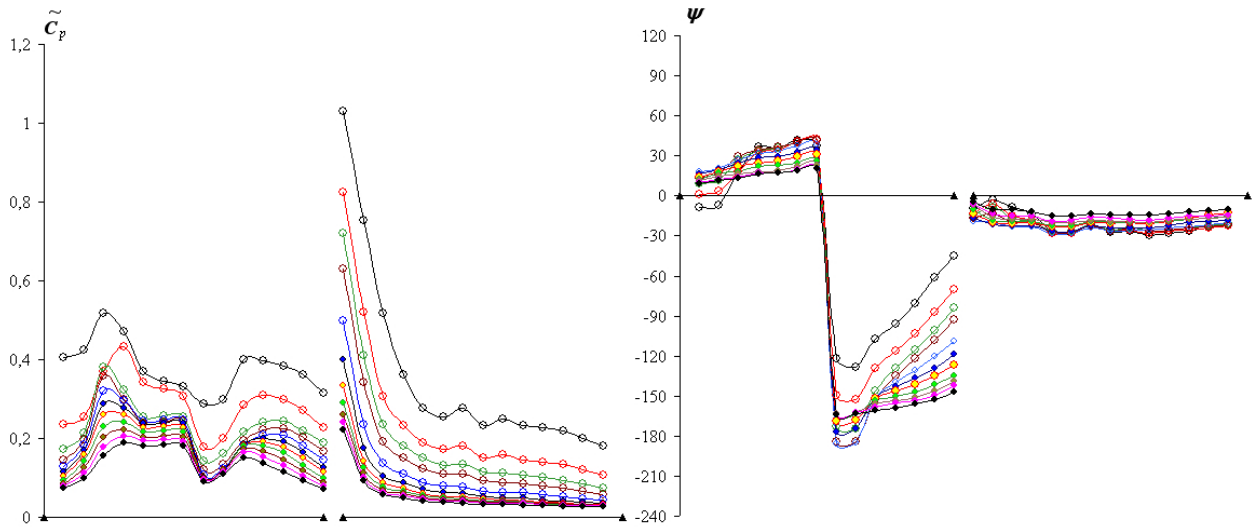

(b) Heaving

Figure 6.12: case $2.0B^*$_VL: two-box B^*/D=20 with gap=$2.0B^*$ and vertical plate in the leeward box

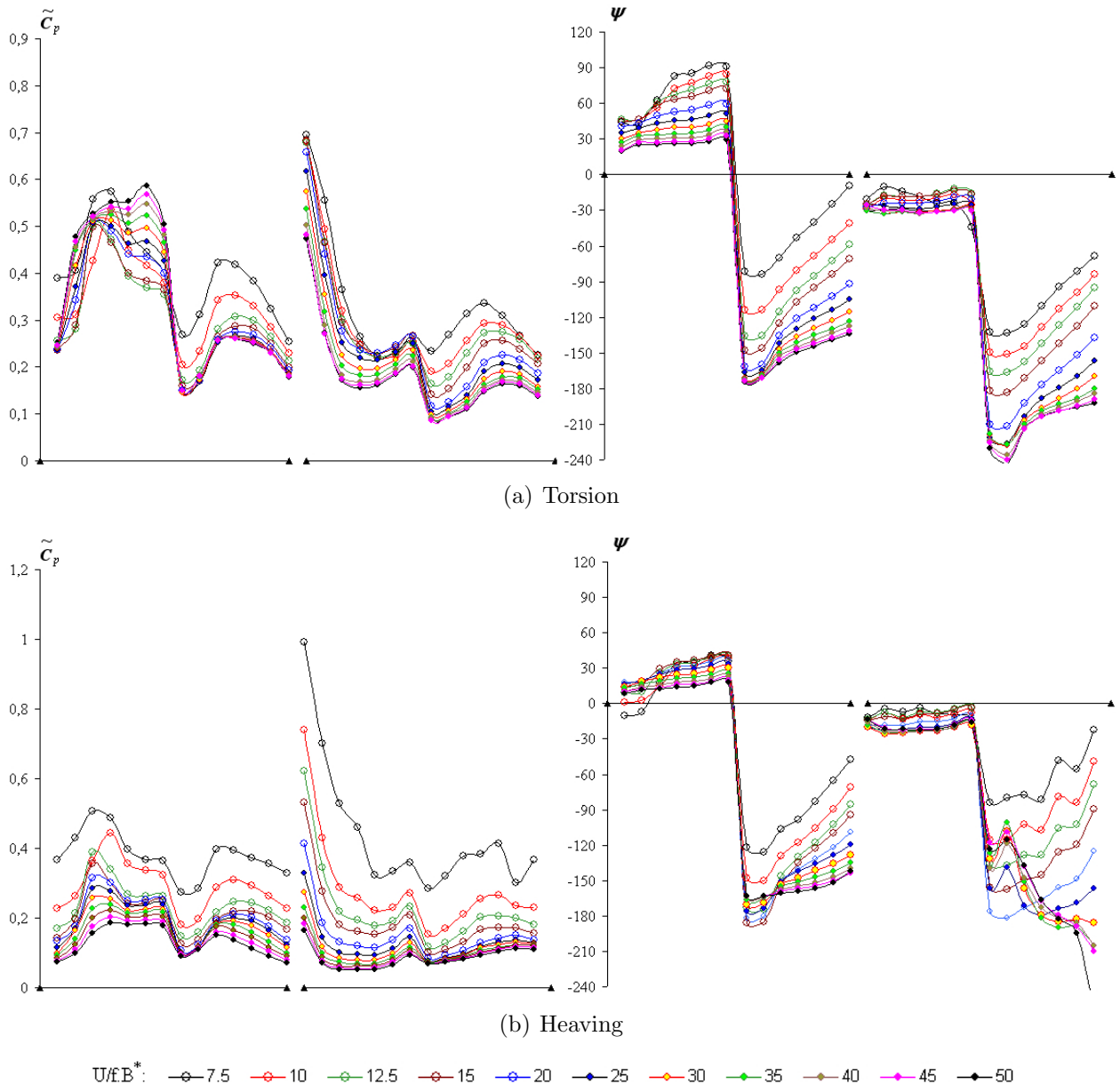

(a) Torsion

(b) Heaving

Figure 6.13: case $2.0B^*$_VB: two-box B^*/D=20 with gap=$2.0B^*$ and vertical plate in the both boxes

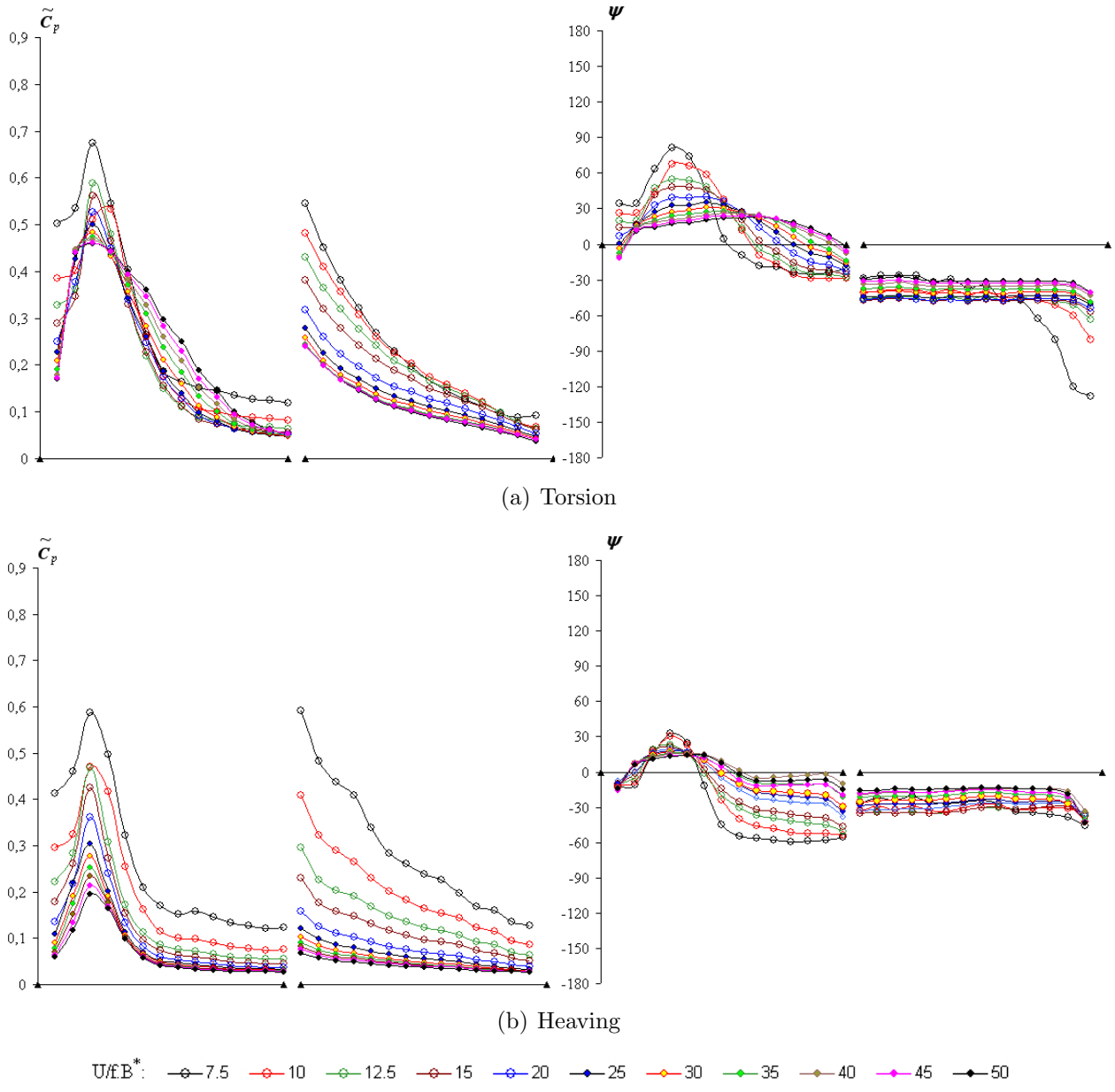

(a) Torsion

(b) Heaving

Figure 6.14: case $2.0B^*$_G: two-box B^*/D=20 with gap=$2.0B^*$and grating

6.3 Overall Analysis

The influences of the gap and of the consequent increase of the total width of the cross-section on the unsteady pressure characteristics of two-box cross-sections composed by B^*/D=20 rectangular cylinders present themselves differently when heaving and torsional systems are compared, breaking the aerodynamic derivatives interdependence.

For the upstream box, the unsteady pressure amplitude $\tilde{C}_p(x^*)$ distributions barely change with the increase of the gap length in both heaving and torsional systems; however, on the phase difference $\psi(x^*)$ distributions the impacts of changing the gap length are quite remarkable. The general aspect of the curves of the phase difference $\psi(x^*)$ distributions is very similar; however, with the increase of the gap length they exhibit a stretching effect, accompanied by a positive *bias effect* in the torsional system.

Comparing the unsteady pressures amplitude $\tilde{C}_p(x^*)$ distributions of the upstream box, Fig.6.1 to Fig.6.14, with the wind tunnel test results of the single B/D=20 rectangular cylinder reported in Fig.4.10, it is possible to verify that the peaks assume similar values for the same reduced wind velocities and their locations agree quite well with the relationship x_0^*=4.4D, also presented in B/D=20 rectangular cylinders. In addition, the shape of the curves can be approximated by an *Weibull distribution*, Eq.4.5, and the broadening of these distributions, which was regarded to an increasing of the *circular wave number* of the phase difference $\psi(x^*)$ distributions and related to the wave length in Chapter 4, can also be observed.

In terms of equations of motion, both boxes of a two-box cross-section oscillating in heaving motion are synchronized and can be represented by the same equation, i.e. a sinusoidal 1 DOF harmonic heaving motion. However, when the system is oscillating in torsion, a 2 DOF system composed by heaving and torsional simultaneous oscillations must be considered for each box. For the upstream box, the torsional motion lags the heaving motion by a phase difference of 90°, and in the downstream box the opposite occurs; in other words, it would be the same as affirming that the heaving motions of the boxes are separated by a phase difference of 180° between each other.

Matsumoto [82] suggested that for B/D=20 rectangular cylinders the resulting unsteady pressure characteristics of such a kind of 2 DOF system would be the resultant of a composition of the pressure characteristics of the two motions, which through a superposi-

tion of effects would produce the final unsteady pressure characteristics of the system. This explains in part the increasing of the differences between the unsteady pressures characteristics of heaving and torsional systems in two-box cross-sections as the gap length increases; with the increase of the gap length, the amplitude of the vertical degree of freedom motion of the torsional system also increases, enhancing its influences on the final result.

Primarily it would be thought that the gap in two-box cross-sections induces modifications in the flow circulation, making the boxes behave separately as a composition of 2 DOF motions, being the superposition of effects regarded to an aerodynamic effect due to the existence of the gap. However, by comparing the distributions obtained for the cases in which grating was used in the gap ($1.0B^*$_G and $2.0B^*$_G) with the unsteady pressure characteristics of the same cross-sections without grating ($1.0B^*$and $2.0B^*$), only slight changes can be observed. Basically, the differences are presented in the peak of the amplitude $\tilde{C}_p(x^*)$ of the downstream box, both in heaving and torsional motions, and no effect at all is produced in the upstream box.

A tentative explanation for that supposed superposition of effects might be regarded to a kind of "arm length" effect, which is not exclusivity of *pure* two-box cross-sections. The changing in the configuration of $\psi(x^*)$ must be related to the non-dimensionalized distance from the center of motion where the pressure signals are measured, resulting in that every cross-section that is slender enough to present relative large non-dimensionalized displacements would present the same effect, by getting its phase difference distribution deformed.

When compared to single-box B/D=20 rectangular cross-sections, Fig.4.10, the unsteady pressure characteristics of the upstream box show strong similarities, in both systems and for both phase difference and amplitude distributions. As for the downstream box, the aerodynamic characteristics are still an open issue in the aerodynamic study of bridges. The influences of the turbulence and of the vorticity generated by the motion of the upstream box, with their inherent dependencies on the shape of the cross-sections and on the characteristics of the gap, impose a complex combination of variables not possible yet to be integrated into simple formulations, resulting in different patterns, compared to the upstream box.

In order to have a glance of these differences, Fig.6.15 [7] shows the results in terms of instantaneous streamlines of CFD simulations on a two-box cross-section formed by B^*/D=5 rectangular cylinders with gap length = $1.0B^*$, in torsional motion at position φ= +2° at two different reduced wind velocities. By comparing this figure with the results produced

in this chapter, Fig.6.1 to Fig.6.14, it is possible to identify some common patterns, even considering that the side ratios of both cases are different. The flow seems to be almost fully attached to the upper surface of the downstream box, being regarded to low levels of velocity fluctuation (Fig.6.15), and this can be related to the nearly constant values of phase difference observed in the downstream box of the models of this Chapter (Fig.6.1 to Fig.6.14).

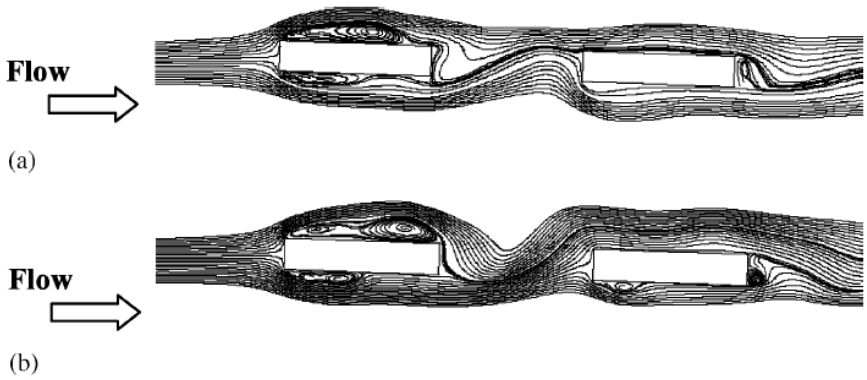

Figure 6.15: Instantaneous streamlines in torsional motion at position φ= +2° of two-box cross-section formed by B^*/D=5 rectangular cylinders with gap length = $1.0B^*$, at (a) U/f.B_{2box}= 5 and at (b) U/f.B_{2box}= 15, extracted from [7]

For single box cross-sections, it has already been verified that the turbulence of the oncoming flow influences the mean pressure distribution by increasing its maximum negative peak and "moving" the distribution upstream, steepening the pressure recovery [106]. This phenomenon is also "felt" by the unsteady pressures amplitude distribution, which shows a similar behavior [124]. In terms of phase difference, the turbulence of the flow induces a reduction of the ondulations length that can be mapped into Eq.4.2 through a decrease in the values of ω_ψ and A_ψ. The graphical response for these modifications is a softening of the distributions towards a straight line. That is exactly what can be noticed in the phase difference distributions of the downstream boxes of Fig.6.1 to Fig.6.14.

This nuance can be illustrated through Fig.6.16, extracted from a study about the effects of turbulence on the unsteady pressure characteristics of B/D=6.67 rectangular cross-sections [5]. This figure shows the comparison between phase difference distributions obtained in different reduced wind velocities, i.e. *3.1*, *8* and *20*, with different levels of longitudinal turbulence intensity, i.e. smooth flow, $I_u = 6\%$ (Case 6a) and $I_u = 12\%$ (Case 12a).

With the increase of the turbulence intensity (left to right) the phase difference distributions tend to become straight lines.

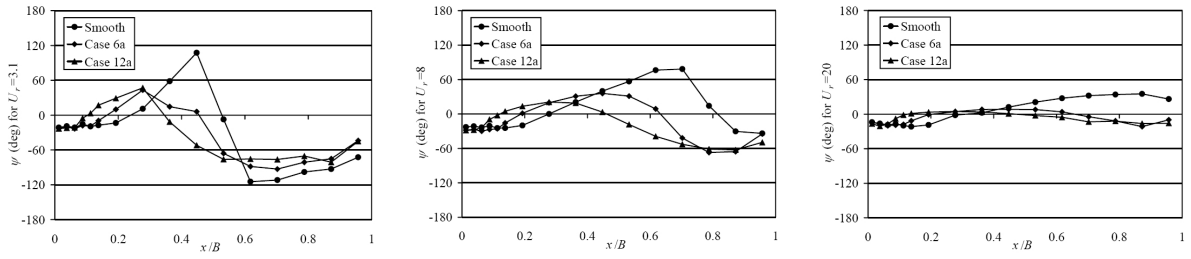

Figure 6.16: Phase difference $\psi(x^*)$ distribution for different levels of turbulence in B/D=6.67 rectangular cylinders

These effects are associated to the reduction of the spanwise correlation of the wind loads, which is also referred to a reduction of the spanwise coherence in the associated aerodynamic derivatives [58]. The net result of all that is translated into aeroelastic stabilizing effects. However, for a larger 3turbulence *scale*, the effects might be different, resulting in an increase of the spanwise coherence of the loads [100].

With the gradual increasing of the gap length, the influences of the upstream box on the downstream box get reduced, leading the unsteady pressure characteristics of the downstream box to exhibit characteristics of a single box. For the amplitude distribution this tendency is very clear, for both heaving and torsional systems; however, for the phase difference the behaviors are different according to each system. Although in the heaving motion the tendency is more prominent, with almost a complete absence of the effects of the gap in the phase difference $\psi(x^*)$ distribution for the lowest reduced wind velocity of the model $3.0B^*$, in the torsional system the *arm length effect* plays an important role and should be considered.

In studies with parallel bridges, it has already been accounted for wake effects for separation distances as long as 8 times the deck width [15] and although in practical terms such a situation probably will never be experienced in real two-box bridges, the aerodynamic effects of the gap on the downstream box of the models could be felt even for gap lengths as long as $3.0B^*$.

Despite the non applicability of such a long gap length for two-box cross-sections, by analyzing the tendencies exhibited by the phase difference $\psi(x^*)$ and amplitude $\tilde{C}_p(x^*)$

distributions with the increase of the gap length, it is possible to check tendencies and catch important information to be used in the manipulation of the unsteady pressure characteristics of two-box cross-sections with shorter gaps, closer to real cases. With that objective in mind, the following analyses were conducted, focusing on clarifying the role played by the gap on the flutter stability as a *geometric singularity* to be considered in the manipulation of the unsteady pressure characteristics of bridge decks.

6.4 Aerodynamic Derivatives

The aerodynamic derivatives for all cases reported in Fig.6.1 to Fig.6.14, calculated through the formulation introduced in Section 2.3.1, are shown in Fig.6.17 and Fig.6.18, corresponding to the reduced wind velocities normalized by the total width of the resulting cross-sections, Eq.6.2. The theoretical values provided by the Theodorsen function, Eq.2.31 to Eq.2.38, are also available for comparison purposes.

$$U_{r_{2box}} = \frac{U}{f.B_{2box}} \tag{6.2}$$

where: B_{2box} is the total width of the two-box cross-section, defined by B_{2box}= 2.B^*+ gap length

The set of wind velocities used in the wind tunnel tests for the acquisition of the data was the same for all configurations of models. This decision was made as an attempt to equalize the impacts of the Reynold's number effects on the unsteady pressure characteristics of the individual boxes, since the main focus of this investigation is exactly on the effects of the gap on the unsteady pressure characteristics of each box. In doing so, the reduced wind velocities calculated through Eq.6.1 provide the same values for all wind velocities, regardless the gap length, and the effects of the gap can be isolated in the differences presented by the unsteady pressure characteristics among the models, which are comparable among all the velocity range, box by box.

However, considering a reduced wind velocity normalized by the total width of the cross-section, according to Eq.6.2 and as used to build Fig.6.17 and Fig.6.18, the aerodynamic

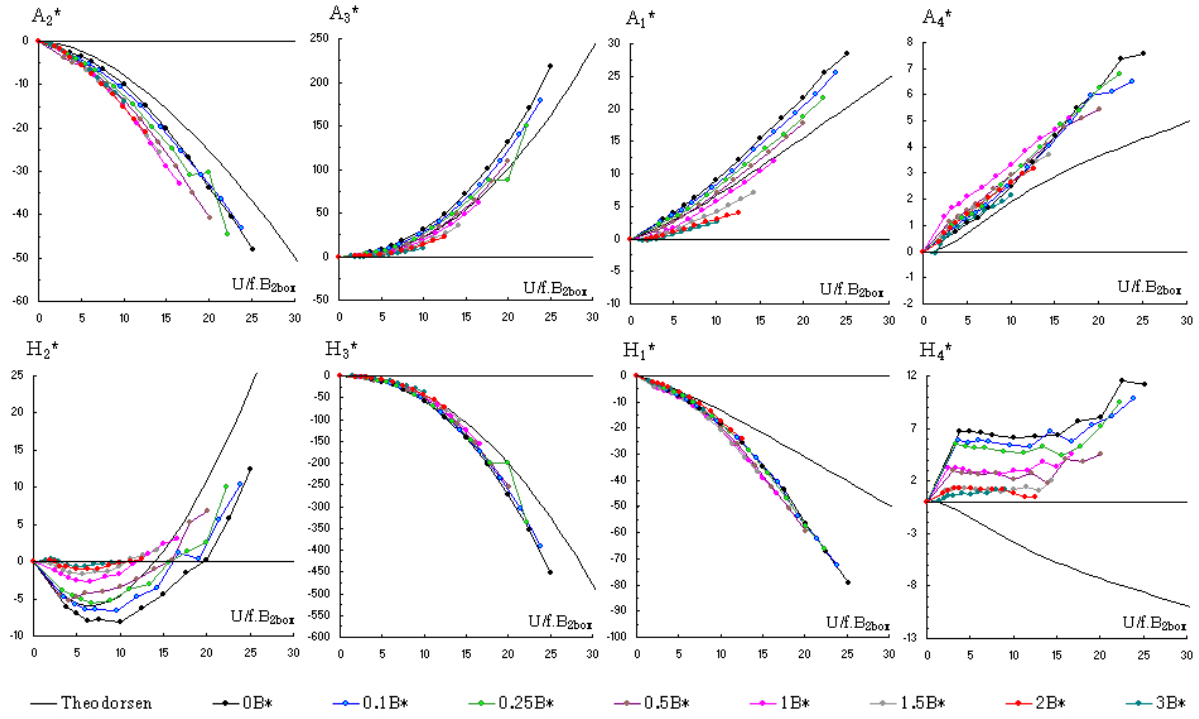

Figure 6.17: Aerodynamic derivatives for two-box cross-sections, not considering the *geometric singularities*

derivatives exhibit different *velocity scales*. For the same wind velocity U, with the increase of the gap length the reduced wind velocities get their values reduced. As a consequence, the comparison between different models can be established only in the lower reduced wind velocity range, since for the models with longer gap lengths the maximum reduced wind velocity is in that range.

Nevertheless, some general conclusions can be drawn from the results reported in Fig.6.17 and in Fig.6.18, considering the tendencies assumed by the aerodynamic derivatives in the lower reduced wind velocity range.

For the cases in Fig.6.17, the increase of the gap length induced a reduction on the absolute values of all aerodynamic derivatives, more or less prominently according to each derivative. For the H_i^* derivatives, this effect was stronger for the *sine* components of the phase difference $\psi(x^*)$ distribution, i.e. H_2^* and H_4^*, and less visible for the *cosine*

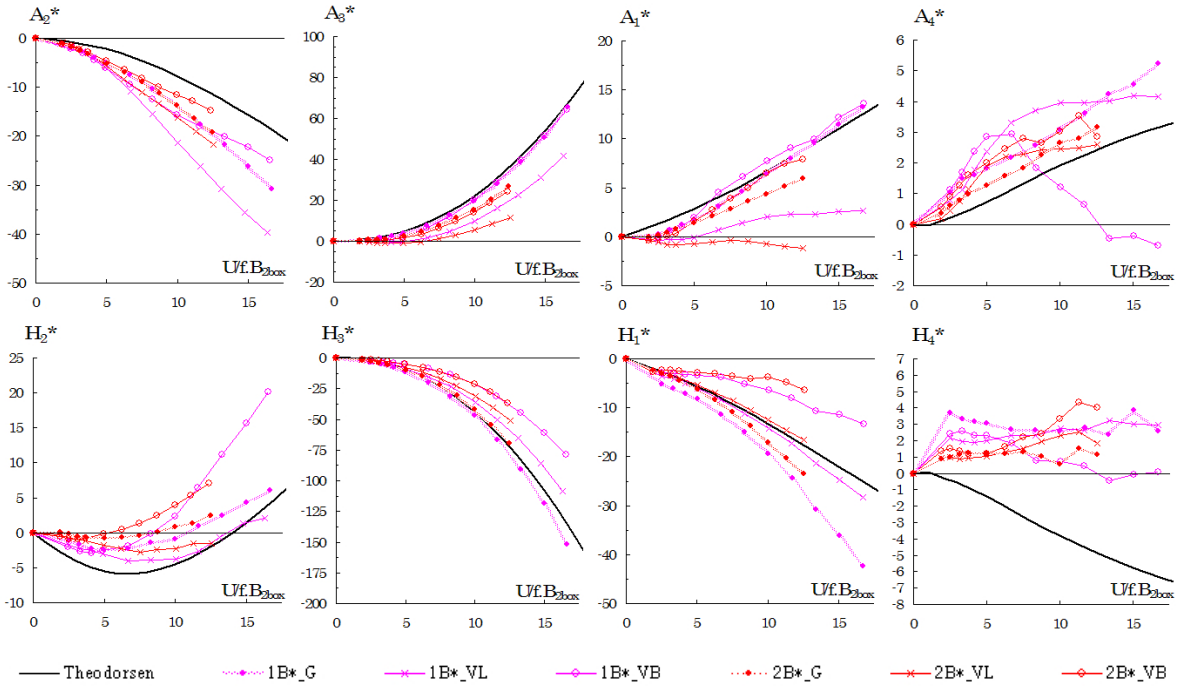

Figure 6.18: Aerodynamic derivatives for two-box cross-sections, considering the *geometric singularities*

components, i.e. H_1^* and H_3^*. As for the A_i^* derivatives, although the effects were more visible in A_1^*, all derivatives presented considerable impacts. The derivative A_2^* presented a particular effect, by getting its absolute values increased with the increase of the gap length until the gap length $= 1.0B^*$, from where the tendency is inverted and the values start to decrease with the increase of the distance between boxes.

Considering the impacts of the aerodynamic derivatives on the flutter stability as in Table 3.1, it is noted that the benefits of the increase of the gap length are mostly related to the impacts it has on the moment components related derivatives, i.e. A_1^*, A_2^* and A_3^*, which can be considered beneficial until the gap length $= 1.0B^*$. In terms of H_1^* and H_3^* the increase of the gap length could not show a major influence, being regarded to secondary effects.

The results reported in Fig.6.18 show more complicated tendencies, harder to be rationalized as done for the cases of Fig.6.17; depending on the gap length, on the arrangements

of the vertical plates and on the use of grating, different tendencies are exhibited for the same gap length. However, a point in common in all derivatives is that the increase of the gap length enhances the effects of the *geometric singularity*.

This complexity in terms of aerodynamic derivatives caused by the interaction between different *geometric singularities* undermines the study of the impacts of geometric modifications on the flutter stability from an aerodynamic derivatives point of view, reinforcing and corroborating the motivation of doing so from an unsteady pressure characteristics point of view.

A more accurate representation of the tendencies imposed by the increase of the gap length on the values of the aerodynamic derivatives can be obtained by presenting the results considering the reduced wind velocities calculated through Eq.6.1. However, in that case the aerodynamic derivatives present *scale distortions* and should be read with care. Fig.6.19 presents the results for all models investigated in this chapter, with the theoretical values (through Theodorsen function) calculated for the half width b.

In Fig.6.19, the reduction of the absolute values of all derivatives with the increase of the gap length gets clearer, even for A_2^*. Although in the models with no *geometric singularities* (vertical plates and gratings) this tendency is quite linear, for the models with *geometric singularities* the relationships between *geometric singularities* and gap length show more complicated patterns, as already pointed out in Fig.6.18. For some derivatives, i.e. A_1^*, H_1^*, H_2^* and H_4^*, although the gap length tends to show more relevant effects and to control the tendencies, the relationships show non linear behaviors. As a consequence, every comparison that might be established at this level would be based on a *case by case* approach, in which all characteristics of the cross-section should be taken in consideration as a whole.

The Theodorsen function has been a benchmark in terms of aerodynamic derivatives in the studies of bridge decks. However, it does not include the effects caused by the aerodynamic interference due to the existence of the gap neither the impacts on the normalized dimensions of the reduction of the solidity ratio with the increase of the gap length. Because of that, its use with two-box girders should be considered with some reserve.

Since the values of the derivatives are calculated by considering a normalized deck width $B = 2$, which is kept constant regardless the gap length, the contributions of the opaque surfaces where the pressures are measured for the composition of the final value of the derivatives get proportionally reduced. A direct consequence of that, in terms of numerical

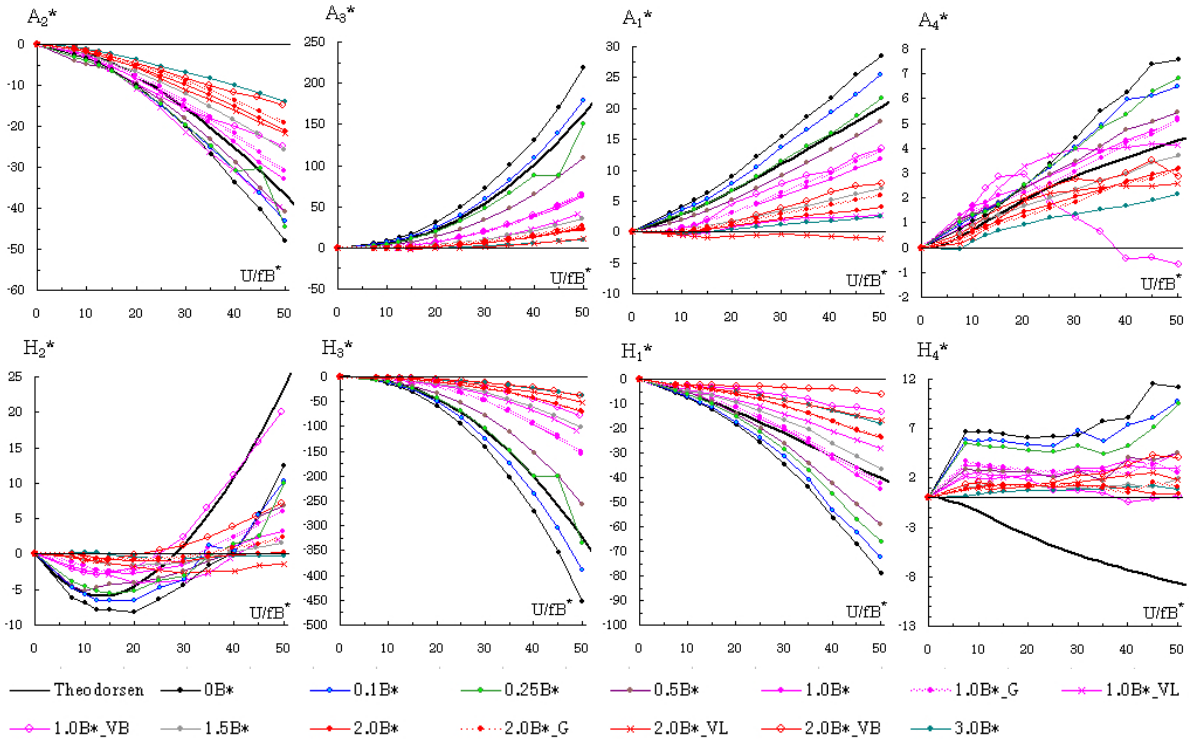

Figure 6.19: Aerodynamic derivatives for two-box cross-sections considering reduced wind velocity normalized by B^* (Eq.6.1)

results, is the deformation of the proportionality between the different models, represented by the tendency of reduction of the absolute values of all aerodynamic derivatives with the increase of the gap length, visible in all cases of this section.

This *deformation* hides the aerodynamic effects of the gap on the whole system. So a better approach would be based on the individual comparison between each model and a standard adapted to include this changing in the solidity ratio of the models, i.e. equivalent Theodorsen function adapted for two-box cross-sections. By comparing the deviations from this new standard, case-by-case, the real aerodynamic influences of the gap length can be better identified.

The adaptation of the Theodorsen function to be used with two-box cross-sections can be attained by considering a system composed by two plates symmetrically disposed around a pivot point, whose midchord points are spaced by a distance a from the center of rotation.

This can be obtained by considering the arm length a in Eq.2.20 to Eq.2.27 as the result of *b+gap length/2*, followed by the necessary adjustments in the reference reduced wind velocity considering that B^* becomes b for gap length = 0, which finally leads to Eq.6.3 to Eq.6.10.

$$k.H_1^* = 2.[-2.\pi.F(k)] \tag{6.3}$$

$$k.H_2^* = 2.\left[-2.\pi.\left(\frac{F(k)}{2} + \frac{G(k)}{k} + \frac{1}{2}\right)\right] \tag{6.4}$$

$$k.H_3^* = 2.\left[-2.\pi.\left(\frac{F(k)}{k} - \frac{G(k)}{2}\right)\right] \tag{6.5}$$

$$k.H_4^* = 2.[2.\pi.G(k)] \tag{6.6}$$

$$k.A_1^* = 2.[\pi.F(k)] \tag{6.7}$$

$$k.A_2^* = 2.\left[\pi.\left(\frac{-F(k)}{2}.(4.a^2 - 1) + \frac{G(k)}{k} - \frac{1}{2}\right)\right] \tag{6.8}$$

$$k.A_3^* = 2.\left[\pi.\left(\frac{F(k)}{k} - \frac{G(k)}{2}.(1 - 4.a^2)\right)\right] \tag{6.9}$$

$$k.A_4^* = 2.[-\pi.G(k)] \tag{6.10}$$

In order to investigate the effects of the gap on the unsteady pressure characteristics through an aerodynamic derivatives point of view, a better comparison between models in a same figure can be tried by calculating the aerodynamic derivatives by considering only the pressure distribution of the boxes, assuming a value of *gap length = 0* in equations Eq.2.52

to Eq.2.59, so that the effects of the arm length and the solidity ratio in the results can be eliminated. By comparing with the equivalent theoretical equations adapted for two-box cross-sections, Eq.6.3 to Eq.6.10, and with the original Theodorsen function, Eq.2.31 to Eq.2.38, the aerodynamic effects of the gap on the unsteady pressure characteristics can be highlighted. The results for the basic cases, i.e. excluding vertical plates and gratings, are reported in Fig.6.20.

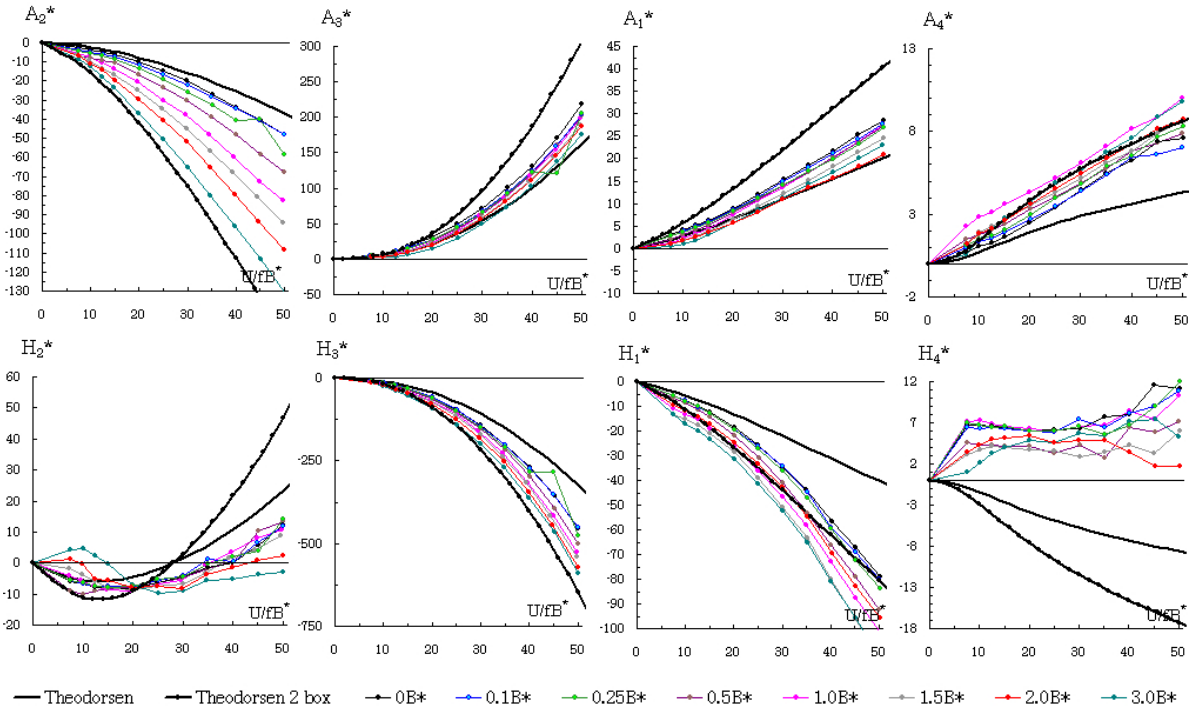

Figure 6.20: Aerodynamic derivatives, not considering the gap length in Eq.2.52 to Eq.2.59

The interpretation of Fig.6.20 is that the closer to the values of the adapted theoretical equations the aerodynamic derivatives are (and the farer from the original Theodorsen function), the smaller the aerodynamic effects of the gap on the unsteady pressure characteristics, since the adapted equations do not take them in consideration. Also, the smaller the oscillations of the values among different models for a same derivative, the smaller the aerodynamic effects of the variation of the gap length.

In this sense, the only aerodynamic derivative which shows a considerably high aerodynamic dependence on variations of the gap length is A_2^*, which gets its value closer to the adapted theoretical equation as the gap length increases. The other aerodynamic derivatives

seem to be not so strongly influenced by it, showing different tendencies: while H_1^* and A_4^* approaches the values of the adapted theoretical formulation, H_2^*, H_3^*, A_1^* and A_3^* are better correlated with the original Theodorsen function; H_4^* presents an independent behavior, similar to the one assumed by B/D=20 rectangular cylinders (Fig.4.9).

The same analysis can be performed with the cases in which *geometric singularities*, i.e. vertical plates and gratings, are used in the models. The results for these configurations are reported in Fig.6.21

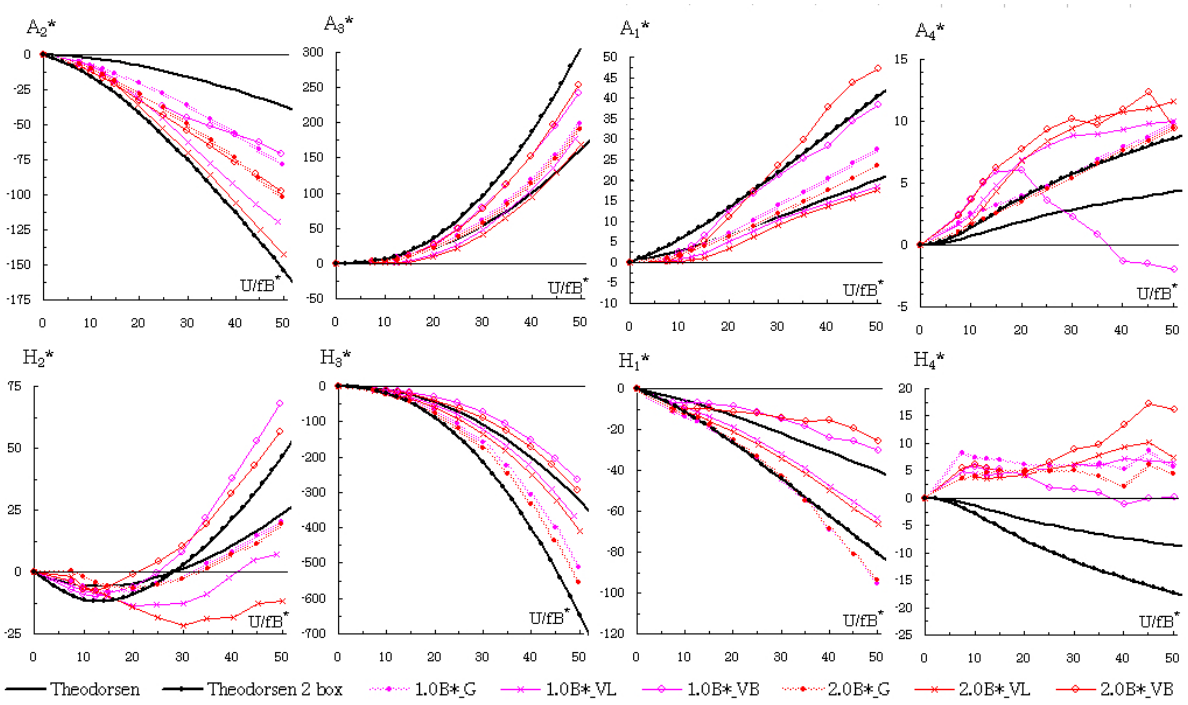

Figure 6.21: Aerodynamic derivatives with *geometric singularities*, not considering the gap length in Eq.2.52 to Eq.2.59

With the exception of A_2^*, the determinant factor for all derivatives was the type of singularity used, since regardless the gap length the curves were grouped two by two according to each one of the singularities. As a conclusion, it can be thought that the effects of the singularities used in the experiments on the unsteady pressure characteristics of the models were independent of the gap length, which plays a minor role in the process of aerodynamic interference, by only enhancing or attenuating the effects of the singularities through the consequent impacts on the solidity ratio and on the arm length used in the

calculation of the aerodynamic derivatives through Eq.2.52 to Eq.2.59. This point of view is indeed supported by the comparison in a singularity by singularity basis of the unsteady pressure characteristics reported in Fig.6.9 to Fig.6.14, which shows only small differences between configurations with the same singularity, even for different values of gap length. In the case of A_2^*, the gap length plays a more significant aerodynamic role for the definition of its final value.

Based on the analyses done on Fig.6.20 and Fig.6.21, it is concluded that the differences presented in Fig.6.17, Fig.6.18 and Fig.6.19 are more related to modifications in the solidity ratio and in the arm length (in the case of A_i^* derivatives) than to modifications on the unsteady pressure characteristics themselves, and this fact reinforces the argument that on the understanding of the effects of the geometric improvements on the flutter stability of a given cross-section the focus should be put on the unsteady pressure characteristics, not directly on the aerodynamic derivatives. Although the existence of the gap induces modifications on the unsteady pressure characteristics of the downstream box, the role of the variation of the gap length is regarded mostly to *mathematical effects* on Eq.2.52 to Eq.2.59, with low aerodynamic effects on the unsteady pressure characteristics of the models.

As a reminder, it must be kept in mind that in the construction of Fig.6.20 and Fig.6.21 the effects of gap length on the equations used to integrate the forces over the surface of the models were neglected. Because of that, the global effects of the gap can only be described by considering the results presented in Fig.6.17, Fig.6.18 and Fig.6.19, which should the ones used in flutter analysis.

6.5 Flutter analysis

Early researches in the development of the concept of perforated decks [38] have already accounted for the increasing of the flutter speed related to the use of such a kind of cross-section, in which two-box cross-sections are included. This improvement comes in the inverse proportion of the solidity ratio, which is a parameter that relates opaque and open surfaces.

A complementary explanation can be obtained by analyzing the unsteady pressure characteristics of Fig.6.1 to Fig.6.14. One of the important effects of the gap is the promotion of a peak in the amplitude distribution downstream the center of the motion, i.e. in the

leading edge of the downstream box, which was already recognized in Chapter 3 to bring stabilizing effects for flutter when associated to values of phase difference located in the *stable zone*.

In general terms, the importance of the downstream box in two-box cross-sections for the stability of the system increases proportionally with the increase of the gap length, since any peak in the amplitude distribution of that box will have its normalized distance from the center of motion increased. So with the increase of the gap length, if the phase difference $\psi(x^*)$ of the location of that peak is in a stable zone, the whole cross-section tends to become more stable; and in case the phase difference is not in a stable zone the cross-section may become unstable.

In order to verify that assumption, complex eigen-value flutter analyses were conducted for the models that produced the unsteady pressure characteristics of Fig.6.1 to Fig.6.14, by using the same structural and wind velocity parameters used in the analyses performed in Chapter 3, which presented among other factors a frequency ratio f_φ/f_η=1.3. Also, the theoretical onset velocities were calculated by using the aerodynamic derivatives calculated through Eq.6.3 to Eq.6.10, not showing instability for any gap length. The results are reproduced in Table 6.1 for the cases without singularities and in Table 6.2 for the cases with singularities, confirming that with the increase of the gap length the flutter tends to be avoided, since the peak at the leading edge of the amplitude $\tilde{C}_p(x^*)$ distribution of the downstream box, associated with "stable" values of phase difference, is automatically moved downstream.

Table 6.1: Flutter onset of two-box cross-sections, frequency ratio f_φ/f_η= 1.3

	$0B^*$	$0.1B^*$	$0.25B^*$	$0.5B^*$	$1.0B^*$	$1.5B^*$	$2.0B^*$	$3.0B^*$
Experimental	9.5 m/s	10.5 m/s	11 m/s	—	—	—	—	—
Theoretical	—	—	—	—	—	—	—	—

Although the presence of a vertical plate in the upstream box contributes for destabilization, due to the values of phase difference $\psi(x^*)$ induced by it, flutter does not occur. This can be explained by two reasons: the unsteady pressure characteristics of the model in locations upstream the vertical plate promote very high stabilizing effects, since the vertical plate creates a zone of high amplitudes $\tilde{C}_p(x^*)$ in its upstream, which associated with the stabilizing effects of the "stable" values assumed by the phase difference at that region con-

Table 6.2: Flutter onset of two-box cross-sections with vertical plates and grating, frequency ratio f_φ/f_η= 1.3

	$1.0B^*$_G	$1.0B^*$_VL	$1.0B^*$_VB	$2.0B^*$_G	$2.0B^*$_VL	$2.0B^*$_VB
Experimental	—	—	18.5 m/s	—	—	14 m/s
Theoretical	—	—	—	—	—	—

tributes strongly for the stabilization; also the downstream box presents very stable unsteady pressure characteristics.

However, the introduction of a vertical plate in the downstream box breaks the benefits caused by the upstream locations of the upstream box and also imposes values of phase difference considered not stable in the downstream box. As expected, the destabilization was more prominent in model $2.0B^*$, which has a larger gap length that consequently enhances the influence of the downstream box on the instability of the system.

Considering the influences of the arm length on the definition of the A_i^* derivatives, especially on A_2^*, the increase of the gap length enhances even more their effects, becoming another nuance of the aerodynamics of two-box cross-sections.

For the cases in which grating was used in the central gap, although the reduction of the peak of the amplitude of the unsteady pressure in the downstream box is expected to reduce the stability of the cross-section, the unsteady pressure characteristics of the whole system show themselves very stable, and flutter does not occur. Comparing the evolution of the damping with the increase of the wind velocity between cases with ($1.0B^*$_G and $2.0B^*$_G) and without grating ($1.0B^*$and $2.0B^*$), Fig.6.22 and Fig.6.23, a decrease in the level of damping can be indeed noticed in $1.0B^*$_G and $2.0B^*$_G cases in the torsional branch in the higher wind velocity range. However the amount of decrease is too small to be considered important and does not affect the stability of the cross-section.

In the theoretical case of a flat plate, whose aerodynamic derivatives are calculated through the original Theodorsen function, the components responsible for the aeroelastic forces are concentrated in the leading edge of the cross-section, due to the peak with "infinite" magnitude inherent to this theoretical cross-section in its amplitude $\tilde{C}_p(x^*)$ distribution. When two of such plates are disposed as the arrangement of two-box cross-section proposed

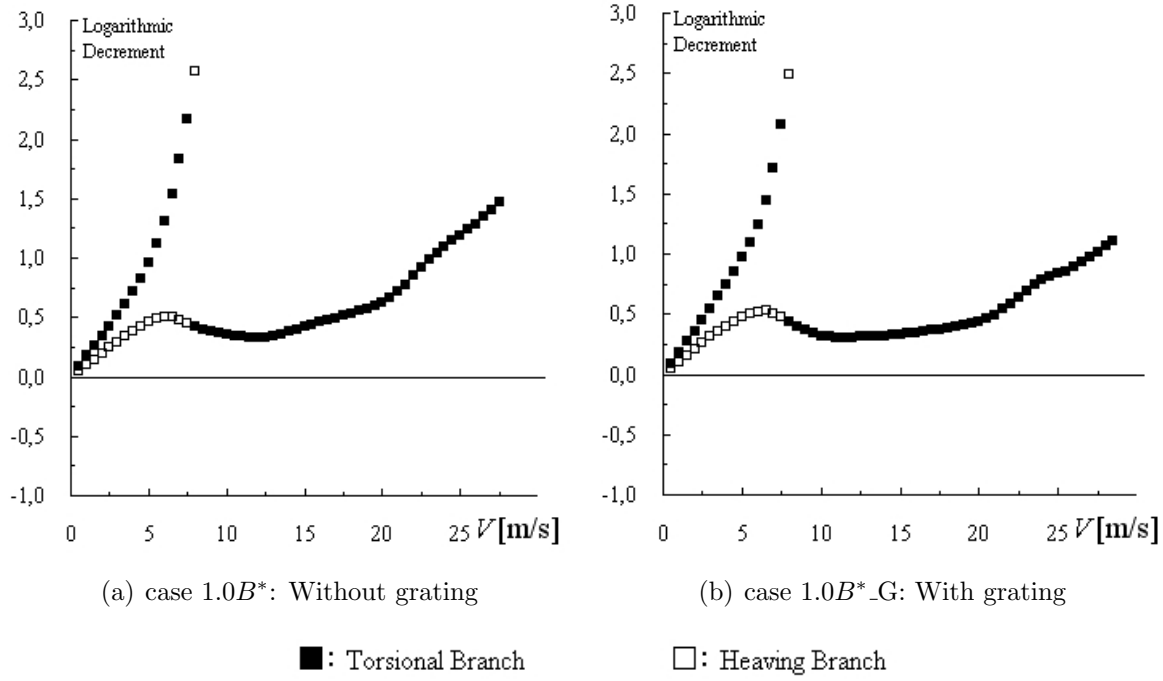

(a) case $1.0B^*$: Without grating

(b) case $1.0B^*$_G: With grating

Figure 6.22: damping for gap = $1.0B^*$

in Section 6.4 through Eq.6.3 to Eq.6.10, the same "infinite" peak will also be presented right downstream the midchord point, in a normalized distance from this midchord point that increases with the increasing of the gap length. According to the discussions of Chapter 3, this situation contributes for flutter stabilization and explains in part the fact that the theoretical values of aerodynamic derivatives have not exhibited flutter instability.

By tracing the evolution of the damping of the torsional branch (the most susceptible to destabilization for these cross-sections) with the increase of the gap length, it is possible to identify the influences of the gap length itself on the stability of two-box cross-sections, Fig.6.24. Since the aerodynamic characteristics of the plates are not affected by any aerodynamic interference (theoretical case), the only variable of the system is the gap length, with its influences on the normalized coordinates of the cross-section and on the distances from the rotation pivot. It shows that in the theoretical case the absence of the aerodynamic interference that would be caused by the upstream box on the downstream box stabilizes the flutter in two box cross-sections.

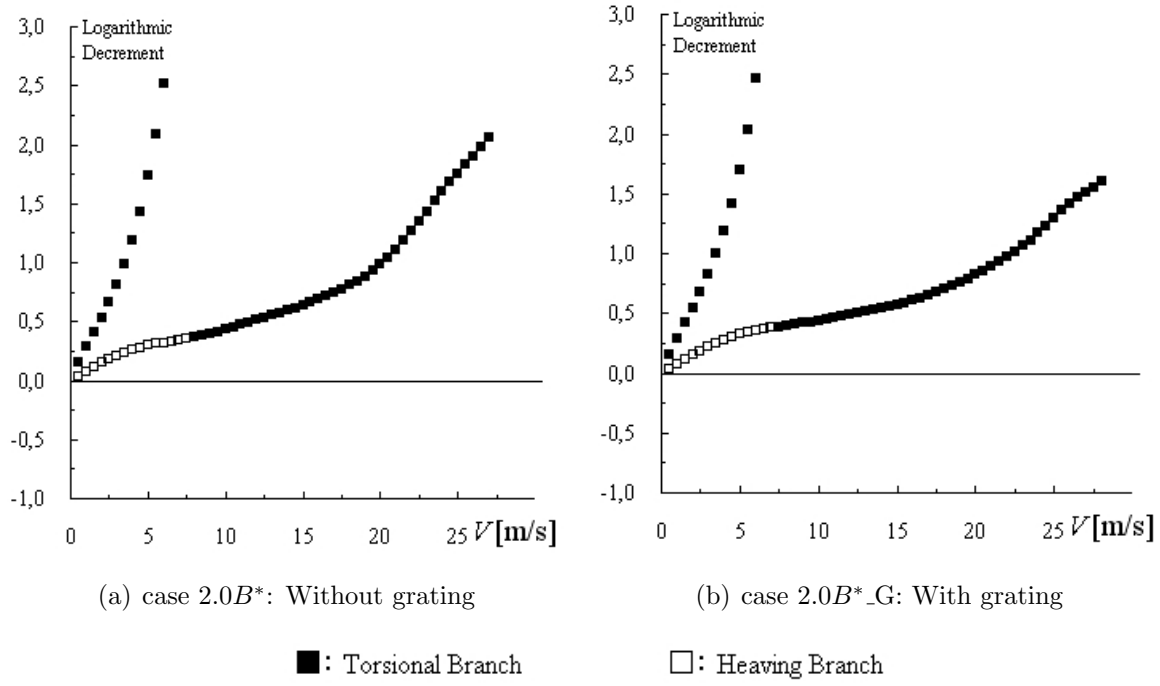

(a) case $2.0B^*$: Without grating

(b) case $2.0B^*$_G: With grating

Figure 6.23: damping for gap = $2.0B^*$

The conclusions drawn from the flutter analyses reported in Table 6.1 and Table 6.2 are important for the understanding of some direct relationships between gap length and flutter onset velocity. However, even considering that the frequency ratios f_φ/f_η of actual bridges have decreased lately, the value of *1.3* is still very conservative (vide Table 2.1). So a new series of flutter analysis was conducted by considering a broader range of values for f_φ/f_η, by keeping the other parameters unchanged though. The results are in Table 6.3 and Table 6.4.

Basically, the same conclusions obtained from Table 6.1 and Table 6.2 can be delineated for the results of Table 6.3 and Table 6.4, i.e. increase of the stability with the increase of the gap length, for both theoretical and experimental cases. Also, it is confirmed that with the increase of the frequency ratio f_φ/f_η the stability also increases, as already mentioned in Chapter 2, resulting in that for values of frequency ratio $f_\varphi/f_\eta > 2$ flutter occurs only in models with gap length $<1.0B^*$and with vertical plates in both boxes, for the same reasons explained before.

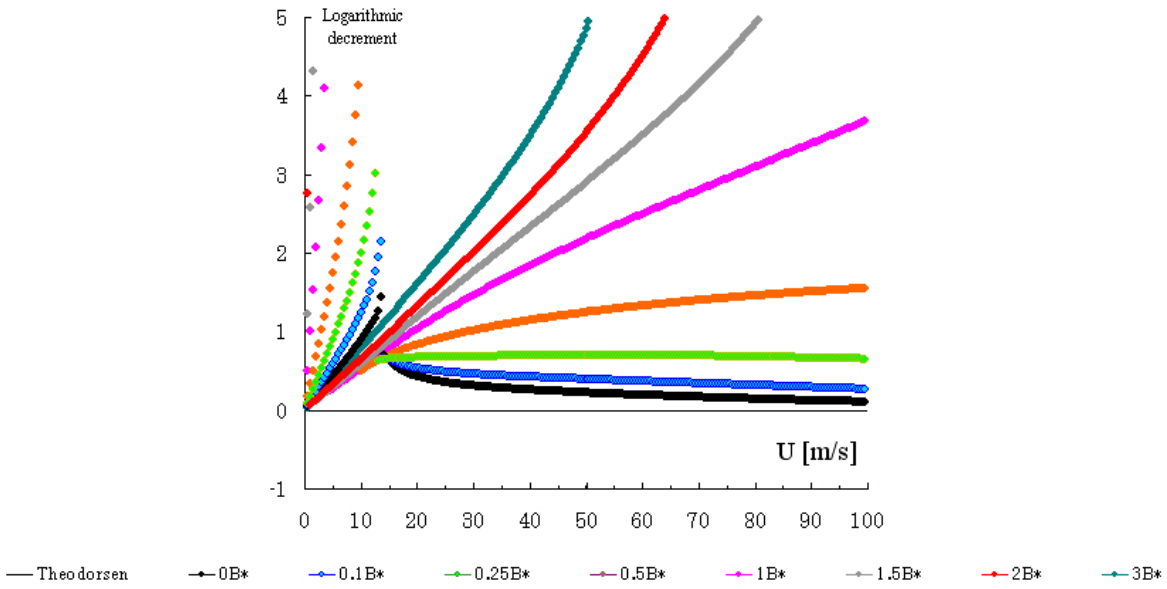

Figure 6.24: Logarithmic decrement of the torsional branch of two-box cross-sections with f_φ/f_η= 1.3

This time, model $1.0B^*$_G also exhibited flutter for higher frequency ratios, and the boundaries of this instability can be understood with the help of Fig.6.25, which shows that with the increase of the frequency ratio the torsional branch gets its damping reduced, contributing for the destabilization of the system, which occurs when damping turns negative.

Although it has been recognized that the installation of grating on bridge decks brings benefits in terms of flutter stabilization [125], for higher frequency ratios the reduction of the peak of the unsteady pressure $\tilde{C}_p(x^*)$ distribution at the leading edge of the downstream box caused by the installation of the grating results in the occurrence of flutter. Considering that the values of wind velocity are related to the model scale, the flutter onset can still be considered high; however, it denotes the destabilizing effects caused by the grating in that case, that does not occur for gap = $2.0B^*$, in which the peak of $\tilde{C}_p(x^*)$ is located more downstream. This should not be treated as a generalization, since the effects of the grating in the flutter stability are highly dependent on the opening ratio [16] and on the Reynold's number effects [122]. Based on that, the results presented herein should be faced only from an unsteady pressure characteristics point of view.

Since the costs of a two-box bridge are proportional to the gap length between girders,

Table 6.3: Flutter onset of two-box cross-sections with different frequency ratios f_φ/f_η - cases without additional singularities

f_φ/f_η		$0B^*$	$0.1B^*$	$0.25B^*$	$0.5B^*$	$1.0B^*$	$1.5B^*$	$2.0B^*$	$3.0B^*$
0.5	*experimental*	—	—	—	—	—	—	—	—
	theoretical	—	—	—	—	—	—	—	—
0.75	*experimental*	—	—	—	—	—	—	—	—
	theoretical	—	—	—	—	—	—	—	—
1	*experimental*	—	—	—	—	—	—	—	—
	theoretical	—	—	—	—	—	—	—	—
1.25	*experimental*	8.5 m/s	9.5 m/s	10.5 m/s	—	—	—	—	—
	theoretical	—	—	—	—	—	—	—	—
1.5	*experimental*	11.5 m/s	12.5 m/s	13 m/s	—	—	—	—	—
	theoretical	—	—	—	—	—	—	—	—
1.75	*experimental*	14.5 m/s	15.5 m/s	16 m/s	18.5 m/s	—	—	—	—
	theoretical	66.5 m/s	—	—	—	—	—	—	—
2	*experimental*	17.5 m/s	18 m/s	18.5 m/s	20.5 m/s	—	—	—	—
	theoretical	56.5 m/s	—	—	—	—	—	—	—
2.25	*experimental*	20 m/s	21 m/s	21 m/s	23 m/s	—	—	—	—
	theoretical	56.5 m/s	87 m/s	—	—	—	—	—	—
2.5	*experimental*	22.5 m/s	23.5 m/s	24 m/s	25.5 m/s	—	—	—	—
	theoretical	59 m/s	78.5 m/s	—	—	—	—	—	—
2.75	*experimental*	25 m/s	26 m/s	26.5 m/s	28 m/s	—	—	—	—
	theoretical	62.5 m/s	77.5 m/s	—	—	—	—	—	—
3	*experimental*	27.5 m/s	28.5 m/s	29 m/s	30.5 m/s	—	—	—	—
	theoretical	66.5 m/s	79 m/s	—	—	—	—	—	—
3.25	*experimental*	30 m/s	31 m/s	31.5 m/s	33 m/s	—	—	—	—
	theoretical	70.5 m/s	81.5 m/s	—	—	—	—	—	—
3.5	*experimental*	32.5 m/s	33.5 m/s	34 m/s	36 m/s	—	—	—	—
	theoretical	75 m/s	85 m/s	—	—	—	—	—	—
4	*experimental*	37.5 m/s	38.5 m/s	39 m/s	41 m/s	—	—	—	—
	theoretical	84 m/s	93 m/s	—	—	—	—	—	—
5	*experimental*	47.5 m/s	48.5 m/s	49.5 m/s	50.5	—	—	—	—
	theoretical	—	—	—	—	—	—	—	—

Table 6.4: Flutter onset of two-box cross-sections with different frequency ratios f_φ/f_η - cases with vertical plates and grating

f_φ/f_η	$1.0B^*$_G	$1.0B^*$_VL	$1.0B^*$_VB	$2.0B^*$_G	$2.0B^*$_VL	$2.0B^*$_VB
0.5	—	—	27 m/s	—	—	13.5 m/s
0.75	—	—	26.5 m/s	—	—	13.5 m/s
1	—	—	19.5 m/s	—	—	13.5 m/s
1.25	—	—	18.5 m/s	—	—	14 m/s
1.5	—	—	18.5 m/s	—	—	14 m/s
1.75	—	—	19 m/s	—	—	15.5 m/s
2	—	—	20.5 m/s	—	—	16.5 m/s
2.25	—	—	22 m/s	—	—	18 m/s
2.5	—	—	23.5 m/s	—	—	20 m/s
2.75	29 m/s	—	26 m/s	—	—	22 m/s
3	31 m/s	—	28 m/s	—	—	23.5 m/s
3.25	33 m/s	—	30.5 m/s	—	—	25.5 m/s
3.5	35 m/s	—	33 m/s	—	—	27 m/s
4	39.5 m/s	—	45 m/s	—	—	30 m/s
5	48.5 m/s	—	45 m/s	—	—	36.5 m/s

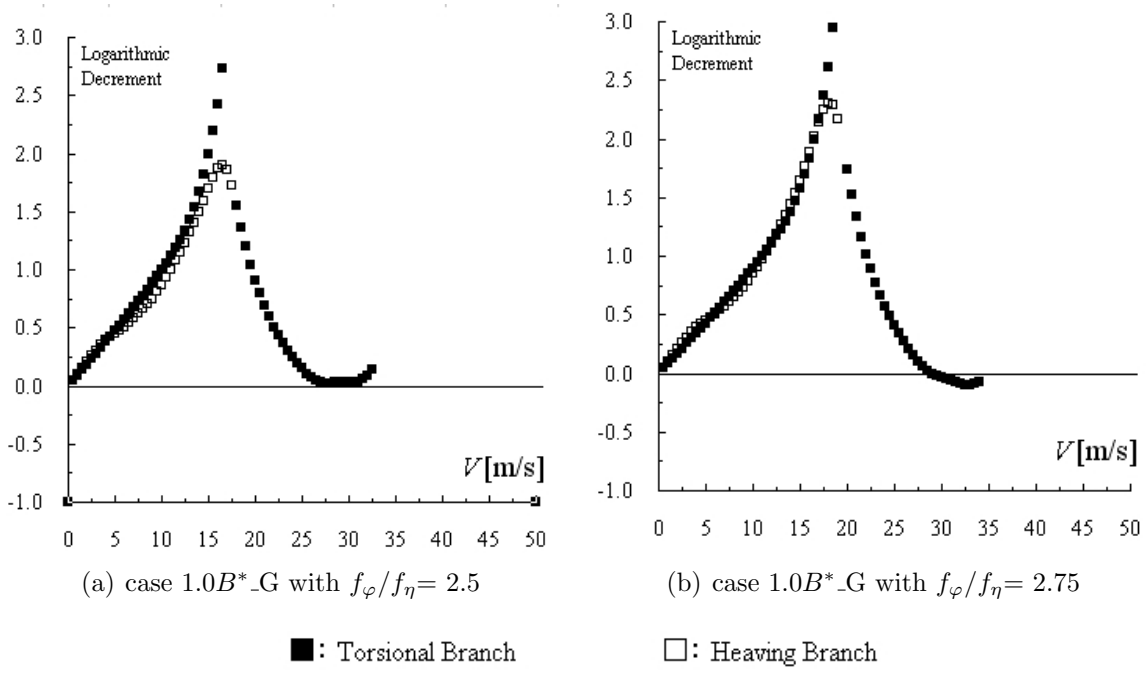

(a) case $1.0B^*$_G with f_φ/f_η= 2.5

(b) case $1.0B^*$_G with f_φ/f_η= 2.75

Figure 6.25: damping for $1.0B^*$_G: gap = $1.0B^*$with grating

short gaps are preferred; and considering the results reported in Table 6.3 and Table 6.4, it is concluded that for the characteristics of the models adopted in this study good values would be in the range of $0.5B^*$ to $1.0B^*$ for frequency ratios $f_\varphi/f_\eta > 1.75$, decreasing with the decrease of f_φ/f_η. Comparing the variation of the damping with the wind velocity obtained for case $0.5B^*$ with $f_\varphi/f_\eta = 1.75$ and case $1.0B^*$ with $f_\varphi/f_\eta = 1.75$, Fig.6.26, it can be said that the stability would be obtained by a small increase in the gap length, since for gap = $0.5B^*$ the damping of the torsional motion is just little negative and for gap = $1.0B^*$ it is in a completely safe zone.

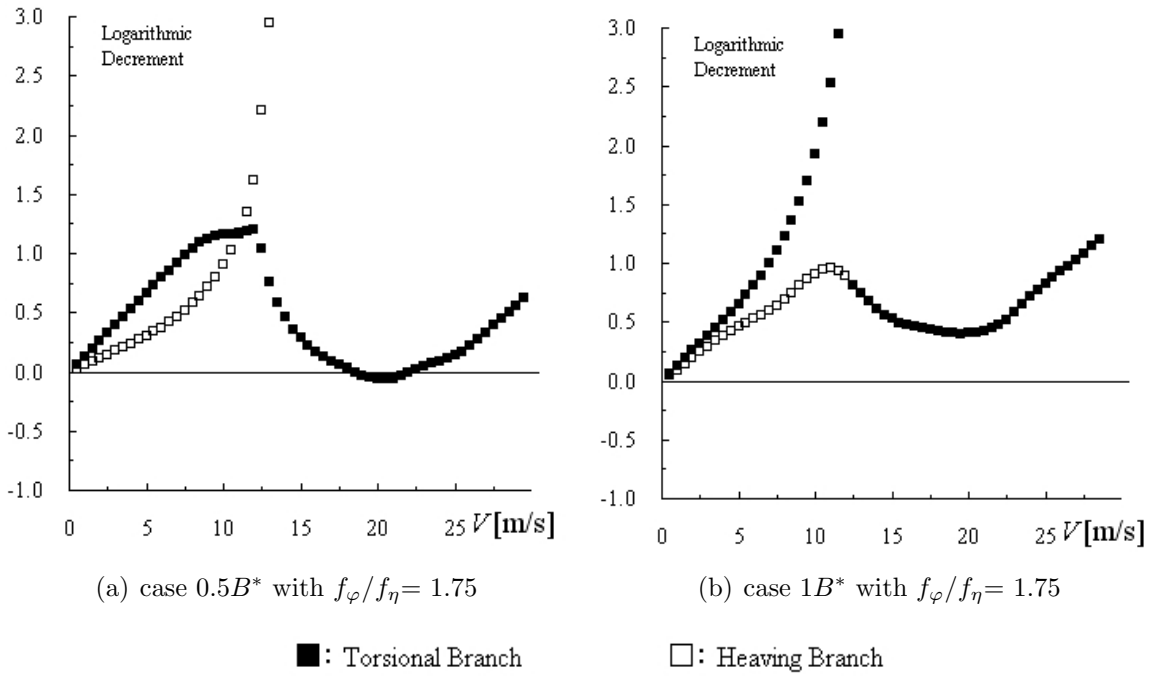

(a) case $0.5B^*$ with $f_\varphi/f_\eta = 1.75$

(b) case $1B^*$ with $f_\varphi/f_\eta = 1.75$

Figure 6.26: damping for $f_\varphi/f_\eta = 1.75$, cases $0.5B^*$ and $1.0B^*$

Although the conclusions above can not be understood as a generalization for all types of cross-sections and dynamic characteristics, they serve as parameter for comparison, showing concordance with values of gap length adopted in real bridges.

As a final comparison, to reinforce the importance of aerodynamic optimizations for the improvement of flutter stability, flutter onset velocities were calculated considering the real properties of the cross-section of Akashi Kaikyo Bridge, Table 6.5, combined with the aerodynamic characteristics of five of the cross-section presented herein, i.e. $0B^*$, $0.1B^*$,

$0{,}25B^*$, $0.5B^*$ and $1.0B^*$. The results are reproduced in Fig.6.27, showing that for the analyzed cross-sections the flutter onset increases with the increasing of the gap, reaching the value obtained for the real bridge, i.e. 78 m/s, with a gap length around $1.0B^*$.

Table 6.5: Properties of the cross-section used in flutter analysis

	width B (m)	mass ($t.s^2/m/m$)	I ($t.m^2.s^2/m/m$)	f_h (Hz)	f_t (Hz)	δ_h	δ_t
Akashi Kaikyo	35.5 m	2.87	736.1	0.0659	0.1592	0.033	0.033

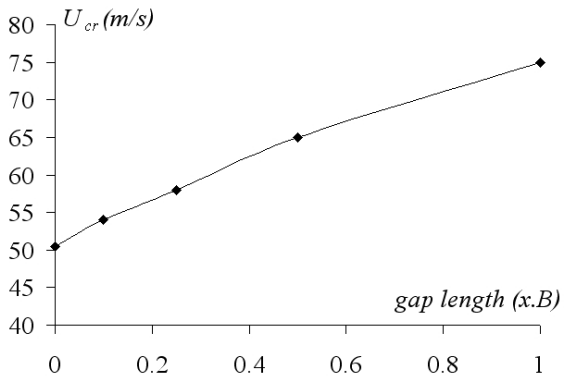

Figure 6.27: Flutter onset U_{cr} for Akashi Kaikyo Bridge combined with aerodynamic characteristics of models $0B^*$, $0.1B^*$, $0.25B^*$, $0.5B^*$ and $1.0B^*$

The results show that for the specific case of Akashi Kaikyo a two-box cross-section based on B/D=20 rectangular cylinders would not be efficient in terms of gap length. Compared with the values of real bridges, this gap length, i.e. around $1.0B^*$, can be considered exaggerated, which implies in that improvements on the cross-section would have to be done in order to reduce this value, as for example the case of the model $1.0B^*$_VL for which flutter stability could be eliminated, Fig.6.28.

The flutter analyses performed in this section were done not only with the objective of providing background regarding the use of rectangular cylinders for the composition of two-box cross-sections, but also to highlight the effects of the gap on the flutter onset velocity of two-box cross-sections as a whole. The next section will focus on the aerodynamic effects of the gap on the unsteady pressure characteristics of such a kind of cross-section, trying to provide hints for how to use their impacts in advantage for flutter stabilization.

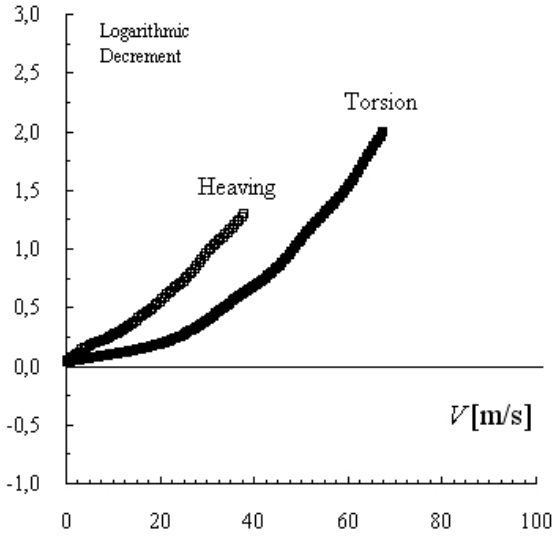

Figure 6.28: Damping for Akashi Kaikyo Bridge combined with aerodynamic characteristics of model $1.0B^*$_VL

6.6 Unsteady Pressure Characteristics

As already mentioned in the Section 6.3, because the unsteady pressure characteristics of each box in two-box cross-sections present themselves differently, the investigations should be conducted by considering them separately.

While the pressure field around the upstream box can be regarded in some extent to the one presented in a single box cross-section, the downstream box is highly affected by the vortices shed from the upwind box, which affect substantially its unsteady pressure characteristics. This vorticity can result in an excitation due to vortex shedding 3 to 4 times stronger than it occurs in mono box girders. The use of geometric improvements has shown good alternatives in the mitigation of this phenomenon, as the use of guide vanes in the bottom plate of Stonecutters Bridge [126]. In the case of that bridge, the efficiency of the geometric improvements showed a high dependence on the Reynold‘s number, and this must be true for other kinds of cross-sections as well.

The differences imposed on the unsteady pressure characteristics by the different values of gap length can be highlighted by comparing them through the superimposition of the

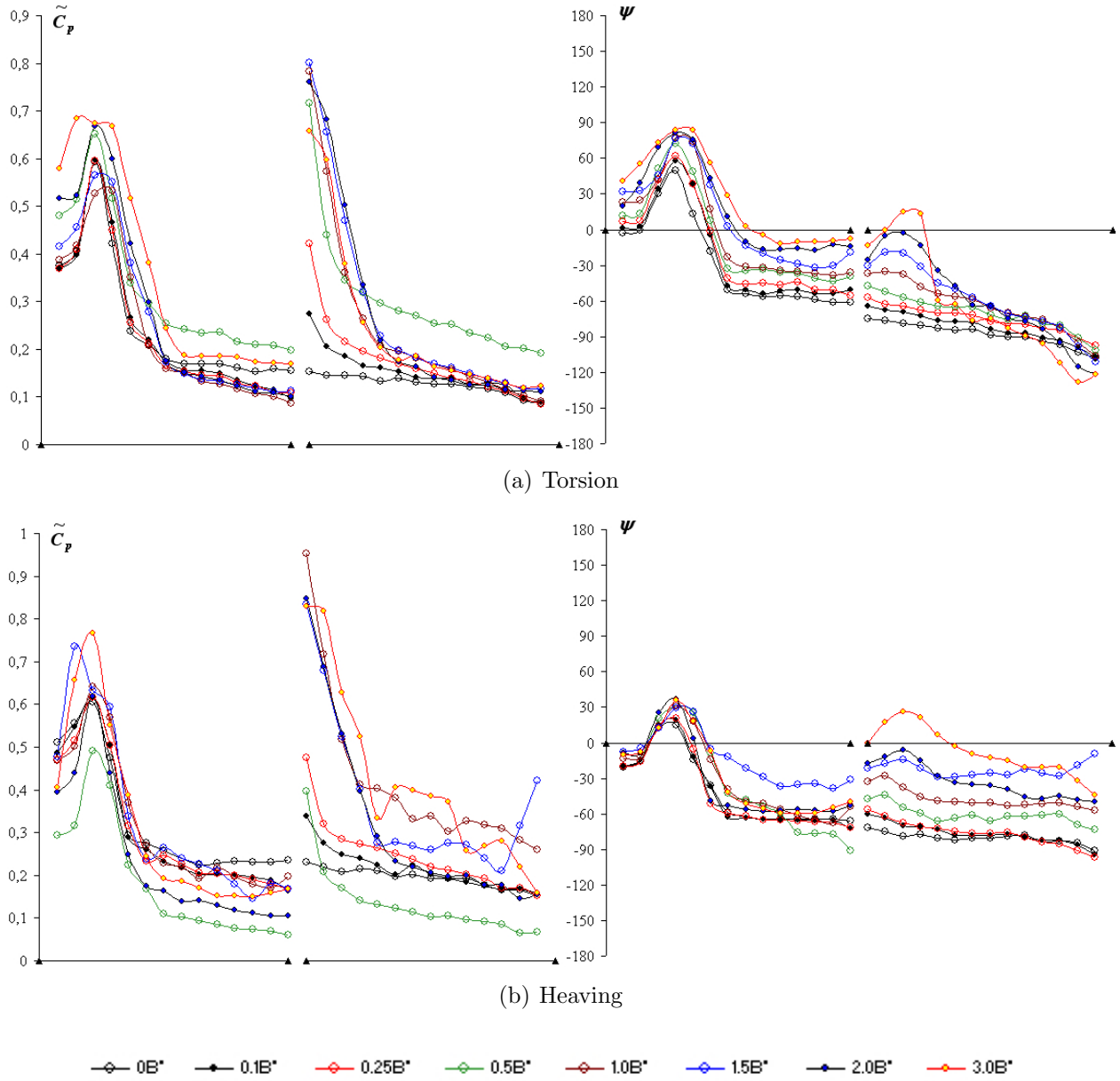

(a) Torsion

(b) Heaving

Figure 6.29: $U/f.B^* = 7.5$

unsteady pressure characteristics obtained for the different models in a velocity by velocity basis, Fig.6.29 to Fig.6.39.

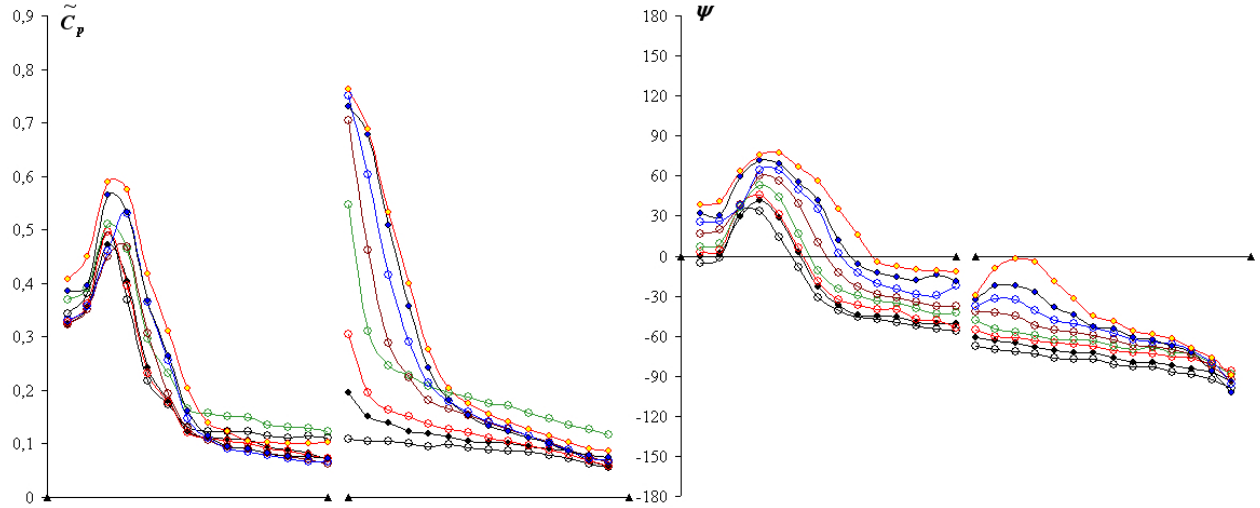

(a) Torsion

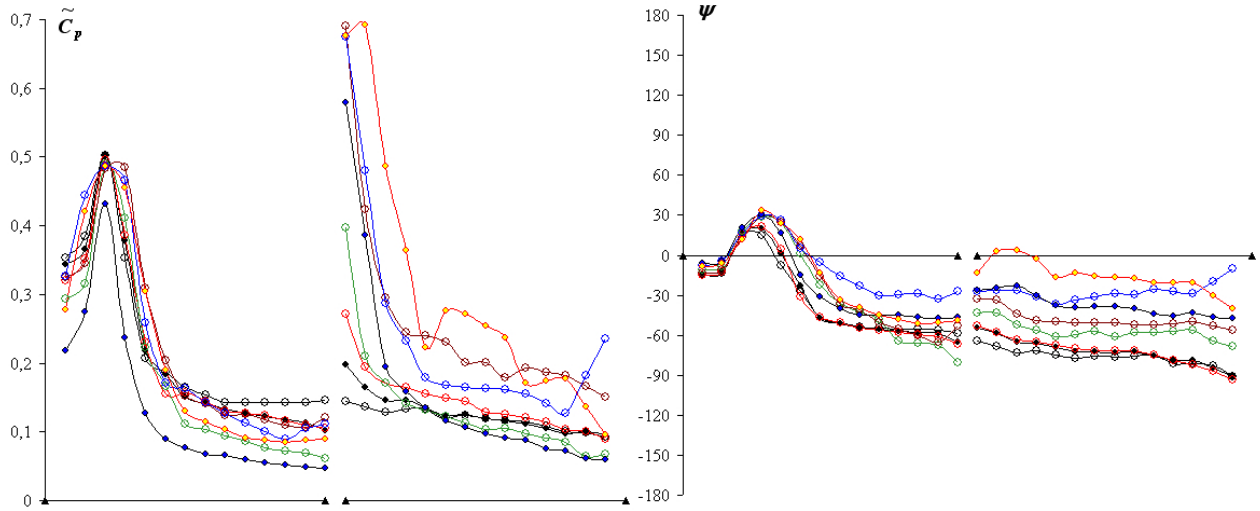

(b) Heaving

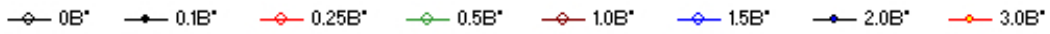

Figure 6.30: $U/f.B^* = 10$

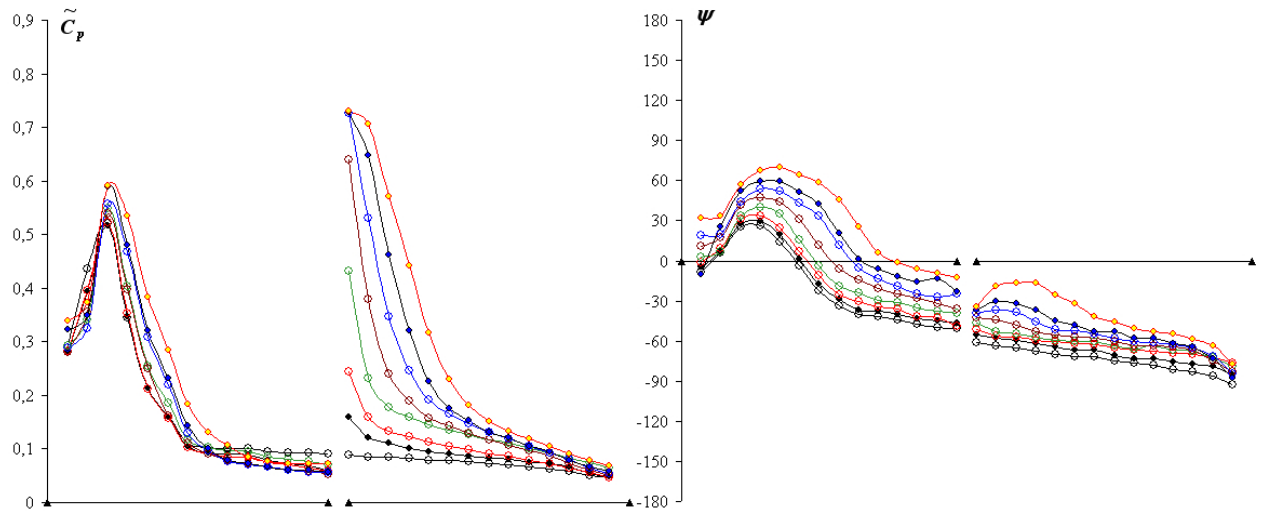

(a) Torsion

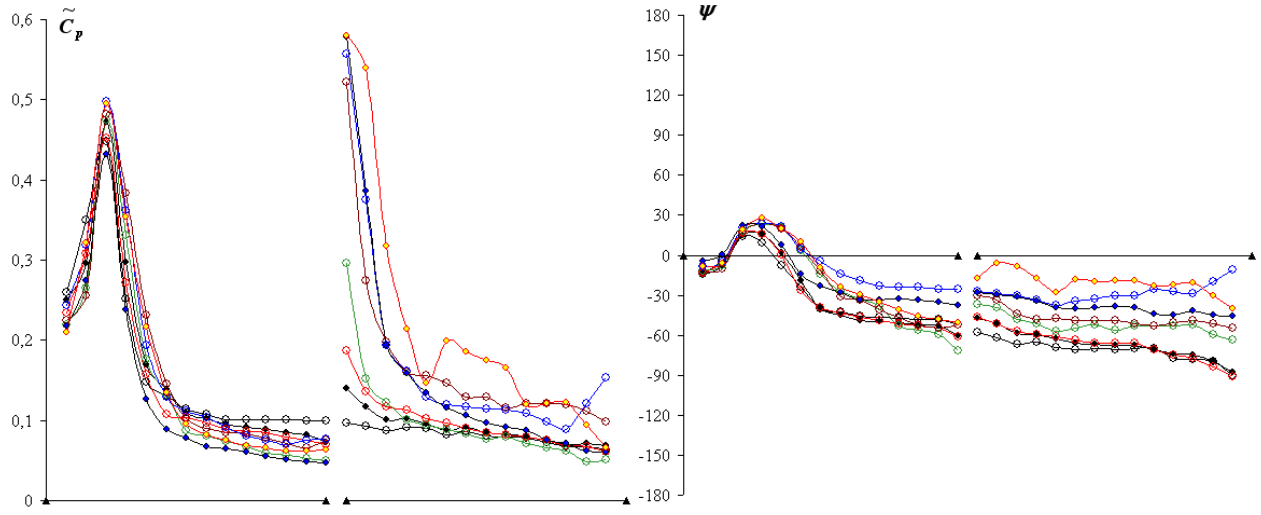

(b) Heaving

Figure 6.31: $U/f.B^* = 12.5$

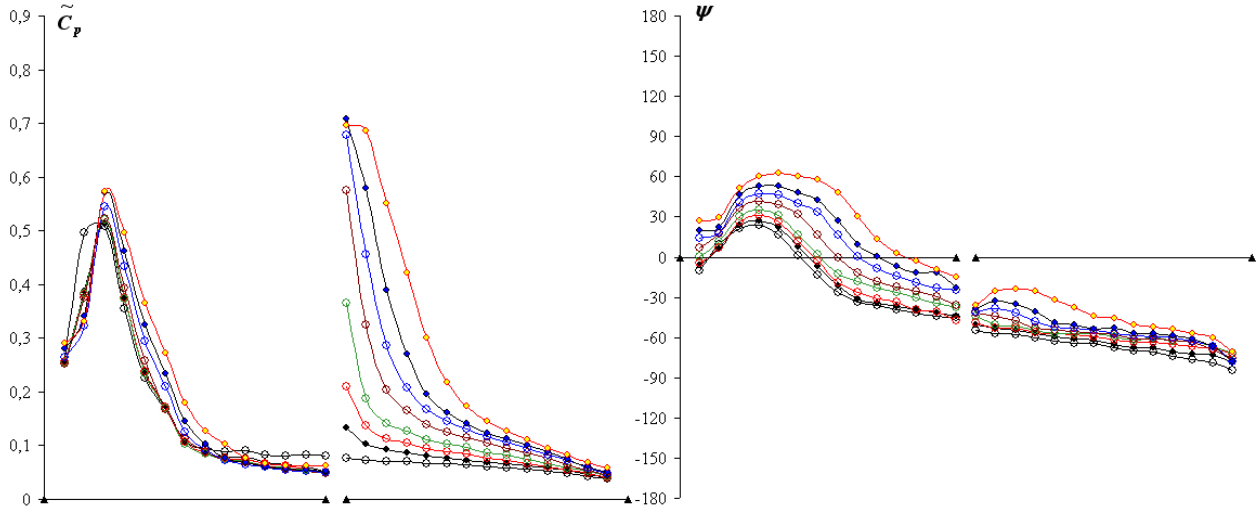

(a) Torsion

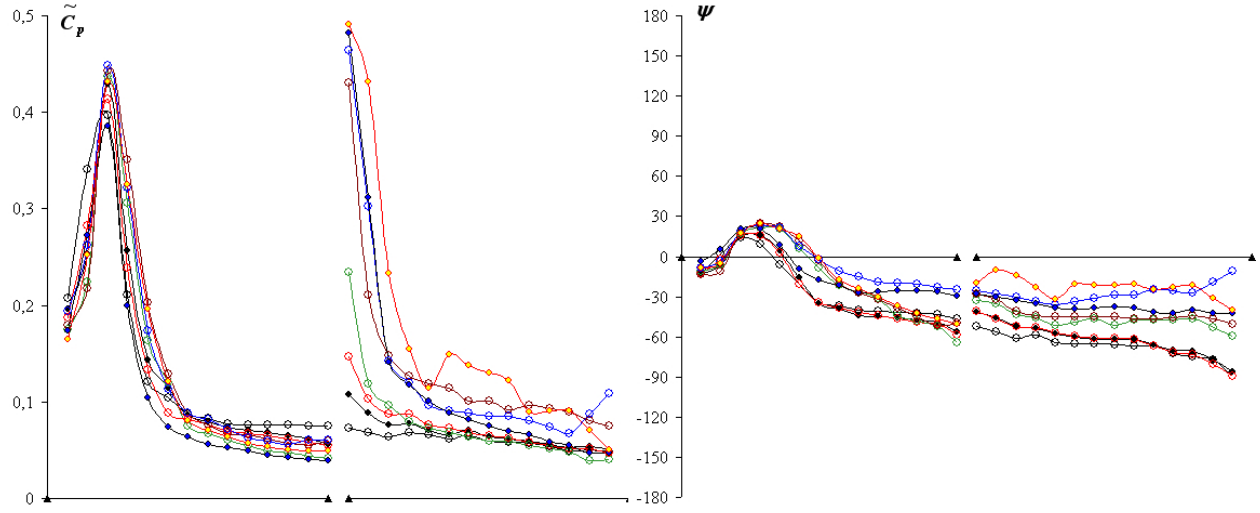

(b) Heaving

Figure 6.32: $U/f.B^* = 15$

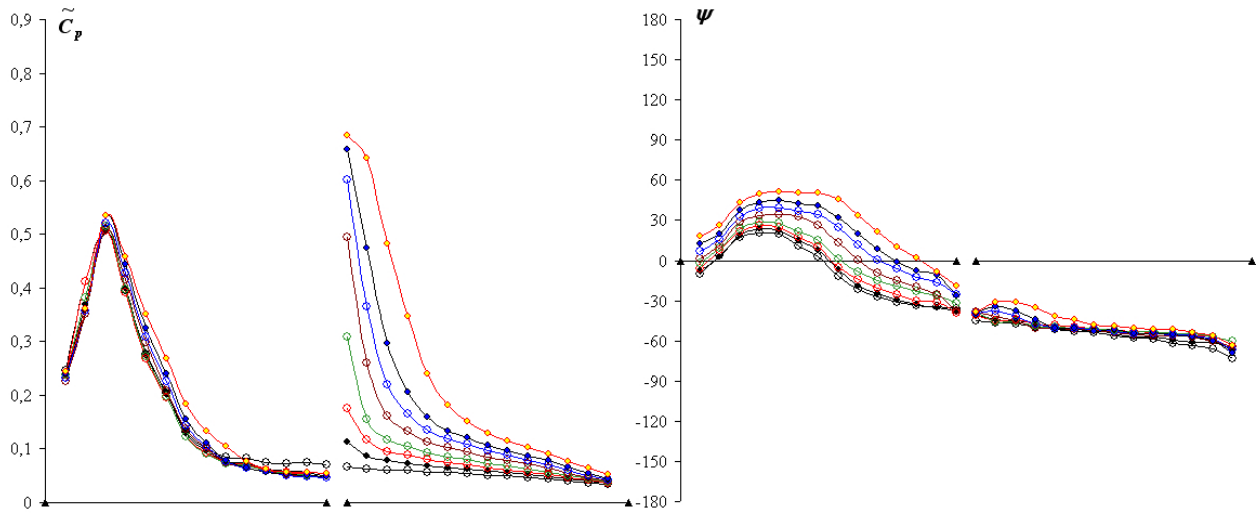

(a) Torsion

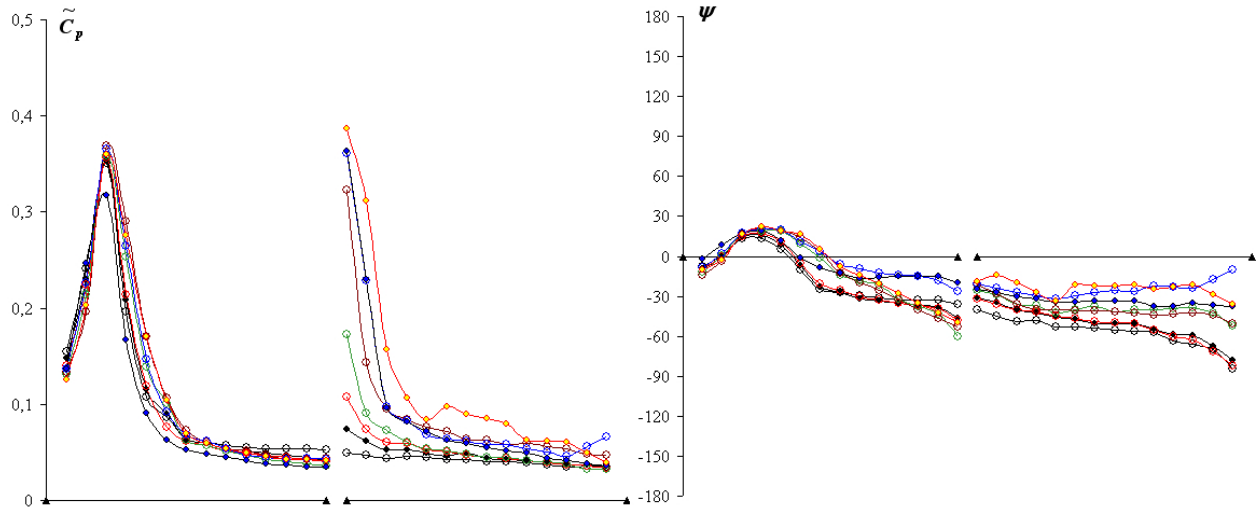

(b) Heaving

Figure 6.33: $U/f.B^* = 20$

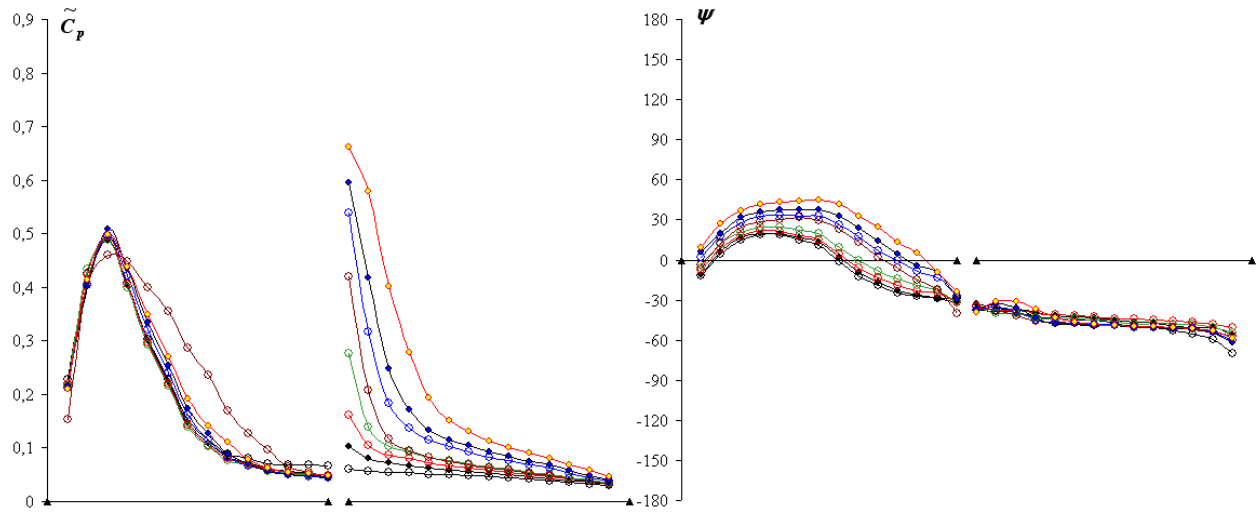

(a) Torsion

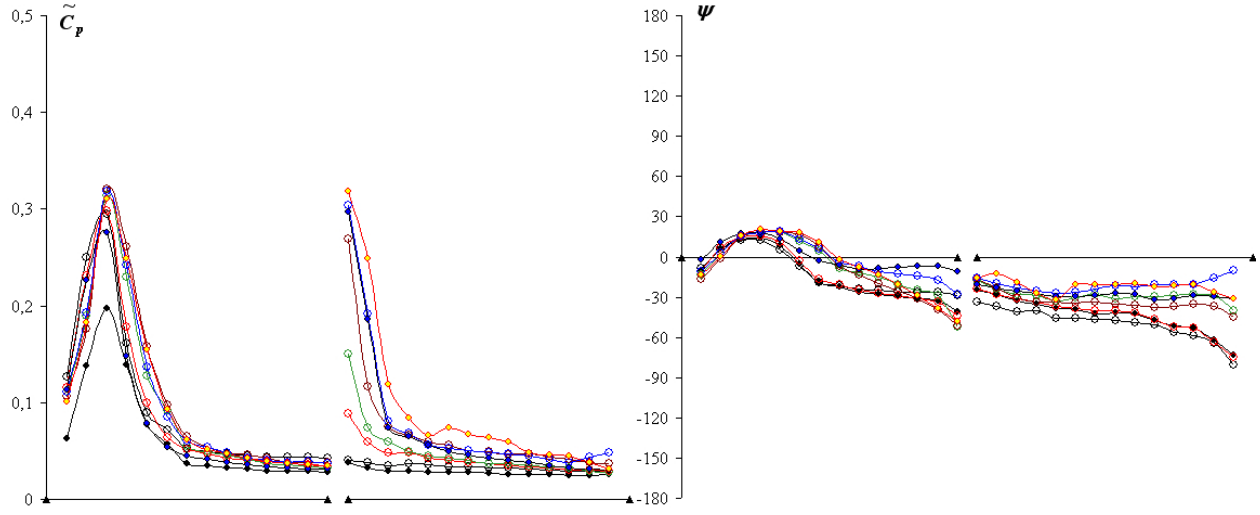

(b) Heaving

Figure 6.34: $U/f.B^* = 25$

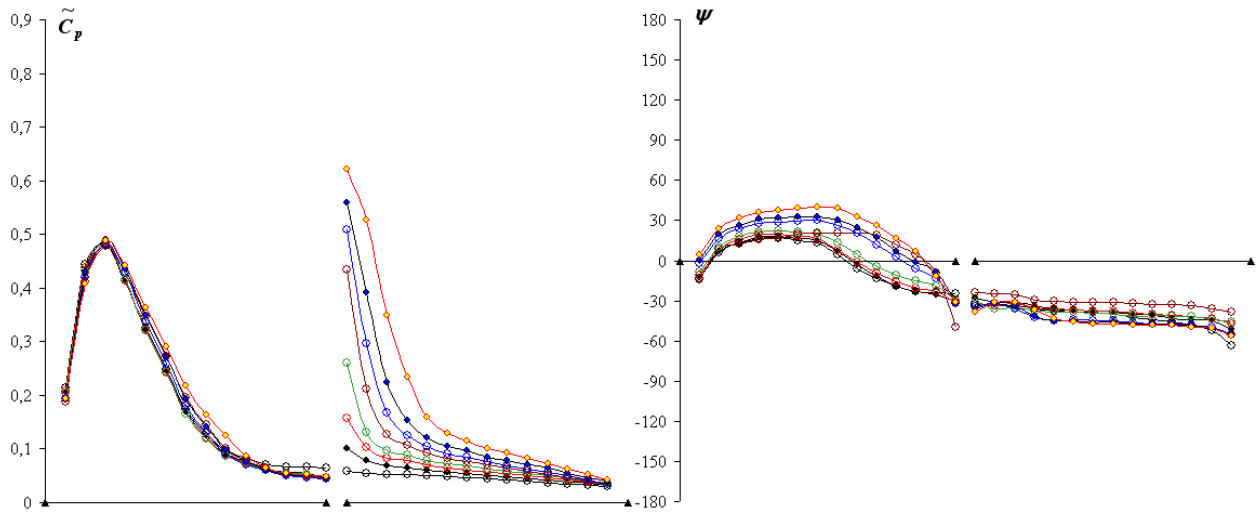

(a) Torsion

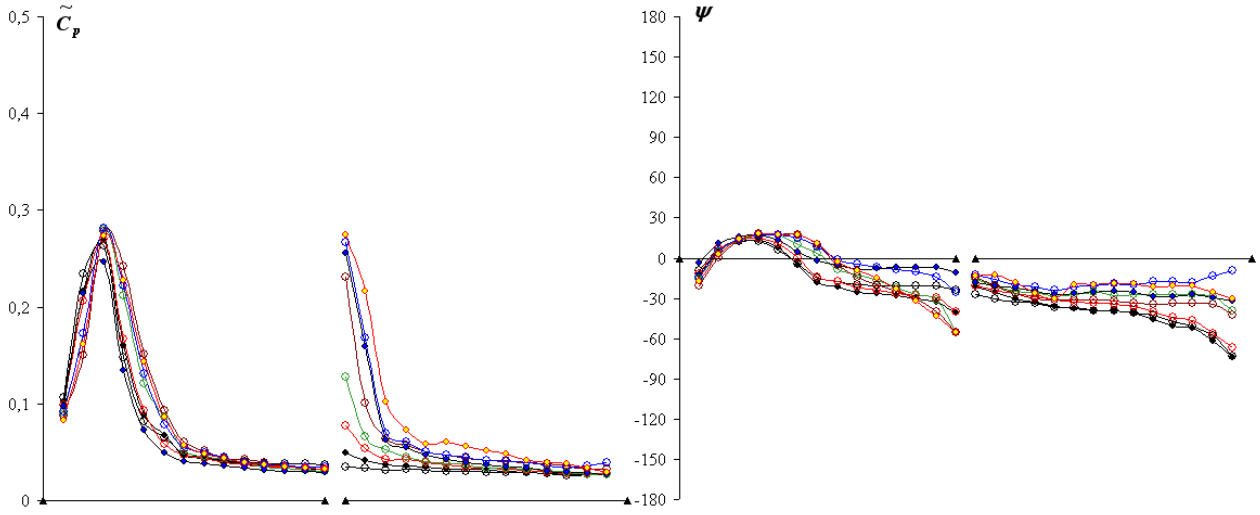

(b) Heaving

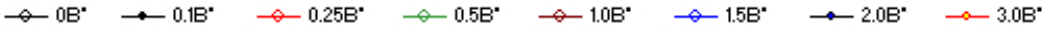

Figure 6.35: $U/f.B^* = 30$

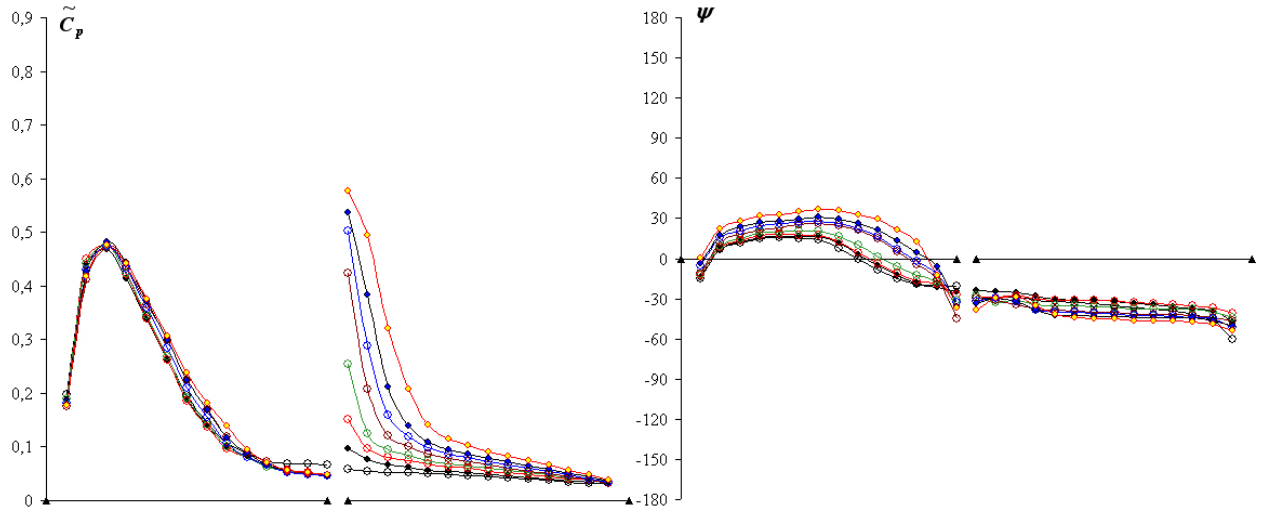

(a) Torsion

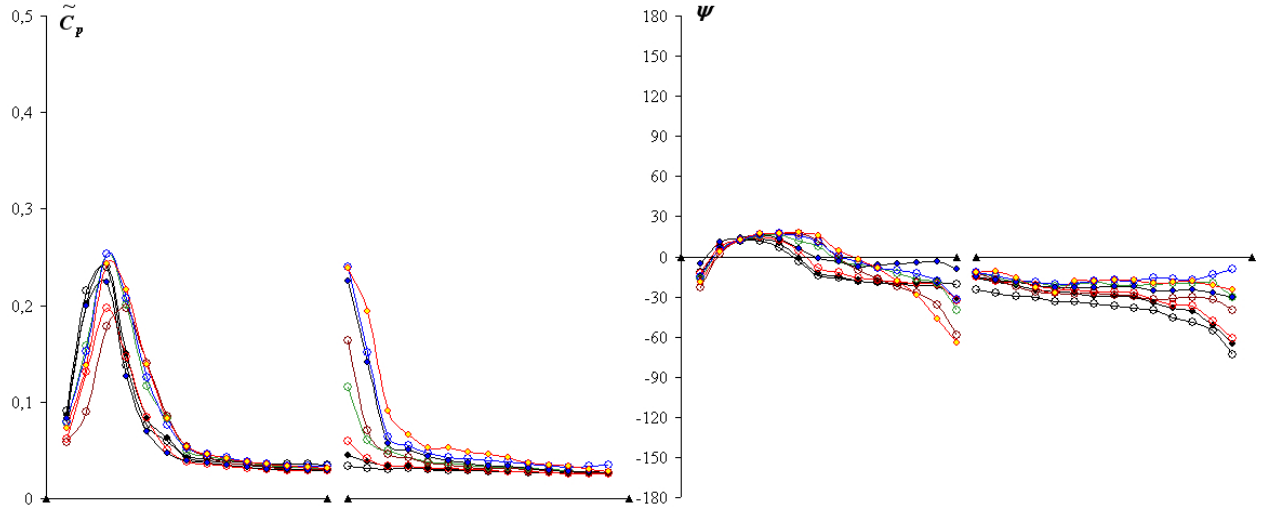

(b) Heaving

Figure 6.36: $U/f.B^* = 35$

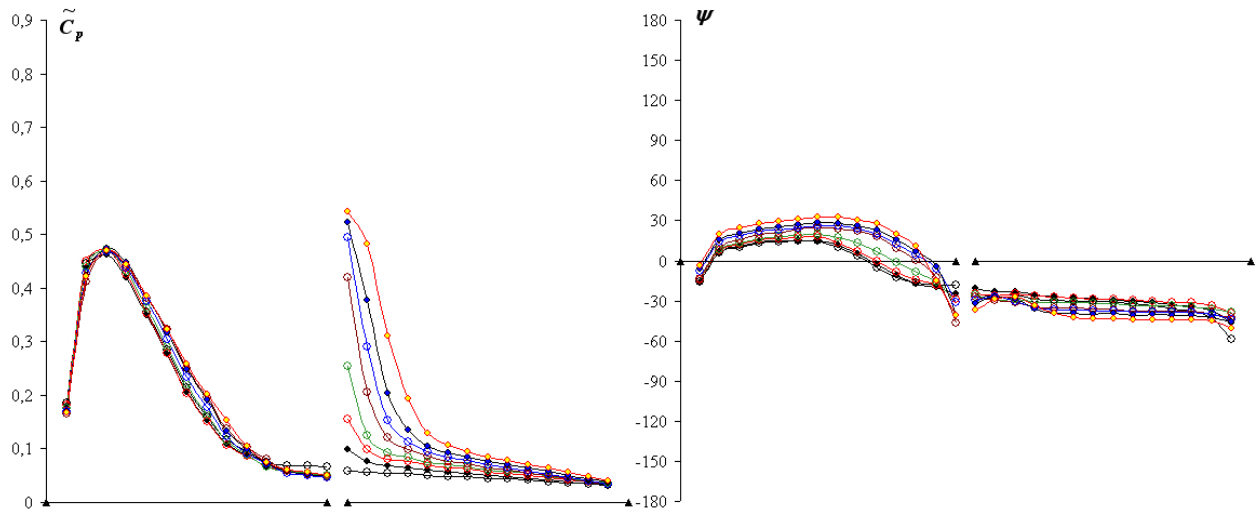

(a) Torsion

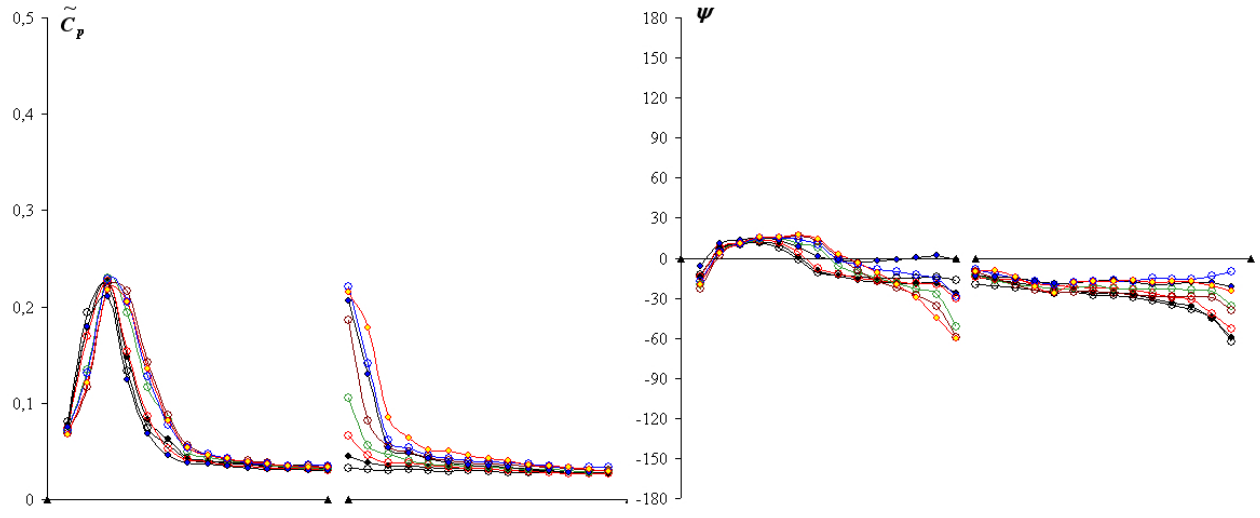

(b) Heaving

Figure 6.37: $U/f.B^* = 40$

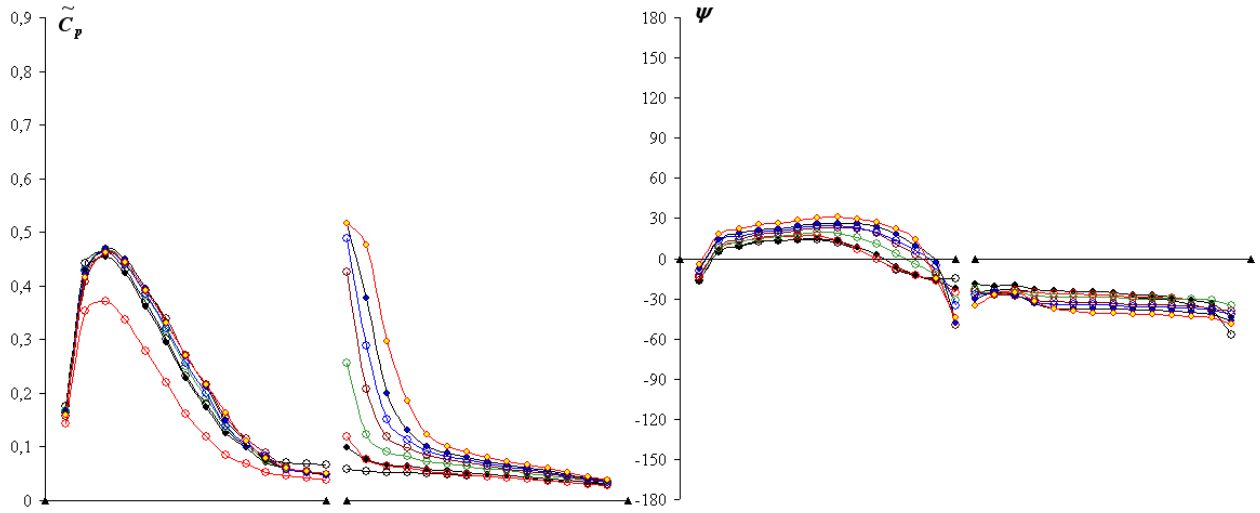

(a) Torsion

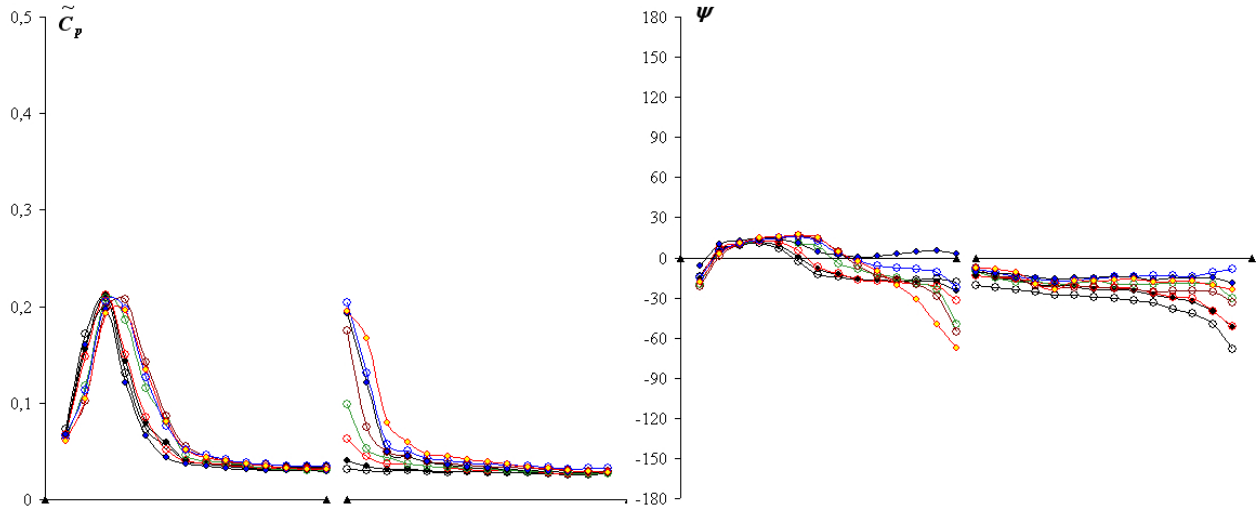

(b) Heaving

Figure 6.38: $U/f.B^* = 45$

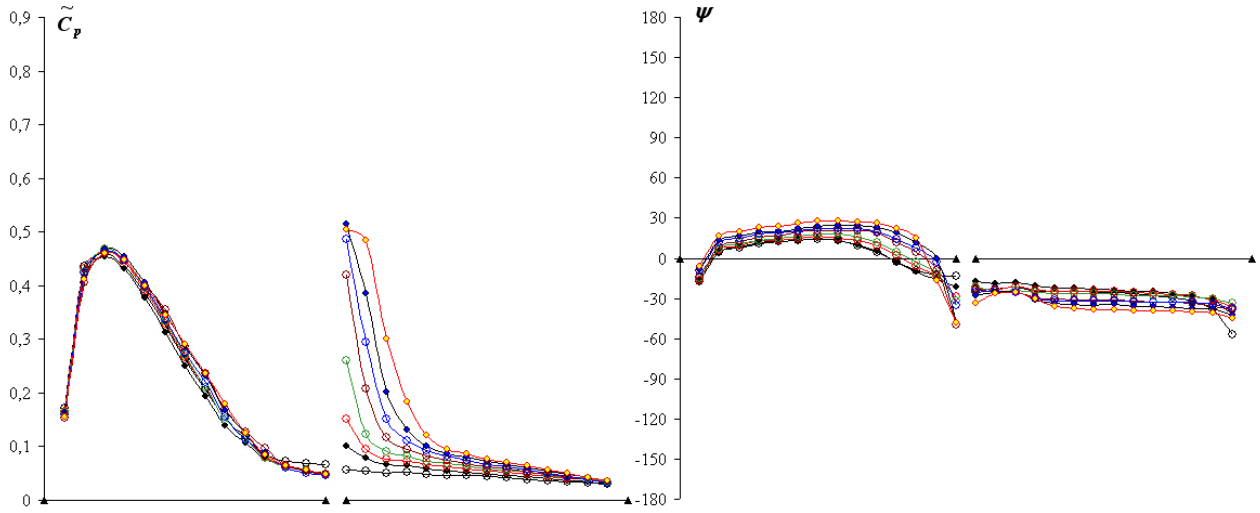

(a) Torsion

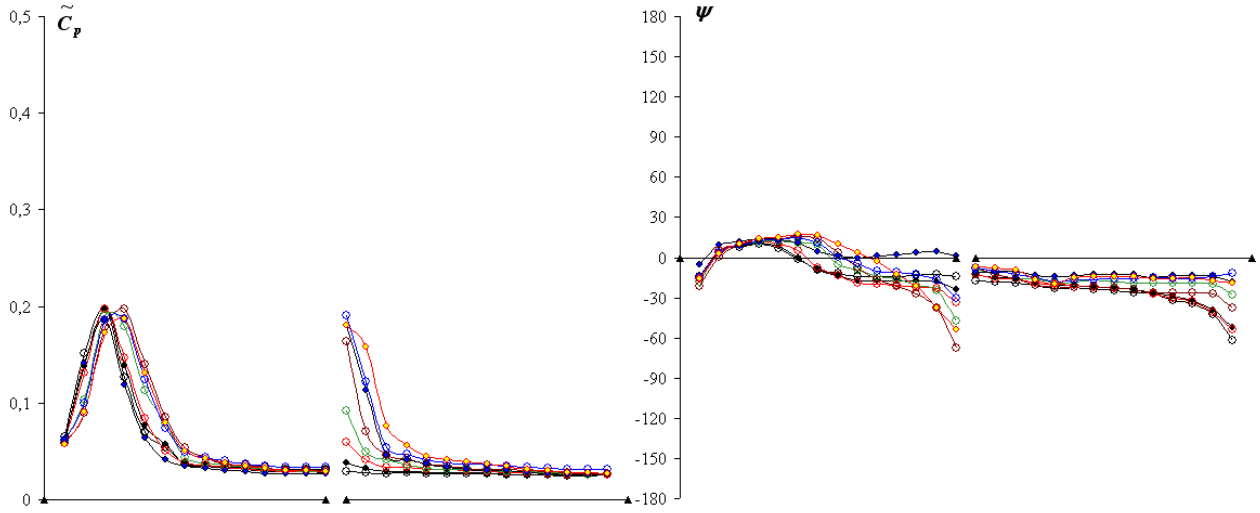

(b) Heaving

Figure 6.39: $U/f.B^* = 50$

By observing Fig.6.29 to Fig.6.39, it is perceived that with the increase of the reduced wind velocity, the unsteady pressure characteristics of all models tend to get similar, both for heaving and torsional motions. Also, the absolute values of phase difference tend to get reduced, presenting the broadening already mentioned in Section 6.3. Another important aspect is a *continuity tendency* from the upstream to the downstream box, in which the phase difference distribution of the downstream box tends to be a continuation of the distribution of the upstream box.

In terms of amplitude $\tilde{C}_p(x^*)$ distribution, the variation of the gap length imposes just slight modifications on the upstream box. In the torsional motion, it is virtually the same distribution for all models along the whole range of reduced wind velocities. With the increase of the wind velocity, the distributions tend to get broadened, with slightly broader distributions for larger values of gap length though. This characteristic is more visible in the lower velocity range, especially in the heaving motion.

In order to quantify the characteristics of the distributions, the unsteady pressure characteristics of the model with gap length = $0B^*$, Fig.6.1, were analyzed according to the framework proposed in Chapter 4; the results are reproduced in Fig.6.40 and Fig.6.41. Because this model is in reality a mono box cross-section with side ratio $B/D = 40$, it can provide comparison parameters with model NF studied in that chapter, complementing its conclusions and helping in the understanding of the relationships in two-box cross-sections as well.

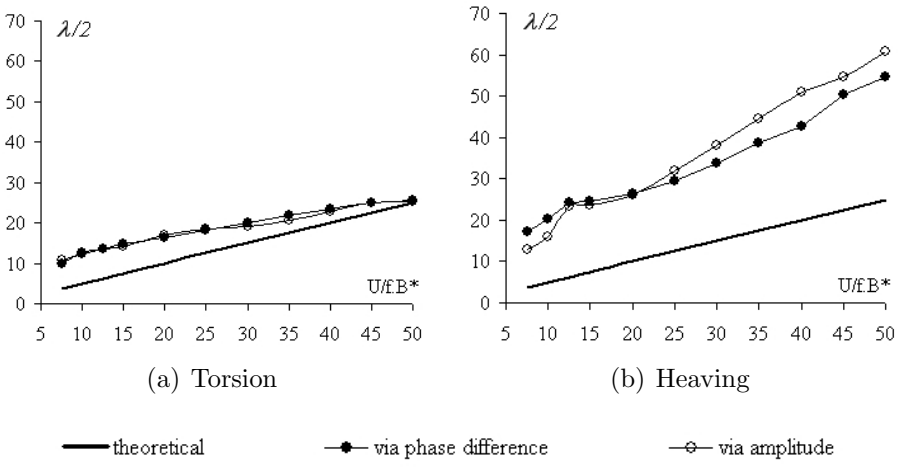

(a) Torsion (b) Heaving

Figure 6.40: Wave half-length for model with gap length = $0B^*$

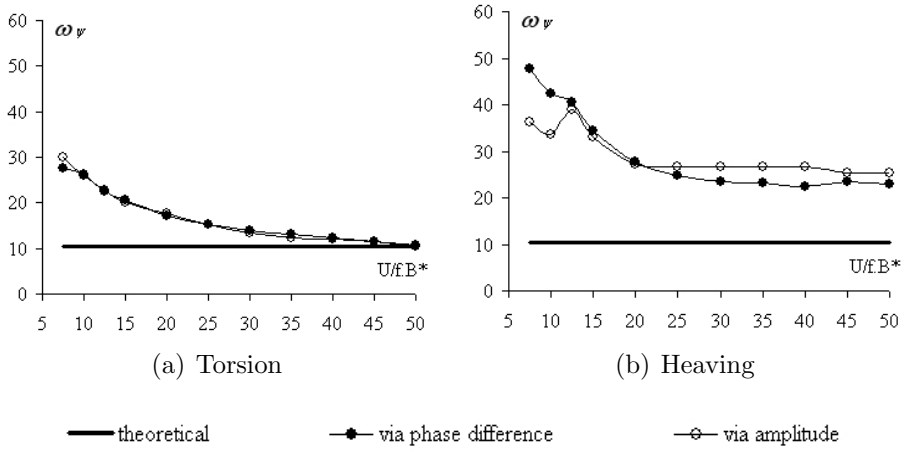

(a) Torsion (b) Heaving

Figure 6.41: Circular wave number ω_ψ for model with gap length = $0B^*$

The agreement between the values obtained for the wave half-length $\lambda/2$ and for the circular wave number ω_ψ through phase difference $\psi(x^*)$, Eq.4.2, and amplitude $\tilde{C}_p(x^*)$, Eq.4.5, distributions was very good, for both heaving and torsional systems, corroborating the method proposed in Chapter 4. However, differently from the $B/D = 20$ rectangular cylinders, Fig.4.15 and Fig.4.16, the values obtained for the $B/D = 40$ rectangular cylinder showed a high discrepancy between torsional and heaving motions. While in the torsional system the values seem to agree quite well with the tendency observed in $B/D = 20$ rectangular cylinders, approaching the theoretical values with the increase of the wind velocity, in the heaving system the values are around the double of the theoretical values.

The lack of agreement observed in the heaving system brings to the scene the *arm length effect* mentioned in section 6.3. The unsteady pressure characteristics obtained for the torsional motion are the resultant of the heaving and torsional motions combined in the torsional system, and in the heaving system only the effects of a pure heaving motion exist.

It is reasonable to think that the wave length must be a function of the aerodynamic conditions at the leading edge and that the increase of the afterbody length would not have much influence on the wave length itself, resulting in the deformation of the relationship between wave length and side ratio, observed in the heaving motion. However, with the increase of the side ratio, the amplitude and velocity of motion of the leading edge in the torsional system are also increased, impacting on the fluid dynamics conditions of the leading edge. This must also be strongly related with the differences between heaving and torsional

systems, since in the heaving motion such a variation does not occur.

In reality, despite the overall agreement obtained in Chapter 4, the results obtained there for the torsional system in terms of wave number ω_ψ, Fig.4.16 and Fig.4.17, were more consistent than the ones obtained for the heaving system. In that case, the side ratio was half of the one of this chapter, which presents around the double of the values of wave number ω_ψ for the heaving system, Fig.6.41-b. This might point to a relationship to be investigated towards an improvement of the framework proposed in Chapter 4; however, in this sense a wider range of side ratios would have to be considered.

Nevertheless, considering the thickness D of the models used in Chapter 4 and the ones used in this chapter, and also the locations where the flow is supposed to reattach, a relationship which explains the discrepancies observed in the heaving motion can be tried by normalizing the wave lengths by the side ratio of the models. In doing so, a good agreement between both cases is obtained also for the heaving system.

For the torsional system, the relationships seem to be independent of the side ratio and the proportionality observed is related to the increasing of the participation of the pressure characteristics of the heaving motion for the the final result, which increases with the increase of the side ratio. The good agreement with the theoretical values, which was also better obtained with B/D=20 rectangular cylinders (see the comments about Fig.4.16 in Chapter 4), must lead to the conclusion that the calculation framework already accounts for that combination of effects.

As for the locations of the flow reattachment, considered coincident with the locations of the peaks of the amplitude $\tilde{C}_p(x^*)$ distributions, the values are around x_R= 0.20 for all cases, which is around 10% lower than the expected x_R= 0.22 (estimated through the relationship x_R= 4.4D). This difference may be related to the resolution adopted for the pressure taps used in the pressures measurement, which are separated by a normalized distance of 0.067, which is much higher than the error of the estimations, i.e. 0.02. Based on that, it is possible to conclude that the flow reattachment agrees very well with the mathematical estimations, occuring at the same position regardless the model is whether in torsional or in heaving motion,

Concerning the downstream box, the influences of the gap seem to result in different patterns for both amplitude and phase difference distributions, in comparison with the ones related to the upstream box. For the phase difference, the *continuity tendency* mentioned

previously may be regarded as the main feature; however, it is also noticed that the larger the gap length is, the lower the modulus of the phase difference, which assumes constant values along almost the entire downstream box. Also, with the increase of the wind velocity, the difference between the values of phase difference $\psi(x^*)$ between the different values of gap length is reduced, agreeing with the same tendency showed in the upstream box.

It has already been accounted for this continuity tendency in Chapter 4, when the description of the phase difference distribution of rectangular cylinders was proposed by dividing it into two branches: the *curvy branch*, regarded to the sinusoidal equation Eq.4.2; and the *steady branch*, with constant values along its development.

In the case of the two-box cross-sections studied herein, this *steady branch* is interrupted by the gap. For the model $0B^*$ the natural tendency of continuing the values from upstream box to downstream box should be expected, since it is a rectangular cylinder, which is indeed confirmed through Fig.6.1. However, by superimposing in the same figure the phase difference $\psi(x^*)$ distributions of all models at a reduced wind velocity U/f.B^*= 50, in non-normalized dimensions and starting from the leading edge of the upstream box, it is noticeable that the same development of the curve is kept for all configurations throughout the whole range of gap lengths, as if the gap did not exist, resulting that every distribution seems to be continued by the next one, Fig.6.42.

Resorting to the configurations in which a vertical plate was installed in the upstream box (Fig.6.9 for gap length = $1.0B^*$ and Fig.6.12 for gap length = $2.0B^*$), it is perceived that despite the large differences presented by the phase difference distributions $\psi(x^*)$ of the upstream box in comparison with configurations without the vertical plate (Fig.6.5 for gap length = $1.0B^*$ and Fig.6.7 for gap length = $2.0B^*$), the phase difference distribution $\psi(x^*)$ of the downstream box behaves virtually the same way it does for models without vertical plate in the upstream box for both values of gap length.

This fact leads to the conclusion that the gap is dominant in the definition of the phase difference distribution $\psi(x^*)$ of the downstream box, canceling the effects and not "propagating" the influences of *geometric singularities* existent in its upstream. In that sense, the continuity tendency from upstream box to downstream box must not hold.

So the description of the characteristics of the phase difference distribution $\psi(x^*)$ of the downstream box can be tried by ignoring in some extent the influences of the upstream box, considering only the existence of the gap, its length and the characteristics of the downstream

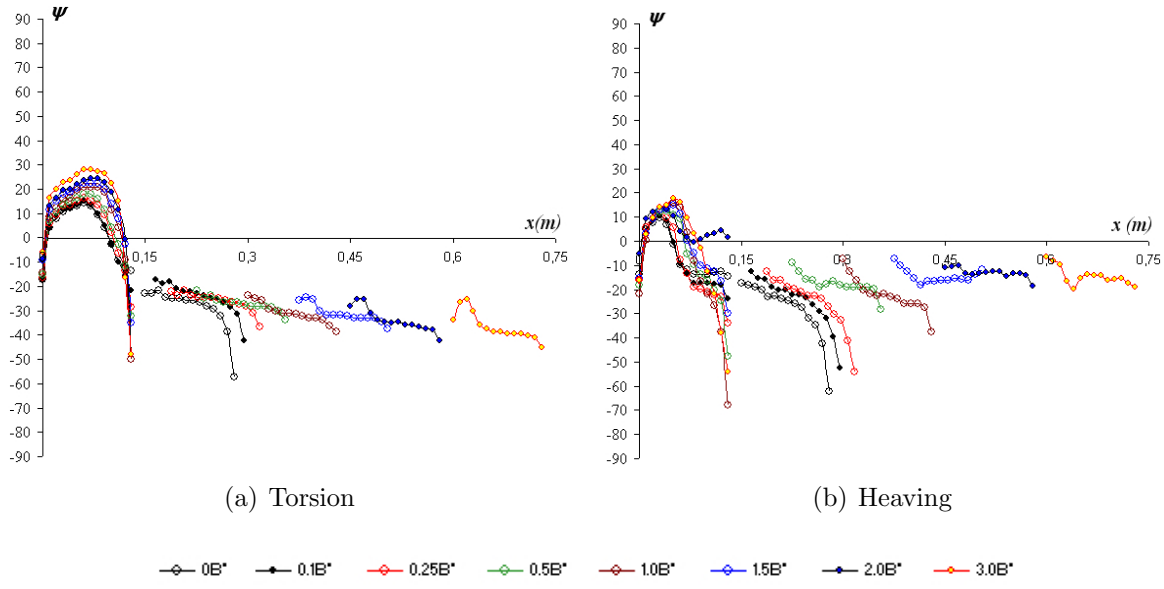

(a) Torsion (b) Heaving

Figure 6.42: Phase difference $\psi(x^*)$ distribution at U/f.B^*= 50 for models with gap length from $0B^*$ to $3B^*$, superimposed from the leading edge of the upstream box

box itself, i.e. a rectangular cross-section in this case.

In this sense, with the increase of the gap length, a "movement" towards the positive direction should be expected for the values of the phase difference $\psi(x^*)$ near the leading edge of the downstream box. This can be expected because with the increase of the gap length the distance from some arbitrary reference point at the middle of the gap also increases, impacting consequently on the time a disturbance takes to bridge that distance. As a consequence, a delay is imposed on the phase difference, which is translated into more positive values.

This tendency can be indeed verified for the heaving motion along the entire velocity range. However, for the torsional motion it is only partially confirmed, more specifically in the lower reduced wind velocity range. In the higher wind velocity range the behavior is the opposite.

Assuming as a reference value the phase difference at the leading edge of the downstream box of model $0B^*$ (actually at the first pressure tap, which is located $10mm$ from

the leading edge) and as a reference position the center of the gap (which coincides with the leading edge of the downstream box of model $0B^*$), it is possible to calculate an *equivalent gap length* for all configurations. This calculation is based on the difference between the values of phase difference at the leading edge of the downstream box of each model and the value at the same position of model $0B^*$. Assuming that one period of oscillation $T = 1/f = 1/2Hz = 0.5s$ corresponds to a phase difference of 360°, an *equivalent time interval* Δt can be calculated. Taking that Δt and the wind velocity U, the *equivalent gap length* is obtained.

Since the reference position is at the middle of the gap, the *equivalent gap length* should be the double of the value found in the calculations. The results obtained for both heaving and torsional systems are reported in Fig.6.43, in which the inclined line represents the expected value (real gap length).

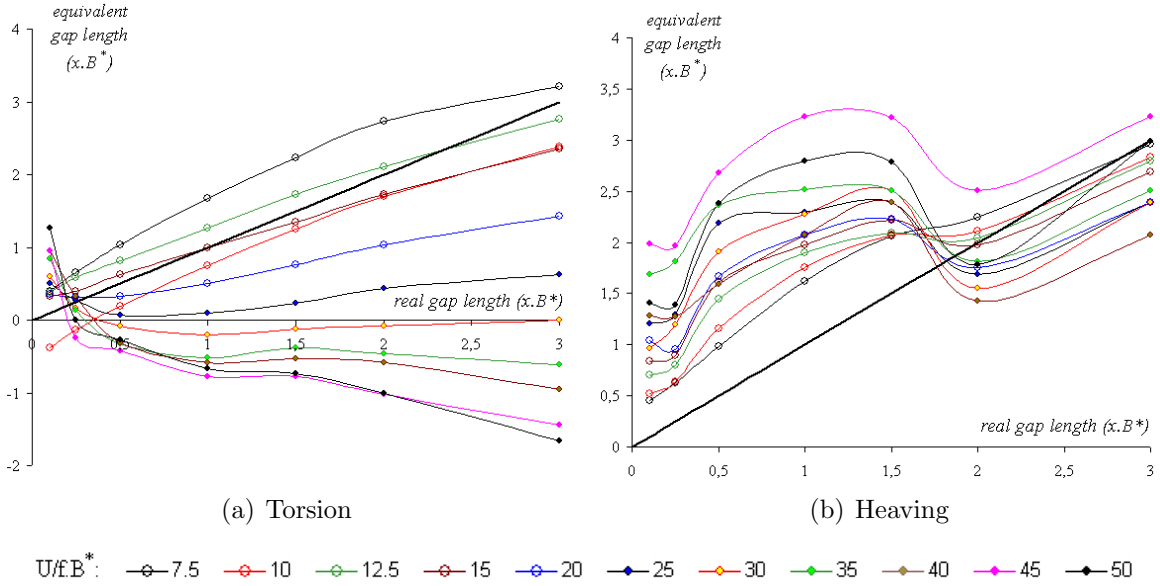

(a) Torsion (b) Heaving

Figure 6.43: Equivalent gap length

Heaving and torsional systems show different behaviors. While the heaving system tends to follow the expected values, the torsional system behaves in a totally different way.

In the heaving system, the inclinations of the curves are kept almost constant throughout all gap lengths and nearly parallel to the curve (straight line) of expected values; this indicates linearity in the relationships. With the increase of the wind velocity, there seems

to be a *bias* added to the values of the *equivalent gap lengths*, and this might be an indicative that the reference point (assumed as at the center of the gap) changes with the variation of the wind velocity or even that the wind velocity in the wake is not exactly the one assumed in the calculations, i.e. the wind velocity of the approaching flow.

The reference point, in reality, must be somehow related to characteristics of turbulence of the wake generated by the upstream box ("inside" the gap), and the clear break of trend existent between the gap length $1.5B^*$ and $2.0B^*$, which gets more prominent with the increase of the wind velocity, must be related to a modification in the structure of the flow inside the gap.

As for the torsional system, the behavior for the lower wind velocity range is similar to what can be observed in the heaving system. However, with the increase of the wind velocity, the inclinations of the curves change and for the higher wind velocity range the *equivalent gap length* becomes negative. One possible interpretation for this phenomenon might be related to an increase of the velocity of the pressure field in a different rate than the wind velocity itself, as if the flow in the gap moved faster than the wind velocity.

This points to a fundamental difference between the flow patterns in the wake of the upstream box between heaving and torsional oscillations. Even though the unsteady pressure characteristics look similar, it is recognized that the flow around bodies in heaving and in torsional motions, especially when *geometric singularities* are presented, may be different.

The reduction of the values of the *equivalent gap length* can be understood as a consequence of the "sheltering effect" caused by the upstream box on the downstream box while in torsional motion. For positive angles of attack, the upstream box shelters the downstream box and for negative angles of attack the flow is kept attached to the upper surface of the upstream box, reaching directly the downstream box without having the change to be fully detached. Compared to the heaving motion, the situation is quite different, since such a "protection effect" does not take place.

A better understanding on these relationships can only be attained with investigations on the pressure field in the gap, through flow visualization and velocity measurement techniques. So the assertions about the velocity of the flow in the gap can be made by considering also the size of the trailing edge vortices, which may whether involve the downstream box or not, depending on the wind velocity, type of motion and shape of the upstream box. In this thesis, since the focus is on the resulting unsteady pressure characteristics, these investiga-

tions were not conducted, despite being essential for the understanding of the aerodynamics related to two-box cross-sections.

As for the amplitude distribution, the main focus should be put on the tendency the peaks show to increase in value and move downstream (in relation to the leading edge of the downstream box) with the increase of the gap length. Both relationships are also directly proportional to the wind velocity and since the latter can be regarded to the reattachment point of the flow, additional insight on the flow field around the downstream box can be provided.

Comparing the shapes of the amplitude $\tilde{C}_p(x^*)$ distributions between the downstream and upstream boxes for the same wind velocity in a same model, the resemblance between them can be described by a truncation of the amplitude $\tilde{C}_p(x^*)$ distribution of the downstream box, as if the separation point of that box was located somewhere inside the gap. With the increase of the gap length this truncation is reduced, and both distributions (in the upstream box and in the downstream box) tend to get similar.

Similarly to Fig.6.42, the amplitude $\tilde{C}_p(x^*)$ distributions for all gap lengths are superimposed in Fig.6.44, for reduced wind velocity U/f.B^*= 7.5, and Fig.6.45, for reduced wind velocity U/f.B^*= 50. From these two figures, it can be seen that although the patterns observed in the low reduced wind velocity differ a little from the ones obtained in the high reduced wind velocity, they can be considered similar.

The first important aspect of these figures is that the values of the peaks in both heaving and torsional systems follow a linear increasing tendency until a certain value of gap length is reached. Above that value of gap length, the behavior is changed, assuming different tendencies in each system. For the lower wind velocity range, the linear tendency is kept until the gap length of $0.5B^*$. For the higher velocity range, this limit is stretched to $1.0B^*$.

After those limit values ($0.5B^*$ and $1.0B^*$), the torsional system follows a parabolic tendency towards the *undisturbed value*, which is expected to be the same as the one observed in the upstream box when its influences are ceased. In the heaving motion, before reaching the undisturbed value, a peak is exhibited and so the values return to an inferior level, where they stabilize. Fig.6.46 shows these considerations for the reduce wind velocity U/f.B^*= 7.5, and Fig.6.47 for U/f.B^*= 50.

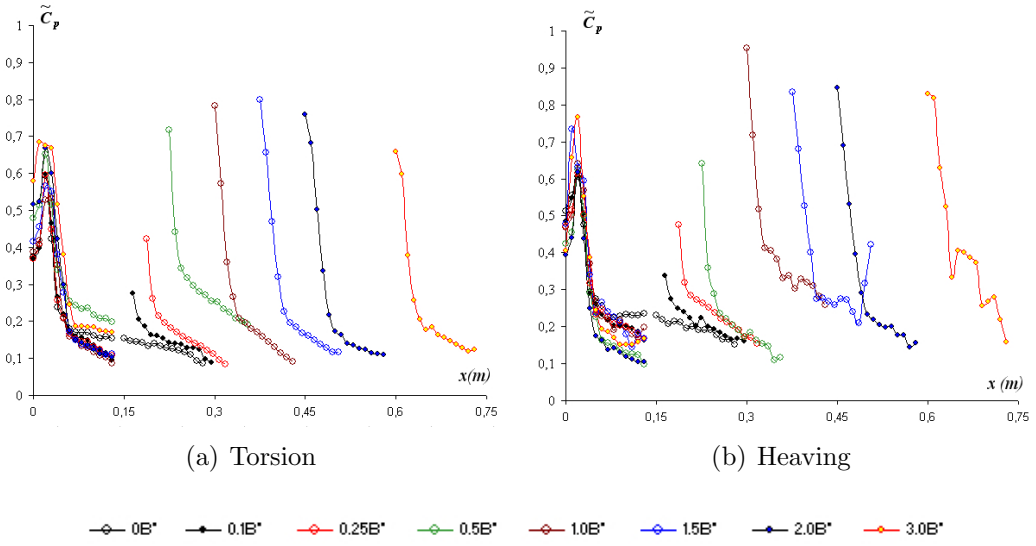

(a) Torsion (b) Heaving

Figure 6.44: Superposition of amplitude $\tilde{C}_p(x^*)$ distribution for two-box cross-sections at reduced wind velocity U/f.B^*= 7.5

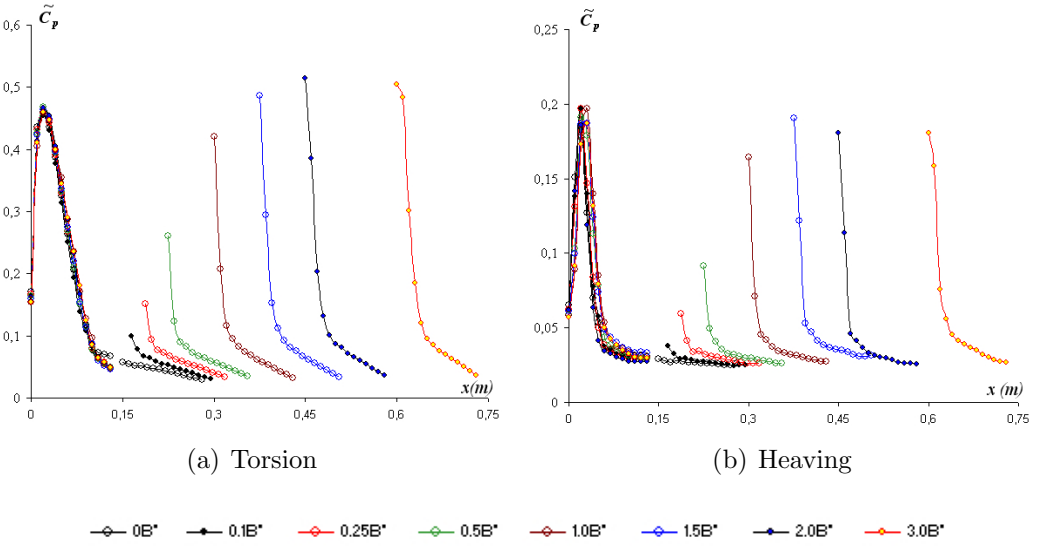

(a) Torsion (b) Heaving

Figure 6.45: Superposition of amplitude $\tilde{C}_p(x^*)$ distribution for two-box cross-sections at reduced wind velocity U/f.B^*= 50

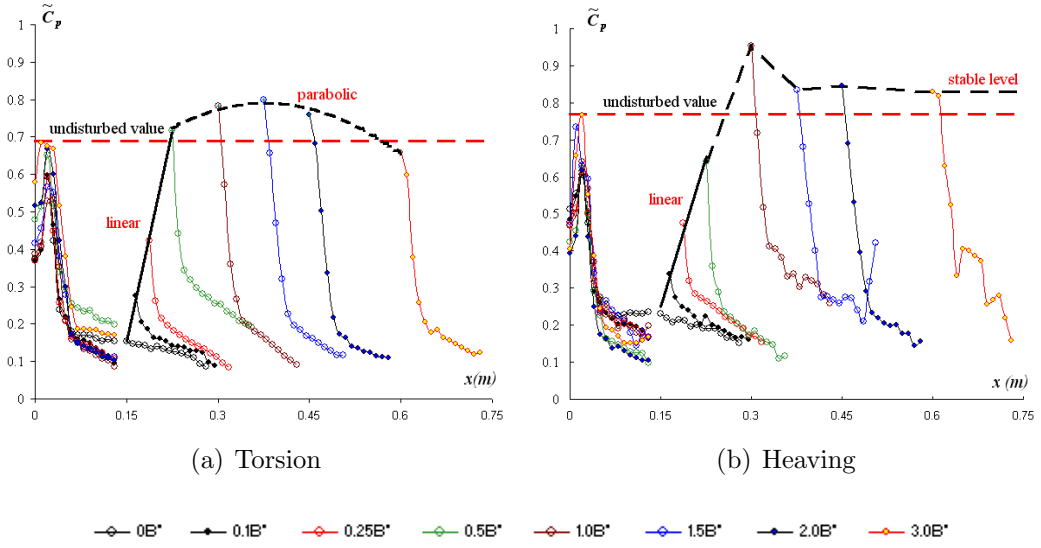

(a) Torsion (b) Heaving

Figure 6.46: Tendencies of the amplitude $\tilde{C}_p(x^*)$ distribution for downstream box at reduced wind velocity U/f.B^*= 7.5

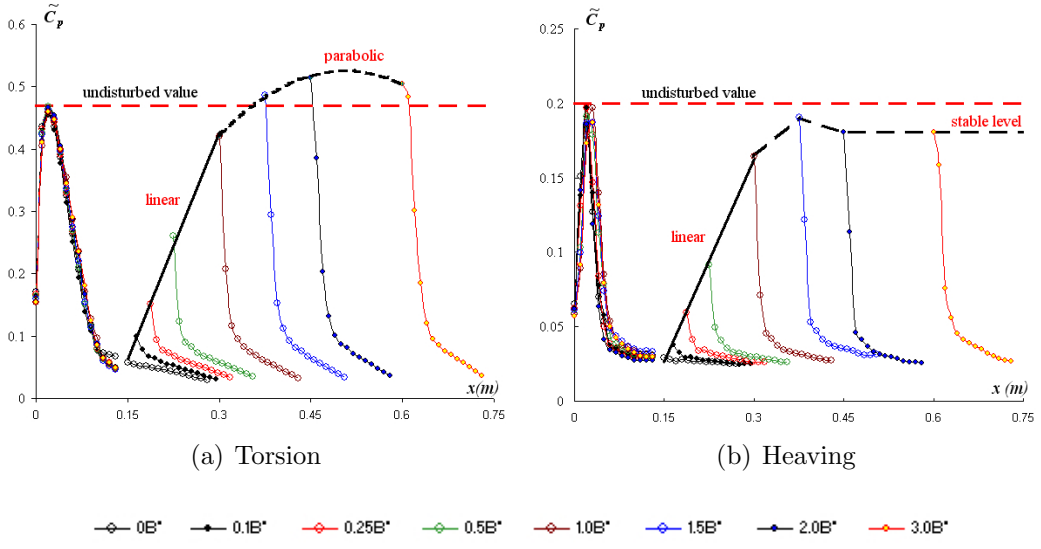

(a) Torsion (b) Heaving

Figure 6.47: Tendencies of the amplitude $\tilde{C}_p(x^*)$ distribution for downstream box at reduced wind velocity U/f.B^*= 50

With the increase of the reduced wind velocity, torsional and heaving systems show opposite tendencies for the *stable value*. While in the heaving system it tends to be located below the *undisturbed value*, in the torsional system it is kept above that limit.

This fact confirms that even for gap length as large as $3.B^*$, the influences of the gap on the amplitude $\tilde{C}_p(x^*)$ distribution of the downstream box is quite prominent, both on its value and on its shape, since the truncation is still remarkable. Nevertheless, for a gap length larger than $1.5B^*$ the effects on the peaks of the $\tilde{C}_p(x^*)$ distributions of the downstream box tend to get reduced. The critical zone is within the range of $0B^*$ and $1.5B^*$, where the influences of the gap are more visible, agreeing with the tendency observed in the phase difference $\psi(x^*)$ distribution of the heaving system, Fig.6.43(b).

6.6.1 Effects of Vertical Plates

The interactions between the effects of vertical plates and slots can be assessed by analyzing the results reported in Fig.6.9, Fig.6.10, Fig.6.12 and Fig.6.13, considering also the effects of the vertical plate on the single B/D=20 rectangular cylinder studied in Chapter 5, reported in Fig.5.29 and reproduced in Fig.6.48.

In Fig.6.48, a vertical plate with size equivalent to the thickness of the rectangular cylinder was installed at the midpoint of its cross-section, which is the same situation of Fig.6.9, Fig.6.10, Fig.6.12 and Fig.6.13 if each box is considered as an individual instance.

Firstly, it should be noted that the effects of the vertical plate in the upstream box are independent of the existence of a vertical plate in the downstream box and of the gap length, since a comparison between cases $1.0B^*$_VL, $1.0B^*$_VB, $2.0B^*$_VL and $2.0B^*$_VB shows essentially the same configurations of unsteady pressure characteristics for the upstream boxes in both heaving and torsional systems.

Comparing the resulting unsteady pressure characteristics of these models ($1.0B^*$_VL, $1.0B^*$_VB, $2.0B^*$_VL and $2.0B^*$_VB) with the ones related to the single box studied in Chapter 5, Fig.6.48, it is possible to verify that they are virtually the same for the same reduced wind velocities, for all cases. So the same conclusions obtained in Chapter 5 can be extended to the upstream box of cases $1.0B^*$_VL, $1.0B^*$_VB, $2.0B^*$_VL and $2.0B^*$_VB.

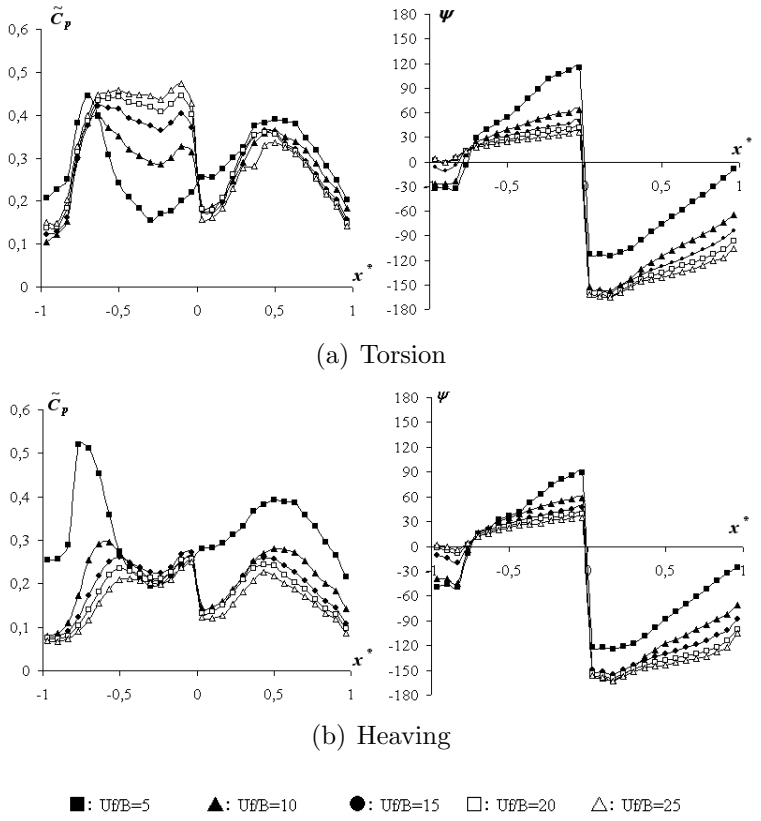

Figure 6.48: Unsteady pressure characteristics of case NF-VII-B

As for the downstream box, it was already mentioned that the gap cancels the continuity tendency from upstream box to downstream box in the phase difference $\psi(x^*)$ distribution. Comparing the cases with and without vertical plate in the upstream box, it is confirmed that the unsteady pressure characteristics of the downstream boxes are the same for both configurations, being only slightly dependent on the gap length. Because of that, it is concluded that a vertical plate installed in the upstream box has minimal influence on the unsteady pressure characteristics of the downstream box.

So analyzing in a gap length basis the cases with vertical plate installed in the downstream box (VB), it is possible to identify that at locations upstream the vertical plate the unsteady pressure characteristics are comparable to the cases without vertical plate. The influences of the vertical plate are essentially the same observed in a single box (Chapter 5), i.e. a "jump" in the phase difference $\psi(x^*)$ distribution and the peaks and "blockage effects"

caused by the vertical plate on the amplitude $\tilde{C}_p(x^*)$ distribution. The magnitude of the "jump" in the phase difference $\psi(x^*)$ distribution is comparable to the one observed in the upstream box and in the single box model. Also, the recovering of the values downstream the vertical plate can be visualized.

As for the amplitude $\tilde{C}_p(x^*)$ distribution, for both values of gap length the results are quite similar. However, comparing with the single box of Fig.6.48 some differences can be identified, mostly in the values of the peaks, which get reduced. Also, the location of the peak after the vertical plate is moved downstream. This can be related to the impacts of the oncoming flow on the influences of vertical plates on the amplitude distribution, already discussed in Chapter 5.

This "weakening" tendency in the peaks of the amplitude distribution was also observed in Chapter 5 for vertical plates installed at the midpoint of the downstream half of the cross-section, i.e. case NF-VI-B reproduced in Fig.6.49. In that chapter, it was observed a tendency of reduction of the influences of the vertical plate on the amplitude distribution with the increase of the distance from the leading edge and this tendency agrees quite well with the phenomenon observed in the cases studied in this chapter.

As a conclusion, it can be understood that the effects of vertical plates on the unsteady pressure characteristics of two-box girders are similar to what can be observed in single box girders, both on phase difference $\psi(x^*)$ and amplitude $\tilde{C}_p(x^*)$ distributions, qualitatively and quantitatively. The gap, however, may cancel their effects. Considering that, studies performed with single box can be extended to two-box girders.

6.7 Conclusion

In this chapter, a study based on wind tunnel tests about the effects of the gap on the unsteady pressure characteristics of two-box cross-sections was presented. The objective was to assess the functions of the gap as a *geometric singularity*, in search of a rationalization of the relationships between its characteristics and the consequent impacts on the unsteady pressure characteristics of each box, considering flutter stabilization as main motivation. A wide range of values of gap length was investigated, including values as small as $0.1B^*$ to values as large as $3.0B^*$. By doing so, it was tried to cover as much as possible the evolution

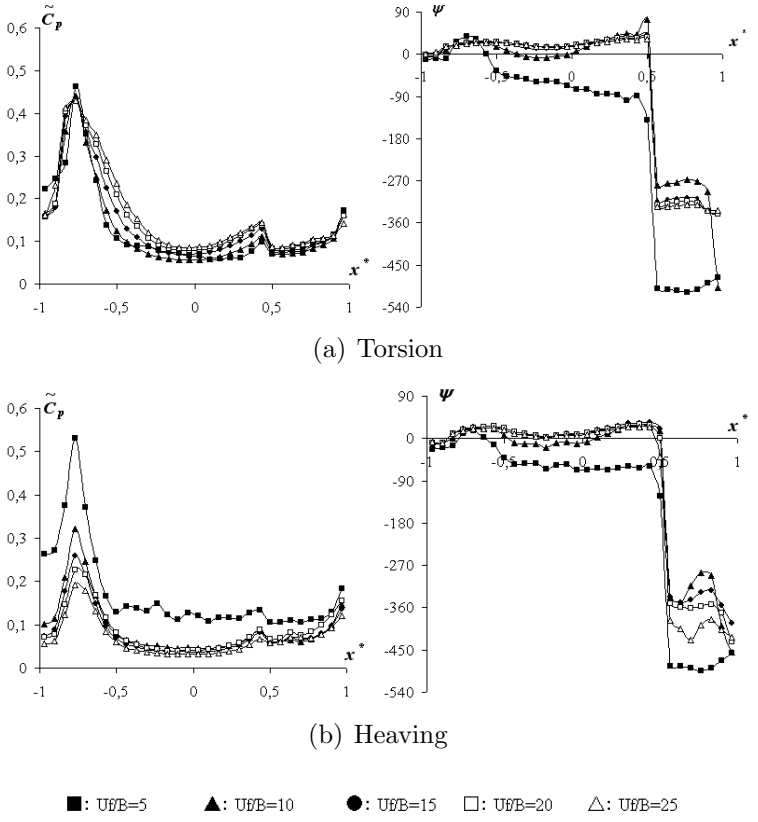

Figure 6.49: Unsteady pressure characteristics of case NF-VI-B

of the effects on the unsteady pressure characteristics and to attain an insight about the aerodynamics, not focusing solely on the design of actual structures.

Since the use of the original Theodorsen function shows itself not to be appropriate for comparison purposes with two-box cross-sections, an *equivalent Theodorsen function* to be used with such a kind a cross-section, which deals with the existence of two plates in synchronized motion, was proposed and used as benchmark for the analysis developed herein.

Depending on the way the reduced wind velocity is normalized, different perspectives of the results are obtained. The normalization in relation to the total width of the cross-section results in different wind velocities U for the same reduced wind velocity U_r, since every value of gap length induces a different resulting total width. Because of that, the Reynold's number

effects may change the relationships between the unsteady pressure characteristics from case to case for the same reduced wind velocity. Since the focus of this study is on the unsteady pressure characteristics of the individual boxes, it was thought to be convenient to use a reduced wind velocity normalized by the width B^* of an individual box, so a comparison between the unsteady pressure characteristics of the boxes of the different arrangements of gap length could be established for all velocities tested, in a reduced wind velocity basis.

Primarily, the impact of the gap on the aerodynamic derivatives was related to a reduction of their absolute values, and the only aerodynamic derivative that showed a considerably high aerodynamic dependence on variations of the gap length was A_2^*. Although the gap was recognized to induce modifications on the unsteady pressure characteristics of the downstream box, the role of the variation of the gap length was regarded mostly to *mathematical effects* on the integrals used to calculate the aerodynamic derivatives (Eq.2.52 to Eq.2.59), with low aerodynamic effects on the unsteady pressure characteristics of the models. This could be verified by comparing the resulting unsteady pressure characteristics of both upstream and downstream boxes among the different configurations of models (in a upstream box to upstream box and downstream box to downstream box basis).

Based on that, it is concluded that the differences exhibited by the aerodynamic derivatives of different arrangements of gap length are more related to the modifications in the solidity ratio and in the arm length (in the case of A_i^* derivatives) than to the modifications on the unsteady pressure characteristics themselves. This phenomenon can be caught only by analyzing the unsteady pressure characteristics, and this fact reinforces the argument that on the understanding of the effects of the geometric improvements on the flutter stability of a given cross-section, the focus should be put on the unsteady pressure characteristics, not directly on the aerodynamic derivatives.

When the gap is associated to other *geometric singularities*, the numerical tendencies assumed by the derivatives change drastically, becoming very difficult to be rationalized. However, from an unsteady pressure characteristics point of view the effects of the presence of singularities were revealed to be quite simple and rationalizable. The vertical plates induce modifications similar to the ones observed in the single boxes of Chapter 5, both on phase difference $\psi(x^*)$ and amplitude $\tilde{C}_p(x^*)$ distributions. Such modifications are independent of the gap length, not modifying neither interfering on the effects of the gap. In this sense, the gap was found to be dominant in the definition of the unsteady pressure characteristics of the downstream box, virtually ignoring the modifications induced by a vertical plate installed in the upstream box, i.e. the unsteady pressure characteristics of the downstream box are

defined mostly by only the existence of the gap.

In the case of using grating, only some attenuation in the effects of the gap could be detected. Intermediary configurations between regular downstream box of a two-box cross-sections and downstream half of single box cross-sections were produced in the downstream box when grating was installed. So the beneficial effects in terms of flutter stabilization provided by the use of grating are indeed regarded to the effects of the arm length on the moment components of the aerodynamic derivatives and to the reduction of the solidity ratio. Every value of permeability of grating may induce different gradations of this intermediary state, and deeper studies would be required for the clarification of these relationships.

Although it could be concluded that the flow reattaches at the same position in the upstream box regardless the model is whether in torsional or in heaving motion, the pressure measurements of the downstream box revealed fundamental differences between the flow patterns in the wake of the upstream box between heaving and torsional oscillations. However, a better understanding on these relationships can be only attained with investigations on the pressure field in the gap, through flow visualization and velocity measurement techniques.

Based on the asymmetry of the influences of each box on the stability of the system, the use of asymmetrical cross-sections should be considered as good strategy in terms of flutter stabilization. The characteristics of the site, as preferential wind directions, or even the use of movable appendages and systems which would be disposed according to the direction of the wind, may be considered in the proposition of this asymmetry.

The conclusions about the use and the impacts of grating and vertical plates are not intended to be definitive, neither the impacts of the gap, since only few cases were investigated. They were used with the intention of promoting differences in the unsteady pressure characteristics in search for rational relationships between them.

Chapter 7

Concluding remarks

Aerodynamic derivatives have been regarded as essential components for the design of long span bridges, concerning flutter stability. However, analytical solutions for their precise evaluation are still not available, leading designers to resort to experimental techniques in order to obtain them, i.e. wind tunnel tests. Along the last decades, the relationships between these empirical coefficients, deck geometry and flutter stabilization have been extensively investigated, resulting in a sort of considerations that has already been reported. So, optimal scenarios in terms of aerodynamic derivatives can be delineated and this knowledge base has guided the process of fine tuning of the geometry of bridge decks towards flutter stabilization.

However, this fine tuning process is still surrounded by uncertainties and every new geometric proposition should be necessarily checked through wind tunnel tests, in order to assess its impacts on the aerodynamic derivatives and, consequently, on the flutter stability. These impacts have shown themselves to be not linear and highly sensitive to the location and to the intensity of the flow separation points, so that direct associations between geometry of bridge decks and these coefficients have lead to a number of situations still difficult to be rationalized.

The aerodynamic derivatives are resultant of the unsteady pressure characteristics developed along the bridge deck and there is a number of techniques used to obtain them empirically. However, most of these techniques are based on "indirect measurements", through

some system identification method which does not provide any information about the pressure distribution along the deck. Obtaining the unsteady pressure distribution through wind tunnel tests may be difficult and counter-productive, resulting in that alternatives methods as the measurements of the unsteady forces have been preferred. That is one of the reasons why the focus has been gradually changed from unsteady pressure characteristics to the aerodynamic derivatives themselves.

In this study, the geometric modifications imposed on the deck geometry were regarded as *geometric singularities*. Through wind tunnel tests, the impacts of some of these *geometric singularities*, i.e. vertical plates, slots, gratings and fairings, on the unsteady pressure characteristics of rectangular cylinders were investigated. As a result, it was found that, compared to the impacts of these *geometric singularities* on the aerodynamic derivatives, their effects on the unsteady pressure characteristics showed a higher degree of linearity and predictability, being possible to be systematized in semi-empirical formulations.

Based on that, it was concluded that the flutter stabilization problem can be better assessed through an unsteady pressure characteristics point of view, instead of the aerodynamic derivatives based approach. So, the main objective of this research was to assess the feasibility of the development of a design framework based on the direct *manipulation* of the unsteady pressure characteristics along the bridge deck, through the use of *geometric singularities*, focusing the flutter stabilization.

Firstly, *optimal unsteady pressure characteristics*, related to flutter proof cross-sections, were investigated, through flutter analysis and based on the role played by each aerodynamic derivative on the flutter stabilization mechanism. These *optimal unsteady pressure characteristics* become the target configurations in the design framework proposed herein, which should be obtained through the use of the *geometric singularities*. So, the impacts of the *geometric singularities* on the unsteady pressure characteristics were assessed, and strategies to *manipulate* them were discussed.

As a main characteristic of these optimal configurations, it was recognized that by moving the peaks of the amplitude distribution to downstream of the cross-section, the flutter stabilization is enhanced, provided the values of phase difference related to these peaks are in the "stability zone". In some circumstances, the flow separation may be a good strategy for flutter stabilization, since it induces a peak on the amplitude distribution and a "jump" on the phase difference distribution. Controlling these modifications in a proper way may bring benefits in terms of flutter stabilization.

In this sense, two box cross-sections can have their good stability characteristics partially explained, since one of the main impacts of the gap on the unsteady pressure distribution of such a cross-section is the induction of a peak on the downstream half of the deck. However, the stabilization mechanism was mostly regarded to the effects the gap have on the pitching moment related aerodynamic derivatives, i.e. A_i^* aerodynamic derivatives, due to the direct impact the gap length has on the arm length of every pressure point in the integration of the moments which compound these derivatives.

The effects of vertical plates were quite measurable and predictable. The impacts they have on single box cylinders can be extended to two-box cylinders linearly. The interactions between the effects of vertical plates and slots on the unsteady pressure distributions were also rationalizable. Essentially, the effects of vertical plates were proved to be quite linear and dependent on their locations along the side surface of the cylinder. By referring to how they impact on the unsteady pressure characteristics is possible to precisely manipulate the aerodynamic derivatives towards flutter stabilization.

It was demonstrated that if no *geometric singularity* is introduced in the bridge deck, its unsteady pressure characteristics will follow their natural tendencies, described by equations proposed in this thesis. The description of the unsteady pressure characteristics along the deck was tried by representing the phase difference distribution by a sinusoidal equation and the amplitude distribution by a Weibull distribution. The approximations provided by these equations, in terms of aerodynamic derivatives, are reasonable, provided the proper coefficients are used. In this study, the coefficients used in the equations were obtained empirically, and because of that further development is required concerning the proposition of strategies to obtain these coefficients analytically. A remarkable characteristic of these equations is regarded to the interconnection between phase difference and amplitude distributions, through the wave length developed along the body surface.

Based on the asymmetry of the influences of each side of the cross-section on the stability of the system, the use of asymmetrical cross-sections should be considered as a good strategy in terms of flutter stabilization. The characteristics of the site, as preferential wind directions, or even the use of movable appendages and systems which would be disposed according to the direction of the wind, may be considered in the proposition of this asymmetry.

All results reinforce the core idea of this study, i.e. the design of long span bridges towards flutter stabilization should be conducted by focusing on the unsteady pressure char-

acteristics developed along the bridge deck. They could be put into equations, whose coefficients show themselves to be rationalizable. The impacts *geometric singularities* have on the unsteady pressure characteristics and consequently on these equations are quite linear and rationalizable, exerting their influences not only downstream their locations but also upstream, depending on the characteristics of the oncoming flow. With the understanding of how the unsteady pressure characteristics are changed due to the presence of *geometric singularities*, it gets easier to infer the effects of geometric modifications on the aerodynamic derivatives, through a more rational procedure, reducing the trial and error approach commonly taken in wind tunnel tests.

So the bridge deck designers can propose the deck geometry by choosing consciously the *geometric singularities*, leading the unsteady pressure characteristics of the deck to behave the way it is necessary: towards to assume characteristics proper for flutter stability.

However, there is still much work to be done. The complete development of such a framework is a very complex task, and this research was limited to prove the feasibility of such approach, by using rectangular cylinders as base geometry in a case study-like approach. The concepts developed herein were proposed in a manner that they can be extended to cover generic cross-sections, as real bridge decks, in future works.

Future development demands obtaining the coefficients for a wider range of cross-sections and the proposition of analytical solutions for them. Also, the study of the impacts of different singularities, as vertical plates with different sizes, guide vanes, perforated vertical plates, etc, should be assessed and compared with the conclusions of this study.

Although reasonable results were obtained, actually no flow visualization was performed, and all the conclusions about the aerodynamics around the bodies were taken by considering pressure measurements, theoretical approaches and past experiences. Also, all test cases were performed with null angle of attack. It is recognized that the angle of attack has high influence on the unsteady pressure characteristics, changing substantially the patterns of the flow field in terms of size of vortices and reattachment points. So an extension of this work should be considered, based on flow visualization techniques, with different angles of attack.

Appendix A

Wind tunnel test – B/D=20 rectangular cylinder with different leading edges and vertical plate

The wind tunnel tests with the B/D=20 rectangular cylinder were conducted in a room-circuit Eiffel type wind tunnel, with working section of $1.8m$ height by $1.0m$ width. The model was made of wood and instrumented with 30 equidistant pressure taps, aligned in the chord direction in the middle of its span, Fig.A.1.

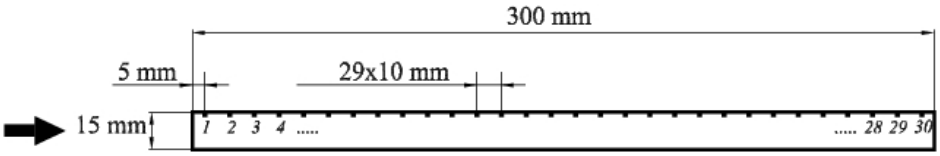

Figure A.1: Cross-section of the B/D=20 rectangular cylinder

The different configurations of leading edges were provided by prismatic bars made of wood with suitable cross-sections and length correspondent to the span of the model, affixed with double-face tape to the front face of the rectangular cylinder. The vertical plates were made of naval wood, with a thickness of $3mm$, and were also fixed to the upper surface of the model by using double-face tapes, Fig.A.2, to be easily removable after each run.

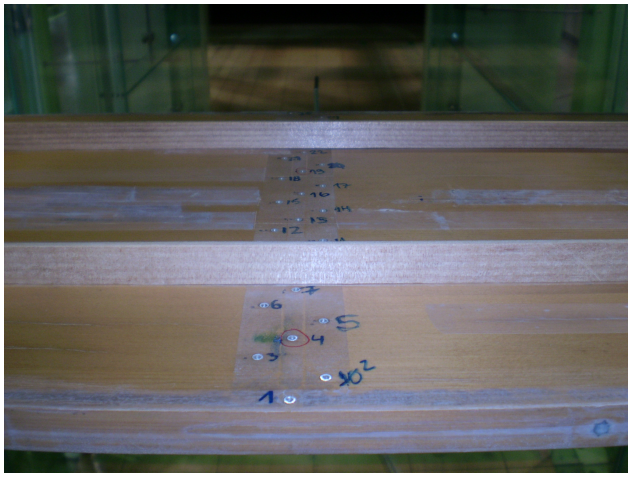

Figure A.2: Vertical plates installed on the upper surface of the B/D=20 rectangular cylinder

The pressure measurements were performed according to the procedures described in Appendix C, in smooth flow with turbulence less than 0.5% through forced heaving/torsional 1-DOF oscillation method. For both motions, the frequency of the forced oscillation was set to $f = 2Hz$. The amplitude of oscillation in the torsional system was $2\varphi = 4°$; for the heaving system it was $2\eta = 20mm$.

For the acquisition of the pressure signals, only 28 channels were available. So the resulting values of phase difference and pressure amplitude corresponding to the pressure taps 10 and 19 were interpolated from the neighbors, i.e. from taps 9 and 11 for tap 10, from taps 18 and 20 for tap 19.

The results, Fig.4.10 to Fig.4.13, are expressed by the amplitude of the unsteady pressures normalized by the dynamic pressure of the flow and by the phase difference between the maximum relative angle of attack and negative peak of surface pressure, according to Section 2.2.

Appendix B

Wind tunnel test – Two-box cross-sections

Similarly to Appendix A, a room-circuit Eiffel type wind tunnel with working section of $1.8m$ height by $1.0m$ width was used in the experiments. The model was made of duraluminium and instrumented with 28 equidistant pressure taps, 14 in each box, aligned in the chord direction in the middle of the span, Fig.B.1.

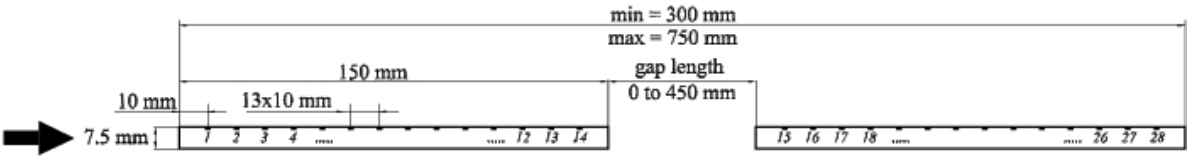

Figure B.1: Two-box cross-section

The gap length in the models was adjusted by a supporting system composed by two horizontal L-bars with numbered holes at pre-defined positions in each side of the model. For every value of gap length, two holes marked the position of each box, which were fixed to the supporting system by a bolt-nut system that compressed the box in a *sandwich* like fixation system, Fig.B.2. By adjusting the supporting system to suitable positions, according to the desired gap length, the various configurations of model could be set, Fig.B.3

The vertical plates were made of naval wood, with a thickness of $3mm$, and were affixed

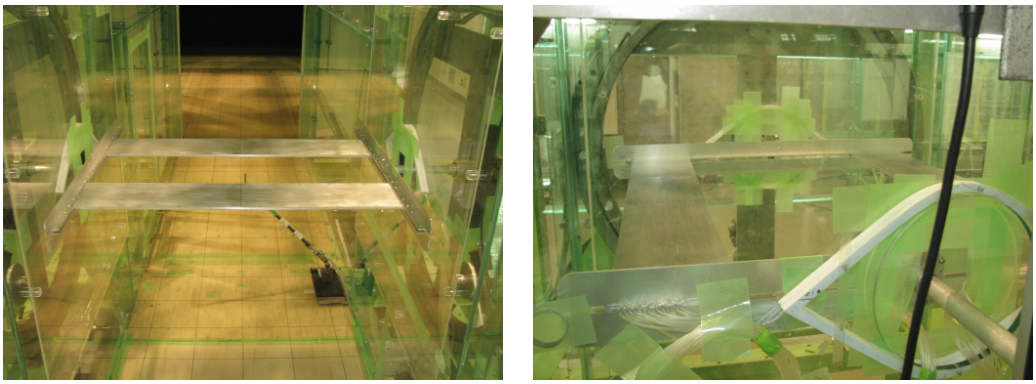

(a) inside the wind tunnel (b) outside the wind tunnel

Figure B.2: Fixation system

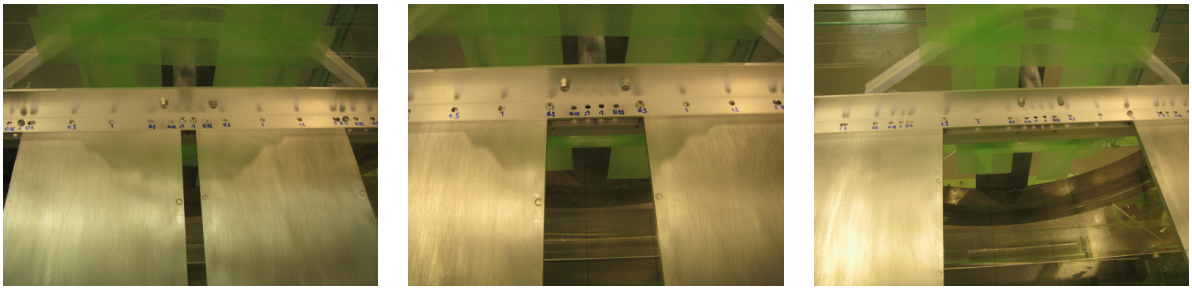

(a) gap length=0.1B^* (b) gap length=0.5B^* (c) gap length=1.5B^*

Figure B.3: Two-box with different gap lengths

to the upper surface of the model by using double-face tapes, Fig.B.4, to be easily removable after each run. As for the gratings, perforated acrylic sheets with opening ratio of 35% were disposed in the gap in order to cover all the space between the boxes, Fig.B.5.

The pressure measurements were performed according to the procedures described in Appendix C, in smooth flow with turbulence less than 0.5% through forced heaving/torsional 1-DOF oscillation method. For both motions, the frequency of the forced oscillation was set $f = 2Hz$. The amplitude of oscillation in the torsional system was $2\varphi = 4°$; for the heaving system it was $2\eta = 20mm$.

The results, Fig.6.1 to Fig.6.14, are expressed by the amplitude of the unsteady pressures normalized by the dynamic pressure of the flow and by the phase difference between

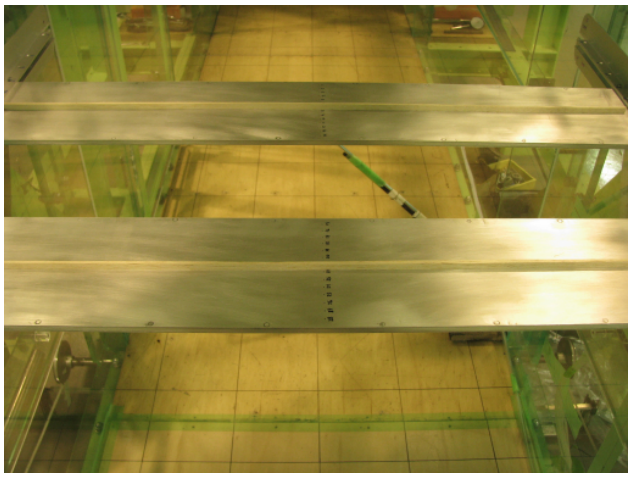

Figure B.4: Vertical plate in two-box cross-section

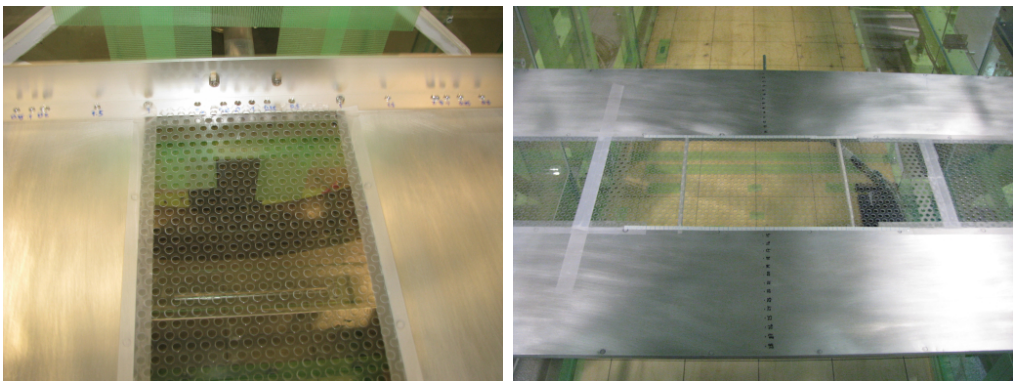

Figure B.5: Grating in two-box cross-section

the maximum relative angle of attack and negative peak of surface pressure, according to Section 2.2.

Appendix C

Wind tunnel test – Pressure measurements

The acquisition of the pressure signals to be used in the evaluation of the unsteady pressure characteristics was conducted by using a system arranged according to Fig.C.1.

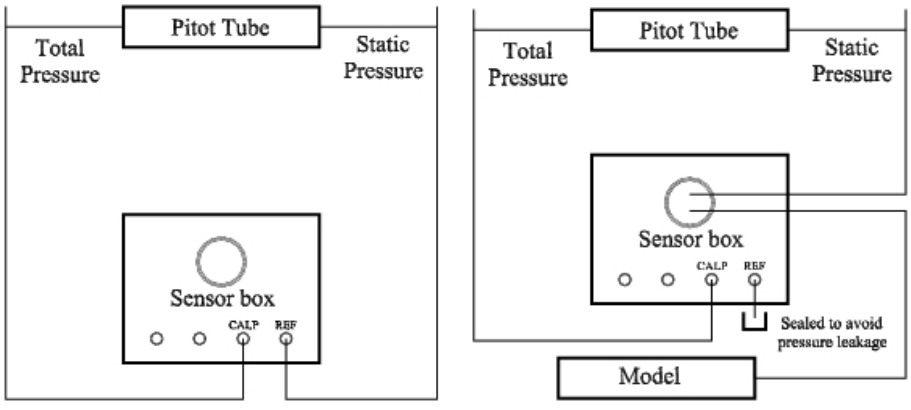

(a) Calibration (b) Measurement

Figure C.1: Pressure measurement system

The pressure signals were carried from the pressure taps installed in the models, Fig.C.2, to the *ZOC 17 sensor box* located outside the wind tunnel, Fig.C.3, through a set of silicone tubes, Fig.C.4. These tubes were kept as short as possible, in order to min-

imize the phase lag of the tubing system, regarded as the lag between the pressure signal arriving in the sensors of the sensor box and the correspondent pressure signal obtained at the surface the models, i.e. pressure taps.

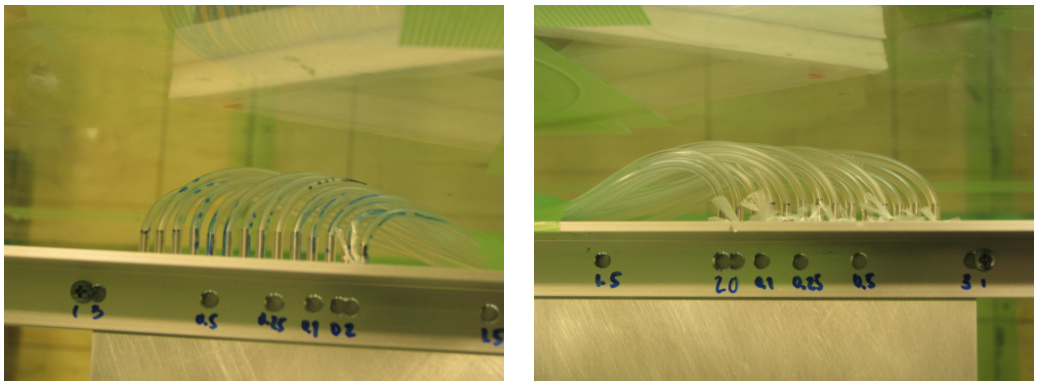

Figure C.2: Tubing from the model

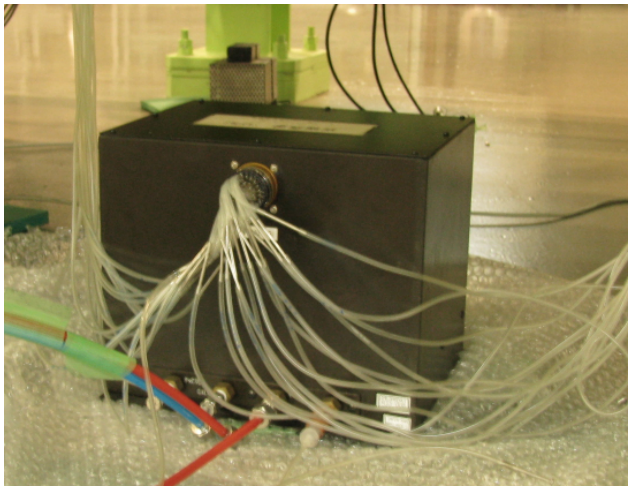

Figure C.3: Sensor box

This phase lag was estimated in 8°, through a technique based on the imposition of a controlled pressure fluctuation inside the wind tunnel test chamber, which was measured by using two different processes, i.e. the pressure measurement system used in the experiments and a *reference measurement system* with no phase lag. In this technique, the pressure fluctuation at a given location is acquired concomitantly by using the two different systems and the comparison between them provides the phase lag of the tubing system. For the *reference measurement system*, a hot-wire probe was used to acquire the velocity fluctuations

Figure C.4: Model in the wind tunnel

and the results presented in Chapter 4, Chapter 5 and Chapter 6 already account for this phase lag.

Concerning the experiments, before every session the equipments should be calibrated. Basically, this process consisted of imposing a wind velocity in the wind tunnel correspondent to a static pressure of $10mm\ H_20$, measured with a pitot tube, Fig.C.1(a). So the electrical signals provided by the sensors were verified and, since they were known to behave linearly in the range of the values used in the experiments, a simple proportionality index to be used during the measurements, Fig.C.1(b), was generated for each one of them. During the measurements, the measured values were the pressure differences from the atmospheric pressure (ATM mode); during the calibration they were referent to the pressure difference from the static pressure (PS mode).

The pressure signals were normalized by the dynamic pressure, providing non-dimensionalized values. The values of phase difference $\psi(x^*)$ were calculated through their *cross-correlation* with the displacements, which were acquired by using non-contact laser

sensors. All the data was processed and analyzed by using routines developed in Matlab.

Appendix D

Scientific production

- **Effects of gap and vertical plates on the unsteady pressure characteristics of two-box cross-sections**. *In this study the role played by the air-gap in the definition of the unsteady pressure characteristics of two-box cross-sections was investigated. Also, the interactions with vertical plates and the use of grating grids were considered in the analyses. A modified Theodorsen function to be used as benchmark for the studies with two-box cross-sections was also presented. All relationshps were proved to follow linear tendencies, showing themselves to be much more "predictable" than the effects on the aerodynamic derivatives.*

  TREIN, Cristiano Augusto; SHIRATO, Hiromichi - Effects of gap and vertical plates on the unsteady pressure characteristics of two-box cross-sections. submitted to Journal of Wind Engineering and Industrial Aerodynamics in September 2009.

- **Study on the unsteady pressure characteristics of modified rectangular cylinders – effects of leading edges and vertical plates**. *In this study, empirical equations to be used in the estimation of the unsteady pressure characteristics of rectangular cylinders are investigated, as part of the development of a bridge deck design framework based on the manipulation of these characteristics. Even modified with different configurations of leading edges, the phase difference distribution of such a bluff body could be approximated through a sinusoidal equation, the amplitude distribution followed a Weibull distribution and both showed themselves to be interrelated through the wave length developed along the body's surface. The efficacy of the approximations could be confirmed through wind tunnel tests. The effects of vertical plates installed at*

different locations along the cylinders' side surface on their unsteady pressure characteristics were also investigated, proving themselves to be more linear than the effects on the aerodynamic derivatives.

TREIN, Cristiano Augusto; SHIRATO, Hiromichi - Unsteady Pressure Characteristics of Modified Rectangular Cylinders. submitted to Journal of Wind Engineering and Industrial Aerodynamics in June 2009. awaiting approval.

- **Coupled flutter stabilization from the unsteady pressure characteristics point of view**. *In this study, coupled flutter stabilization is discussed from the unsteady pressure characteristics point of view. Based on the role played by the aerodynamic derivatives, configurations of unsteady pressure characteristics suitable for flutter stabilization, namely optimal unsteady pressure characteristics, are discussed along with their effects on each aerodynamic derivative. It was found that by moving the peaks of the amplitude $\tilde{C}_p(x^*)$ distribution to downstream, beneficial effects in terms of flutter stabilization can be obtained, provided the phase difference is in the stable zone. Contrarily, the peaks usually presented at the leading edge of the cross-sections reduce the flutter onset. The important role played by the aerodynamic derivative A_1^* in the flutter stabilization is confirmed.*

  TREIN, Cristiano Augusto; SHIRATO, Hiromichi - Coupled flutter stabilization from the unsteady pressure characteristics point of view. submitted to Journal of Wind Engineering and Industrial Aerodynamics on 2009/may/15. awaiting approval.

- **On the Unsteady Pressure Characteristics of Modified Rectangular Cylinders**. *Empirical equations to be used in the estimation of the unsteady pressure characteristics of rectangular cylinders are investigated, as part of the development of a bridge deck design framework based on the manipulation of these characteristics. Even by using different leading edges it could be verified that the phase difference distribution can be approximated by a sinusoidal equation, the amplitude distribution follows a Weibull distribution and both are interrelated by the wave length developed along the body's surface. The efficacy of the formulation could be confirmed through wind tunnel tests.*

  TREIN, Cristiano Augusto; SHIRATO, Hiromichi; MATSUMOTO, Masaru - On the Unsteady Pressure Characteristics of Modified Rectangular Cylinders. submitted to Asia-pacific Conference on Wind Engineering VII – APCWE-VII – on 2009, feb. 25^{th}. Taipei, Taiwan. 2009, Nov. already accepted.

- **Unsteady Pressure Characteristics of Modified Rectangular Cross-sections**. *In this study, empirical equations to be used in the estimation of the unsteady pressure*

characteristics of rectangular cylinders are investigated, as part of the development of a bridge deck design framework based on the manipulation of these characteristics. Even by using different leading edges it could be verified that the phase difference distribution of such a bluff body can be approximated by a sinusoidal equation, the amplitude distribution follows a Weibull distribution and both are interrelated by the wave length developed along the bodys surface. The efficacy of the formulations could be confirmed through wind tunnel tests.

TREIN, Cristiano Augusto; SHIRATO, Hiromichi; MATSUMOTO, Masaru - Unsteady Pressure Characteristics of Modified Rectangular Cross-sections. Proceedings of 1^{st} Open Seminar on Fluid Sciences. $2008, march18^{th}$, Kyoto University, Katsura Campus - Japan

- **Investigation of coupled flutter mechanism and Selberg's formula**. *The flutter phenomenon is one of the divergent oscillations which directly leads to the failure of structure. So, the flutter stabilization is one of the most important subjects in the design of long-span bridge girders. For flutter analysis method, Complex Eigen-Value analysis is commonly used. Complex Eigen-Value analysis is not enough to discuss flutter control, while it is enough to discuss flutter stabilization. Then, Step-by-Step analysis which is based on flutter generation mechanisms was proposed. However some differences between both solutions have been observed. In Step-by-Step analysis, harmonic vibration is assumed, however its assumption is disadvantageous. When damping vibration is assumed and convergence calculations associated to flutter frequency and damping are carried out simultaneously, both solutions show the good agreement. In addition, new strategies for flutter control are investigated. And it is clarified that A_1^* is the most important aerodynamic derivative to stabilize the coupled flutter instability, considering the mutual relationships of aerodynamic derivatives. Moreover, it is made a study on Selberg's formula by Step-by-Step analysis and its elicitation process is clarified.*

  Masaru MATSUMOTO; Yasuaki ITO; Hisato MATSUMIYA; *Shinya FUJIWARA; TREIN, Cristiano Augusto - Investigation of coupled flutter mechanism and Selberg's formula. The 20^{th} KKCNN Symposium on Civil Engineering, South Korea, 2007.

- **Evaluation of Branch Switching Characteristics in Coupled Flutter through Revised Step-by-Step Analysis**. *Branch switching characteristics for coupled flutter of structural rectangular sections are analyzed using step-by-step flutter analysis (SBSA). Prior to the appearance of coupled flutter instability, the torsional branch (TB) controls the instability. However, after flutter onset both TB and heaving branch (HB) coexist, with sudden switching in particular velocity ranges. For lower velocity ranges, very good agreement can be obtained between conventional Complex Eigen*

Value Analysis (CEVA) and SBS method, but for higher velocity ranges this agreement cannot be attained. So SBSA is revised, leading to fairly good convergence between both methods.

TREIN, Cristiano Augusto*; MATSUMOTO, Masaru; ITO, Yasuki; MATSUMIYA, Hisato; FUJIWARA, Shinya - Evaluation of Branch Switching Characteristics in Coupled Flutter through Revised Step-by-Step Analysis. Proceedings of 62^a edition of Academic Meeting and National Convention on Civil Engineering, Japanese Society of Civil Engineering, JSCE 2008/1 monthly issue. Hiroshima, Japan 2007

- **Equivalent Aerodynamic Derivatives and their Influences on Coupled Flutter Instability**. *Flutter instability is a catastrophic oscillation and its stabilization is an important issue in the design of long span bridges. In this study, a strategy for coupled flutter stabilization of long-span bridges is presented. The approach is based on the reduction of the absolute values of the aerodynamic derivatives A1* and H3*, by a proper arrangement of multiple bridge girders along the span direction of the bridge, which was proved effective through wind tunnel tests.*

  TREIN, C.A*.; MATSUMOTO, M.; ITO, Y.; MATSUMIYA, H.; KIM, G.; FUJIWARA, S. - Equivalent Aerodynamic Derivatives and their Influences on Coupled Flutter Instability. Proc. of Academic Meeting and National Convention on Civil Engineering, Japanese Society of Civil Engineering - Kansai Shibu. Osaka, Japan 2007.

- **Controlled Aerodynamic Instability Phenomena - An Alternative Approach for Wind Power Generation Systems**. *In this study the concept of Controlled Aerodynamic Instability Phenomena is proposed, as an alternative approach for Wind Power Generation systems. The concept is based on the idea that aerodynamic instability phenomena, such as Karman Vortex Shedding, Flutter, Galloping and Buffeting, can be driven into a useful motion and be used to extract energy from the flow. A case study using the flutter instability is presented and the concept is proved feasible. By using a forced torsional oscillation, the heaving motion is induced in a bluff body, so the energy generated by the heaving motion is estimated by both analytical and experimental processes, converging to the same conclusion. Finally, the results are discussed and alternatives for future developments are introduced.*

  MATSUMOTO, M.; TREIN, C*.; ITO, Y.; OKUBO, K.; MATSUMIYA, H.; KIM, G. - Controlled Aerodynamic Instability Phenomena - An Alternative Approach for Wind Power Generation Systems. The Nineteenth KKCNN Symposium on Civil Engineering, Japan, 2006.

- **Branch switching characteristics of coupled flutter instability**. *As a bridge gets longer and slender, one of the main problems that have to be faced is the flutter instability of bridge girders such as the torsional flutter and the coupled flutter.*

Especially, the coupled flutter instability has become the most concerning issue in the design of long-span bridges, and the precise understanding on its generation mechanism is indispensable in order to effectively stabilize this divergent oscillation. In this study, the heaving/torsional 2-DOF flutter analyses and wind tunnel tests are carried out, focusing on the branch switching characteristics of the coupled flutter using B/D=20 rectangular section. Moreover, the branch co-existing characteristics in flutter onset velocity range is investigated in detail.

MATSUMOTO, M.; OKUBO, K.; ITO, Y.; MATSUMIYA, H.; TREIN, C.; KIM, G*. - Branch switching characteristics of coupled flutter instability. The Nineteenth KKCNN Symposium on Civil Engineering, Japan, 2006.

Bibliography

[1] Y. NAKAMURA. On the aerodynamic mechanism of torsional flutter of bluff structures. *Journal of Sound and Vibration*, 67:163–177, 1979.

[2] E.L.HOUGHTON; N.B.CARRUTHERS. *Wind Forces on Buildings and Structures: an Introduction*. Edward Arnold (Publishers) Ltd, London, 1976. ISBN: 0 7131 3361 9.

[3] Masaru MATSUMOTO. Aerodynamic damping of prisms. *Journal of Wind Engineering and Industrial Aerodynamics*, 59:159–175, 1996.

[4] M. MATSUMOTO; Y. KOBAYASHI; H. SHIRATO. The influence of aerodynamic derivatives on flutter. *Journal of Wind Engineering and Industrial Aerodynamics*, 60:227–239, 1996.

[5] Frederick Louis HAAN. *The Effects of Turbulence on the Aerodynamics of Long-Span Bridges*. University of Notre Dame. Ph.D. Thesis, USA, 2000.

[6] Masaru MATSUMOTO; Tetsuya HIKIDA; Keisuke MIZUNO. On improvement of flutter stability for long-span bridge girders - the case of separated box girders. *Proceedings of the 8th International Conference on Flow-Induced Vibration*, II:403–408, July6-9, 2004.

[7] Shuji SHIRAI; Toshio UEDA. Aerodynamic simulation by cfd on flat box girder of super-long-span suspension bridge. *Journal of Wind Engineering and Industrial Aerodynamics*, 91:279–290, 2003.

[8] Xinzhong CHEN. Improved understanding of bimodal coupled bridge flutter based on closed-form solutions. *Journal of Structural Engineering*, 60:22–31, 2007.

[9] Masaru MATSUMOTO; Hiromichi SHIRATO; Tomomi YAGI; Rikuma SHIJO; Akitoshi EGUCHI; Hitoshi TAMAKI. Effects of aerodynamic interferences between heaving and torsional vibration of bridge decks: the case of tacoma narrows bridge. *Journal of Wind Engineering and Industrial Aerodynamics*, 91:1547–1557, 2003.

[10] M. MATSUMOTO; K. MIZUNO; K. OKUBO; Y. ITO H. MATSUMIYA. Flutter instability and recent development in stabilization of structures. *Journal of Wind Engineering and Industrial Aerodynamics*, 95:888–907, 2007.

[11] Hiroki YAMAGUCHI; Manabu ITO. Mode-dependence of structural damping in cable-stayed bridges. *Journal of Wind Engineering and Industrial Aerodynamics*, 72:289–300, 1997.

[12] Xinzhong CHEN; Ahasan KAREEM. Advances in modeling of aerodynamic forces on bridge decks. *Journal of Engineering Mechanics*, 128:1193–1205, 2002.

[13] CHEN; Ahsan KAREEM; Masaru MATSUMOTO Xinzhong. Multimode coupled flutter and buffeting analysis of long span bridges. *Journal of Wind Engineering and Industrial Aerodynamics*, 89:649–664, 2001.

[14] Cristiano Augusto TREIN; Masaru MATSUMOTO; Yasuki ITO; Hisato MATSUMIYA; Shinya FUJIWARA. Evaluation of branch switching characteristics in coupled flutter through revised step-by-step analysis. *Proceedings of the* 62^a *edition of Academic Meeting and National Convention on Civil Engineering*, January 2008.

[15] K.KIMURA; K.SHIMA; K.SANO; Y.KUBO; K.KATO; H.UKON. Effects of separation distance on wind-induced response of parallel box girders. *Journal of Wind Engineering and Industrial Aerodynamics*, 96:954–962, 2007.

[16] M.MATSUMOTO; M.NAKAJIMA; Y.TANIWAKI; R.SHIJO. Grating effect on flutter instability. *Journal of Wind Engineering and Industrial Aerodynamics*, 89:1487–1497, 2001.

[17] Hiroshi SATO; Shigeki KUSUHARA; Ken ichi OGI; Hiroteru MATSUFUJI. Aerodynamic characteristics of super long-span bridges with slotted box girder. *Journal of Wind Engineering and Industrial Aerodynamics*, 88:297–306, 2000.

[18] K. OGAWA; H. SHIMODIO; T. ORYU. Aerodynamic characteristics of a 2-box girder section adaptable for a super-long span suspension bridge. *Journal of Wind Engineering and Industrial Aerodynamics*, 90:2033–2043, 2002.

[19] C.A.TREIN; M.MATSUMOTO; Y.ITO; H.MATSUMIYA; G.KIM; S.FUJIWARA. Equivalent aerodynamic derivatives and their influences on coupled flutter instability. *Proc. of Academic Meeting and National Convention on Civil Engineering*, 2007.

[20] Michel Virlogeux. Recent evolution of cable-stayed bridges. *Engineering Structures*, 21:737–755, 1999.

[21] Francesco RICCIARDELLI. On the wind loading mechanism of long-span bridge deck box sections. *Journal of Wind Engineering and Industrial Aerodynamics*, 91:1411–1430, 2003.

[22] Masatsugu NAGAI; Yozo FUJINO; Hiroki YAMAGUCHI; Eiji IWASAKI. Feasibility of a 1,400 m span steel cable-stayed bridge. *Journal of Bridge Engineering*, pages 444–452, Set-Oct 2004.

[23] Xinjun ZHANG; Bingnan SUN. Parametric study of the aerodynamic stability of a long-span suspension bridge. *Journal of Wind Engineering and Industrial Aerodynamics*, 92:431–439, 2004.

[24] Xinzhong CHEN; Ahsan KAREEM. Curve veering of eigenvalue loci of bridges with aeroelastic effects. *Journal of Engineering Mechanics*, 129:146–159, February, 2003.

[25] Yozo FUJINO. Vibration, control and monitoring of long-span bridges – recent research, developments and practice in japan. *Journal of Wind Engineering and Industrial Aerodynamics*, 58:71–97, 2002.

[26] G.DIANA; F.RESTA; M.BELLOLI; D.ROCCHI. On the vortex shedding forcing on suspension bridge deck. *Journal of Wind Engineering and Industrial Aerodynamics*, 94:341–363, 2006.

[27] Virote BOONYAPINYO; Toshio MIYATA; Hitoshi YAMADA. Advanced aerodynamic analysis of suspension bridges by state-space approach. *Journal of Structural Engineering*, 125:1357–1366, 1999.

[28] Ming GU; Ruoxue ZHANG; Haifan XIANG. Identification of flutter derivatives of bridge decks. *Journal of Wind Engineering and Industrial Aerodynamics*, 84:151–162, 2000.

[29] Yoshinobu KUBO; Eijirou YUKOKU; Vinod J. MODI; Eiki YAMAGUCHI; Kusuo KATO; Shin ichi KAWAMURA. Control of flow separation from leading edge of a shallow rectangular cylinder through momentum injection. *Journal of Wind Engineering and Industrial Aerodynamics*, 83:503–514, 1999.

[30] Masaru MATSUMOTO; Yoshinori TANIWAKI; Rikuma SHIJO. Frequency characteristics in various flutter instabilities of bridge girders. *Journal of Wind Engineering and Industrial Aerodynamics*, 90:1973–1980, 2002.

[31] Masaru MATSUMOTO; Yoshiyuki DAITO; Fumitaka YOSHIZUMI; Yasuo ICHIKAWA; Tadahiro YABUTANI. Torsional flutter of bluff bodies. *Journal of Wind Engineering and Industrial Aerodynamics*, 69-71:871–882, 1997.

[32] M. MATSUMOTO; F. YOSHIZUMI; T. YABUTANI; K. ABE; N. NAKAJIMA. Flutter stabilization and heaving-branch flutter. *Journal of Wind Engineering and Industrial Aerodynamics*, 83:289–299, 1999.

[33] Y.X.YANG. Two-dimensional flutter mechanism and its application long span bridges. *Ph.D.Thesis*, 2002. supervised by H.F.Xiang and Y.J.GE.

[34] Y.J.GE; H.F.XIANG. Recent development of bridge aerodynamics in china. *Journal of Wind Engineering and Industrial Aerodynamics*, 96:736–768, 2008.

[35] C.BORRI; M.MAJOWIECKI; P.SPINELLI. The aerodynamic advantages of a double-effect large span suspension bridge under wind loading. *Journal of Wind Engineering and Industrial Aerodynamics*, 48:317–328, 1993.

[36] Toshio MIYATA; Hitoshi YAMADA; Kohji KAZAMA. Discussion on aeroelastic detail and control in the flutter occurrences of long-span bridges. *Journal of Wind Engineering and Industrial Aerodynamics*, 69-71:839–849, 1997.

[37] Makoto KITAGAWA. Studies on suspended structures for super long-span suspension bridges. *Proceedings of the First International Conference on Advances in Bridge Engineering*, June, 2006.

[38] J.R.RICHARDSON. *The Development of the Concept of the Twin Suspension Bridge*, volume 1. National Maritime Institute, UK, 1981.

[39] G. BARTOLI; M. RIGHI. Flutter mechanism for rectangular prisms in smooth and turbulent flow. *Journal of Wind Engineering and Industrial Aerodynamics*, 94:275–291, 2006.

[40] W.C.BROWN. *Improvements in Bridges*. U.K. Patent Specification. 1523 811, UK, 1978.

[41] Le-Dong ZHU; Guang-Zhao CHANG; Chao LI. Skew wind effect on 2-dof coupled flutter of a flat-box deck. *Journal of Wind Engineering and Industrial Aerodynamics*, 108:497–500, 2006.

[42] Y. NAKAMURA. An analysis of binary flutter of bridge deck sections. *Journal of Sound and Vibration*, 57(4):471–482, 1978.

[43] Xinjun ZHANG. Influence of some factors on the aerodynamic behavior of long-span suspension bridges. *Journal of Wind Engineering and Industrial Aerodynamics*, 95:149–164, 2007.

[44] Haifan XIANG; Yaojun GE. Refinements on aerodynamic stability snalysis of super long-span bridges. *Journal of Wind Engineering and Industrial Aerodynamics*, 90:1493–1515, 2002.

[45] T. MIYATA; M. MIYAZAKI; H. YAMADA. Pressure distribution measurements for wind induced vibrations of box girder bridges. *Journal of Wind Engineering and Industrial Aerodynamics*, 14:223–234, 1983.

[46] Robert H. SCANLAN; John J. TOMKO. Airfoil and bridge deck flutter derivatives. *Journal of the Engineering Mechanics Division*, pages 1717–1737, 1971.

[47] T. THEODORSEN. General theory of aerodynamic instability and the mechanism of flutter. *NACA Report No. 496*, 1935.

[48] F. TUBINO. Relationships among aerodynamic admittance functions, flutter derivatives and static coefficients for long-span bridges. *Journal of Wind Engineering and Industrial Aerodynamics*, 93:929–950, 2005.

[49] Sungmoon JUNG; Jamshid GHABOUSSI; Soon-Duck KWON. Estimation of aeroelastic parameters of bridge decks using neural networks. *Journal of Engineering Mechanics*, 130:1356–1364, November, 2004.

[50] C.H. CHEN. Determination of flutter derivatives via a neural network approach. *Journal of Sound and Vibration*, 263:797–813, 2003.

[51] G.MORGENTHAL; F.A.McROBIE. A comparative study of numerical methods for fluid structure interaction analysis in long-span bridge design. *Wind and Structures*, 5:101–114, 1996. ISSN 1226-6116.

[52] L.BRUNO; D.FRANSOS. Evaluation of reynolds number effects on flutter derivatives of a flat plate by means of a computational approach. *Journal of Fluids and Structures*, 24:1058–1076, 2008.

[53] D.G.MABEY. A review of scale effects in unsteady aerodynamics. *Prog. Aerospace Sci.*, 28:273–321, 1991.

[54] Kazutoshi MATSUDA; Masafumi TOKUSHIGE; Tooru IWASAKI. Reynolds number effects on the steady and unsteady aerodynamic forces acting on the bridge deck sections of long-span suspension bridge. *IHI Engineering Review*, 40:12–26, 2007.

[55] K.MATSUDA; K.R.COOPER; H.TANAKA; M.TOKUSHIGE; T.IWASAKI. An investigation of reynolds number effects on the steady and unsteady aerodynamic forces on a 1:10 scale bridge deck section model. *Journal of Wind Engineering and Industrial Aerodynamics*, 89:619–632, 2001.

[56] Gianni BARTOLI; Claudio MANINI. A simplified approach to bridge deck flutter. *Journal of Wind Engineering and Industrial Aerodynamics*, 96:229–256, 2008.

[57] M. NODA; H. UTSUNOMIYA; F. NAGAO; M. KANDA; N. SHIRAISHI. Effects of oscillation amplitude on aerodynamic derivatives. *Journal of Wind Engineering and Industrial Aerodynamics*, 91:101–111, 2003.

[58] Robert H. SCANLAN. Amplitude and turbulence effects on bridge flutter derivatives. *Journal of Structural Engineering*, 123:232–236, 1997.

[59] Airong CHEN; Xianfei HE; Haifan XIANG. Identification of 18 flutter derivatives of bridge decks. *Journal of Wind Engineering and Industrial Aerodynamics*, 90:2007–2022, December, 2002.

[60] Xinzhing CHEN; Masaru MATSUMOTO; Ahsan KAREEM. Aerodynamic coupling effects on flutter and buffeting of bridges. *Journal of Engineering Mechanics*, 126:17–26, 2000.

[61] Xinzhong CHEN; Ahsan KAREEM. Identification of critical structural modes and flutter derivatives for predicting coupled bridge flutter. *Journal of Wind Engineering and Industrial Aerodynamics*, 96:1856–1870, 2008.

[62] Andreas G.JENSEN; Rüdiger HÖFFER. Flat plate flutter derivatives – an alternative formulation. *Journal of Wind Engineering and Industrial Aerodynamics*, 74-76:859–869, 1998.

[63] A.ZASSO. Flutter derivatives: Advantages of a new representation convention. *Journal of Wind Engineering and Industrial Aerodynamics*, 60:35–47, 1996.

[64] Andreas G.JENSEN. Fluid dynamic derivatives: Marine and wind engineering approaches. *Journal of Wind Engineering and Industrial Aerodynamics*, 69-71:777–793, 1997.

[65] P.P.SARKAR. *New identification methods applied to the response of flexible bridges to wind*. The Johns Hopkins University. Ph.D. Thesis, Baltimore, Maryland, USA, 1992.

[66] Ming GU; Ruoxue ZHANG; Haigan XIANG. Parametric study on flutter derivatives of bridge decks. *Engineering Structures*, 23:1607–1613, 2001.

[67] J.Bogunović JAKOBSEN; E.HJORTH-HANSEN. Determination of the aerodynamic derivatives by a system identification method. *Journal of Wind Engineering and Industrial Aerodynamics*, 57:295–305, 1995.

[68] T.KUMARASENA; Robert H.SCANLAN; Fazl EHSAN. Recent observations in bridge deck aeroelasticity. *Journal of Wind Engineering and Industrial Aerodynamics*, 40:225–247, 1992.

[69] S.STOYANOFF; G.L.LAROSE. Identification of aerodynamic derivatives: A parametric study. *International Coloquium, BBAA V*, 2004.

[70] N.K.POULSEN; A.DAMSGAARD; T.A.REINHOLD. Determination of flutter derivatives for the great belt bridge. *Journal of Wind Engineering and Industrial Aerodynamics*, 41-44:153–164, 1992.

[71] Partha P.SARKAR; Nicholas P.JONES; Robert H.SCANLAN. System identification for estimation of flutter derivatives. *Journal of Wind Engineering and Industrial Aerodynamics*, 41-44:1243–1254, 1992.

[72] Ming GU; Xian-Rong QIN. Direct identification of flutter derivatives and aerodynamic admittances of bridge decks. *Engineering Structures*, 26:2161–2172, 2004.

[73] R.H. SCANLAN; N.P. JONES; L. SINGH. Inter-relations among flutter derivatives. *Journal of Wind Engineering and Industrial Aerodynamics*, 69-71:829–837, 1997.

[74] M. MATSUMOTO; Y. NIIHARA; Y. KOBAYASHI; H. SHIRATO. Flutter characteristics of bluff bodies. *1st International Conference on Flow Interaction*, 1994.

[75] M. MATSUMOTO; Y. KOBAYASHI; Y. NIIHARA; H. SHIRATO; H. HAMASAKI. Flutter mechanism and its stabilization of bluff bodies. *Proceedings of 9ICWE*, 1995.

[76] Y. DAITO; M. MATSUMOTO; K. ARAKI. Torsional flutter mechanism of two-edge girders for long-span cable-stayed bridge. *Journal of Wind Engineering and Industrial Aerodynamics*, 90:2127–2141, 2002.

[77] M.MIYAZAKI; M.ITO. Effect of under-girder clearance on aerodynamic response of box girders. *Journal of Wind Engineering and Industrial Aerodynamics*, 33:377–384, 1990.

[78] Masaru MATSUMOTO; Kazumasa OKUBO; Yasuaki ITO; Hisato MATSUMIYA; Ginam KIM. The complex branch characteristics of coupled flutter. *Journal of Wind Engineering and Industrial Aerodynamics*, 96:1843–1855, 2008.

[79] Masaru MATSUMOTO; Hiromichi SHIRATO; Keisuke MIZUNO; Rikuma SHIJO; Tetsuya HIKIDA. Flutter characteristics of h-shaped cylinders with various side-ratios and comparisons with characteristics of rectangular cylinders. *Journal of Wind Engineering and Industrial Aerodynamics*, 96:963–970, 2008.

[80] T.MIYATA; H.YAMADA. Coupled-flutter estimate of a suspension bridge. *Journal of Wind Engineering and Industrial Aerodynamics*, 33:341–348, 1990.

[81] Arne SELBERG. Oscillation and aerodynamic stability of suspension bridge. *Civil Engineering and Building Construction Series*, 13:1–69, 1961.

[82] M. MATSUMOTO; N. SHIRAISHI; H. SHIRATO; K. SHIGETAKA; Y. NIIHARA. Aerodynamic derivatives of coupled/hybrid flutter of fundamental structural sections. *Journal of Wind Engineering and Industrial Aerodynamics*, 49:575–584, 1993.

[83] H.G. KUSSNER. Zusammenfassender bericht über den instationären auftrieb von flügeln. *Luftfahrtforschung Bd. 13*, pages 410–424, 1936.

[84] Th. VON KÀRMÀN; W.R. SEARS. Airfoil theory for non-uniform motion. *Journal of the Aeronautical Sciences*, 5:379–390, 1938.

[85] J. PANDA; K.N.M.Q. ZAMAN. Experimental investigation of the flow field of an oscillating airfoil and estimation of lift from wake surveys. *Journal of Fluid Mechanics*, 265:65–95, 1994.

[86] Jiankun YUAN. *Circulation Methods in Unsteady and Three-dimensional Flows*. Doctor Degree Dissertation in Mechanical Engineering, Faculty of the Worcester Polytechnic Institute, March, 1994.

[87] Christopher JOHNSTON. Review, extension, and application of unsteady thin airfoil theory. *CIMMS Report No.04-101*, August, 2004.

[88] Mac GAUNNA. Unsteady 2d potential-flow forces on a thin variable geometry airfoil undergoing arbitrary motion. *RISO-R-1478(EN)*, July, 2006.

[89] W.J. McCROSKEY. Unsteady airfoils. *Annual Reviews of Fluid Mechanics*, 5:285–311, 1982.

[90] Rajendra K. BERA. A new look at theodorsen‘s method in airfoil theory. *International Journal for Numerical Methods in Fluids*, pages 251–262, 1989.

[91] William R. SEARS. Some aspects of non-stationary airfoil theory and its practical application. *AIAA Journal*, 8:104–108, 1941.

[92] Theodore THEODORSEN; I.E.GARRICK. Mechanism of flutter - a theoretical and experimental investigation of the flutter problem. *NACA Report No. 685*, 1940.

[93] Robert H. SCANLAN; Jean-Guy BÉLIVEAU; Kathleen S. BUDLONG. Indicial aerodynamic functions for bridge decks. *Journal of the Engineering Mechanics Division*, pages 657–672, 1974.

[94] Arne SELBERG; Erik HJORTH-HANSEN. The fate of flat plate aerodynamics in the world of bridge decks. *Proceedings of the Theodorsen Colloquium*, 1976.

[95] Julian H. ALLEN. A simplified method for the calculation of airfoil pressure distribution. *Technical Notes - National Advisory Committee for Aeronautics No.708*, May, 1939.

[96] W.J. McCROSKEY. Inviscid flowfield of an unsteady airfoil. *AIAA Journal*, 11:1130–1137, 1973. AIAA 5th Fluid and Plasma Dynamics Conference, June 26-28, 1972.

[97] Haruo YOSHIKI; Nobuhisa KAMIKAWA; Yasukata TUITSUI; Nobuyuki TAKAMA. Pressure distributions around an airfoil placed in periodically fluctuating air flow. *Bulletin of JSME No.230*, 27:1592–1597, 1984. 1^{st} Report, a Flat Plate Approximation.

[98] Y.CHEN; G.A.KOPP; D.SURYY. Interpolation of wind-induced pressure time series with an artificial neural network. *Journal of Wind Engineering and Industrial Aerodynamics*, 90:589–615, 2002.

[99] Y.CHEN; G.A.KOPP; D.SURYY. Prediction of pressure coefficients on roofs of low buildings using artificial neural networks. *Journal of Wind Engineering and Industrial Aerodynamics*, 91:423–441, 2003.

[100] S.R.MUNSHI; V.J.MODI; T.YOKOMIZO. Aerodynamics and dynamics of rectangular prisms with momentum injection. *Journal of Fluids and Structures*, 11:873–892, 1997.

[101] G.L.LAROSE; A.D'Auteuil. On the reynolds number sensitivity of the aerodynamics of bluff bodies with sharp edges. *Journal of Wind Engineering and Industrial Aerodynamics*, 94:365–376, 2006.

[102] Allan LARSEN. Advances in aeroelastic analyses of suspension and cable-stayed bridges. *Journal of Wind Engineering and Industrial Aerodynamics*, 74-76:73–90, 1998.

[103] C.G.BUCHER; Y.K.LIN. Effects of wind turbulence on motion stability of long-span bridges. *Journal of Wind Engineering and Industrial Aerodynamics*, 89:619–632, 2001.

[104] Haruo YOSHIKI; Nobuhisa KAMIKAWA; Yasukata TUITSUI; Nobuyuki TAKAMA. Pressure distributions around an airfoil placed in periodically fluctuating air flow. *Bulletin of JSME No.246*, 28:1592–1597, 1985. 2^{nd} report.

[105] P.J.SAATHOFF; W.H.MELBOURNE. The generation of peak pressures in separated/reattaching flows. *Journal of Wind Engineering and Industrial Aerodynamics*, 32:121–134, 1989.

[106] M.KIYA; K.SASAKI. Free-stream turbulence effects on a separation bubble. *Journal of Wind Engineering and Industrial Aerodynamics*, 14:375–386, 1983.

[107] Masaru MATSUMOTO; Tetsuya HIKIDA; Keisuke MIZUNO. On improvement of flutter stability for long-span bridge girders - the case of separated box girders. *Flow Induced Vibration*, July, 6-9th, 2004.

[108] Y.SAKAI; K.OGAWA; H.SHIMODOI; T.SAITOH. An experimental study on aerodynamic improvements for edge girder bridges. *Journal of Wind Engineering and Industrial Aerodynamics*, 49:459–466, 1993.

[109] F.NAGAO; H.UTSUNOMIYA; T.ORYU; S.MANABE. Aerodynamic efficiency fo triangular fairing on box girder bridge. *Journal of Wind Engineering and Industrial Aerodynamics*, 49:565–574, 1993.

[110] T.YOSHIMURA; Y.MIZUTA; M.G.SAVAGE; G.LIU. Half-circular and half-elliptic edge modifications for increasing aerodynamic stability of stress-ribbon pedestrian bridges. *Journal of Wind Engineering and Industrial Aerodynamics*, 69-71:861–870, 1997.

[111] Dryver R. HUSTON; Harold R. BOSCH; Robert H. SCANLAN. The effetcs of fairings and of turbulence on the flutter derivatives of notably unstable bridge deck. *Journal of Wind Engineering and Industrial Aerodynamics*, 29:339–349, 1988.

[112] M.EL-GAMMAL; H.HANGAN; P.KIN. Control of vortex shedding-induced effects in a sectional bridge model by spanwise perturbation method. *Journal of Wind Engineering and Industrial Aerodynamics*, 95:663–678, 2007.

[113] Abe SILVERSTEIN; Upshur T. JOYNER. Experimental verification of the theory or oscillating airfoils. *NACA Report No. 673*, 1939.

[114] Y.KUBO; K.HIRATA. Aerodynamic responses and pressure function of shallow h-section cylinder. *Journal of Wind Engineering and Industrial Aerodynamics*, 33:123–130, 1990.

[115] T. TAMURA; Y. ITOH; A. WADA; K. KUWAHARA. Numerical study of pressure fluctuations on a rectangular cylinder in aerodynamic oscillation. *Journal of Wind Engineering and Industrial Aerodynamics*, 54/55:239–250, 1995.

[116] H.SHIRATO; M.MATSUMOTO. Unsteady pressure evaluation on oscillating bluff body by vortex method. *Journal of Wind Engineering and Industrial Aerodynamics*, 67-68:349–359, 1997.

[117] J.V.SEGURO; T.W.LAMBERT. Modern estimation of the parameters of the weibull wind speed distribution fo energy analysis. *Journal of Wind Engineering and Industrial Aerodynamics*, 85:75–84, 2000.

[118] Hiroshi SATO; Nobuyuki HIRAHARA; Koichiro FUMOTO; Shigeru HIRANO; Shigeki KUSUHARA. Full aeroelastic model test of a super long-span bridge with slotted box girder. *Journal of Wind Engineering and Industrial Aerodynamics*, 90:2023–2032, 2002.

[119] M.PECORA; L.LECCE; F.MARULO; D.P.COIRO. Aeroelastic behaviour of long span bridges with "multibox" type deck sections. *Journal of Wind Engineering and Industrial Aerodynamics*, 48:343–358, 1993.

[120] H.SATO; R.TORIUMI; T.KUSAKABE. Aerodynamic characteristics of slotted box girders. *Proceeding of Bridges into the* 21^{st} *century*, pages 721–728, 1995.

[121] Yongxin YANG; Yaojun GE; Haifan XIANG. Flutter control effect and mechanism of central-slotting for long-span bridges. *Front.Archit.Civ.Eng.*, 1(3):298–304, 2007.

[122] G.DIANA; M.FALCO; S.BRUNI; A.CIGADA; G.L.LAROSE; A.DAMSGAARD; A.COLLINA. Comparisons between wind tunnel tests on a full aeroelastic model of the proposed bridge over stretto di messina and numerical results. *Journal of Wind Engineering and Industrial Aerodynamics*, 54/55:101–113, 1995.

[123] A.ZASSO; A.CIGADA; S.NEGRI. Flutter derivatives identification through full bridge aeroelastic model transfer function analysis. *Journal of Wind Engineering and Industrial Aerodynamics*, 60:17–33, 1996.

[124] P.J.SAATHOFF; W.H.MELBOURNE. Effects of free-stream turbulence on surface pressure fluctuations in a separation bubble. *Journal of Fluid Mechanics*, 337:1–24, 1997.

[125] M.MATSUMOTO; K.ABE; N.NAKAJIMA; Y.TANIWAKI. Flutter characteristics of 2-box girders for super-long span bridges. *Proceedings of the 7th International Conference on Flow-Induced Vibration*, pages 157–164, 19-22 June 2000.

[126] Allan LARSEN; Mike SAVAGE; Andréane LAFRENIÈRE; Michael C.H.HUI; Søren V.LARSEN. Investigation of vortex response of a twin box bridge section at high and low reynolds numbes. *Journal of Wind Engineering and Industrial Aerodynamics*, 96:934–944, 2008.